



The
University
Of
Sheffield.

A Distortion Modelling Method for Aerospace Wing Structures

Andrew Cooper

A thesis submitted in partial fulfilment of the requirements for the degree of
Doctor of Engineering

The University of Sheffield
Faculty of Engineering
Department of Mechanical Engineering

April 2023

Abstract

Distortion in large monolithic aircraft wing rib components is a recurring issue for aerospace manufacturers globally. Excessive distortion in these components has resulted in high levels of concession, rework and scrap due to failing geometric tolerance limits on inspection. Vast business capital is lost through scrap or corrective treatments to bring distorted components back in line with the design intent. Distortion in machined components is caused by the redistribution of bulk residual stresses after material removal and the introduction of machining-induced residual stresses due to the high thermal and mechanical loads imparted by the cutting action. Modelling of distortion due to residual stresses can be achieved using numerical tools that account for these sources of residual stress.

A detailed literature review has been conducted to understand the sources of residual stresses and their influence on distortion. Additionally, the review focused on the current state-of-the-art modelling of residual stress-related machining distortion. From the review of previous work, a series of objectives were conceived to address the gaps in knowledge on the impact of machining strategy on residual stress formation and part distortion and to develop a modelling technique capable of simulating both residual stress-related distortion and distortion-related part quality issues.

The developed modelling concept was designed as a multi-step simulation process with machining-induced stress defined as a function of the tool path strategy. The simulation concept can account for the bulk and machining-induced stress influence on inter-process and post-process distortion. Experimental trials were conceived and conducted to explore the influence of machining sequencing on machining-induced residual stress formation, where no influence on the final machining-induced stress was found under the developed test regime. Furthermore, machining trials were conducted to understand tool path strategy selection and the influence of inter-process machining conditions on machining-induced stress formation. It was determined that tool path strategy significantly influences the machining-induced stress state in the component, and machining-induced residual stresses vary according to local cutting condition variations, although only in very localised regions for the trialled cutter path. The developed modelling method has been validated against other methods from literature and against experimental trials where the machining of a representative component has been conducted and the distortion measurements captured for comparison to the numerical results.

Acknowledgements

I am incredibly grateful to my supervisory team Dr Christophe Pinna, Dr Sabino Ayvar-Soberanis and Dr Panos Efthymiadis, for the guidance and technical discussions during the project. I very am grateful to Professor Wouter Wilson & Job Eilander, whose technical support was invaluable to the project. Many thanks to Dr Dan Graham for providing me with the opportunity and guidance towards completing the EngD.

I also thank the IDC machining science management for the support and developmental opportunities provided throughout the project. I would also like to acknowledge the Engineering and Physical Science Research Council (EPSRC) for the financial support and GKN Aerospace for both financial and technical support for the work.

Lastly, I would like to thank my partner, daughter, parents and all my family, who sacrificed time spent together to make this work a reality. Their unwavering support helped keep me going during periods of personal challenge. Without them all, I simply would not have persevered.

List of contents

Abstract.....	ii
Acknowledgements.....	iii
List of contents.....	iv
List of Figures	vi
List of Tables	xi
Nomenclature	xii
Declaration.....	xv
1 Introduction	1
1.1 Background	1
1.2 Scope & Research Objectives.....	4
1.3 Organisation of the Thesis	6
2 Literature review.....	7
2.1 Machining of aerospace structural components	7
2.2 Aluminium in aerospace applications.....	16
2.3 Residual stress and Distortion	20
2.4 Measurement of residual stress	26
2.5 Sources of residual stress and impact on distortion in machining	32
2.6 Modelling and simulation of residual stress and part distortion.....	61
2.7 Concluding statements	82
3. Objectives and methods	84
3.1. Numerical modelling.....	85
3.2. Experimental investigations.....	90
3.3. Concluding statements	91
4. Distortion Modelling Procedure	92
4.1. The finite element method	92
4.2. Distortion modelling procedures	98

4.3.	Distortion modelling execution	114
4.4.	Concluding statements	124
5	Experimental methods.....	125
5.1	Experimental Rationale.....	125
5.2	Influence of sequential machining operations on machining-induced residual stress	131
5.3	Influence of local cutting conditions variations on MIRS.....	141
5.4	Bulk residual stress layer removal method.....	149
5.5	Distortion demonstrator machining trials	153
5.6	Concluding statements	163
6	Experimental Results & Discussions	164
6.1	Sequential machining influence on MIRS	164
6.2	Influence of local cutting conditions variations on MIRS.....	167
6.3	Bulk residual stress measurements	187
6.4	Distortion demonstrator machining trials	188
6.5	Concluding statements	193
7	Modelling Results & Discussions.....	195
7.1	Validating the MIRS concept against a different modelling methodology.....	195
7.2	Modelling residual stresses.....	203
7.3	Modelling Component Distortion	212
7.4	Comparing modelling methodologies.....	226
7.5	Concluding statements	235
8	Conclusion & Outlook	237
8.1	Conclusion.....	237
8.2	Outlook	239
	References	242
	Appendix A.....	254

List of Figures

Figure 1-1: Airbus projected deliveries [2].....	1
Figure 1-2: Typical structure of aircraft wing [8]	3
Figure 1-3: Machining of wing rib [9].....	4
Figure 1-4: Modelling workflow for distortion modelling [12]	4
Figure 2-1: Various machining methods categorisation based on energy consumption [13].....	7
Figure 2-2: Chip formation by way of machining [14]	8
Figure 2-3: end milling [17] (left) & Grinding wheel [18] (right).....	9
Figure 2-4 Orthogonal plane chip formation [21].....	10
Figure 2-5: Merchant's Circle diagram [22]	10
Figure 2-6: Milling cutting forces; in the work piece coordinates (left) and tool coordinates (right) [24].	11
Figure 2-7: Measuring milling cutting forces by dynamometer [25]	12
Figure 2-8: Face milling trial schematic (left) and cutting forces measured by dynamometer (right) [27]	12
Figure 2-9: Stages of Machining Aerospace structural component (images from [28]–[30])	13
Figure 2-10: Milling process types [21].....	14
Figure 2-11: The digital process chain for CNC machining	15
Figure 2-12: (left) Hall-Hérault process and (right) Direct chill casting methods [31].....	16
Figure 2-13: Aluminium alloy & temper designation system [31].....	17
Figure 2-14: Diagram of the phase transformation displaying the solution treatment, quenching and ageing temperatures accompanied by precipitation across the resulting grain structure (left). Typical heat treatment time plot for T6 material condition (right).	18
Figure 2-15: FCC crystal lattice structure (left) & Miller indices slip planes (right) [39],[40]	20
Figure 2-16: Stresses acting at a point [43]	21
Figure 2-17: Residual stress fields length scales [46].....	22
Figure 2-18: Effects of residual stress in metallic components [10].....	23
Figure 2-19: The coupling effect of residual and external stresses [47].....	24
Figure 2-20: (Top) Component location in stock material with an indication of residual stress field, and (bottom) distorted component post material removal [48].....	25
Figure 2-21: wing box rib on granite surface table under own weight.....	25
Figure 2-22: Residual stress measurement techniques [52].....	26
Figure 2-23: Layer removal [10].....	27
Figure 2-24: Crack compliance method with strain gauge location [35]	28
Figure 2-25: Semi-destructive measurement methods (a) centre-hole drilling (b) ring core (c) Deep hole drilling [52].....	29
Figure 2-26: Bragg's law [52].....	30
Figure 2-27: Through thickness ultrasonic measurement configurations [52].....	31
Figure 2-28: Capabilities of destructive and non-destructive measurement [61].....	32
Figure 2-29: Difference in cooling rates between the surface and centre of an aluminium plate during quench	33
Figure 2-30: Bulk residual stress profile in 77.9mm thick AA7050-T7451 after stretch stress relief [35]..	34
Figure 2-31: Impact of quench process on bulk residual stress and distortion [62]	36
Figure 2-32: Offset of T-specimen produced in the trials conducted by Zhang et al. [67]	37
Figure 2-33: effects of mechanical (left) and thermal (right) loads on residual stress formation [19]	39
Figure 2-34: The layers over which the thermo-mechanical induced residual stress form behind the tool [73].....	39
Figure 2-35: Subsurface RS profile induced by machining [74]	40
Figure 2-36: 3 cases for machining-induced residual stress profiles [75].....	40

Figure 2-37: Machining-induced residual stress generation process [12].....	41
Figure 2-38: Graphs depicting the effects of cutting speed (top left), Feed per tooth (top right), coolant (middle) and corner radius on machining-induced residual stress formation (bottom) [78]	44
Figure 2-39: Varying contact lengths (shown as red) for different micro geometries	45
Figure 2-40: Effects of corner radius on surface and subsurface temperature (left) and stress in the through-thickness of the part (right) [62].....	46
Figure 2-41: compressive residual stress generating tool [74].....	48
Figure 2-42: (top) max cutting force & max temperature vs. flank wear (left) residual stress profile perpendicular to feed (right) residual stress profile parallel to feed [89]	50
Figure 2-43: Li et al. [86] (a) impact of DoC on cutting forces and temperature (b) the experimental set-up and DoC.....	52
Figure 2-44: Sequential cut FEM (left) and normal stresses (right) [18].....	53
Figure 2-45: Sequential DoC for orthogonal turning and planning [84]	54
Figure 2-46: variable MIRS profiles (left) and influence on final part distortion (right) [99].....	55
Figure 2-47: The process of shot peening [106]	56
Figure 2-48: Smart picture frame fixture [108].....	58
Figure 2-49: Fixture system for low-stress machining [111].....	58
Figure 2-50: Influence of machining-induced stresses on flat plate distortion [6].....	60
Figure 2-51: Important considerations for part distortion in aerospace components [97]	61
Figure 2-52: Bulk stress FE model [114].....	62
Figure 2-53: AdvantEdge face milling [137].....	65
Figure 2-54: Schematic diagram of a simple fuzzy system [140]	67
Figure 2-55: Results of the fuzzy model [140]	67
Figure 2-56: Master fuzzy system (left) modelling space (right) [141]	67
Figure 2-57: (a) Feed Forward and (b) Radial Basis Function ANN Structures (Matlab) [143]	68
Figure 2-58: Various material removal techniques.....	70
Figure 2-59: Work flow for distortion mitigation [66]	71
Figure 2-60: Boolean deletion procedure [148]	72
Figure 2-61: FEM model taking into consideration the bulk and MIRS [121].....	73
Figure 2-62: FEM strategy for coupled analysis (left) and AdvantEdge FEM (right) [98]	74
Figure 2-63: Distortion simulation structure [3]	75
Figure 2-64: Tool path MIRS (a) and effect of machining strategy on component distortion (b) [3].....	75
Figure 2-65:Modelling scheme from [145]	76
Figure 2-66: Boolean operations with the localised re-meshing procedure [144].....	77
Figure 2-67: FEM distortion mapping by machining induced stress determined by fuzzy model [156]	78
Figure 3-1: Proposed implementation of the FEM distortion model in the process programming phase	87
Figure 3-2: Data passing schematic for integrated process modelling.....	87
Figure 4-1: Processes associated with FEA [159].....	92
Figure 4-2: ABAQUS solid continuum element types [161]	96
Figure 4-3: Bulk residual stresses applied to the billet with respects to coordinate system	99
Figure 4-4: Boolean removal of pocket from machined component	101
Figure 4-5: Boolean part clean up procedure	102
Figure 4-6: Mesh refinement of boundary layer	103
Figure 4-7: Process flow for generating MIRS element candidate set.....	105
Figure 4-8: Swept tool volume.....	106
Figure 4-9: Tool path mesh identification routine	107
Figure 4-10: Types of work holding utilised in this work	109
Figure 4-11: 6 degrees of freedom	109

Figure 4-12: 3-2-1 constraint [162].....	110
Figure 4-13: Surface-to-surface contact [161].....	111
Figure 4-14: Hard contact behavior [161].....	112
Figure 4-15: effect of contact overclosure on Boolean operation.....	113
Figure 4-16: Distortion modelling process.....	115
Figure 4-17: Machining simulation Python script processes	116
Figure 4-18: Solution transfer between elements.....	117
Figure 4-19: Application of MIRS as a function of the tool path progression	118
Figure 4-20: Assignment of the MIRS in the boundary layer.....	119
Figure 4-21: Application of user subroutines and key words in ABAQUS/standard execution.....	120
Figure 4-22: Process of inter-stage fixturing.....	122
Figure 5-1: Example of sequential DoC machining	126
Figure 5-2: Depth of cut and MIRS affected zone.....	126
Figure 5-3: Chip thinning effect: (a) at 50% tool diameter engagement; (b) <50% tool engagement; and (c) increased feed rate to maintain chip load.....	128
Figure 5-4: Variable cutter engagement: (a) straight line cutting: and (b) corner cutting	128
Figure 5-5: Pocket geometry where; W = width, L = Length & D = Depth.....	129
Figure 5-6: Conventional pocket milling tool paths; (a) zigzag, (b) helical spiral & (c) unidirectional.....	130
Figure 5-7: TPC1 test piece design	134
Figure 5-8: TPC1 bolting sequence diagram (a) and bolted to machine bed (b).....	134
Figure 5-9: Sequential machining coupon (a) initial configuration (b) first roughing pass (c) n roughing pass (d) after finish machining.....	135
Figure 5-10: TPC1 ICHD measurement locations (dashed red lines indicate tool centre path)	136
Figure 5-11: 45° Strain gauge rosette schematic with respects to the relieved strain orientation.....	137
Figure 5-12: ICHD strain gauge specification	140
Figure 5-13: ICHD drilling: location of the measurement position (a), application/alignment of the strain gauge rosette (b), and locating the zero depth (c)	141
Figure 5-14: helical roughing (a) Dynamic Roughing (b) and helical finishing tool paths (c).....	142
Figure 5-15: MIRS pocket coupon stock condition	143
Figure 5-16: MIRS pocket coupon design	143
Figure 5-17: Kennametal Kor 5 solid carbide (a) Walter roughing (b) and Walter finishing tool (c).....	144
Figure 5-18: Experimental setup.....	145
Figure 5-19: ICHD drilling rig.....	146
Figure 5-20: Measurement of surface stresses by XRD	148
Figure 5-21: Electro-polishing (a) and CMM measurements (b)	149
Figure 5-22: Diagram of layer removal method: (a) test setup; (b) milling of the test sample; and (c) process of clamp release and beam deflection measurement	150
Figure 5-23: TPC2 stock material and stress measurement coupons map (all dimensions in “).....	152
Figure 5-24: Distortion demonstrator.....	153
Figure 5-25: Demonstrator stock condition (all dimensions in mm)	153
Figure 5-26: Demonstrator design dimensions (all dimensions in mm).....	154
Figure 5-27: Stage 1 machining of distortion demonstrator component; (a) rough face milling; (b) finish face milling; and (c) drilling stage 2 bolt holes	154
Figure 5-28: Stage 2 face milling operation	156
Figure 5-29: Stage 2 pocket milling; (a) roughing and (b) finishing	156
Figure 5-30: Stage 2 machining of break-off tabs.....	157
Figure 5-31: Stage 1 fixture configuration diagram.....	158
Figure 5-32: TPC2 stage 1 work holding on machine.....	158

Figure 5-33: TPC2 stage 2 part design.....	159
Figure 5-34: Bolting of TPC2 stage 2 (a) and repeat bolting sequence (b)	159
Figure 5-35: End of TPC2 stage 2 machining.....	160
Figure 5-36: DTI distortion measurement schematic diagram	161
Figure 5-37: Position of TPC2 stage 1 distortion measurement locations.....	161
Figure 5-38: TPC2 stage 1 distortion measurements on CMM.....	162
Figure 5-39: TPC2 stage 2 CMM measurement lines.....	162
Figure 5-40: TPC2 stage 2 measurement 3-2-1 boundary conditions (a) and location of ground blocks providing Z displacement boundary conditions (b)	163
Figure 6-1: MIRS profile description	164
Figure 6-2: TPC1-4 repeat measurements.	165
Figure 6-3: Standard deviation of the ICHD repeat measurements versus depth.	165
Figure 6-4: Roughing MIRS.....	166
Figure 6-5: Variable machining DoC MIRS	167
Figure 6-6: Conventional roughing cutting force.....	168
Figure 6-7: Conventional roughing tool path cutting at a corner (a) and a straight pass (b)	169
Figure 6-8 Dynamic roughing cutting force	170
Figure 6-9: Coupon 7 floor machining cutting forces	171
Figure 6-10: Coupon 8 floor machining cutting forces	171
Figure 6-11: Coupon 8 symmetry check measurements	172
Figure 6-12: Coupon 8 machining induced residual stress profiles	173
Figure 6-13: ICHD measurement points for coupons 6, 7 & 8.....	174
Figure 6-14: Replicate measurement results.....	174
Figure 6-15: Coupon 4 outward helical roughing machining induced residual stresses	176
Figure 6-16: Coupon 2 Dynamic roughing machining induced residual stresses	178
Figure 6-17: Coupon 7 machining induced residual stress measurement locations and profiles.....	180
Figure 6-18: XRD measurement locations and stress profiles for coupon 7	182
Figure 6-19: Straight line composite curve finish machining.....	183
Figure 6-20: Corner point composite curve finish machining	183
Figure 6-21: Debye 2D diffraction patterns for (a)mild carbon steel 1018 and (b) aluminum 6061 [176]	184
Figure 6-22: Example Debye rings of (a) non-uniformity and (b) improved uniformity from [176] and (c) Debye ring from pocket machining experiment coupon measurement (location C7 P10 – see figure 6-18)	185
Figure 6-23: Residual stress in Kaiser 7050 T7651 plate.....	188
Figure 6-24: Average stage 1 measured deflection profiles	189
Figure 6-25: TPC2 Stage 1 peak distortion.....	189
Figure 6-26: TPC2 stage 2 distortion measurements.....	190
Figure 6-27: TPC2 Stage 2 peak & average distortion	190
Figure 6-28: Stages of bulk residual stress release during stage 1 machining; (a) initial clamped condition; (b) the material removed in the clamped condition; and (c) residual stress redistribution after clamp release.....	192
Figure 7-1: Cantilever beam [150]	198
Figure 7-2: Comparison of the analytical and numerical MIRS modelling methods [150]	199
Figure 7-3: Dreier's function 1 MIRS profile [150]	200
Figure 7-4: Beam bending due to MIRS using the Dreier method of stress implementation.	200
Figure 7-5: Dreier method applied MIRS values extracted from the FEM model.	201

Figure 7-6: Beam bending due to MIRS using the UMAT method of stress implementation developed in this work.	202
Figure 7-7: UMAT applied MIRS stress values extracted from FEM model.	202
Figure 7-8: Longitudinal and long-transverse bulk stress data and fits	204
Figure 7-9: FEM longitudinal bulk stress.....	205
Figure 7-10: FEM long-transverse bulk stress.....	205
Figure 7-11: face milling MIRS data and fits in (a) feed direction; and (b) normal direction.	207
Figure 7-12: end milling MIRS data in (a) feed direction; and (b) normal direction.....	208
Figure 7-13: Flat plate boundary layer test (left) plate design and (right) deformed plate due to MIRS (deformed scale = 100)	209
Figure 7-14: FEM vs Fit face milling MIRS	210
Figure 7-15: Peak distortion vs boundary layer discretisation for face milling MIRS	210
Figure 7-16: FEM vs Fit end milling MIRS.....	211
Figure 7-17: Peak distortion vs boundary layer discretisation for end milling MIRS.....	212
Figure 7-18: Various mesh densities trialed for the mapping of bulk residual stresses.....	214
Figure 7-19: Longitudinal residual stresses extracted from various mesh refinements against the data set	214
Figure 7-20: Long-transverse residual stresses extracted from various mesh refinements against the data set.....	214
Figure 7-21: Boolean removal for stage 1 machining operations.....	215
Figure 7-22: Peak distortion vs global seeding size	215
Figure 7-23: Boolean removal for stage 2 machining operations.....	216
Figure 7-24: Development of the component displacement post-material removal.....	217
Figure 7-25: Tool path MIRS applied in the distortion modelling.....	218
Figure 7-26: Nodal selection following stage 1 face milling simulation.	219
Figure 7-27: Nodal selection during stage 2 pocket one end milling simulation.....	219
Figure 7-28: Stage 1 boundary conditions	220
Figure 7-29: Stage 2 model boundary conditions	221
Figure 7-30: 3-2-1 boundary conditions applied to the distortion demonstrator component.	222
Figure 7-31: Stage 1 nodal displacement lines with reference to the measured profiles.....	223
Figure 7-32: Stage 2 nodal displacement lines with reference to the measured profiles.....	223
Figure 7-33: Stage 1 CMM vs FEM distortion	224
Figure 7-34: Stage 2 CMM vs FEM distortion	225
Figure 7-35: Recreating Dreier's modelling method where: (a) is the part geometry; (b) the mesh; and (c) the distorted model	227
Figure 7-36: Comparison of stage 2 simulation results against CMM measurement profile line 'A'	229
Figure 7-37: Comparison of stage 2 simulation results against CMM measurement profile line 'B'	230
Figure 7-38: Comparison of stage 2 simulation results against CMM measurement profile line 'C'	230
Figure 7-39: Thickness inspection lines: wall 1 (W1); Wall 2 (W2); and Floor (F).....	231
Figure 7-40: Identification of wall and floor thicknesses.....	231
Figure 7-41: W1 - wall thicknesses.....	232
Figure 7-42: W2 - wall thicknesses.....	233
Figure 7-43: Distortion in U2 (Y coordinate) after machining simulation step 7.....	233
Figure 7-44: Distortion in U2 (Y coordinate) after machining simulation step 8.....	233
Figure 7-45: F – Floor Thickness.....	234
Figure 7-46: COPEN identifying gaps between the bottom of the machined component and machined bed	235

List of Tables

Table 2-1: wt% alloying elements for AA7050 & AA7010 [33], [34]	17
Table 2-2: T7651 Supply condition	17
Table 2-3: Sinusoidal variables ranges	64
Table 2-4: A comparison of key distortion modelling research methods.....	80
Table 2-5: Key distortion modelling research reported measurement methods and model accuracy.....	81
Table 3-1: Strengths and weaknesses of FE modelling methods.....	85
Table 4-1: Elastic material properties	108
Table 5-1: 7050 T7651 material properties	132
Table 5-2: 7050 T7651 alloy composition	132
Table 5-3: Face milling cutters	133
Table 5-4: Insert geometry.....	133
Table 5-5: Mitsubishi tool machining parameters	133
Table 5-6: Iscar tool machining parameters	133
Table 5-7: TPC1 Test Matrix	135
Table 5-8: Machining coupon manufacture detail.....	142
Table 5-9: Machining parameters for tools used in trials	144
Table 5-10: Stage 1 test identification and machining DoC.....	155
Table 5-11: stage 2 test identification numbers	157
Table 6-1: Conventional roughing tool path absolute max and average forces.....	168
Table 6-2: Dynamic roughing tool path absolute max and average forces	169
Table 6-3: Dynamic roughing tool path absolute max and average forces	170
Table 7-1: Sinusoidal fit parameters for function 1 [150].....	199
Table 7-2: Longitudinal polynomial coefficients (to 2 DP).....	204
Table 7-3: Long-transverse polynomial coefficients (to 2 DP).....	204
Table 7-4: Face milling SDF parameter values (to 2 DP)	207
Table 7-5: End milling SDF parameter values (to 2 DP)	208

Nomenclature

Latin Symbols

h_{ex}	Chip thickness (mm)
h_l	Lever arm length (mm)
h_r	Boundary layer height (mm)
$\hat{A}(H, h)$	Strain relaxation per unit depth (mm)
M_b	Bending moment (N/m)
V_c	Cutting speed (m/min)
V_f	Feed rate (mm/min)
\bar{a} & \bar{b}	hole drilling coefficients (-)
a_e	Radial engagement (mm)
d_0	Depth of stress affected zone (mm)
d_{max}	Depth of max compressive stress (mm)
f_z	Feed per tooth (mm/tooth)
z_{eff}	Effective number of cutting teeth (-)
F_x, F_y & F_z	Cutting forces in cartesian coordinate system (N/m ²)
F_f, F_{fn} & F_a	Cutting forces in workpiece coordinate system (N/m ²)
F	Active force (N/m ²)
h	Sample height (mm)
x, y, z	Cartesian coordinates (-)
D	Global nodal displacements (-)
K	Global stiffness matrix (-)
L	Matrix of the partial differential (-)
N	Element shape function (-)
U	Displacement field vector (-)
A	Surface Area (m ²)
\bar{A} & \bar{B}	Incremental hole drilling calibration constants (-)
C	Amplitude (MPa)
D	Diameter (mm)
E	Young' modulus (N/m ²)
EA	Engagement angle (°)
F	Force (N)
G	shear modulus (N/m ²)
I	Second moment of area (mm ⁴)
$P(H)$	Mean normal 'pressure' stress (MPa)
$Q(H)$ and $T(H)$	Shear components of the 'pressure' stress (MPa)
Zf	Floor thickness (mm)
b	Width of the beam (mm)
d	Inter-planar spacing (mm)
e	Current sample thickness (mm)
i	Radius of inertia (mm)
k	Position of neutral fibre/axis (mm)
n	Spindle speed (RPM)
p	Measured strain relaxation (μm)
p	Polynomial coefficient (-)

s	Unit length (mm)
$w(x)$	Beam bending (mm)
\mathbf{B}	Strain-displacement matrix (-)
\mathbf{d}	Nodal displacement vector (-)

Greek Symbols

σ	Normal Stress (MPa)
τ	Shear Stress (MPa)
ε	Strain ($\mu\text{m}/\text{m}$)
σ_{Macro}	Macroscopic stresses (MPa)
σ_{II}	Intergranular stresses (Pa)
σ_{III}	Microscopic stresses (Pa)
σ_x	Stress acting in x coordinate (MPa)
σ_y	Stress acting in y coordinate (MPa)
σ_{IBRS}	Bulk residual stress (MPa)
σ_{MIRS}	Machining-induced residual stress (MPa)
σ_{\parallel}	Stress parallel to the feed direction (MPa)
σ_{\perp}	Stress normal to the feed direction (MPa)
σ_0	Surface stress (MPa)
σ_{max}	Max compressive stress (MPa)
σ_M	Bending stress (mm)
ζ	Damping coefficient (-)
ω_d	Damping frequency (mm^{-1})
ω_0	Undamped frequency (mm^{-1})
ϕ	Phase angle ($^{\circ}$)
ρ	Curvature (m^{-1})
ν	Poisson's ratio (-)
β	Angle from max principal stress and strain gauge axis ($^{\circ}$)
θ	Diffraction angle ($^{\circ}$)
λ	X-ray wavelength (m)
α	Azimuthal angle ($^{\circ}$)
η	Angle between the incident beam and diffracted beam ($^{\circ}$)
ψ	Tilt angle ($^{\circ}$)
χ	Shear correction factor (-)

Abbreviations

AI	Artificial intelligence
ANN	Artificial neural network
CAD	Computer-aided Design
CAE	Computer-aided engineering
CAM	Computer-aided Manufacturing
CMM	Coordinate measurement machine
CNC	Computer numerically controlled
DoC	Depth of cut

DoE	Design of experiment
DoF	Degree of freedom
DTI	Dial test indicator
EDM	Electrical Discharge Machining
F	Floor inspection line profile
FE	Finite element
FEM	Finite element model
GD&T	Geometric dimensioning and tolerancing
GMS	Global mesh seeding size
GUI	guided user interface
HEXRD	Synchrotron
ICHD	Incremental hole drilling
L	Longitudinal
LT	Long-transverse
MIRS	Machining-induced residual stress
MQL	Minimum quantity lubrication
PCD	Polycrystalline Diamond
PSO	Particle swarm optimisation
RMSE	Root-mean-square error
RP	Reference point
TOF	Time of flight
TPC	Test piece configuration
W1 & W2	Wall one & Wall two inspection line profile
WCS	Work coordinate system
XRD	X-ray diffraction

Declaration

I, the author, confirm that the Thesis is my own work. I am aware of the University's Guidance on the Use of Unfair Means (www.sheffield.ac.uk/ssid/unfair-means). This work has not been previously been presented for an award at this, or any other, university.

1 Introduction

1.1 Background

The production of commercial aircraft is set to increase in the near future. In 2020, Boeing aerospace forecasted a return to pre-pandemic air traffic levels by 2024 and delivery of 41,170 new aircraft to the market over the next 20 years [1]. Airbus global market forecast for 2022-2041 projects a demand for 39,490 new passenger and freighter aircraft over the same period [2], as highlighted in Figure 1-1. This is despite the aviation market going through a tumultuous period where both the COVID-19 pandemic and Russia’s war on Ukraine having notable impacts on commercial air travel globally in recent years. To provide context, the cost of the COVID pandemic to airline operators was approximately \$324 bill USD [3]. However, due to the requirement to replace old aircraft fleets with a new generation of fuel-efficient and economic aircraft combined with the increase in passenger footfall as the market recovers, the aerospace sector is expected to see renewed market growth. Therefore, manufacturers of aerospace components can expect to see increased manufacturing rates over the coming years.

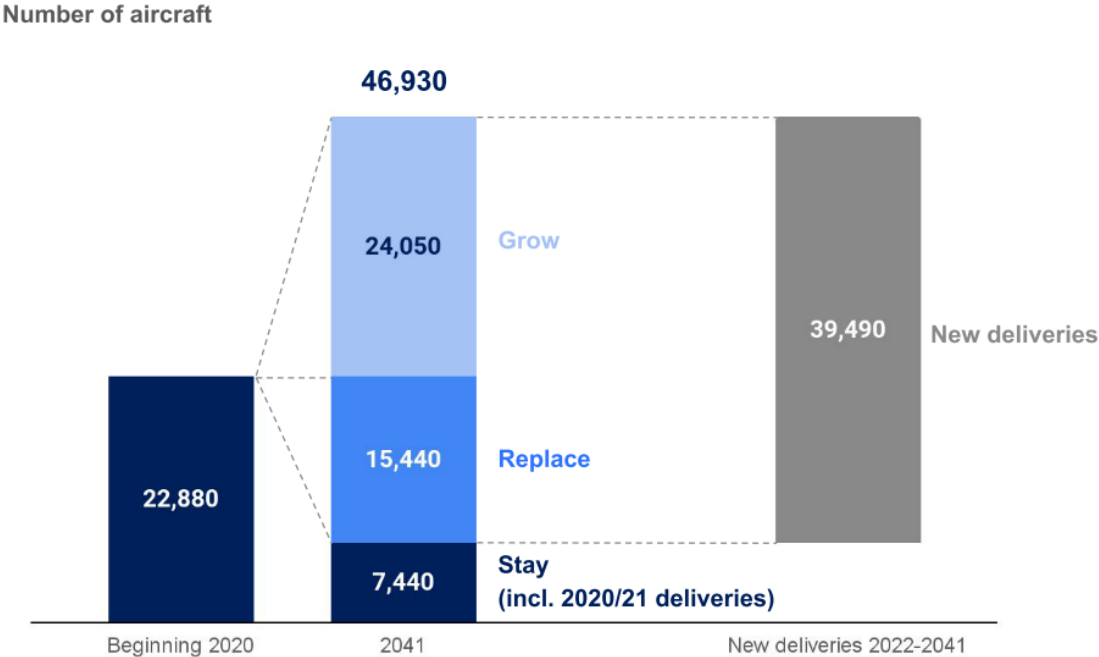


Figure 1-1: Airbus projected deliveries [2]

The aerospace materials market size was valued at \$36.42 billion in 2021 and is forecasted to grow to \$67.42 billion by 2030 [4]. Although composite materials have seen a rapid increase in market share in recent history due to their high strength-to-weight ratio, aluminium still is heavily utilised in short-haul aircraft, largely down to the fatigue performance required for the increased number of airframe loading cycles due to a higher number of take-off and landing compared with longer haul aircraft. Of the 39,490 new aircraft forecasted by Airbus, approximately 80% will be Single-Aisle aircraft. These types of aircraft are approximately 80% aluminium by weight. As one of the largest first-tier suppliers to the global aviation industry, GKN Aerospace LTD is in a strong position to realise the benefits of this projected market growth.

In 2021 GKN Aerospace LTD recorded £2.1 Billion in sales and employs 15,000 people in 38 manufacturing locations in 12 countries [5]. GKN Aerospace at Filton, Bristol makes up a large section of the company's global wing structures manufacturing and assembly operations. This includes the site's integrated machining facility (IMF), which has the capability of high-speed machining of steel, titanium & aluminium components. In an effort to remain as a leading tier one supplier of aircraft wing structures, GKN must strive to become ever more competitive in the growing global marketplace. Therefore, the development and implementation of technology solutions must be embedded in production to deliver increased productivity, to outperform competitors in emerging markets.

The requirement for lighter, more fuel-efficient aircraft has called for components such as large monolithic wing structures to be designed optimised for weight-saving considerations [6]. Such components are shown in Figure 1-2. The optimised designs include thin-walled sections which are susceptible to unfavourable distortion. These aluminium components are typically manufactured from rolled or extruded plate material, where up to 90% of the stock material is removed using high-speed CNC machining centres, as shown in Figure 1-3. Upon removal of the excess material, the thin-walled parts can undergo distortion. Distortion can be described as the twisting, curling and bending that results in non-conformance with respect to the intended geometrical/dimensional design [7]. Excessive distortion in these types of components have resulted in high levels of concession, rework and even scrap. This has subsequently resulted in a high underlying recurring cost to the aero-component manufacturers. This recurring cost appears in the form of scrap and required corrective processes.

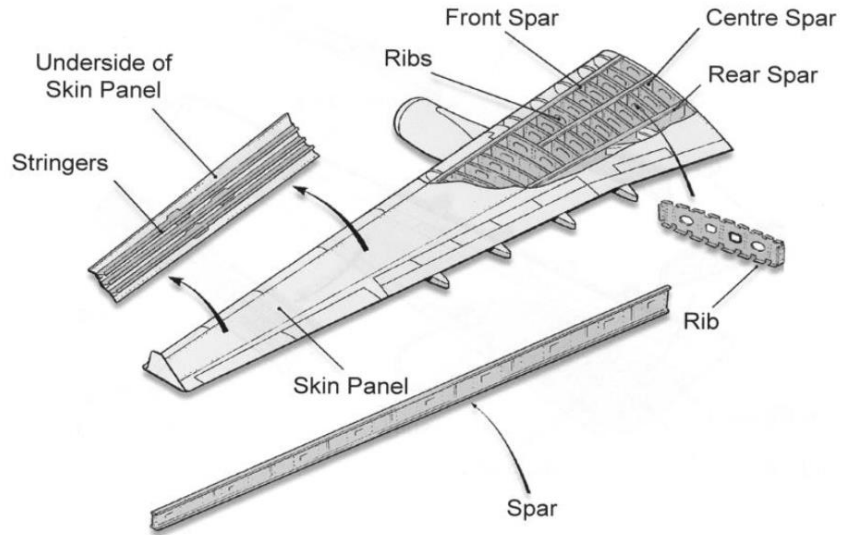


Figure 1-2: Typical structure of aircraft wing [8]

The described machining-related distortion can be attributed to residual stresses that are internal body stresses in equilibrium when no external loading is in effect [10]. Residual stresses are generated in high-strength aerospace aluminium materials due to the complex manufacturing history, which imparts severe thermo-mechanical loads upon the material. There are two primary types of residual stresses which influence part distortions in the aforementioned machined components. The first, known as the bulk or inherent material residual stress, arises due to the manufacturing process of the stock material. The second source, termed machining-induced residual stress, is imparted by machining operations themselves. The machining strategies chosen to produce a component determines the extent of the part distortion by influencing the generation and/or redistribution of both types of residual stress. Therefore, measures need to be taken at the process planning stage in the engineering production chain to account for this and avoid costly part distortion and reduce the reliance on corrective processes. If total process control is to be achieved and conform to right-first-time manufacturing practices, manufactures of such components need to develop a part distortion control strategy to accommodate residual stress-related part distortion.

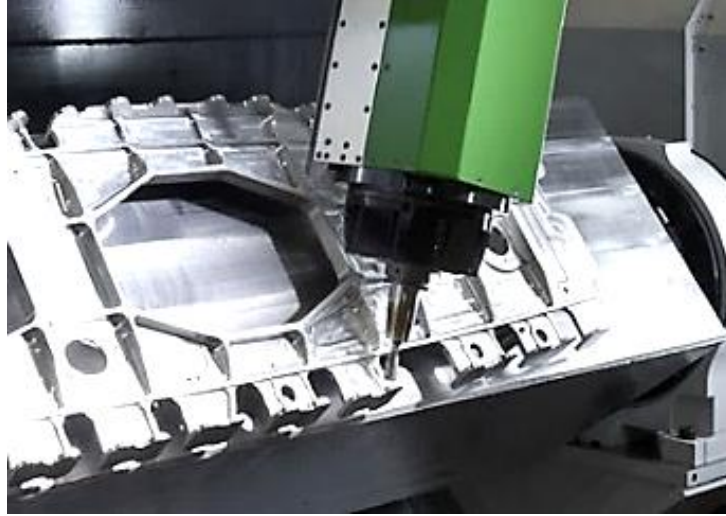


Figure 1-3: Machining of wing rib [9]

1.2 Scope & Research Objectives

Historically to overcome residual stress-related distortion, manufacturing process engineers would adopt costly ‘trial-and-error’ methods to mitigate quality issues [11]. These mitigations are based on observed/qualitative results and rely heavily on the expertise and experience of the engineer to interpret the cause of the distortion and formulate corrective actions. Traditionally, finite element modelling (FEM) has been used to study component distortion during machining due to residual stresses. The modelling approach utilises numerical methods to simulate the machining history of such components to quantify distortion by the process summarised in Figure 1-4.

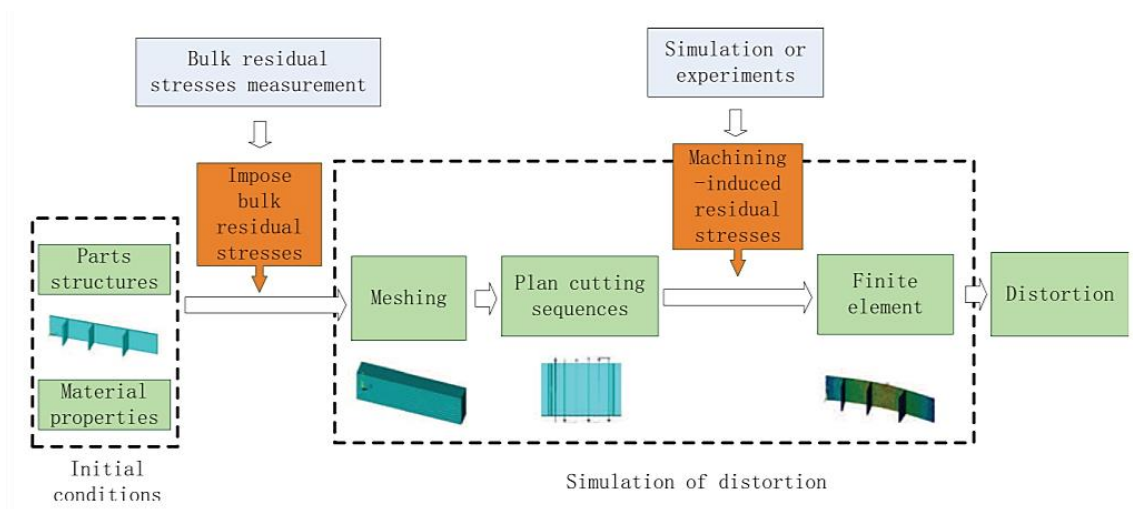


Figure 1-4: Modelling workflow for distortion modelling [12]

However, the adoption of this type of modelling to predict part distortion is low in the aerospace industry, owing to the complexity of the model set-up and interpreting results. The main objective of this work is to develop a numerical distortion prediction modelling methodology capable of informing aerospace CAM engineers of suitable machining strategies to mitigate the effect of costly non-conformance due to residual stress-related distortion. This work will look to build on the already comprehensive distortion modelling research area by proposing a model that can account for machining-induced residual stresses that arise due to the choice of machining parameter and tool path as well the influence of the redistribution of the inherent bulk material stress in the stock material during and post machining. The developed modelling method will look to improve on state-of-art by developing a simulation approach that can account for the bulk and machining-induced residual stresses on post-process component distortion, as well as inter-process distortion and associated product quality errors, where current modelling methods are limited to describing either component only. As industry standard distortion modelling software and methods do not currently exist the accuracy of the model (i.e., ability to capture resulting distortion from machining processes) will look to match or improve upon those reported in literature. A review of the accuracy of previous distortion modelling efforts reported in literature will be given in this body of work. Based on these requirements, the following research objectives have been formed:

- A thorough literature review in residual stress and part distortion focused on numerical methods for distortion modelling.
- Undertake a series of experimental trials to:
 1. Generate understanding of machining-induced residual stress formation due to machining strategy selection and the impact of machining strategy on resulting workpiece distortion.
 2. Generate residual stress data for input to the numerical models based on targeted processes and produce metrology data to validate those models.
- Develop a numerical simulation procedure to model the coupled effects of bulk material and machining process-induced residual stress on final part distortion with material removal sequenced based on the tool path progression.

1.3 Organisation of the Thesis

Chapter 1 is an introduction to provide context for the work undertaken. Scope and research objectives are defined. The problem statement is raised and communicated. Chapter 2 presents a literature review on the current state of residual stress related part distortion. The review covers the machining processes of aeronautical components, machining-related residual stresses and current modelling approaches with respect to part distortion. The genesis of the modelling methodology is derived from a detailed appraisal of the work undertaken in the field. Consideration is given to the production variables considered of significant influence in the outcome of part distortion.

Chapter 3 sets out the objectives, requirements and approach of the work into residual stress related part distortion, including experimental and modelling goals. Chapter 4 details the concepts and procedures of numerical modelling for residual stress and machining-related distortion. Firstly, attention is placed upon the overall approach and necessary prerequisites for each of the modelling methodologies considered. Then the chosen modelling approach is discussed. Next the fundamental governing mechanics of the modelling scheme are stipulated.

Chapter 5 lays out the experimental procedures utilised in this work. This includes the machining trials undertaken to; (a) explore in the influence of various machining variables considered to be influential on final part distortion; and (b) produce samples for residual stress measurements and model verification. Chapters 6 and 7 present the results of the experimental and modelling work outlined in chapters 5 and 6, respectively. A discussion and summary of the results are also included.

Chapter 8 delivers the overall conclusion and outlook of the work. The conclusion covers the implications of the experimental and modelling work and highlights potential exploitation and future development.

2 Literature review

The content of this review of the current literature in the field of residual stress and part distortion is as follows. Section 2.1 will consider machining principles and technologies used in the high-speed machining of aerospace components. Section 2.2 briefly overviews aluminium alloys and their use in the aerospace sector. Section 2.3 will then introduce residual stress and distortion in metallic components. Section 2.4 has been dedicated to describing the various measurement techniques of residual stresses. Section 2.5 describes the sources of residual stress in manufacturing. Section 2.6 assesses the current state-of-the-art research in modelling and simulating residual stresses and part distortion. Finally, Section 2.6.4 will conclude the literature review and establish gaps and further work.

2.1 Machining of aerospace structural components

Machining, a subtractive manufacturing process, can be described as the multistep removal of material from stock geometry to achieve a desired shape. The machining process is conducted for many modern manufacturing materials such as super alloys, carbon fibre-reinforced plastics and polymers. There are various categories for which machining methods can be grouped, as summarised in Figure 2-1, where the top-level categories are defined by the energy method from which the machining action occurs; mechanical, thermal and chemical [13].

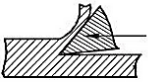
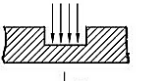
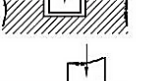
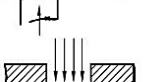
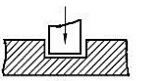
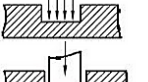


Category of basic process	Fundamental removal method	Examples of processes
Mechanical	I 	Cutting Turning Milling Drilling Grinding, etc.
	II 	Water jet cutting Abrasive jet machining Sand blasting, etc.
	III 	Ultrasonic machining
	IV 	Blanking Punching Shearing
Thermal	II 	Thermal cutting (melting) Electron beam machining Laser machining
	III 	Electrodischarge machining (EDM)
Chemical	II 	Etching Thermal cutting (combustion)
	III 	Electrochemical machining (ECM)

Figure 2-1: Various machining methods categorisation based on energy consumption [13]

Mechanical group I refers to the cutting processes, which is defined by the standard DIN 8589 as the separation of material from a workpiece in the form of chips employing a cutting tool with geometrically defined cutting edges [14]. The material removal during cutting is attributed to the thermo-mechanical interaction between a sharp wedge-shaped tool with the surface layer of the workpiece material, which causes separation from the stock material in the form of chips [15]. Such examples of this form of machining include milling, turning, drilling and grinding. These processes are referred to as conventional methods of material removal. Machining processes that fall within mechanical II and III categories, also called the thermal or chemical categories, are termed unconventional or non-traditional machining methods.

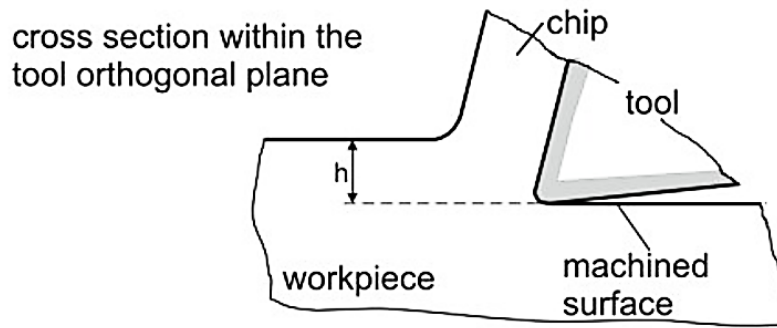


Figure 2-2: Chip formation by way of machining [14]

The mechanical group I cutting category can be split down further into two sub-categories; cutting action associated with geometrically defined edges and non-geometrically defined edges. Geometrically designated cutting edges refer to the cutting action by tools with distinct features, such as end mills (Figure 2-3 – left), where the number of flutes, rake and flank angle can all be attributed some value. In contrast, material removal with non-geometrically defined edges refers to cutting tools with numerous cutting edges randomly distributed across the tool, i.e. grinding disks (Figure 2-3 - right). Geometrically designated cutting edges are single or multi-point cutting tools, such as turning and milling [16]. The focus of this literature review will consider cutting by geometrically defined edges as those are used primarily in machining aerospace components i.e. milling. The following sections of this report will review the mechanics and associated models that describe the cutting action associated with geometrically defined cutting edges and how they are applied in aerospace component manufacture.

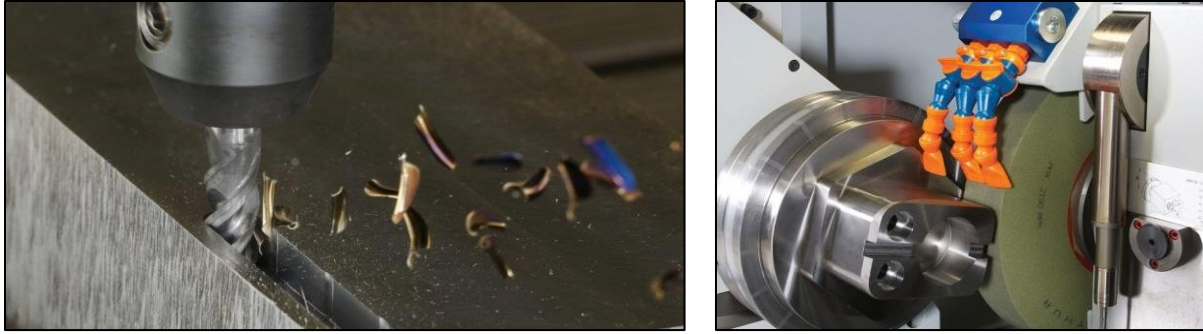
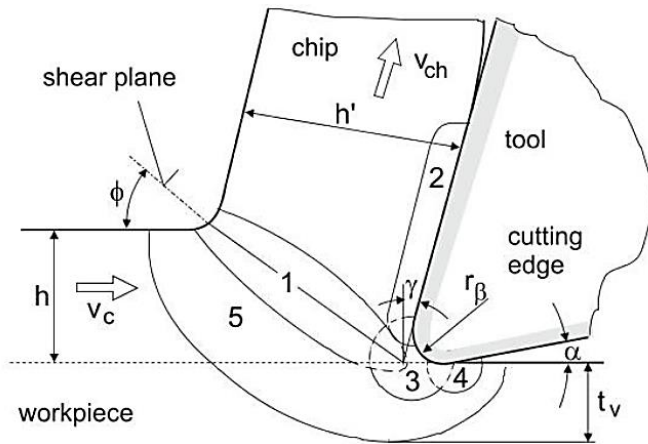


Figure 2-3: end milling [17] (left) & Grinding wheel [18] (right)

2.1.1 Machining mechanics

The principal objective of metal cutting mechanics research has been described well by Davim [19]: "*to determine the cutting force and cutting power through analysing the thermomechanical processes involved in the cutting process.*" The importance of determining such process conditions as cutting forces, temperature and stress/strains is that all influence process outputs such as workpiece finish and surface integrity, tool wear and dynamic behaviour, as well as the chip formation, material flow and power requirements. Over the last 75 years or so, many types of models have been proposed to predict key variables of machining and chip formation (i.e. temperature, forces, chip thickness). Such modelling approaches include analytical, numerical, empirical and artificial intelligence, where combining two or more methods is termed hybrid modelling [20]. These methods can also be utilised to predict key machining performance indicators (i.e. surface integrity) and discussed later in this review during section 2.6.2.

The orthogonal model of machining (seen Figure 2-4 [21]) considers the tool cutting edge angle perpendicular to the direction of the cutting, forming a two-dimensional plane. Orthogonal was the first analytical model to be developed and is most widely used due to its relative simplicity. The most notable include the shear plane model expressed by Merchant's circle diagram from 1945. In this model, the chip formation is governed by material shearing along a plane known as the shear plane. The model describes the forces associated with material removal with respect to the tool-chip-workpiece interface as seen in Figure 2-5 [10].



- | | |
|--|----------------------------|
| 1 : primary shear zone | γ : rake angle |
| 2 : secondary shear zone at the rake face | α : clearance angle |
| 3 : secondary shear zone at the stagnation zone/separativ zone | ϕ : shear angle |
| 4 : secondary shear zone at the flank face | t_v : deformation depth |
| 5 : preliminary deformation zone | |

Figure 2-4 Orthogonal plane chip formation [21]

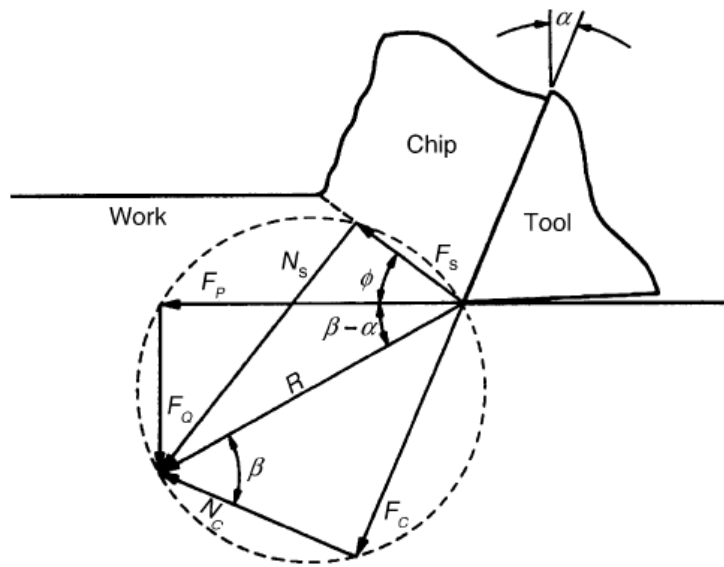


Figure 2-5: Merchant's Circle diagram [22]

Davim [19] reports on the issue associated with analytical models in that they only reflect simplified cutting conditions, and rarely does this scale well to the actual phenomena of 3D complex metal cutting to any level of disenable accuracy. The source of these inaccuracies is twofold [23]. First, the vast number of application-sensitive variables associated with the cutting process are generalised across the various cutting schemes. That is, models developed for turning applied for milling/drilling do not translate well.

The second is that the complex manifestation of high stress/strain in a small working area at high speed requires highly multiplex models that are prone to oversimplification. This oversimplification leads to discrepancies between the theoretical models and experimental results. In reality, machining is a complex 3D mechanical process where variables such as the machine tool, fixturing, coolant, tooling geometry, cutting strategy and parameters all influence part and process quality.

Milling is considered as the primary machining process for this work as it is utilised in the machining of the aerostructure components at the centre of this study. Milling is performed with a circular rotating tool with a specified number of cutting edges. The rotation of the tool and the relative movement of the work piece determines the feed rate of the tool (V_f) and facilitates the removal of material by generation of chips. Chip formation is a thermo-mechanical process that results in cutting forces as the workpiece material resists the cutting action of the milling tool. Figure 2-6 shows the cutting forces evaluated in both in workpiece and tool coordinate systems for milling operation.

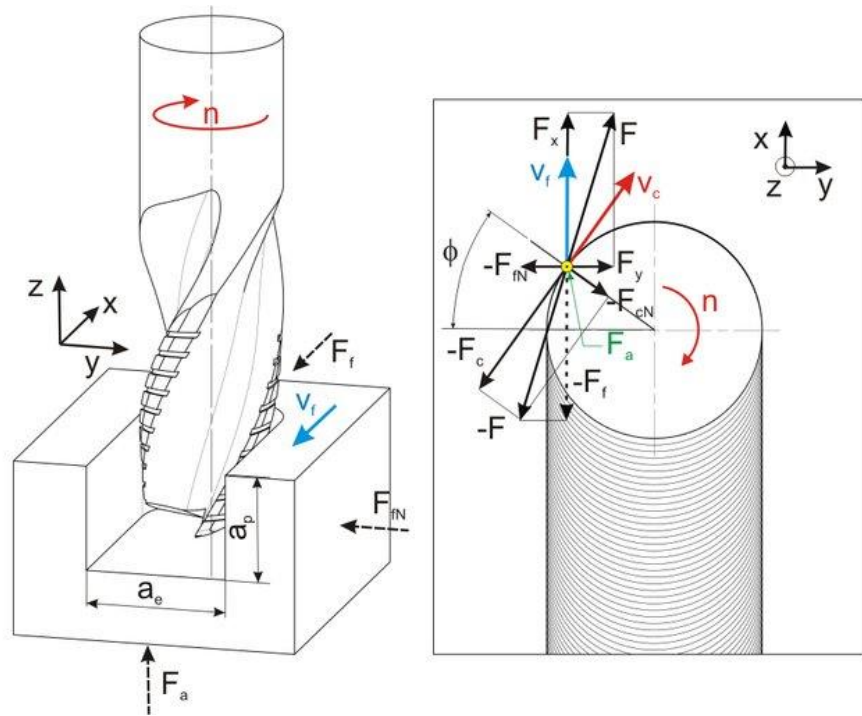


Figure 2-6: Milling cutting forces; in the work piece coordinates (left) and tool coordinates (right) [24]

The measurement of milling cutting forces can be carried out through various methods but in research it is routinely carried out using stationary dynamometers that use piezoelectric sensors [25]. Figure 2-7 depicts a standard experimental set up for measure milling cutting forces with a stationary table type dynamometer. The measured forces are reported in the table coordinate system.

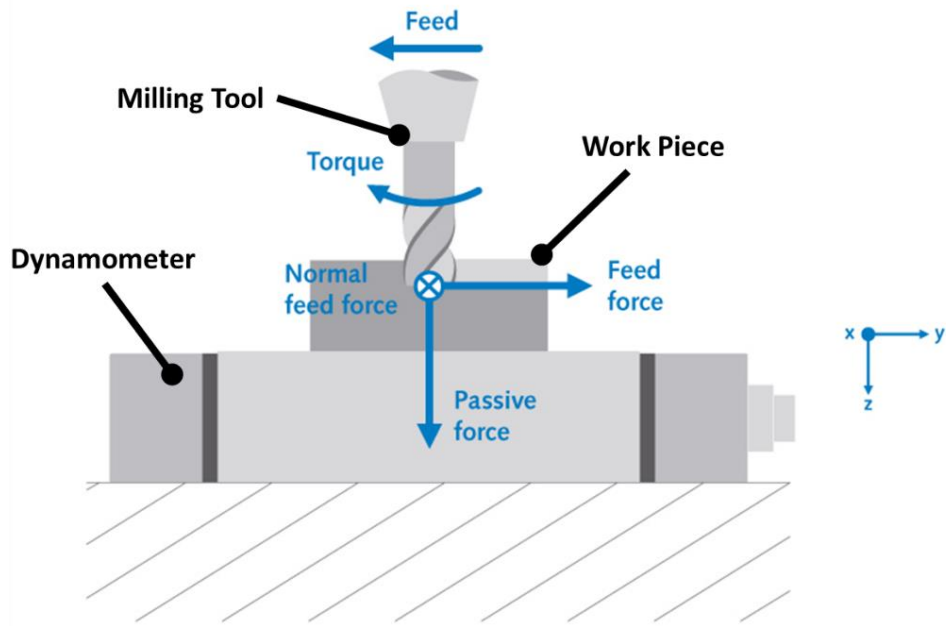


Figure 2-7: Measuring milling cutting forces by dynamometer [25]

Researchers have utilized this type of testing for cutting force coefficient determination and studying key machining parameter influence on the cutting force response. Furthermore, the cutting force response have been reported to attempt to link the impact of variables on machining response outcomes such as surface integrity [26]. Figure 2-8 shows typical cutting forces for liner face milling cuts when investigating influence of cutting speed on surface integrity [27].

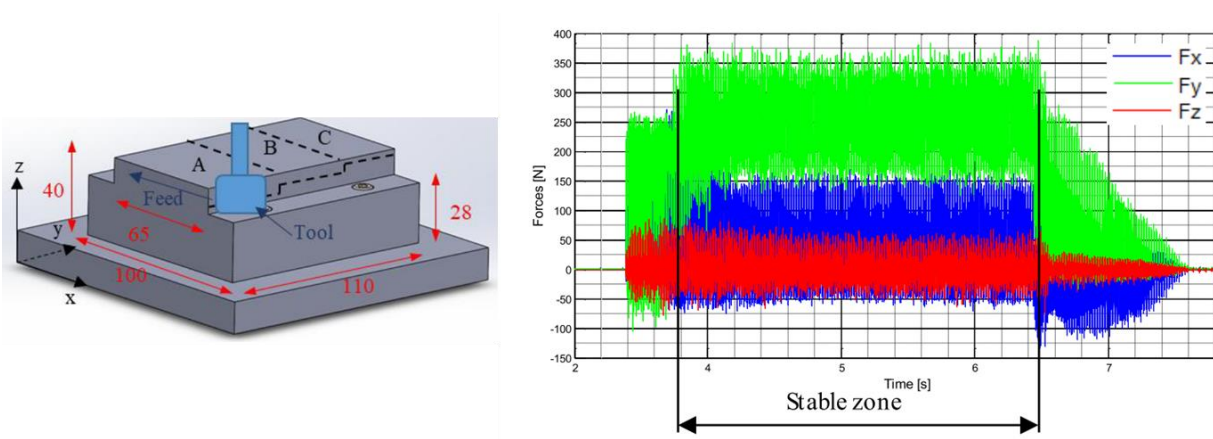


Figure 2-8: Face milling trial schematic (left) and cutting forces measured by dynamometer (right) [27]

2.1.2 Machining application

Aero-structural wing components are typically manufactured from an aluminium rolled plate or extrusion on large computer numerically controlled (CNC) machining centres to obtain the functional product design shape (as shown in Figure 2-9) to specified tolerances, typically in the order of tens or hundreds of microns. Milling machining, of which there are several types, is the primary form of material removal for such components. The various milling methods are summarised in Figure 2-10. The machining centre houses one or multiple rotating spindles in which milling tools are held through tool-holding devices. Workpieces are loaded onto the machine using modular or bespoke fixtures to constrain the stock material during machining. Depending upon the architecture of the machining centre, the workpiece is fed into the rotating tool, or vice-versa, to initiate the cutting process. The relative motion of the tool vector and the tool cutting edge rotation to the workpiece is known as machining feed and speed, respectively. These parameters and motions are governed by the CNC program compiled by the machine controller. CAD/CAM programming software is required to produce CNC programs, especially for components with intricate geometry, where complex tool-workpiece interactions are required with 5-axis tool vector positioning. The CAD/CAM is carried out in the process planning stage of machining, which will be discussed in more detail in the following section.

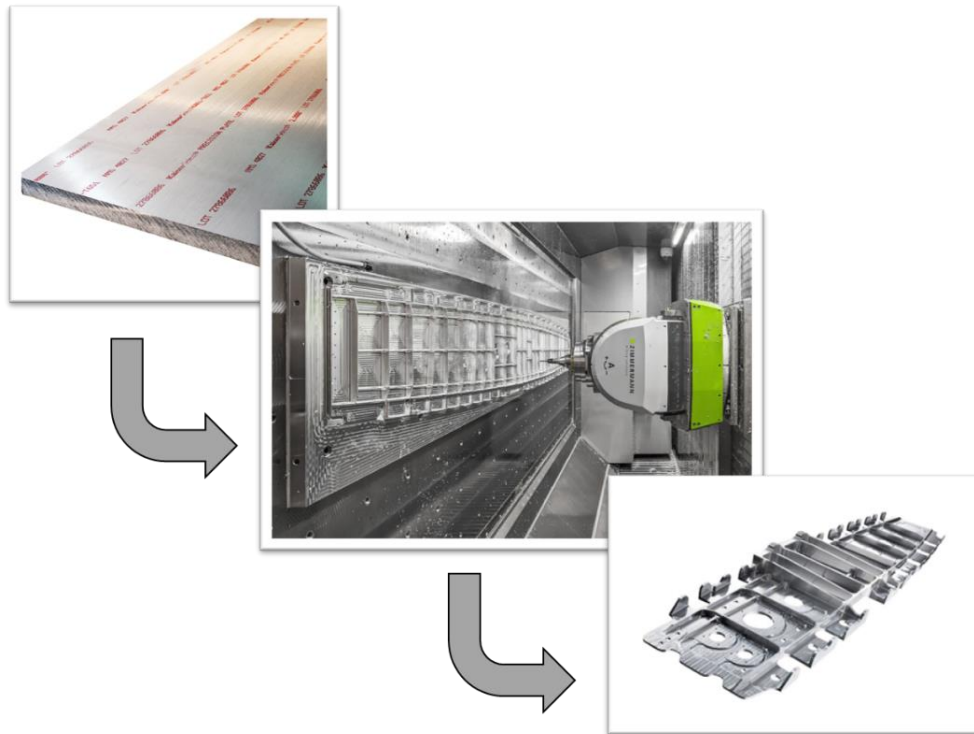


Figure 2-9: Stages of Machining Aerospace structural component (images from [28]–[30])

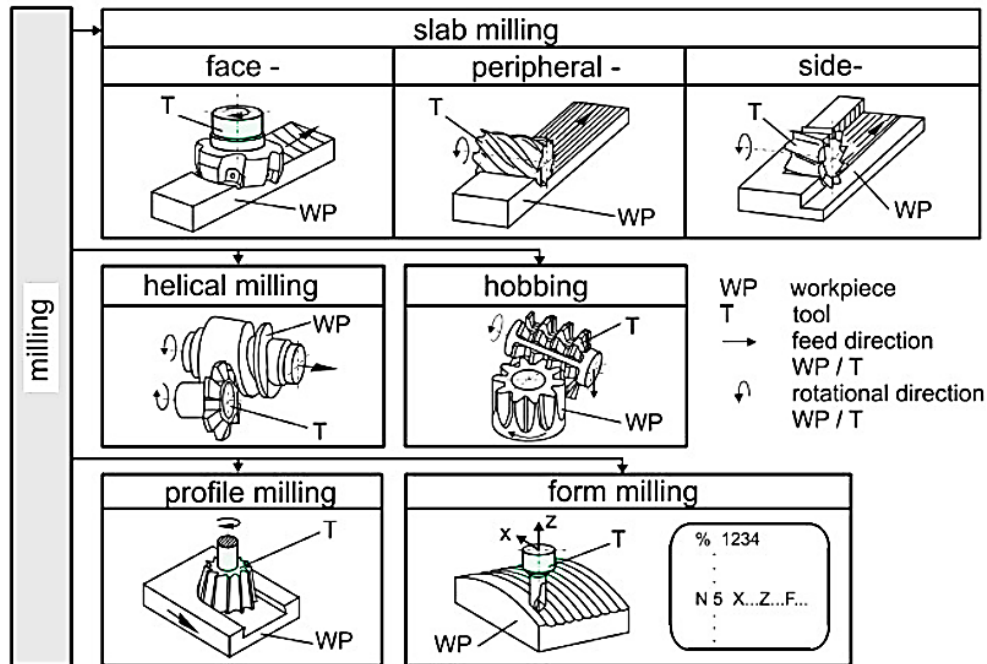


Figure 2-10: Milling process types [21]

Machining process chain

To efficiently manufacture complex components, digital processes are required to plan and control manufacturing activities. The machining process design is carried out during the process planning stage of the manufacturing process chain, as depicted in Figure 2-11. The process is initiated at the design stage when the component geometry and geometric dimensioning and tolerancing are defined, driven by component performance conditions (i.e. strength, load and weight requirements).

The process engineer then uses the part geometry to plan and program the machining tool paths in CAD/CAM software, which can be included in the CAD software or separately. The fixturing methodology to hold the part during machining is also defined and modelled. The tool path data is generated in a universal format by the CAD/CAM software, which is converted to machine control-specific syntax by the post-processor software. The reformatted tool path file is then checked in a separate verification software which utilises a virtual model to simulate the machine kinematics, tool and workpiece interactions by modelling the tool path motions. Verification is conducted to check for collisions and, in some software, force spikes. If any sources of error are found at this stage, the engineer will update the CAM program to account for the error, re-post and re-verify the updated code.

Once the toolpath is accepted, the CNC file is transferred to the machine controller for physical cutting. If any problems arise during the machining production stage, this is fed back to the CAM program for updates. Post-machining, components undergo a series of geometric, surface and metrological inspections, and if any discrepancies between design and physical components are reported, the program is updated to account for this. Fixing defects via machining trials or unexpected errors is costly due to the time and capital required. Some simulation software is currently used in production to diagnose potential sources of quality issues (i.e. Vericut force), such as part abuse due to force spikes. However, other critical sources of poor quality, such as vibration/chatter or part distortion, are only rectified after diagnosis at the production stage, by which point the quality escape and the associated cost have occurred.

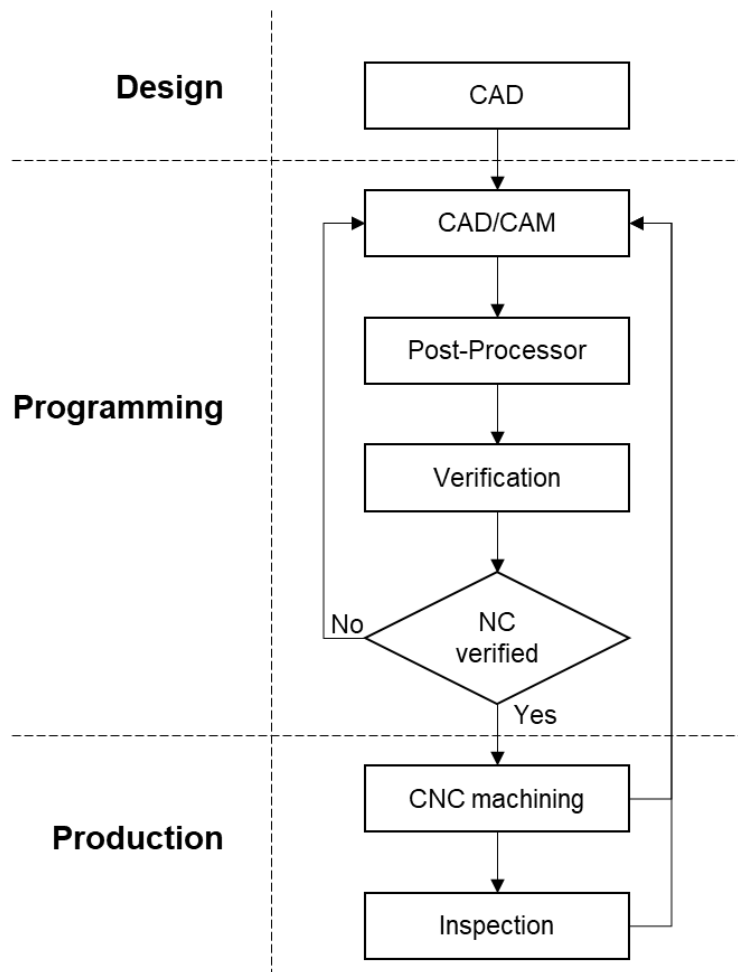


Figure 2-11: The digital process chain for CNC machining

2.2 Aluminium in aerospace applications

Of all the elements in the earth's crust, aluminium is the 3rd most abundant, behind oxygen and silicon. Due to its beneficial material properties, it is used in various applications and industries, including the aerospace sector. Aluminium is low density (one-third that of steel), high strength, ductile and resistant to various forms of corrosion [31]. Aluminium is extracted as alumina from bauxite oxide ore by the Bayer process. Alumina is subjected to an electrolysis smelting known as the Hall-Héroult process, in which molten cryolite reacts with the alumina to form molten aluminium, as shown in Figure 2-12 (left). The direct-chill casting method is employed to turn Ingots into aerospace components, Figure 2-12 (right).

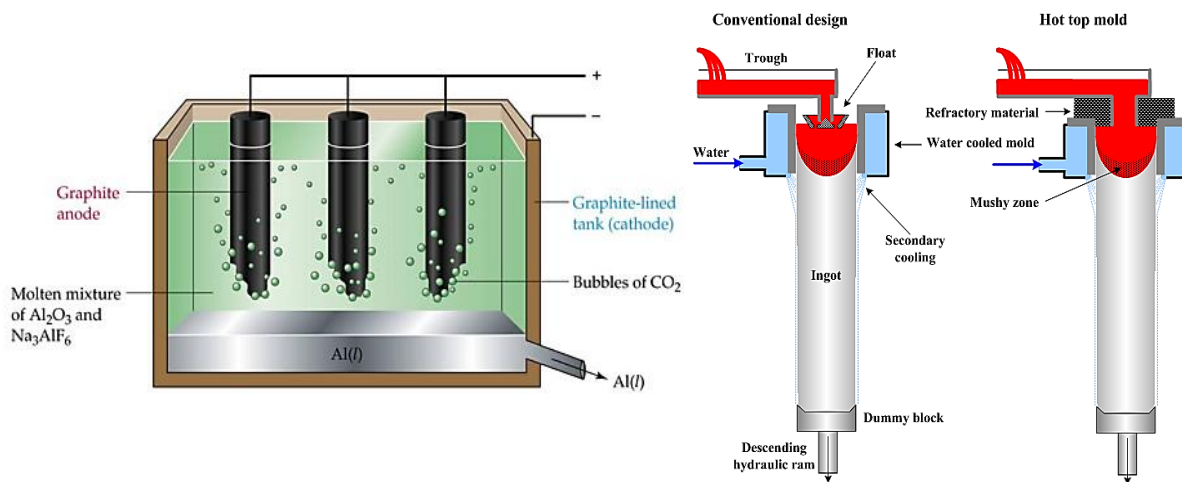


Figure 2-12: (left) Hall-Héroult process and (right) Direct chill casting methods [31]

Aluminium is commonly paired with alloying element additions when cast to improve mechanical properties such as strength, density, and fabrication ability [31]. Aluminium alloys are designated by their constituent alloying content and temper condition, as displayed in Figure 2-13. 2XXX and 7XXX series aluminium are the most widely used in aerospace structural applications due to their favourable strength-to-weight ratio, fracture toughness and fatigue resistance [32]. They also exhibit good machinability and attractive cost compared to 'hard' alloys such as titanium. Typical alloying content by wt% is displayed in Table 2-1 [19], [20]. Wing ribs are typically manufactured from aluminium alloy 7010 or 7050 billets cut from rolled plate in a T7651 temper condition. A conventional T7651 billet is supplied by the mill, as detailed in Table 2-2.

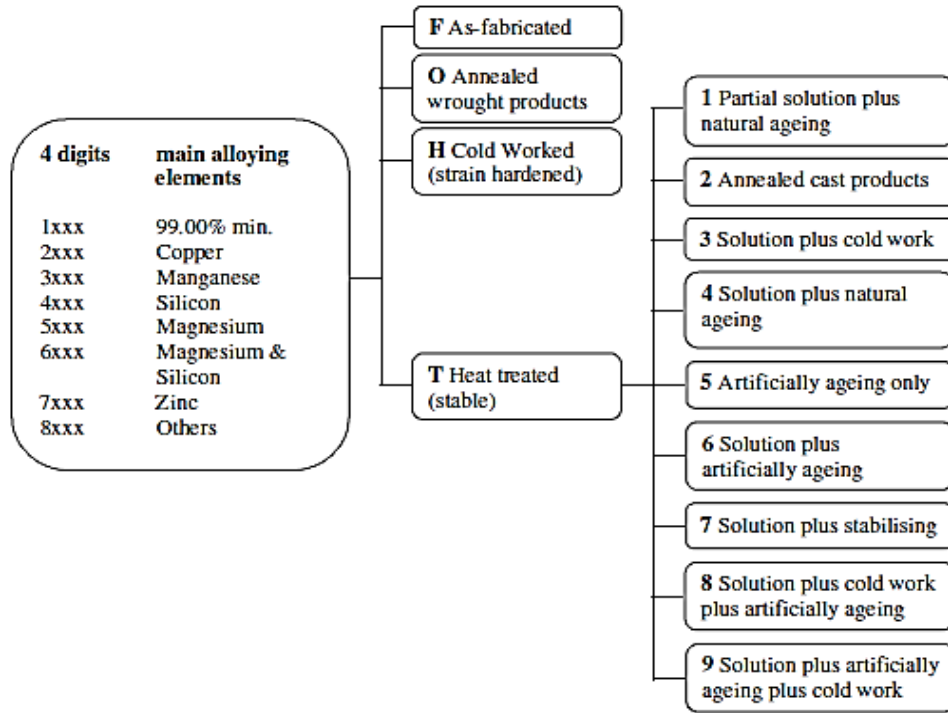


Figure 2-13: Aluminium alloy & temper designation system [31]

Table 2-1: wt% alloying elements for AA7050 & AA7010 [33], [34]

Alloy	Cu %	Mg %	Zn %	Mn %	Si %	Fe %	Cr %	Ti %	Zr %
AA7050	2.0 - 2.6	1.9 - 2.6	5.7 - 6.7	<= 0.1	<= 0.12	<= 0.15	<= 0.04	<= 0.06	0.08 - 0.15
AA7010	1.5 - 2.0	2.1 - 2.6	5.7 - 6.7	<= 0.1	<= 0.12	<= 0.15	<= 0.05	<= 0.06	0.10 - 0.16

Table 2-2: T7651 Supply condition

Process	Value
Solution treated	465 - 485°C
Water Quench	40°C
Controlled stretched	1.5 – 3.0 %
Aged	117 - 123°C /t=10h. + 169 - 175°C /t=8h

The process of manufacturing billets of aluminium for aerospace applications will include a heat treatment process to obtain the sought-after beneficial material properties necessary for aerospace applications. These beneficial properties include high strength, stress-corrosion-cracking resistance, and toughness [35] T7651 temper designation includes solution treatment, quenching, and controlled stretching and ageing. The process of creating the designated aluminium billet, detailed in Table 2-2, is as follows:

- Casting: As previously discussed, an Ingot is produced by melting and mixing the aluminium and alloying elements. Alloy with elements such as zinc (Zn), magnesium (Mg) and copper (Cu) improve the material performance including strength increase through solid solution and corrosion resistance.
- Rolling: Is performed to reduce the cast material to a usable gauge. The process will also close pores created in casting and break up constituents at grain boundaries. These two effects of rolling render the material more ductile and improve strength attributes [31].
- Solution treating: Heating the material above the specified solvus temperature for a specified amount of time (dependent upon the desired condition). This is conducted so the alloying elements can be diffused throughout the material. This precipitation process and temperature range are displayed as point 2 and 3 in Figure 2-15 (left). The underlying process of particulate diffusion is displayed next the phase diagram for aluminium alloy in Figure 2-14 (left). Figure 2-14 (right) displays a typical heat treatment profile for T6 temper condition, including the quenching and aging temperature.

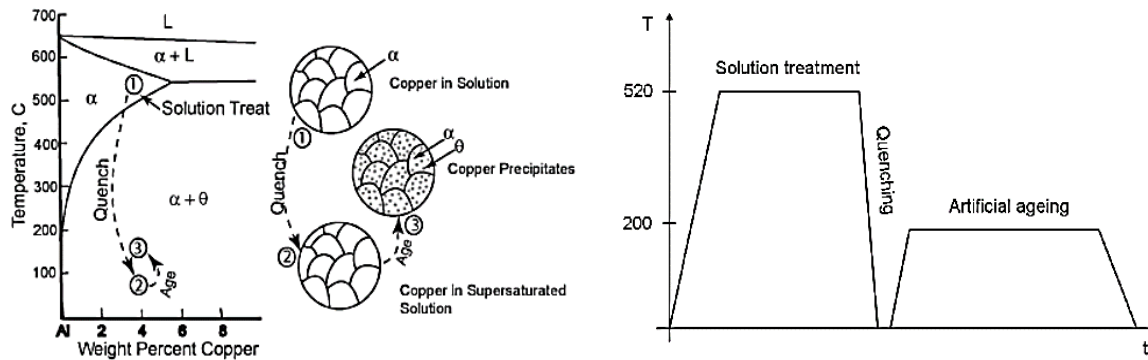


Figure 2-14: Diagram of the phase transformation displaying the solution treatment, quenching and ageing temperatures accompanied by precipitation across the resulting grain structure (left). Typical heat treatment time plot for T6 material condition (right).

- Water quench: Rapidly cooling the material below the solvus temperature, between point 1 and 2 in Figure 2-14 (left). Done immediately after solution heat treatment will result in alloying elements locked into a supersaturated solid solution (SSSS). This step avoids the formation of large particulates

which can cause embrittlement in the end product. This process step is critical in forming residual stresses and will be discussed in section 2.5.1.

- Controlled stretched: The part is mechanically stretched, causing gradual near-surface plastic deformation. This stretch relief reduces the large gradient of residual stress experienced throughout the total thickness of the part [36].
- Artificially aged: The billet material is subjected to sustained elevated temperature, allowing for the precipitation of small alloying element particles, shown in point 3 Figure 2-14 (left). The formation of precipitate provides the material with essential properties previously mentioned. Also, by raising the temperature of the billet, thermal stress relieving is achieved, albeit not achieving a significant drop in mean stress levels [37].

Aluminium comprises a face-centred-cubic (FCC) crystal lattice structure, as shown in Figure 2-15 (left). The lattice structure of aluminium governs its deformation characteristics during machining. Deformation occurs along slip planes defined in the cubic crystal structure by the Miller indices, as shown in Figure 2-15 (right). In essence, aluminium is relatively ductile and more manageable to machine than 'harder' materials such as titanium and nickel super alloys. Therefore, it is associated with comparatively lower cutting forces and temperatures. However, its ductility also raises challenges with the adhesion of the machined workpiece material to the cutting tool surface, referred to as built-up edge (BUE) [38]. BUE has disastrous effects on the surface finish and tool wear rates. Specialised tooling cutting-edge geometry, or chip-breakers, can separate long-stringy chips formed during continuous cutting into more manageable chips.

Furthermore, selecting the correct machining parameters, coolant delivery, and tool coatings are all additional means to controlling chip formation when machining aluminium alloys. Moreover, the relative ease of cutting aluminium makes it possible to utilise aggressive machining tactics, also called high-speed machining. High-speed machining is associated with high levels of material removal, fast cutting speeds and elevated feed rates. Nevertheless, these hostile machining conditions make for high augmented cutting forces and temperatures even for the comparatively easy-to-machine aluminium. The forces and temperatures can have an adverse effect on the surface integrity of the final machined component. Later sections of this report will consider what influence changing the process conditions has on the stress state of the machined workpiece.

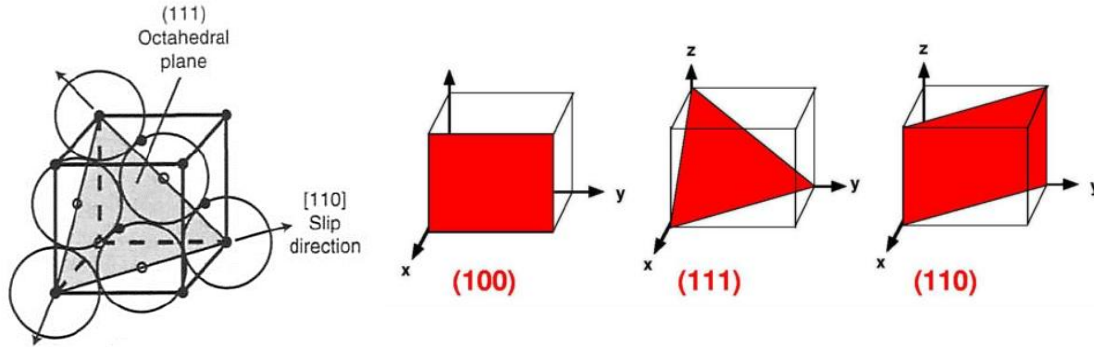


Figure 2-15: FCC crystal lattice structure (left) & Miller indices slip planes (right) [39],[40]

2.3 Residual stress and Distortion

Distortion due to residual stress is a researched area that has seen a rapid increase in the number of studies into the phenomena over the past three decades. The extent of the issue can be suggested to be of high significance due to the perceived cost of distortion to manufacturing industries [7] and also the number and size of projects which have been commissioned in order to study residual stresses that effect distortion in the final component formed during the manufacturing processes.

An example of a notable research project is C.O.M.P.A.C.T [41]: A Concurrent Approach to Manufacturing Induced Part Distortion in Aerospace Components. The project took 48 months and included research from 12 academics globally. It aimed to “fill the knowledge gap and to advance the state-of-the-art in predicting and managing distortion”. The project included investigations into the effects of material processing, bending, correction processes and machining on residual stress and developing measuring techniques, finite element modelling and designing against distortion protocol.

Although many publications and works on this subject matter have been undertaken, it will become evident that much more work is still needed to fully understand the sources and formation of residual stresses and subsequent influence on part distortion. The aim of section 2.3 is to collate and analyse the knowledge in the topic subject area, which will be used to develop future project direction. First, a description of residual stress and distortion will be given.

2.3.1 Residual Stress

Stress, under certain constraints, can be described as the “intensity of internal force acting on a specific area passing through a point” [42]. Stress can be defined as either normal or shear. Normal stresses (denoted by σ) describe the intensity of the force, F , normal to a given plane of cross-sectional area, A :

$$\sigma = \lim_{\Delta A \rightarrow 0} \frac{\Delta F}{\Delta A} \quad 2-1$$

Shear stresses (denoted by τ) describe the intensity of the force acting tangent to the plane:

$$\tau = \lim_{\Delta A \rightarrow 0} \frac{\Delta F_S}{\Delta A} \quad 2-2$$

Considering a 3D element representing the material point, the normal stresses and shear stresses defined with respect to each principal direction are depicted in Figure 2-16. This image represents the state of stress at a given point. The unit of stress is the Pascal, Pa , which comes from the force per unit area or Newton per meter square (N/m^2), where $1 Pa = 1 N/m^2$.

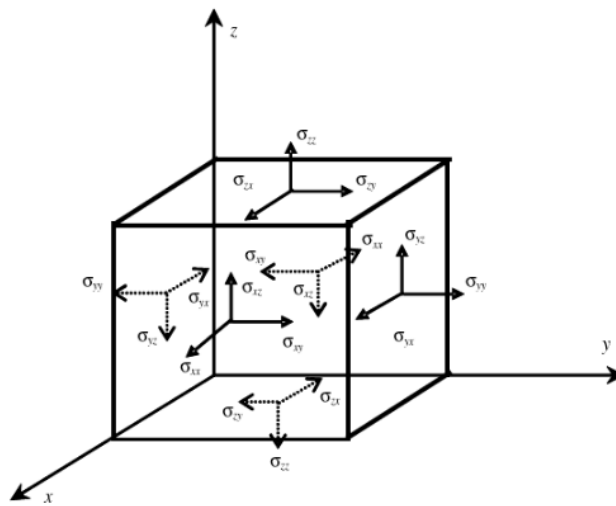


Figure 2-16: Stresses acting at a point [43]

Strain (denoted by ε) is the measure of the deformation of a body that can be caused by stress. Strain is exhibited through a change in length per unit length. Strain condition where $\Delta s \rightarrow 0$:

$$\varepsilon = \lim_{\Delta s \rightarrow 0} \frac{\Delta s' - \Delta s}{\Delta s} \quad 2-3$$

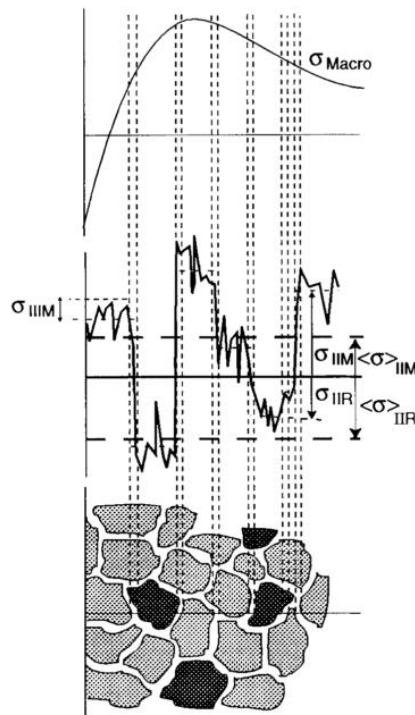
Where; Δs is the original length and $\Delta s'$ is the deformed length. The relationship between stress and strain depends on the material's properties under load and the loading condition that the body is experiencing, i.e. either elastic or plastic deformation. Under linear elastic conditions (i.e., the material has not surpassed the yield stress and deformation is reversible), stress and strain can be related via Young's modulus (denoted by E) where:

$$\sigma = E \times \varepsilon$$

2-4

Residual stress can be described as a combination of tensile and compressive stresses experienced internally by a body when no external loading is applied [44]. These internal stresses of various signs counterbalance one another, causing the body to be in equilibrium. The internal residual stress profile will vary part-to-part dependent upon the material properties, process history of the material and parameters used in the manufacturing processes. Factors influencing residual stress manifestation will be discussed further in section 2.5 of this literature review.

Residual stresses are characterised by the length over which they equilibrate. There are three types in all, described by Withers and Bhadeshia [45], [46] in Figure 2-17. Type 1 (σ_{Macro}) concerns the macroscopic stresses that arise from non-uniform plastic deformation and large thermal gradients and equilibrate across the entirety of the component. Type 2 (σ_{II}) refers to the intergranular stresses due to the mismatch of various material phases that arise due to phase transformation, especially in polycrystalline materials. Grain orientations and differences in thermal properties will also alter the stress state. Type 3 (σ_{III}) describes the stress on a microscopic and atomic structure scale caused by the incoherency at grain interfaces.



M and R denote matrix and reinforcement respectively

Figure 2-17: Residual stress fields length scales [46]

Of primary concern in this work is type 1 macroscopic stresses, which are linked to the material performance of metallic aerospace components. The effects of residual stresses are well summarised by Brinksmeier *et al.* [10], as displayed in Figure 2-18. Regarding static strength, residual stresses will alter the material yield point depending on the loading conditions by acting as a pre-stress state in the component (Figure 2-19). Residual stress can have negative or positive effects on component fatigue life depending on the state of the residual stress experienced throughout the part and at surfaces [47]. The resulting surface condition can dramatically affect dynamic or fatigue strength. Compressive near-surface residual stresses benefit the fatigue life of an aero component in service, as these restrict crack initialisation and propagation. A more tensile near-surface residual stress profile will limit the fatigue endurance of a stress-loaded component, causing it to fail prematurely. The principle of shot peening works by inducing compressive residual stresses at the surface of a component, in order to prevent crack initiation [44]. Stress corrosion cracking sensitivity and instability of the crystallographic structure are the main ways in which residual stresses effect chemical resistance and magnetization, respectively. Of main interest in the proposed body of work is the affect of residual stresses on deformation/distortion.

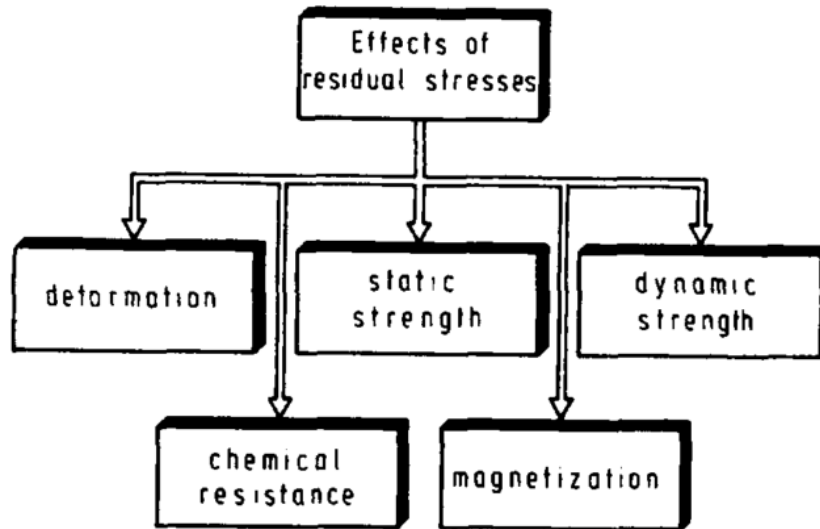


Figure 2-18: Effects of residual stress in metallic components [10]

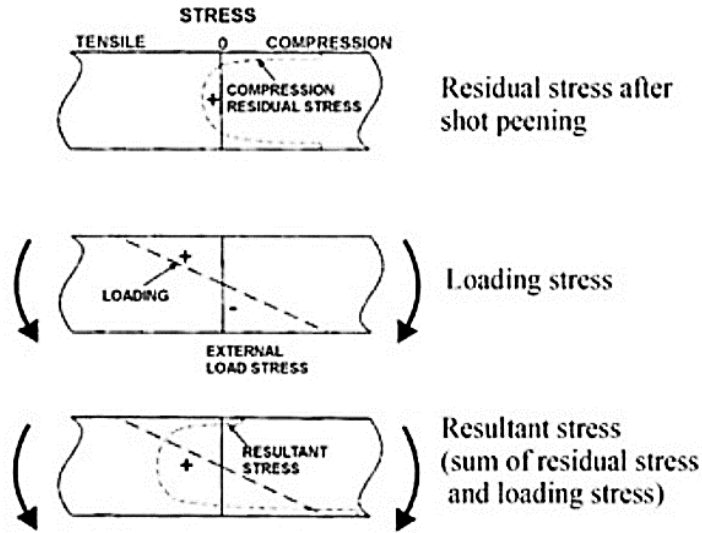


Figure 2-19: The coupling effect of residual and external stresses [47]

Distortion due to residual stresses arises during manufacture caused by processes that upset the stress equilibrium by altering the initial residual stress field or imposing new residual stresses. Machining-related distortion caused by residual stress arises through two mechanisms:

- Redistribution of bulk stresses caused by material Removal: The aluminium plate from which wing components are machined has through-thickness residual stresses ‘locked in’ from the quenching process. When material is removed from the initial volume of the plate, the through-thickness residual stresses that once were in equilibrium (i.e. a section of compressive forces balancing another section of tensile stress) become unbalanced. The component will distort through internal bending moments about the natural axis caused by redistributing the initial residual stress to regain internal stress balance. Figure 2-20 (top) shows a component positioned within the starting ‘stock’ volume of material with balanced stress profiles running through the thickness. The material is removed around the part by machining, upsetting the stress balance, resulting in the distorted component Figure 2-20 (bottom).
- Machining Induced residual stresses caused by the cutting action: Chip separation is an energy-intensive process characterised by high strain, strain rate and temperature. The severe thermo-mechanic loads imparted by the cutting action cause near-surface residual stress that occurs over a couple of hundred microns but can be relatively high compared to the initial bulk residual stresses.

The formation and influence of these two types of residual stress sources will be discussed in depth in later sections of this literature review.

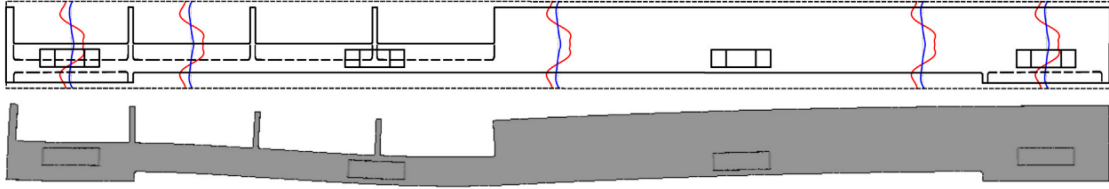


Figure 2-20: (Top) Component location in stock material with an indication of residual stress field, and (bottom) distorted component post material removal [48]

2.3.2 Distortion

Croucher [36] describes the phenomena of distortion well in that it is the “*manifestation of the lack of dimensional stability*”. Distortion can be described as the twisting, curling or deformation which causes a deviation from the intended design shape of the manufactured part. Figure 2-21 shows a wing rib under its weight on a granite surface table. The part is designed to be flat, but distortion has manifested as a curvature or bow of the component's base.

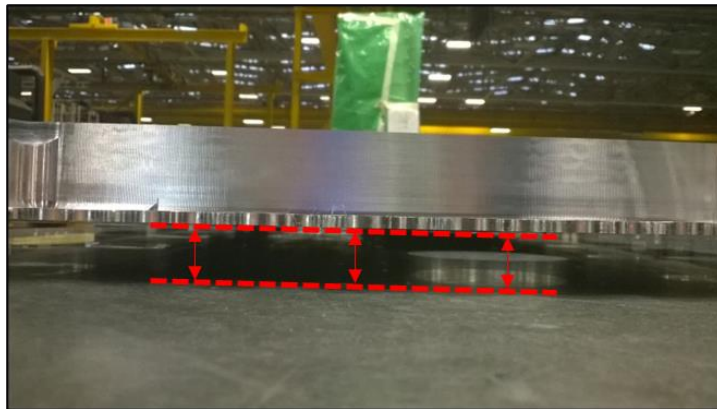


Figure 2-21: wing box rib on granite surface table under own weight

The effect of distortion includes a loss of locational accuracy during assembly and material property alteration, as described by Chatelain *et al.* [49]. Depending on the magnitude of distortion and rigidity of the part, the loss of locational accuracy will affect the joining during assembly [7]. In order to bring the parts back into assembly tolerance, costly and time-consuming corrective processes must be carried out. However, this process will not produce a fully corrected part returning to exact dimensions. Therefore, parts may have to be flexed into position to fit into assembly jigs for mechanical or chemical fastening affecting the end product's fit-up and in-service stress state [50]. The modified stress state can reduce the actual life of the product and its performance capability to carry loads. Also, If the distortion is so severe that it exceeds the customer's requirements, then parts are scrapped, causing lost revenue to the manufacturer.

2.4 Measurement of residual stress

Residual stress measurement is necessary to evaluate a material's performance before and during in-service loading [51]. Furthermore, accurate measurement is paramount in establishing accurate input data for modelling activities. Various residual stress measurement techniques can be split into three main categories: destructive, semi-destructive and non-destructive. Figure 2-22 summarises the more established residual stress measurement techniques and maps them concerning the material removal requirement and measurement depth attainable for steels [52]. The paper by Withers & Bhadeshia [46] reviews residual stress measurement principles and includes a table summary collating the most popular measurement procedures and their associated spatial resolution, accuracy and penetration depth. However, the figures in this table undersell some of these technologies due to recent advances in the technique [53], [54]. When selecting a stress measurement technique, it should be considered what type of stresses are being measured (i.e. machining induced stresses close to the surface or through the whole cross-section of the material) and what level of certainty is desired [55]. Although it should be observed that stress is not directly measured, instead strain relaxation is captured from which stresses are calculated.

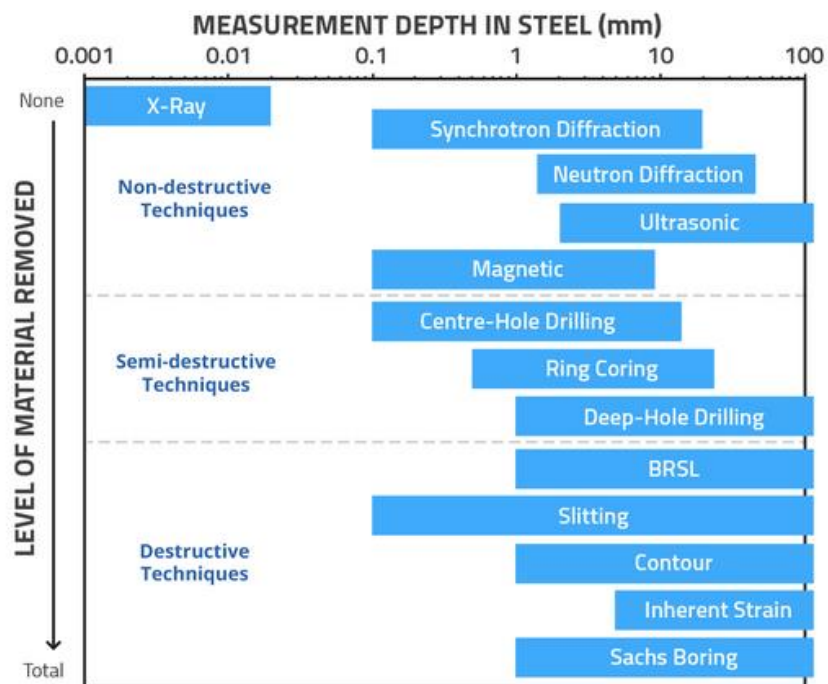


Figure 2-22: Residual stress measurement techniques [52]

2.4.1 Destructive techniques

As per the description, for destructive measurement, various subtractive methods of material removal can be employed to incrementally remove sections of the material to upset the stress equilibrium condition, causing it to distort. These measurements are also called indirect methods, as stresses are not measured immediately, but their effects are in the form of strain relaxation. Compliance functions are then implemented to back-calculate the stresses by how much the material deforms to reestablish equilibrium conditions. In most cases, these incremental distortions are related to the residual stresses in the form of a first-order Volterra integral equation [56].

BRSL (Block removal, splitting and layer removal), layer removal method, Sachs Boring, slitting and crack compliance are all destructive measurement techniques where the stresses are inferred from distortions and inverse calculations. The layer removal method (Figure 2-23) is a well-established residual stress measurement for simple geometries such as plates and cylinders. Dreier & Denkena detail the process well [57], where strain gauges are used to measure the resulting deformation from released stresses by incremental layer removal of the sample. For simple beam-like geometry, Euler–Bernoulli beam theory and an inverse relationship are utilised to calculate the stress in the removed layers. The authors proposed a novel solution by performing the layer removal method of residual stress determination on a computer numerically controlled (CNC) machining centre, utilising on-machine inspection (OMI) to measure the distortions after stress redistribution. Based on the crack compliance method, the main assumptions are that the stresses are uniform in the large layers of material it removes. However, this solution poses a fast, inline measurement option for large billets.



Figure 2-23: Layer removal [10]

The contour method is a favoured approach to measuring through-thickness residual stress profiles, as the full field stress values are obtainable and bi-directional when making multiple cuts. It requires the splitting of plate material by wire EDM, CMM measurement of the cut surface and FEM to calculate the

stress required to return the plastically deformed surface flat, which is proportional to the original bulk stress state. For aluminium billets, inherent residual stresses are predominantly characterised using layer removal, crack compliance [35] (Figure 2-24), and contour method measurements due to the relatively low cost and being well-established and studied.

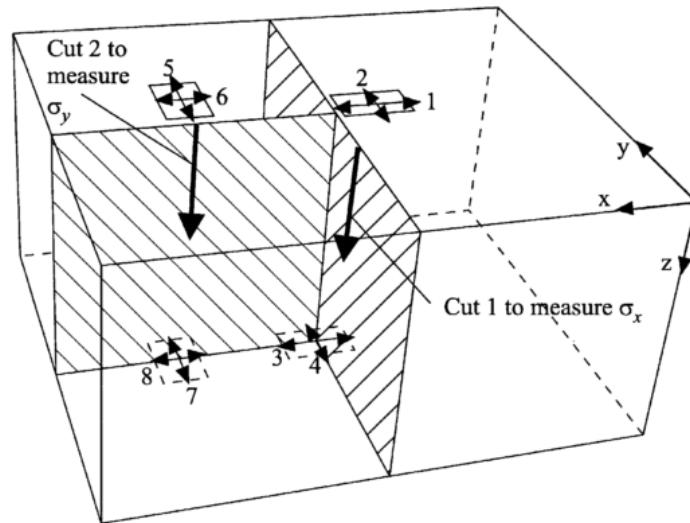


Figure 2-24: Crack compliance method with strain gauge location [35]

2.4.2 Semi-destructive techniques

As with destructive residual stress measurement, semi-destructive techniques will also require material removal to incite measurable stress redistribution. However, the amount of material to be removed is comparatively small. Therefore, these measurement forms will allow the remaining material to be used in another capacity. The semi-destructive measurement options are displayed in Figure 2-25. Centre-hole drilling is the most conventional of the three techniques and is well utilised in the research for machining-induced stress characterisation [27]. The principle of these methods is based on measuring the deformation of material surrounding a drilled hole or core caused by the stress redistribution after successive depths of cut. This deformation by the strain of the surface material is measured by strain gauge rosette and back-calculated to determine stresses.

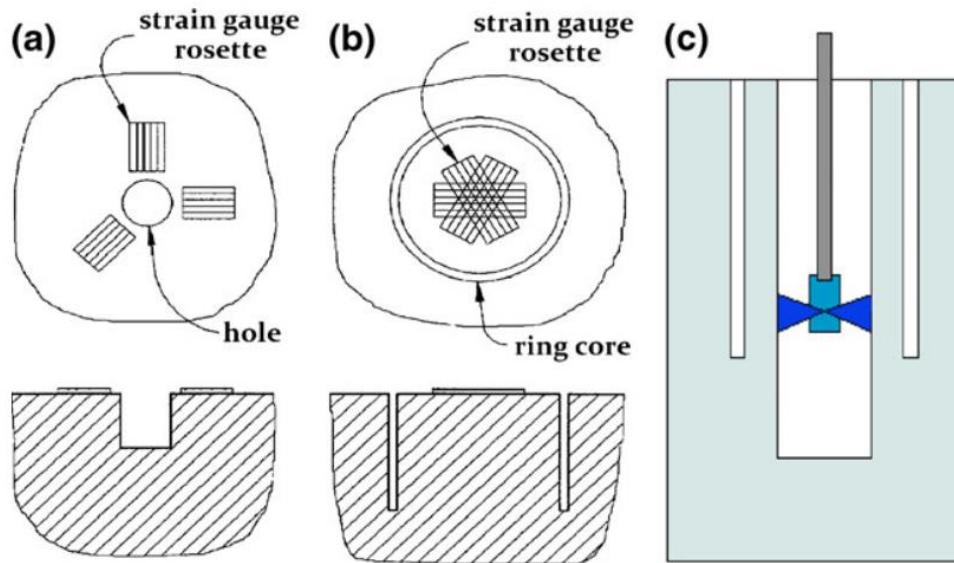


Figure 2-25: Semi-destructive measurement methods (a) centre-hole drilling (b) ring core (c) Deep hole drilling [52]

2.4.3 Non-destructive techniques

Non-destructive techniques can be split into two sub-categories; diffraction and non-diffraction methods. Diffraction methods include X-ray (XRD), synchrotron (HEXRD) and neutron, all of which work on the principle that variations in lattice spacing of a polycrystalline material grain structure can be measured and related to the internal stress state. Resolving these stresses utilises Bragg's law (seen Figure 2-26). In the case of XRD, Bi-axial residual stress measurements can be made, and results are typically accurate to ± 7 MPa for aluminium. The technique is also associated with a small gauge volume and is highly accurate for significant stresses. However, this technique has a small penetration depth of $15 \mu\text{m} - 30 \mu\text{m}$ unless partnered with material removal (i.e. electropolishing), where it can be extended up to $150 \mu\text{m} - 300 \mu\text{m}$. The accuracy of this process is also susceptible to errors due to variations in grain size and orientation and requires precise surface preparation not to affect the accuracy [58].

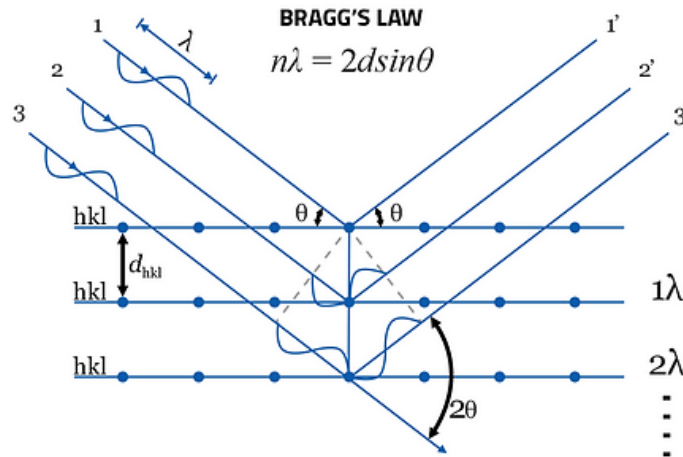


Figure 2-26: Bragg's law [52]

Synchrotron or high energy x-ray diffraction (HEXRD) works on the same principle as XRD. The X-rays produced in a Synchrotron are of high energy and intensity, in the order of a million times more than those produced in an XRD [58]. Therefore, this method has a much larger comparative depth of penetration and produces greater spatial resolution. It is also capable of producing tri-axial measurements through component manipulation. However, this method is less suitable for varying specimen sizes and is associated with long lead times for measurements. The neutron diffraction method has even greater penetration depths than the x-ray methods mentioned, making it suitable for bulk stress measurement [59].

The second form of non-destructive testing, non-diffraction methods, include ultrasonic, eddy current, magnetic and Piezo-spectroscopic methods. The ultrasonic method is based on ultrasonic wave propagation and time-of-flight (TOF) through a given material which is affected by the internal stress state due to the acoustoelastic effect [60]. By comparing the TOF of emitted ultrasonic waves within a stressed and unstressed sample, the difference is proportional to the internal stress state. There are two primary forms of ultrasonic measurement characterised by the distance over which the measurements are being made; Sub-surface and through-thickness. In the former, critically refracted longitudinal waves are passed parallel to the surface by the transducer receiving the waves back. According to Snell's law, the transducer is set on a wedge at an angle dependent on the investigated material. For through-thickness measurement, longitudinal and shear acoustic waves are utilised to measure stresses in the through-thickness and perpendicular distance, respectively. Two configurations of through-thickness measurement can be employed, as shown in Figure 2-27.

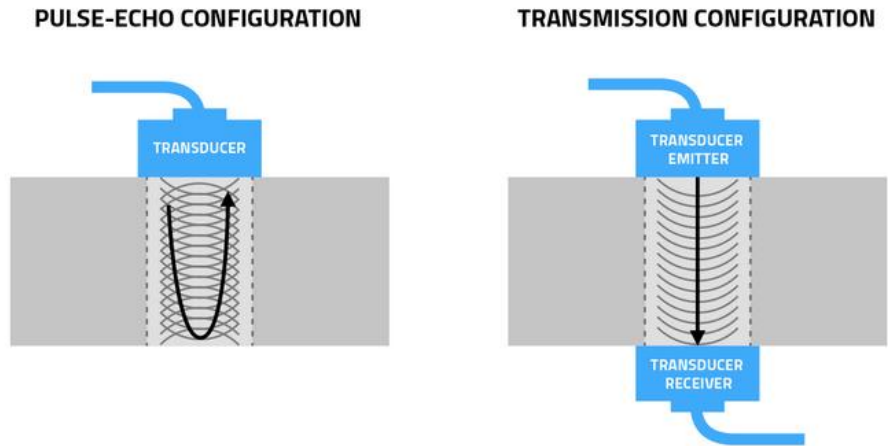


Figure 2-27: Through thickness ultrasonic measurement configurations [52]

The significant benefit of the ultrasonic method is that it shares various advantages with the diffraction methods, including lab-based measurement, tri-axial stress establishment and accurate measurement for stresses of high magnitude. Additionally, this method is relatively quick, has large measurement penetration depths and is theoretically applicable to various materials. However, the method postulates average stress values over a sizeable gauge volume, limiting the determined stresses' resolution. Some other drawbacks include the sensitivity to microstructural changes and the requirement for flat and well-prepared surfaces, which must be parallel. Additionally, this method cannot be conducted on irregularly shaped components. Therefore, it would be suitable to characterise bulk stresses in large heat-treated billets but not in complex final geometries.

The other non-diffraction methods seem less well utilised, and such will be briefly discussed here. Magnetic methods work on the principle that for ferromagnetic materials by magnetostriction, the alignment of wall domains will change due to the residual stress state [61]. Eddy current measurements are conducted by measuring the change in electrical conductivity in the material's surface when establishing eddy currents within the surface [46]. Piezo-spectroscopic approaches such as the Raman and optical fluorescence can be utilised to detect changes in the hydrostatic stress measured by optical methods. Although these methods can achieve good spatial resolution, only surface measurements can be produced.

2.4.4 Summary of section

As can be seen, many various methods can be utilised to measure residual stress within materials. When selecting the measurement method, the application's practical, material and measurement characteristics should be contemplated as posed by Kandil et al. [61]. Furthermore, each method will have limitations for spatial resolution and penetrations that must be considered, as visualised in Figure 2-28. It is widely accepted two measurement forms can be utilised to validate less mature measurement methods [46], [54].

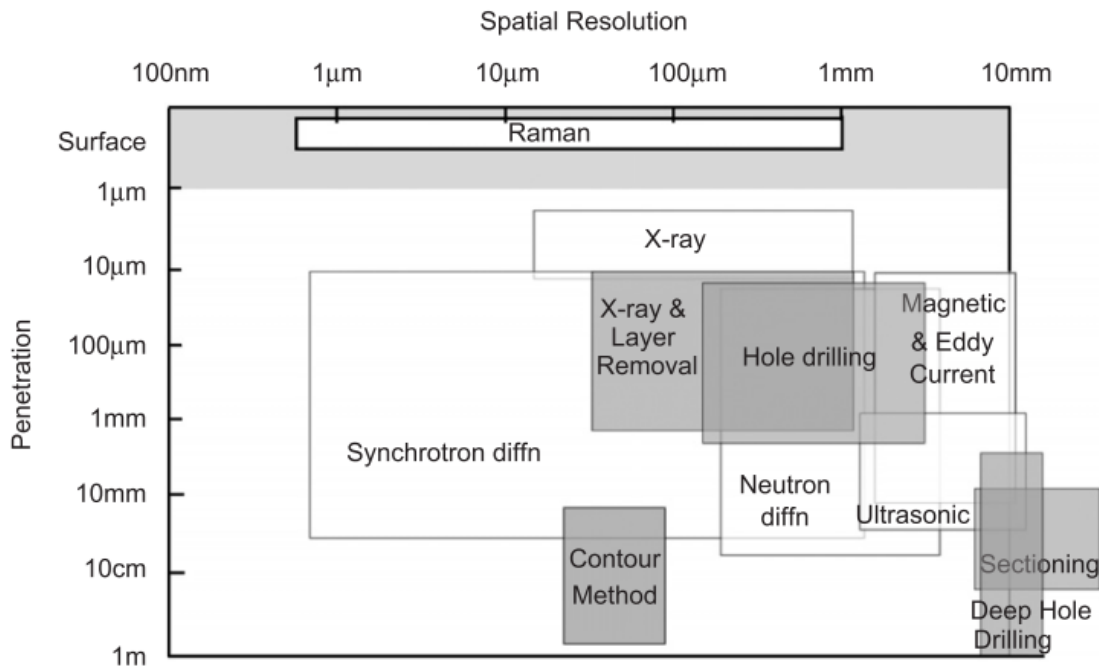


Figure 2-28: Capabilities of destructive and non-destructive measurement [61]

2.5 Sources of residual stress and impact on distortion in machining

2.5.1 Bulk material residual stresses

Inherent, initial or bulk residual stress results from the processes utilised to manufacture the billet material as described in section 2.2. Various pieces of literature refer to this type of residual stress with different terminology. For this project, the stress-induced at the material processing stage will be referred to as bulk material residual stress.

Aluminium alloys can be produced and supplied in various forms, i.e. extrusions and rolled plates. These stock material types are manufactured using various methods of production that result in very different manifestations and magnitudes of bulk residual stress. The variation between the types of stock material

arises due to varying thermal processing histories and the amount of mechanical work employed to reduce residual stress levels [6]. In this body of work, the formation of the bulk stress within aluminium rolled plate material from which typically monolithic components are machined shall be considered.

Bulk material residual stresses formation

As discussed in section 2.2, the manufacture of the rolled plate aluminium alloy includes quenching. Quenching is typically done by submerging the heat-treated material into quenchant medium in specialist baths or spray systems. However, a large thermal gradient is created between the centre of the part and the surface [36], [62]. The surface, being in direct contact with the quenching medium, cools much faster than the internal regions of the material (Figure 2-29). The image illustrates a potential thermal cooling profile for the extremity and core of the plate material where the solid black line represents the billet external surface temperature and the dashed red line the billet core temperature. During cooling, the outer portion of the material contracts and plastically deforms whilst the internal medium is still hot and elastically responsive. As the centre portion begins to cool, it contracts to pull on the now plasticised outer surface. As a result, the outer section of the part is placed into compression. The internal section of the part exhibits equilibrating forces, which are tensile [36]. A typical RS profile for rolled plate is displayed in the graph shown in Figure 2-30 [35].

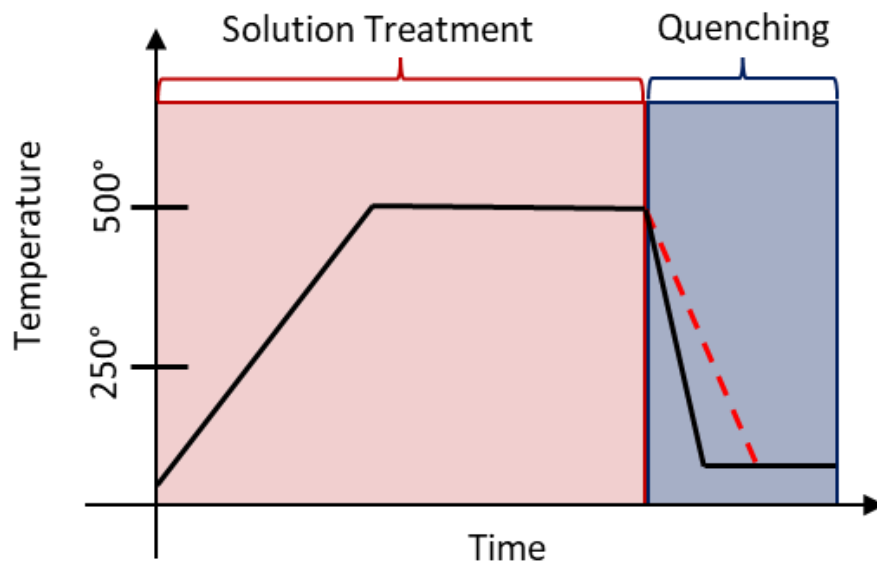


Figure 2-29: Difference in cooling rates between the surface and centre of an aluminium plate during quench

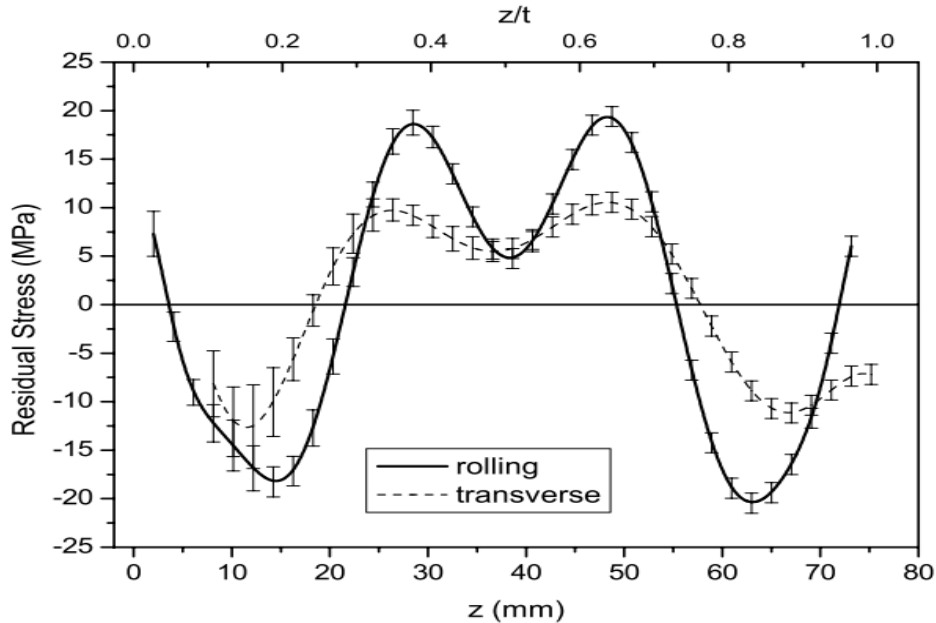


Figure 2-30: Bulk residual stress profile in 77.9mm thick AA7050-T7451 after stretch stress relief [35]

Bulk material residual stresses influence on machining distortion

The components at the centre of this study are large, monolithic structures. In order to achieve the final component geometry from stock material, computer numerically controlled machine milling is used to remove up to 90% of the material [63]. Part distortion due to inherent residual stress occurs during material removal during machining, which upsets the internal stress equilibrium [64]–[66]. As shown in Figure 2-30 the through-thickness stress profile of the aluminium plate is homogeneous and balanced throughout the thickness of the part. When a proportion of the material is removed, the stresses remaining will be unconstrained and therefore redistribute to reach a new state of equilibrium. It completes this redistribution by bending and twisting about the natural axis of the new shape. The magnitude of the distortion and mode shape is a combination of the magnitude and distribution of stress states (tensile or compressive) in the remaining material of the final machined product [65]. Wing-rib components central to this study are susceptible to residual stress-related distortion post-machining. Wing ribs can be grouped into two categories based on a main geometrical characteristic; double-sided and single-sided features. Within GKN, out-of-plane distortion manifests significantly more in the single-sided ribs. Single-sided ribs are composed of flat datum surfaces, with the opposite surface having pockets and wall stiffener geometry. Double-sided ribs are generally symmetrical about through thickness mid-plane. More distortion is observed in single-sided ribs because components are more prone to distortion with increasing machining asymmetry due to the location within the initial stock geometry [67][11].

Various sources of literature have investigated methods of controlling the material processing methods to decrease the inherent residual stress, resulting in part distortion for aluminium components. The work of Chatelain, Lalonde, & Tahan [49] included an experimental study of two forms of aluminium created with different processing histories. The material trialled was 7475 with temper designations T7351 and another with unspecified heat treatment denoted as “special recipe”. Residual stress was measured in both parts before and after machining, which showed the “special” recipe material to have lower peak bulk residual stress of up to ± 18 MPa. The distortion in the final test pieces showed that the magnitude of inherent residual stress significantly influences the final distortion mode after machining. Investigated as part of the C.O.M.P.A.C.T project, the process of over-ageing was found to lower inherent residual stress from quenching by 50% compared to quenched and stretched [41]. Younger and Eckelmeyer [37] found that the magnitude of residual stress introduced during material processing can be substantially reduced by quenching in warm or hot water (limited by section thickness and the quench rate sensitivity of the alloy) but minimal strength reduction would occur.

Polymer and uphill quench methods were found to reduce residual stress and distortion in the resultant components considerably compared to standard water quenching for cylindrical aluminium alloy parts [62]. Polymer quenching elicits a reduced bulk residual stress by wrapping the submerged hot plate in polymer fibres that solidify from solution to form on the surface, creating an insulating effect that facilitates uniform cooling. Uphill quench (also known as cryogenic treatment) is the process of subjecting the conventionally water quenched product to low temperature (i.e. -180°C) and then expose to a high temperature (i.e. 200°C). Theoretically the inverse thermo-mechanical response should occur in the plate and therefore formation of residual stresses that counter those left from the conventional quenching method. Figure 2-31 shows the impact of various quench methods on post-machining distortions as can be seen the various processing routes lead to very different bulk residual stress and machining distortion response. Similarly, Araghchi *et al.* proposed developing the cryogenic or uphill quenching method in AA2024 material processing [68]. The work analysed the material residual stress state by the hole-drilling method for materials processed with traditional ageing, artificial ageing and uphill cryogenic methods. Cryogenic treatment has been proposed to reduce the bulk residual stresses by 71% compared to conventional processing methods and slightly increase the material strength. However, these trials were conducted on a relatively small sample size. The economic consideration for larger billets could be a constraint on this method being commercially viable. The previously reviewed literature suggests promising distortion mitigation prospects concerning the control of Inherent residual stress at the material processing stage.

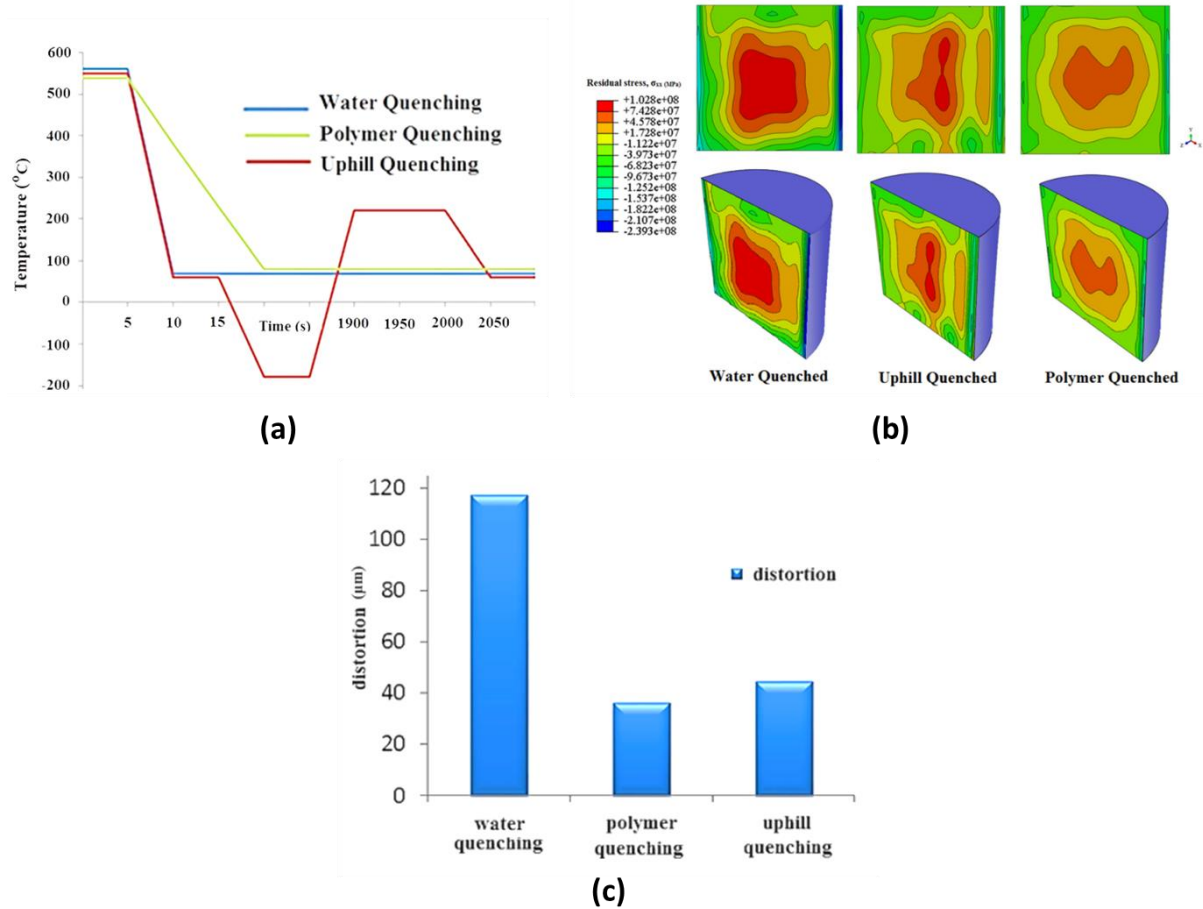


Figure 2-31: Impact of quench process on bulk residual stress and distortion [62]

Other researchers have turned their attention to controlling the machining process to limit bulk residual stress-related distortion. The offset can be described as the location of the final component within the prescribed billet stock geometry (as shown in Figure 2-32), and depending on its position within the billet, the final component could experience any number of varying combinations of resultant residual stress left within the material remaining post machining. The work of Sim [6] utilised a monolithic demonstrator test piece to study the effects of offset and machining strategy. It was shown that the position within the billet from which the component is machined would affect the final part profile regarding the amount and mode of distortion. This work is backed up by the findings of Huang *et al.* [69] that the distortion of their demonstrator test piece is more significant when located within the tensile residual stress section of the billet and lesser when located within the compressive zone. Furthering this, the work of Zhang *et al.* also concluded that offset (shown in Figure 2-32) is an essential factor in controlling distortion and demonstrated, through amending the machining strategy, that distortion in the final component could be reduced [67].

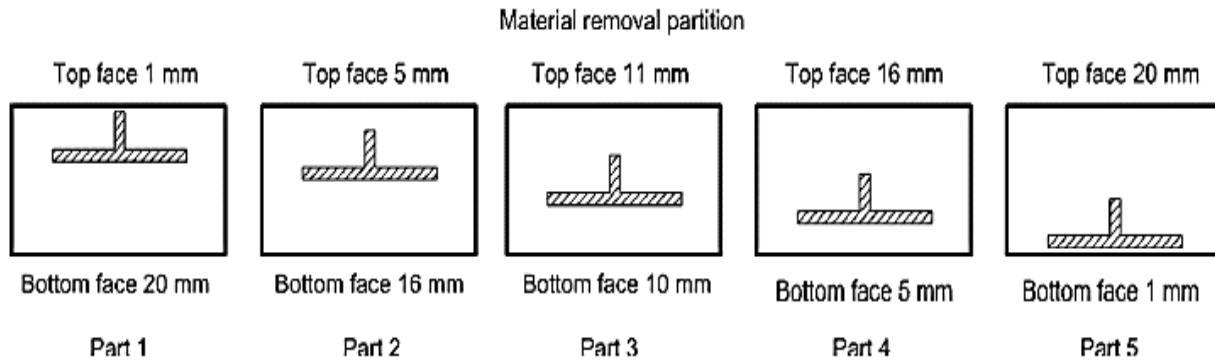


Figure 2-32: Offset of T-specimen produced in the trials conducted by Zhang *et al.* [67]

However, further studies have shown that the influence of offset on final part distortion can be limited by the thickness of the part [6], [69], [70]. At a certain critical thickness (dependent on the part geometry), the machining-induced residual stresses competes with the inherent stresses for the primary source of distortion. The thinner the part, the less influence the inherent residual stress has. Sim reported that this value occurred for the component thickness of 2 mm to 3 mm whereas the work of Huang *et al.* suggested this occurred around 1.25mm. Garcia *et al.* [71] tried to develop this work by varying the offset of a scaled-down representative monolithic component. High, mid and low offset regions were chosen within a billet of AL7050 T74, much the same as the previously mentioned work. However, the observed distortion lacked variation, as would be expected. The thickness of the floor sections of the test components that attributed most to the distortions due to the inherent residual stress was 3.18mm, close to the critical thickness reported in [6]. It should also be noted that the material utilised by Garcia *et al.* [71] in the experiments had high levels of inherent residual stress, with approximate max tensile and compressive residual stresses in the ± 150 MPa range. It should be considered that the aerospace-grade aluminium used in manufacturing large monolithic aerospace components is of the T7451 temper condition. The material is subjected to stress-relieving stretching during its processing history. Residual stress levels for these materials are approximately between 25 - 30 MPa. As indicated in [62], increasing magnitudes of bulk stresses result in greater instability and distortions when the equilibrium condition is disturbed by removing material when machined. Therefore, in industrial applications, the bulk residual stress levels will be much lower than reported in [71] and have a lesser influence on distortions.

2.5.2 Machining-induced residual stress

As detailed in the C.O.M.P.A.C.T report, machining can induce inhomogeneous, near-surface plastic deformation of the workpiece, resulting in residual stresses at the surface and sub-surface of a component [41]. The machining-induced residual stresses (MIRS) are generated by a combination of thermal and mechanical loads that arise during the material removal process [10]. Depending on the prevailing machining conditions, these induced stresses can be predominantly compressive or tensile [72]. These residual stresses also contribute to the distortions seen in thin-wall aluminium components [10].

Machining-induced residual stresses formation

Davim defines three mechanisms associated with thermo-mechanical machining loads that induce residual stress; mechanical plastic deformation, thermal plasticising effects and microstructural changes due to elevated temperatures [19]. The mechanical plastic deformation and associated high strain rates placed upon the workpiece material by the cutting action introduce tensile residual stresses immediately after the passing tool in the newly generated surface. The highly strained surface undergoes elastic recovery due to overstraining, which results in compressive stress formation, as displayed graphically in Figure 2-33 (left).

Thermal plasticising of the near-surface region occurs by the heat energy dispersion from the primary shear plane formation and frictional action between the tool clearance face and the workpiece surface. The temperature gradient between the newly generated surface and sub-surface restrains the surface from expanding. As a result, the plastic deformation of the surface layer by compressive actions occurs. The rapid cooling forms tensile residual stress as the tool moves away from the near-surface layer, which attempts to contract but is constrained by the plasticising effect. The stress generated by this action is plotted against the temperature, shown in Figure 2-33 (right).

Thermal microstructural changes induce residual stress through volumetric alteration associated with phase transformation. This can either be through volumetric increase or decrease, placing the near-surface zone into a state of compression or tension governed by material behaviour. Expansion is typical of metallic material, such as aluminium, and therefore compressive residual stress forms. Mechanically induced stresses have been shown to form over the most significant distance into the sub-surface of the workpiece material for machined metallic materials, whereas thermally induced residual stresses typically form at the surface. This is displayed in Figure 2-34, where layers denoted S, D and B relate to the surface/near surface, sub-surface and non-affected regions, respectively. Typical depths over which induced stresses are observed can be between 250 μ m and 300 μ m [73].

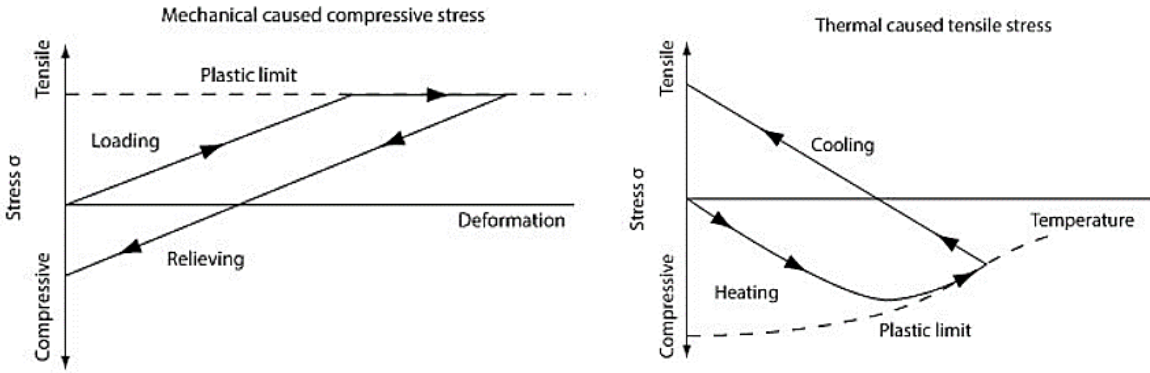


Figure 2-33: effects of mechanical (left) and thermal (right) loads on residual stress formation [19]

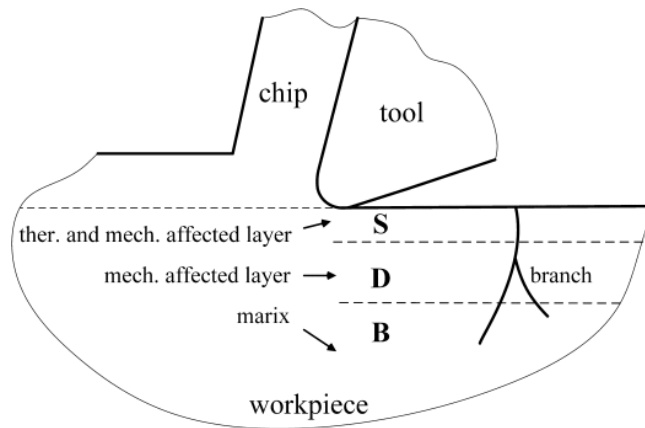


Figure 2-34: The layers over which the thermo-mechanical induced residual stress form behind the tool [73]

A typical machining-induced residual stress profile is shown in Figure 2-35 [74]. The shape of the stress profile that forms in the principal directions is directly proportional to the machining parameters that affect the thermo-mechanical loading, as discussed. The work of Jacobs *et al.* [75] consisted of orthogonal and oblique machining of annealed AISI 4340 to investigate the effects of tool edge radius and depth of cut on edge ploughing and shearing in the formation of near-surface and sub-surface residual stresses. Part of this work included an interpretation of the residual stress profiles that arise in the near-surface & subsurface of material due to the various combinations of the thermo-mechanical straining of the material. It follows that when the material is placed under thermal or mechanical tensile strain, the resulting residual stress is predominantly compressive. The opposite is true of compressive strains forming tensile residual stress regions.

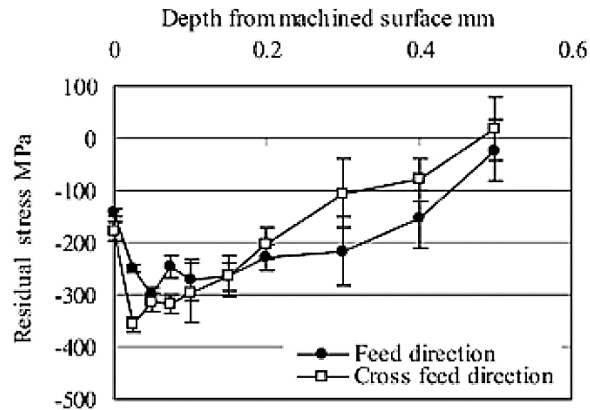


Figure 2-35: Subsurface RS profile induced by machining [74]

Figure 2-36 shows the 3 cases offered by Jacobs *et al.* Case 1 describes a situation where the mechanically induced subsurface tensile plastic strain is more significant than near-surface thermally induced compressive strains. This loading case results in compressive residual stresses in both the surface and subsurface regions. For Case 2, considerable surface temperatures induce large compressive strains greater than those developed by the tensile mechanical action in the subsurface layers. This results in a near-surface tensile residual stress region moving to compressive stresses in the subsurface region. This combination of stress sign regions is typical of a stress profile produced by milling operations where large plastic deformation results in deeper compressive stresses into the material, and thermal effects increase the stress to a more tensile state at the surface [10]. In Case 3, near-surface and subsurface strains induced are compressive, resulting in tensile residual stresses. In all cases, stresses will recover to near zero to satisfy equilibrium conditions.

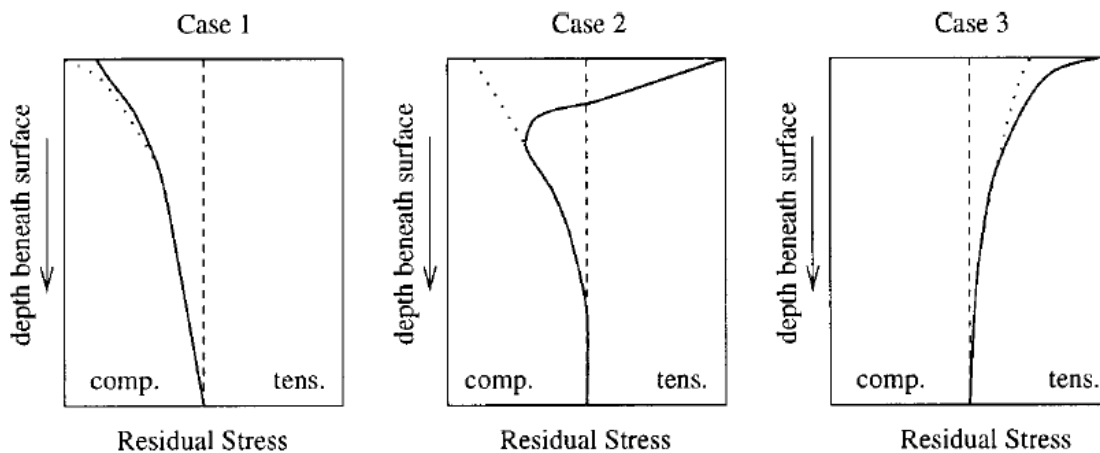


Figure 2-36: 3 cases for machining-induced residual stress profiles [75]

Other studies looked to build upon Jacobs *et al.* [75] observations by showing that the mechanical loads can also generate tensile residual stresses, including the work of Miguélez *et al.* by finite element modelling and experimental validation of orthogonal turning on AISI316L workpieces [76]. The variances in stress formation can be attributed to the complex nature of the interactions between the thermal and mechanical loads, which act simultaneously during machining, making it difficult to distinguish the influence of specific parameters. Figure 2-37, produced by Guang & Wang [12], provides a good overview of the conditions influencing the material removal process and residual stress formation. Next, this review will examine the research that has attempted to study such conditions on residual stress formation.

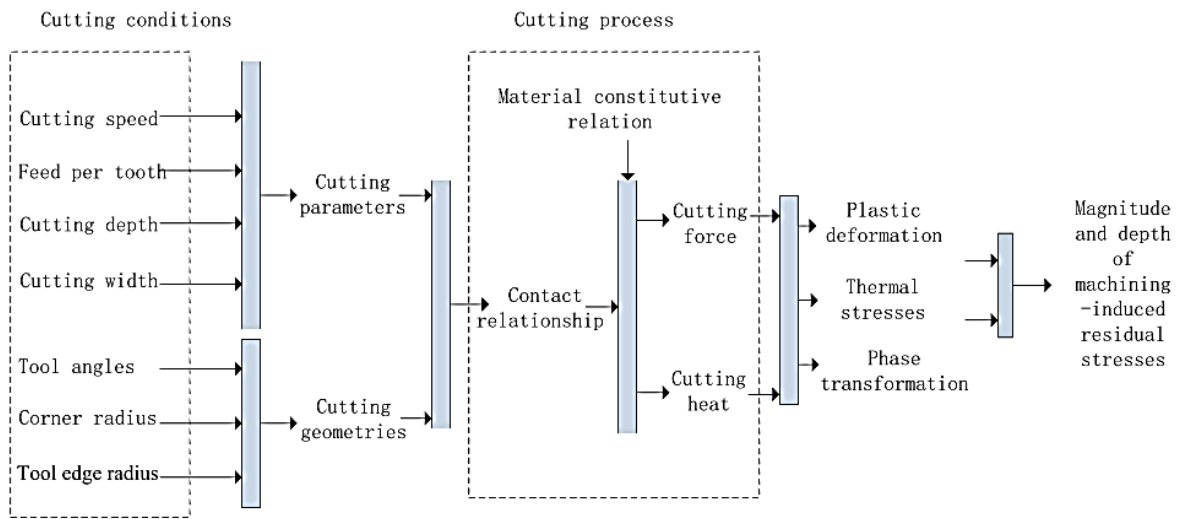


Figure 2-37: Machining-induced residual stress generation process [12]

Variations in the cutting conditions, tooling geometry and material

As previously suggested, machining-induced stresses are influenced by a complex combination of variables including, but not limited to, tool geometry, feed rate, cutting speed, radial/axial depth of cut, chip formation and the cooling method associated with the machining method. Notable work carried out in this area was that which formed part of the C.O.M.P.A.C.T project and the subsequent publications [26], [70], [77], [78]. These works form a comprehensive study into machining-induced residual stress development that considers the influence of cutting speed, feed, coolant, tool-material engagement and tool geometry, including rake angle, helix angle, clearance angle and corner radius.

Denkena, De León-García & Kohler [70] was the first of the publications that used side milling of AL7449 T7541 to understand the effects of part design and machining parameters on residual stress-related

distortion. Both significantly impacted the ensuing deformation after machining. The material workpiece geometry was found to be the primary influence of the mode of distortion. For the two offsets, bending distortions in the test component were either sagging or hogging in nature. However, this distortion is attributed to the bulk residual stresses from material processing and not machining-induced stresses. On the machining parameters, increasing speed was shown to vary the magnitude of the resulting distortion. It is important to note that the complex interaction of the material bulk stresses and design alters distortion magnitudes and shapes. In this work, no actual residual stress measurements were made, and distortions measured by CMM were speculated upon with respect to the impact of the induced residual stress. However, from this work, more extensive research themes were distinguished.

The work published by Denkena & Leon [78] comprised the shoulder milling of Al7449 T7651 blocks by 63 mm and 40 mm diameter tools with inserts of varying corner radius. The induced stresses were measured using the x-ray diffraction 2-circle Bragg technique with electro-polishing to characterise the residual stresses up to 300 μm . The results indicate that increasing the cutting speed increases surface tensile residual stress and subsurface compressive residual stresses (Figure 2-38 top left) due to decreasing machining forces and temperature increase at the tool/surface contact regions.

The increase in tensile surface residual stress formation agrees with Jacobs et al.'s findings that thermally induced stresses will occur at the surface and be tensile in description [75]. Subsurface compressive residual stress is also present due to the mechanical forces acting on the material caused by the cutting process. The increase of feed per tooth was shown to increase the maxima subsurface compressive residual stress, which is suggested to be the direct result of the increase in machining forces (Figure 2-38 top right). Of the effects of the coolant, the residual stress profile shifts downwards into a slightly more compressive position. The influence of coolant is true at high and low settings for cutting speed and feed per tooth. However, for the parameter ranges set for these trials, coolant has little significance on the residual stress formation (Figure 2-38 middle).

The speeds utilised in these trials are well below what is expected for aerospace milling of aluminium, which can typically reach 28,000 rpm and above. The effects of pushing the speeds further would most certainly expect an increase in the thermal loads and, therefore, the importance of the coolant on residual stress formation. The main finding of this report was the apparent dominating effect of the tool geometry, more specifically, the tool edge radius, on residual stress formation. It was found that increasing the edge radius from 0 mm to 3.2 mm reduces the compressive stress levels in the machined material surface and subsurface, and the profiles become more neutral (Figure 2-38 bottom). The link between the corner

radius and uncut chip thickness was indicated as the reason for this variation. The authors conclude that along regions of the cutting edge of the tools with corner radius, the minimal uncut chip thickness did not exceed the critical chip thickness, and therefore, the true cutting action is not achieved. Instead, the material is compressed without shearing, which increases the frictional forces at the flank face (Zone 3) associated with thermal loading.

As thermal loads are associated with the formation of tensile residual stresses, the movement of the stress profiles into a less negative region is rationalised. This phenomenon is known as material 'ploughing' where the uncut chip material advances to the cutting edge but is forced under the tool and elastic-plastically deformed instead of proceeding to flow across the rake face forming a chip. However, the impact on uncut chip thickness is less easy to study in milling applications than in turning operations, as chip thickness varies during the engagement of one tooth of the cutting tool. Jiang [79] looked to provide more insight into the influence of uncut chip thickness by describing the residual stresses formed in terms of discrete points on the radial cutting path for one milling cutter tooth. By FEM and experimental validation, they determined that residual stresses induced by the cutting action vary in the distribution in the tangential and feed directions as a function of the size of the uncut chip thickness.

Nowag *et al.* [80] showed similar results through turning experiments, where rings of 100Cr6 were subjected to varying cutting parameters and tool geometry. The work concluded that increasing the feed rate and nose radius of the cutter increases the magnitude of the sub-surface tensile residual stress value. In comparison, increasing the depth of cut and cutting speed was found to have the opposite effect. However, this deduction is not in accordance with the findings of Thiele *et al.* [81], which demonstrated that more significant maximal compressive stresses are formed for increased edge hone (radius). Similarly, Hua *et al.* (2005) demonstrated that increasing the feed rate and cutting edge radius resulted in a more significant compressive residual stresses during the turning of steel components [82].

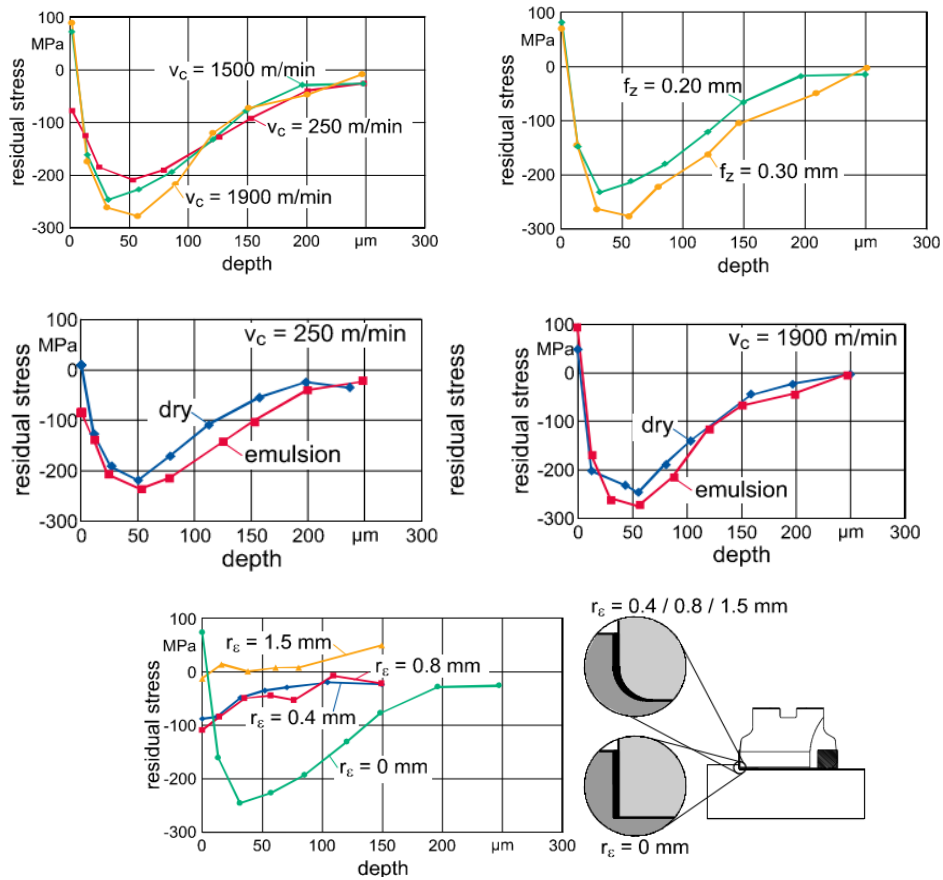


Figure 2-38: Graphs depicting the effects of cutting speed (top left), Feed per tooth (top right), coolant (middle) and corner radius on machining-induced residual stress formation (bottom) [78]

In reality, tool geometries are highly complex, as is their influence on chip formation. The understanding of the tool edge impact was further developed by the effort of Ventura, Breidenstein, & Denkena in which 5 PCBN inserts with varying edge forms (Figure 2-39) were trialed in turning of hardened AISI 5115 steel [83]. They concluded that the residual stress could be directly correlated to the process forces and the contact length to the tool-workpiece interface, which is dictated by the insert edge micro geometry. The latter was rationalised due to its direct effect on chip deformation, friction and ploughing of the machined surface by the tool-material interaction. Therefore, it can be seen that in each case, the variation in the tool geometry will result in different mechanical responses of the surface and near-surface material.

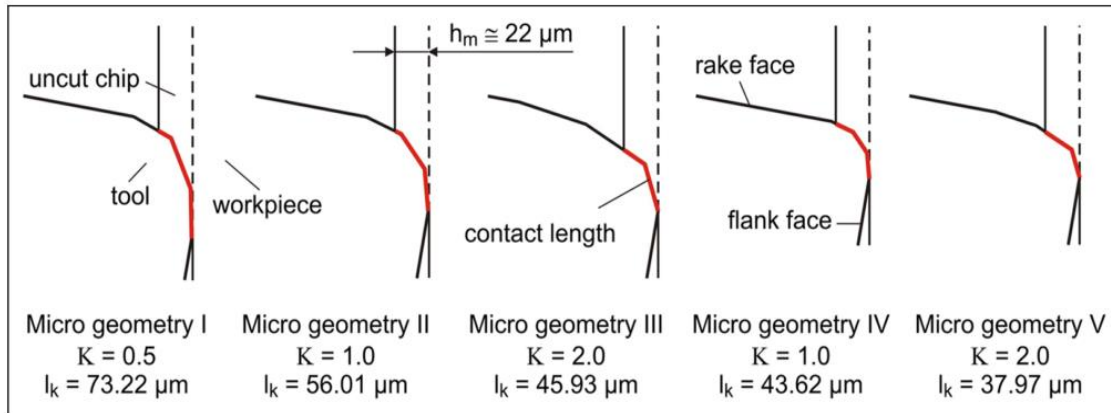


Figure 2-39: Varying contact lengths (shown as red) for different micro geometries

Further work of Denkena & Leon [26] looked to study the significance of varying other features of the cutting tool geometry on the residual stress manifestation. The experiments linked machining parameters with varying tool geometry when end-milling aluminium with 20 mm diameter solid carbide tools. The change in the cutting forces generated and the resulting residual stress that forms perpendicular and parallel to the cutting direction were observed. Again, it was concluded that increasing the feed and speed has little influence on the stress variation for the parameter range explored. Also, the radial clearance and helix angles had little bearing on the residual stress formation. Nevertheless, increasing the tool corner radius and rake angle reduces the surface value and minimal compressive stress value during machining. The increase in the rake angle was shown to reduce the cutting forces and, therefore, the mechanical loading placed upon the workpiece, reducing compressive stress in the subsurface. However, the increase in corner radius showed no significant effect on the machining forces. As in previous work, the relationship between the critical uncut chip thickness and corner radius was cited as the development in subsurface stresses.

Denkena, Garcia and Kohler [77] looked to further investigate the role of corner edge radius through finite element modelling to create an understanding of its influence in residual stress formation (Figure 2-40 - bottom) by varying the thermo-mechanical action of the cutting procedure. The model was produced in Deform 3D version 6.0, where the stress formed is defined as a function of the strain, strain rate and temperature. The tool-workpiece interaction was varied using a tool with no corner radius and one with a 1 mm corner radius. It was found that the temperature profiles below the newly machined surface were very similar for both tools, as shown in Figure 2-40 (left). Regarding thermal effects, the area of highest temperature by FEM was found to be in the secondary shear zone between the cut chip and rake face and

was lower for the tool with a corner radius. However, the max temperature cannot be used to indicate the residual stress formed as the mechanism relies on the temperature variation at the newly created surface and surrounding areas.

The authors determined that the temperature profiles were independent of the corner radius for the tooling used. Due to the restriction in the corner radius size that they could model, because of computation expense, the investigation into the effects on temperature-driven stress variations by increasing the corner radius could not be correctly investigated. The mechanical loading differed for the two radii, as seen in Figure 2-40 (right). The tool with a corner radius produced a higher stress gradient nearer the machined surface, whereas the stress created by the tool with no corner radius formed deeper into the material. This depth into the workpiece over which the mechanical forces act results in a more compressive residual stress profile by tools with no corner radius. The thermal effects which counterbalance the near-surface mechanical effects in the corner radius condition do not penetrate deep enough to affect the stresses formed by the tool with no corner radius.

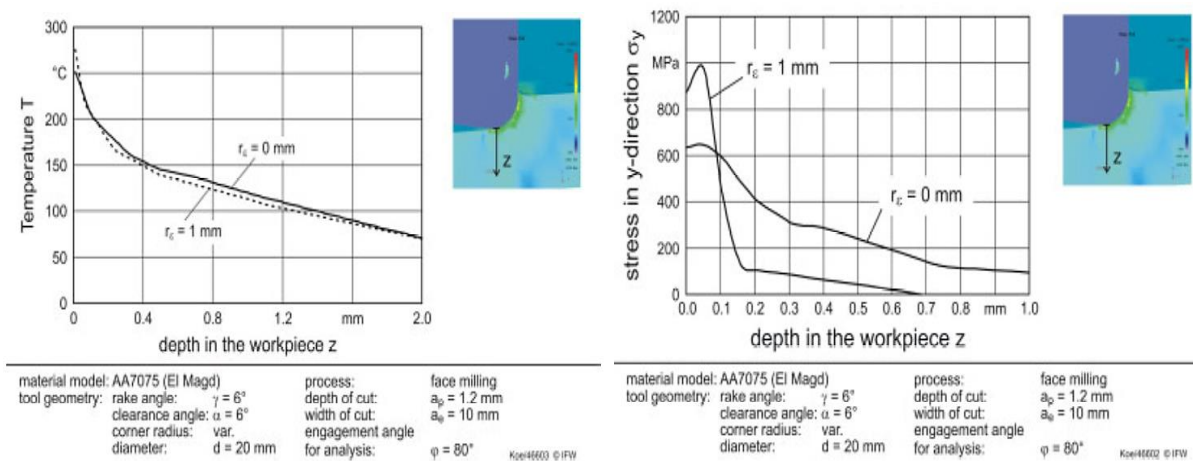


Figure 2-40: Effects of corner radius on surface and subsurface temperature (left) and stress in the through-thickness of the part (right) [62]

Nespor *et al.* [84] conducted orthogonal turning, orthogonal planning and ball end milling trails on Ti-6Al-4V test coupons to determine the prominent variables in altering the machining-induced material stress for each of the processes whilst attempting to draw comparisons. Cutting speed, un-deformed chip thickness and the cutting edge radius were chosen as variables for the orthogonal trials. Feed per tooth, step over, lead angle and cutting edge radius were considered for the ball end milling.

The results from the orthogonal trials supported the findings of Denka *et al.* [78] that corner radius significantly affects the residual stress formation in the cutting and perpendicular directions, as does the uncut chip thickness, whereas the speed has a limited effect on the cutting direction; but strong influence in the axial path. Due to the variation in the process kinematics between the orthogonal machining and ball end milling, the principal stress direction varies. In the orthogonal case, the principal directions are in line with and perpendicular to the cutting direction. Whereas, with ball end milling, the principal directions relate to the cutting strategy and inclination angle. Furthermore, the complex kinematics of milling compared with orthogonal turning has been described as a possible reason for the larger variance in induced stresses seen in the former and where the minimum stress occurs when increasing the edge radius. These findings enforce the importance of the studied machining application and surface generation method on residual stress formation.

Rao & Allamraju [85] investigated the influence of depth of cut (DoC) and cutting speed on microhardness and residual stress formation when turning AL7075. X-ray diffraction (XRD) was utilised to measure the process-induced residual stresses. The cutting speed was shown to have a bell-curve relationship with respect to the residual stress formation. For low speeds, the trend is positive and then changes to a negative direction when a particular value is reached. The DoC had an increasing effect on the trend of residual stress. Li *et al.* [86] also establish that DoC increases the residual stress when end-milling aerospace-grade aluminium. They proposed reducing distortion in a test piece component by optimising DoC using FEA guidance.

The effort of Masoudi *et al.* (2014) considered the impact of the cutting tool material (solid carbide and polycrystalline diamond) and machining parameters (cutting speed and feed speed) on residual stress formation and distortion in turning of AL7075 T6 thin wall components [72]. The machining forces in the turning operation were measured using a Kistler piezoelectric dynamometer, and the tool-workpiece interface temperature was measured by a thermal infrared camera with an uncooled Amorphous Silicon micro-bolometer. The emissivity coefficient of the camera was selected by matching the readings of a thermocouple attached to an artificially heated chip. Efforts were made to link the cutting tool material and machining parameters with the force, temperature variations, and residual stress found in the material in the cutting direction. Significant findings of the research included that the tooling material had an important effect on the force and temperature generation. The poly carbide crystalline (PCD) tool produced lower cutting forces and temperatures at the cutting edge than the carbide tool. The lower forces were explained by the lower coefficient of friction between the workpiece material and the

rake/clearance faces of the PCD over the conventional carbide. Additionally, the increase in thermal and mechanical loading was shown to cause a rise in maximum residual stress magnitudes. It was concluded that the inherent material stresses affected the distortions, and that further work was required to validate this claim.

Work has been discussed concerning the significant impact of the machining parameters, tooling geometry and tooling material in establishing the machining-produced residual stresses. The literature shows that the tool's geometry strongly influences stress formation due to the effect on the chip formation and resulting cutting forces. Furthermore, most papers suggest that the tool geometry can be chosen for a given machining application to limit surface-generated induced stresses. Some have even gone as far as developing new tooling concepts to develop beneficial surface compressive stresses. Segawa *et al.* [74] developed a compressive residual stress-generating tool which combines end mill machining and burnishing by novel end geometry of the solid HSS tool (Figure 2-41). Machining parameters are secondary regarding the effect on residual stress formation but still play a significant role.

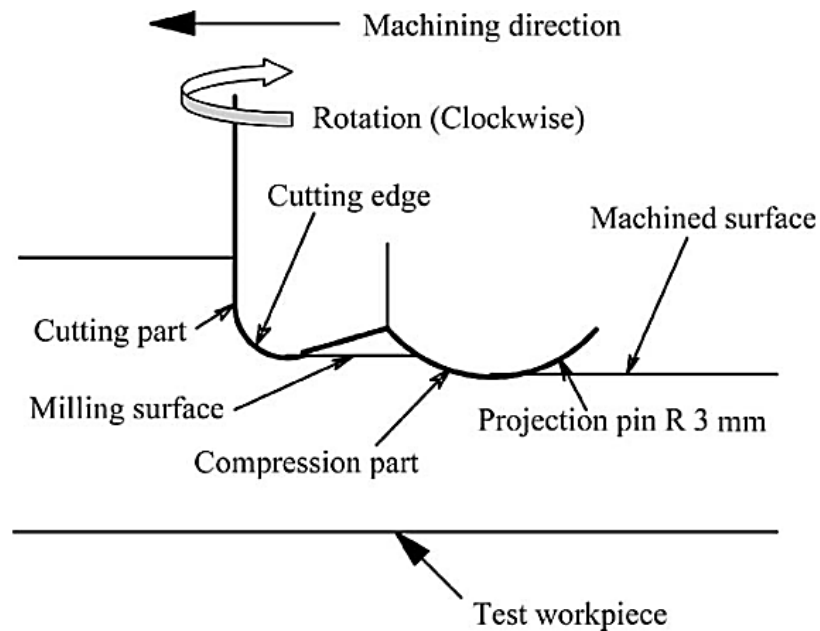


Figure 2-41: compressive residual stress generating tool [74]

Variations in the in-process conditions

The previously discussed literature has considered the machining strategy, including cutting parameters, tooling geometries and materials on the induced stress. As will be identified, the in-process variations will also impact the formation of residual stresses. Another important consideration in generating induced residual stresses by machining is the type and delivery of coolant in the machining operation. Turning experiments by Ji & Liang [87] were carried out to investigate the influence of MQL delivery from an external nozzle system on the residual stress formation in the turning of AISI 4130 tubing. An X-ray diffractometer was utilised to measure residual stress. The cosine amplitude method was used to make a conclusion on the most influential factor. Cutting speed was shown to have the greatest effect on cutting temperature. The depth of cut and heat transfer coefficient had the most impact on the cutting forces. It was determined that the latter had the most significant impact on the residual stress, more specifically, the maximum and average residual stresses. In terms of the minimum quantity lubrication (MQL), the mechanical loads are altered by the frictional coefficient effect and temperature by the convection cooling, leading to changes in thermo-mechanical loads and, therefore, residual stress formation.

Kenda et al. [88] performed trials with various MQL/cryogenic cooling conditions when turning Inconel 718. Dry, MQL, Cryogenic and MQL/cryogenic conditions were tested and supplied by an external nozzle system. By vector space analysis, considering stress generation in the cutting and axial directions, they showed that the cryogenic methods lead to more compressive mean stresses. They also reported improved hardness.

Tool wear is an important consideration in the formation of machining-induced residual stresses. Tang *et al.* [89] studied the effects of flank wear on mechanical and thermal loads induced during milling of 7050-T7451 and correlated them to the residual stress creation [89]. The findings indicated that increasing flank wear has a positive trend on both the maximum cutting force and temperature (Figure 2-42). The resulting residual stresses formed are increasingly tensile at the surface and compressive at the sub-surface with increasing flank wear. The compressive stresses were also observed to reach deeper into the workpiece, which led the authors to conclude that mechanically induced compressive stresses are the dominant factor.

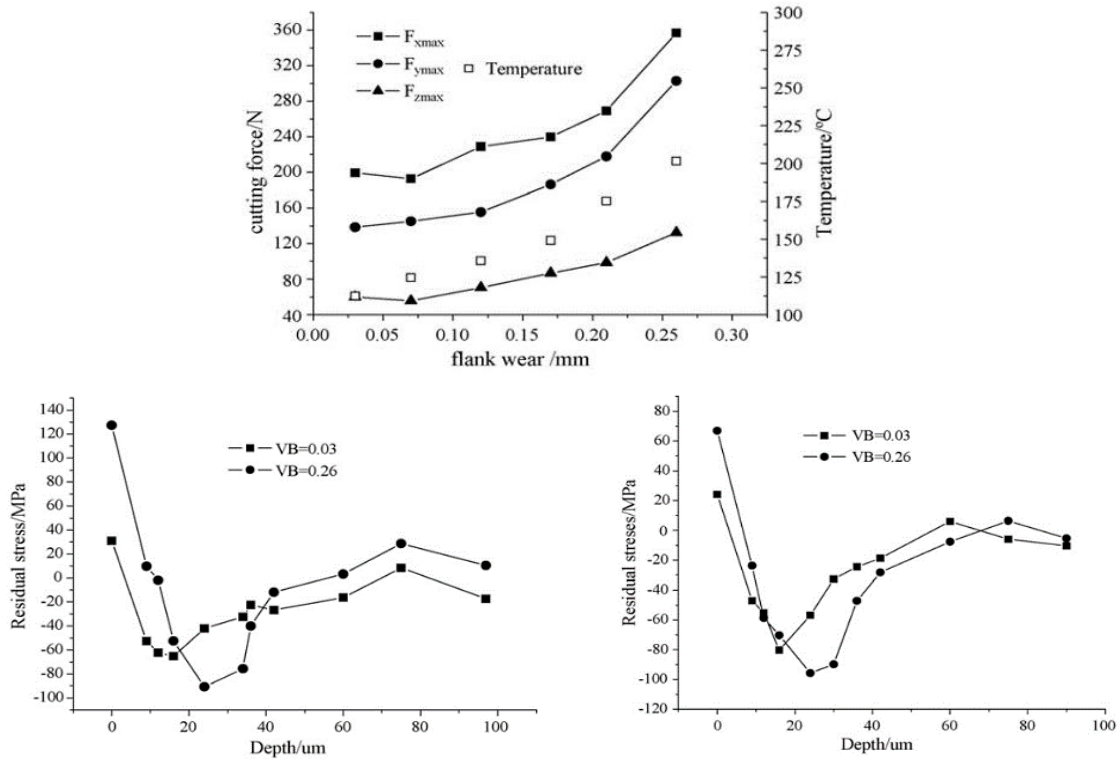


Figure 2-42: (top) max cutting force & max temperature vs. flank wear (left) residual stress profile perpendicular to feed (right) residual stress profile parallel to feed [89]

Similarly, Chen et al. [90] investigated the residual stress formation in the orthogonal turning of Ti-6Al-4V concerning tool flank wear and chip formation variations. It was noted that increasing flank wear from 0.03 mm to 0.20 mm resulted in a more tensile residual stress profile. The increase in tensile stress was believed to be due to increased thermal loading. Also, compressive stresses formed deeper into the part due to the increase in machining forces, which agrees with the conclusion of Tang *et al.* [89]. Therefore components machined with geometrically identical tooling can experience variations in the induced stresses if the tool is in a new or worn condition.

Other researchers have shown that the tool and workpiece dynamics can also affect stress generation at the surface. Outeiro *et al.* [91] investigated the effect of chatter on induced residual stress through an orthogonal machining experiment with AISI 316L austenitic steel. Assuming that the residual stress that develops during turning follows a cyclic variation and so does the vibration, then it can be modelled using a sinusoidal function. The results showed some coherence between the model data and the residual stress values in the axial, radial and circumferential directions obtained by neutron diffraction. Although some disparities are evident, which is suggested to be due to the error in the residual stress measurements, a decent correlation between the chatter and induced stresses was observed.

Variations in the workpiece material supply condition

Previously in this section, the influence of tooling, process parameters and machining conditions have been considered. Another influence is that of the workpiece material. Material properties impact machinability directly and the forces produced in cutting. Santos et al. (2016) suggest that increases in mechanical strength and hardness of the workpiece material, either by thermal or mechanical treatment, reduce the chip-tool contact length, which in turn reduces the mechanical forces up until a point when high deformation and strain cause cutting forces to increase [92]. Therefore, it can be said that the residual stresses by mechanical action or process forces are affected by the workpiece material condition.

For example, Thiele *et al.* [81] studied the influence of workpiece hardness on residual stress formation in turning AISI 52100 steel. The design of experiment (DoE) method was presented to explore the influence of the material-related variables. The results of the tests indicate that increasing workpiece hardness resulted in a more compressive residual stress formation. The authors attributed this to phase transformation in the surface layer. Hua *et al.* [82] investigated workpiece hardness, cutting conditions and tool edge geometry on the formation of the induced residual stress in hard turning of AISI 52100. The work included the development of a finite element model that used a hardness-based flow stress formulation within an elastic-viscoplastic model. The authors concluded that more compressive residual stress is formed for increasing material hardness. Nasr et al. [93] used FE modelling and orthogonal machining of various AISI alloys to study the effects of the initial yield strength, strain hardening coefficient and strain hardening exponent on residual stress formation. It was found that surface tensile residual stress value increases when yield strength increases and strain hardening properties decrease. Compressive stresses are formed when the opposite is true. Much research has been carried out in this area for different grades of steels and hard metals such as Titanium, Nickels and Inconel. In comparison, less intensive research has been performed on the variations of heat treatable aluminium alloys.

On machining-induced residual stress formation, various researchers have highlighted the importance of material condition, machining parameters and tool geometry on the near-surface residual stress formation [10], [27], [70], [72], [77], [85], [94], [95]. Furthermore, researchers have considered the history of the machining process on the final surface/sub-surface influenced stressed layer [48], [63], [96]–[101]. As seen in literature, machining-induced residual stresses are typically characterised by a specific tool/workpiece contact regime and prescribed machining parameters. Near-surface stress measurement techniques are produced after a single tool pass [102]. However, roughing and finishing passes can be used for large complex wing parts to achieve the final part geometry.

Sequential Machining Operations

Some researchers conclude that sequential machining processes eliminate the machining-induced stress in the semi-finish product imparted from previous cutting passes. Therefore the intermediary machining stress state does not impact the final stress state in the finished component. Ma, Goetz and Srivatsa [100] conceptualised a virtual workflow to model the impact of machining and bulk stress on engine and aerostructures components. Their work used a linear stress model to interpolate an empirically determined machining-induced stress over a surface mesh to understand the impact of distortion in thin-walled components. Their model assumed that the effects of induced residual stress from previous cuts are removed by succeeding machining passes. They showed a good correlation between the experimental distortion test piece and FEM results, modelling the distortion of said test piece when mapping the machining-induced stress generated in a coupon using only one machining pass.

Li *et al.* [86] performed end mill slotting in Al2024-T3 plates to study the impact of sequential machining operations. They performed sequential machining passes with progressively smaller DoC (Figure 2-43) and measured the residual stresses in the feed and perpendicular directions by XRD. Their results indicate that if the residual stresses imparted by machining extend into the component deeper than the successive finishing pass, performing progressively smaller DoC results in a less pronounced stress machining-induced stress field.

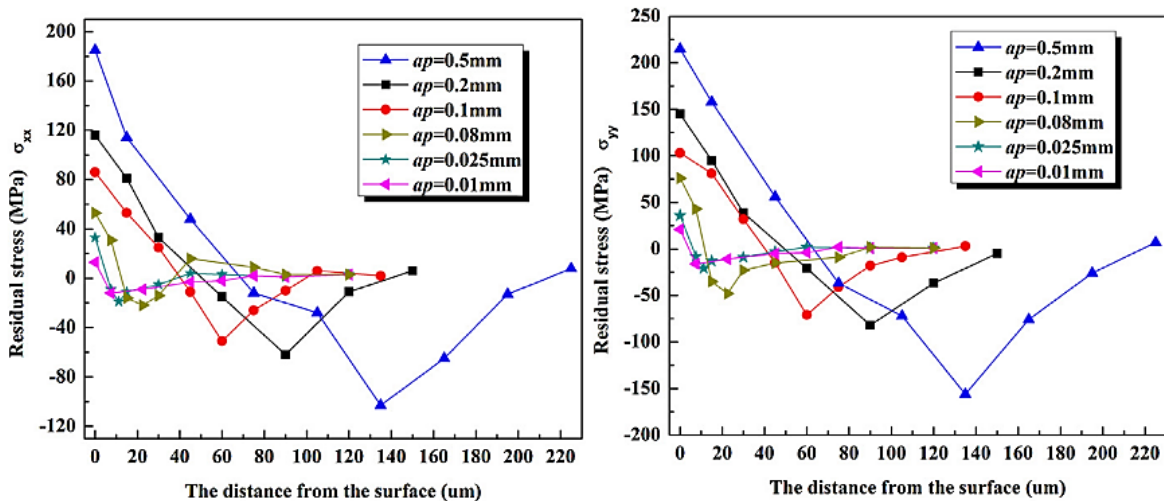


Figure 2-43: Li *et al.* [86] (a) impact of DoC on cutting forces and temperature (b) the experimental set-up and DoC

Fergani *et al.* [103] performed multistep end milling, including roughing and finishing processes on the AA2024-T3 plate. The machining-induced residual stresses after each pass was measured by X-ray diffraction. The measured stresses are then used as input data to an analytical model to predict distortion by classical beam theory. The aim was to observe the effects of initial know stresses and subsequent machining passes on the final near subsurface stress profile and subsequent distortion. They concluded that each subsequent pass removes the machining-induced stresses imparted by the previous machining passes. Therefore, only the contribution of plastic deformation in the final pass is attributed to the final residual stress state.

However, Fergani, Jiang & Welo [97] presented an uncoupled elastic-plastic analytical approach to predict machining-induced stresses a year later. This work included a regeneration algorithm to consider the impact of the previous near-surface stress state imparted by previous machining passes in the calculated approach. The model accounted for cyclic plasticity caused by the cutting action and utilised a kinematic hardening model to update the constitutive material description for the subsequent machining pass. The model showed good agreement with empirical residual stress results obtained by XRD. The results suggest that the influence of previous cuts should be considered for the parameters and DoC chosen.

Liu & Guo [104] used an elastic-plastic coupled FE model to simulate the impact of sequential orthogonal machining passes on machining-induced residual stresses in 304 stainless steel. 2 passes are simulated where the state of the surface after the first pass becomes the starting condition of the model for the second pass. The setup and results are summarised in Figure 2-44. The model results suggest that the previous machining step influences the second cut moderately.

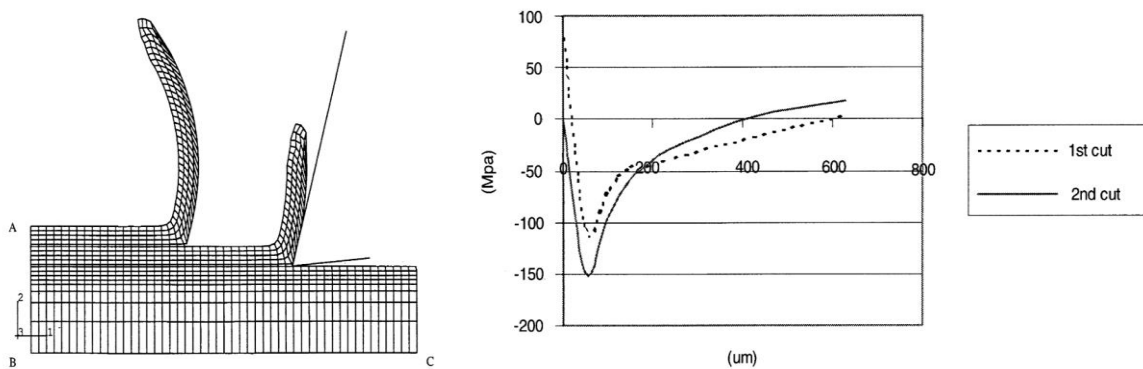


Figure 2-44: Sequential cut FEM (left) and normal stresses (right) [18]

Nespor *et al.* [84] compared the machining-induced stresses by ball-end milling and orthogonal machining of Ti-6Al-4V. As part of the work, they concluded that sequential cuts when orthogonal turning lead to higher compressive stresses (Figure 2-45). However, a small unreformed chip thickness was used, suggesting that the previous machining state would be more prominent in the subsequent cut.

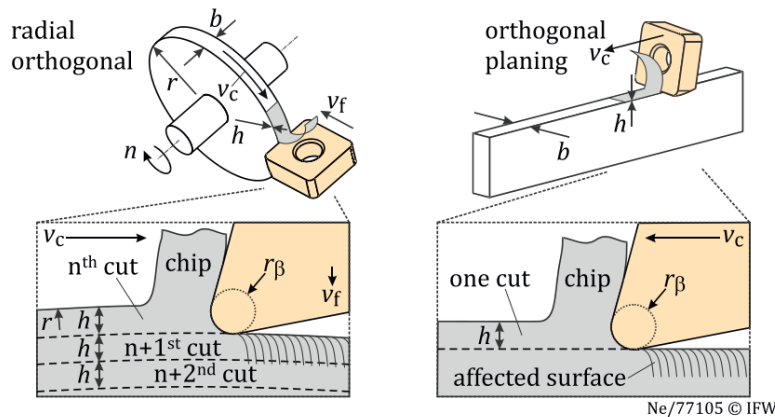


Figure 2-45: Sequential DoC for orthogonal turning and planing [84]

Ma *et al.* [102] used experiment and FEM to investigate the impact of consecutive machining passes on the depth and magnitude of process-induced stresses when turning high-strength steel. Their experimental methodology included heat treating the test samples to significantly reduce initial residual stresses and clamping/workpiece design to eliminate the impact of work-holding stresses. They trialed a combination of two variable roughing and two variable finishing machining processes to understand the contribution of each on the final machined stress state. It was concluded that although the last cutting pass firmly controls the final surface residual stress state, if the stress influence range and amplitude imparted by the roughing process is large enough, it will influence the final subsurface residual stress state. Although, this was not attributed to any impact on final workpiece distortion.

Therefore, the influence of previously machined surfaces is not considered in simulations that use machining-induced stress data generated from a test coupon subjected to only one machining pass. The assumption that measuring the induced residual stress after the final machining pass could be valid since machining-induced residual stress fields form over small depths in the order of hundreds of microns. Therefore, if the subsequent machining pass is larger than the depth over which the residual stress state left by a prior machining pass extends, it will not influence the newly generated surface/sub-surface stress condition. However, researchers do not have a consensus on the impact of sequential cutting, and the literature is quite contradictory.

Machining-induced residual stresses influence on distortion

Little work has been carried out to understand the sole influence of machining-induced residual stresses on part distortion. Much work has been done on interpreting their contribution towards part distortion in conjunction with bulk residual stresses. For example, the work of Madariaga *et al.* studied the influence of variable machining-induced residual stress conditions on the deformation of 7175-T7351 aluminium plate material by FEM and experiment. Machining trials with variable parameters (machining speed and axial DoC) were conducted, and near-surface induced stress was measured by incremental hole drilling. The measured machining-induced stress profiles exhibited variable compressive peak magnitudes and penetration depth, as shown in Figure 2-46. Both experimental measurement and FEM results showed a good correlation between distortion mode and magnitude. The different machining-induced stress profiles generated were shown to cause variable distortion [99].

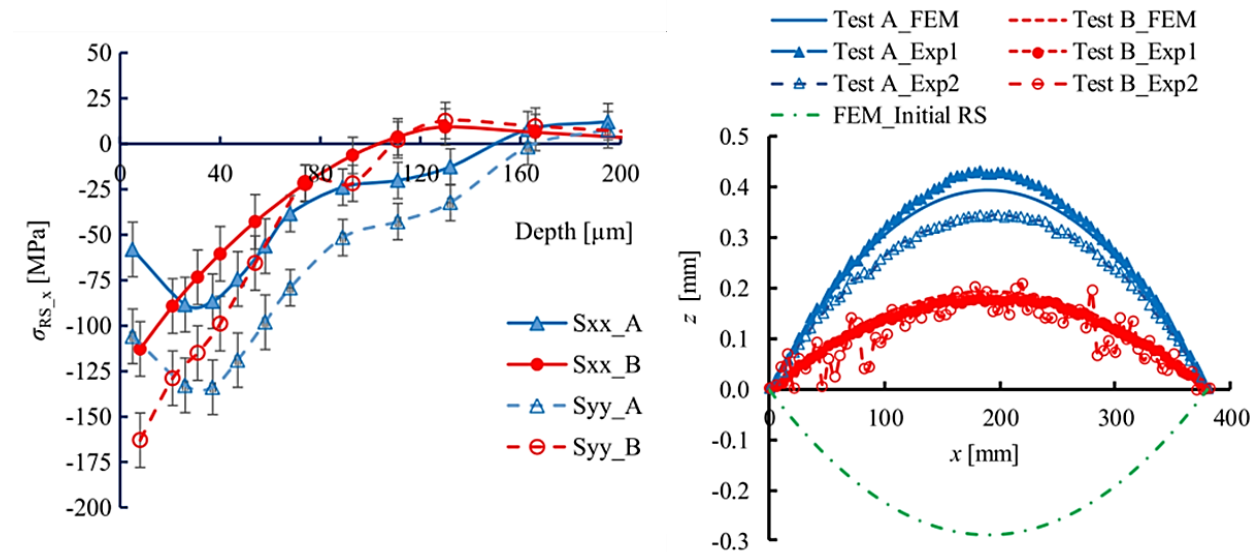


Figure 2-46: variable MIRS profiles (left) and influence on final part distortion (right) [99]

2.5.3 Secondary Sources of Residual Stresses

This section considers ancillary processes surrounding the machining process that does not directly influence the formation of bulk material or machining-induced residual stresses but affect the redistribution of residual stress or impart secondary sources of residual stresses other than machining.

Shot Peening

Shot peening is conducted to reduce the effects of surface and sub-surface tensile residual stresses left behind from machining operations to improve the fatigue life for a given component [105]. Shot peening is the process of discharging small and spherical particles at high velocity towards the surface of a component. The shot induces a tensile 'stretching' stress which causes the material to yield plastically. As a result, the subsurface material near the shot area responds through an opposite compressive reaction changing the RS profile (Figure 2-47) [106]. At this point, the forces are unbalanced, and as a result, the part will deform in order to reach equilibrium.

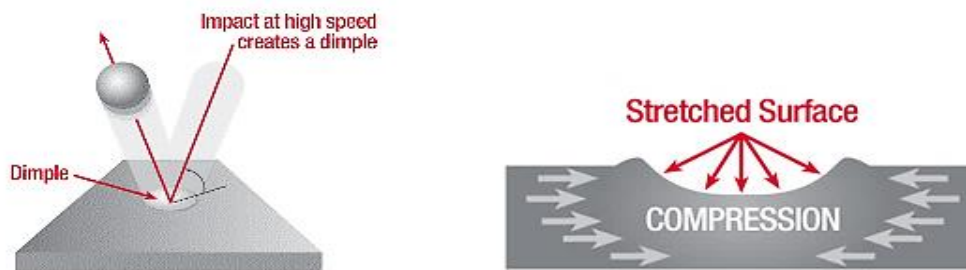


Figure 2-47: The process of shot peening [106]

The plastic deformation at the surface alters the sub-surface residual stress state of the part, resulting in distortion. This distortion can be utilised as a post-machining distortion correction method. Shot peening is used today in aircraft wing structural components to: 1. Improve the fatigue life of the ribs through saturated peening; and 2. Selectively peen areas of high distortion to bring the part back within distortion tolerance. Although saturated shot peening is necessary for improving the fatigue life of a part, selective shot peening is required only as downstream distortion control [107]. If possible, machining, design or manufacturing (upstream processes) should be adapted to address the issue of part distortion due to RS and reduce the reliance on costly corrective shot peening.

Clamping and fixture

Clamping forces are required to locate, restrain and eliminate the movement of components during machining operations [108]. Typically, traditional fixturing of large aerospace components locks down the 6 degrees of freedom of the component throughout the machining process. However, if the clamping

forces are excessive, they will cause elastic deformation of the workpiece as the rigidity is lowered by the removal of stock material during roughing operations, reducing the precision of the finishing machining operations [109]. Furthermore, the redistribution of the internal residual stress during the bulk material removal is constrained by fixturing. Only upon release of the fixtures are the resulting distortions perceived.

First, researchers have considered fixture systems that limit the impact of cutting-induced deflection on the workpiece that is not caused by residual stress. The review paper by Gameros *et al.* [110] summarises the significance of suitable fixturing on workpiece deflection during manufacture. Additionally, Gamero's work presented the use of deformable diaphragms to work hold complex blade geometry work pieces for machining.

Additionally, multiple research projects have looked to determine optimal clamping conditions as a means of reducing final distortion by redistribution of residual stress during/post-machining. Clamping has been shown to alter the residual stress distribution within a component but not its mean value [80]. If correct clamping procedures are assigned, then the changes to the internal stress state of the component do so elastically, and the forces associated do not induce plastic deformation. Therefore, when released from clamping, when no plastic deformation has occurred, the part will return to its previous stress state. Therefore, the effect of clamping on the final distortion of the part occurs post-machining operations when unloading. The boundary conditions, including resultant force direction and magnitude, will alter how the low-rigidity parts deform during material removal due to the redistribution of internal residual stresses. To this end, some authors have addressed this issue through experiments and numerical modelling.

In the review paper of the work conducted as part of the INTEFIX European research project, Möhring & Wiederkehr [108] presented a smart fixture system for workpiece distortion control. The picture frame fixture (Figure 2-48) allowed for dual-sided machining and is comprised of adaptive clamping units, which altered the retaining force based on active feedback control using strain gauges. The system allows the thin wall aluminium component to relax during milling machining. Thus, the residual stress has already been redistributed prior to clamp release.

Yingguang *et al.* developed an adaptive machining fixture (Figure 2-49) to account for distortions during machining using clamps that respond to the movement of the part between machining operations [111].

Similarly, Gonzalo *et al.* developed a clamping system to react to the deformation of an aero-engine component during machining [112].

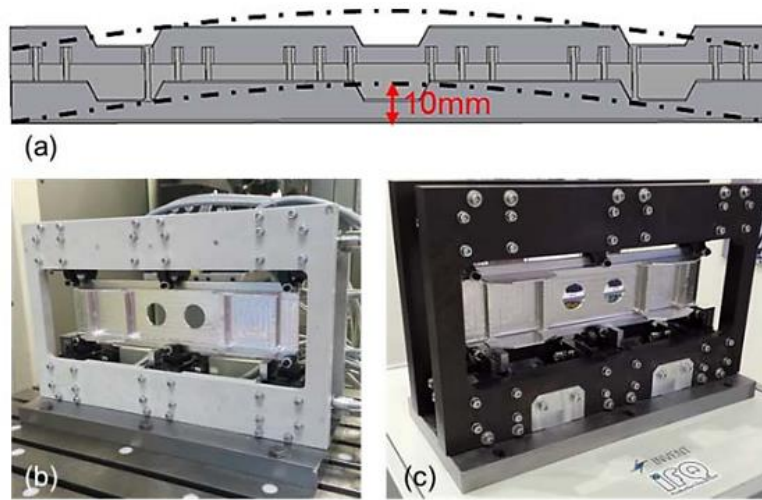


Figure 2-48: Smart picture frame fixture [108]

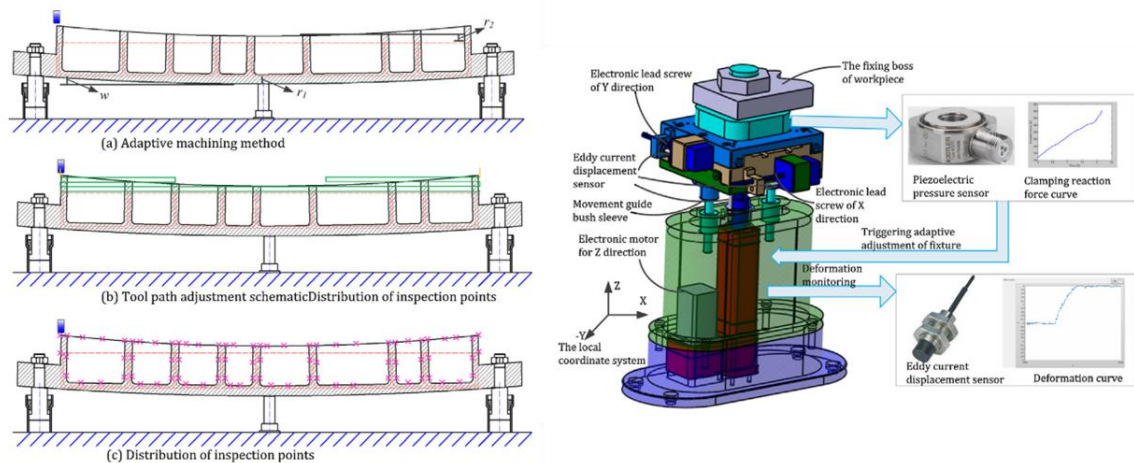


Figure 2-49: Fixture system for low-stress machining [111]

The previous clamping studies discussed posed reactive clamping methods to reduce machining-related distortions. Cerutti [48] studied the influence of several clamps and clamping locations on bulk stress redistribution, driven by part deflection through an experiment and finite element modelling. He found that less clamping constraint would allow the part to distort more in-process, causing geometrical error in the final component due to overcutting.

Reviewing literature concerning clamping and residual stress showed that clamping strategies are important in preventing machining inaccuracies caused by over-undercutting. Also, the distortion arising

from the redistribution of residual stress interacts with the chosen fixturing. Adaptive 'smart' fixturing is an innovative development, based on the concept allowing parts to redistribute residual stresses during machining operations as a method of managing distortion related quality issues.

2.5.4 Summary of section

Aerospace wing rib components have complex designs with various features that differ in thickness and geometry throughout the component, from very thin floor sections to thicker web and stiffener sections, for weight and strength considerations. These design requirements and a complex manufacture history, including thermo-mechanical processes, make determining the main source of distortion difficult. Moreover, this is reflected in the literature, as various authors have presented contradictory conclusions concerning the prime cause of part distortion due to residual stress.

Bulk residual stresses form during the mechanical and thermal treatments of the stock material and have considerable influence on the final component distortion due to the re-equilibration of residual stresses after material removal by machining. The magnitude and distribution of the bulk residual stresses can be controlled by applying specific processing techniques or conditions during treatments. Machining-induced stresses form in the near-surface of machined components due to the severe thermal and mechanical loads caused by the shearing and rubbing action between the cutting tool and workpiece material. They also have a significant influence over the final distortions in machined components. Researchers have spent much effort in determining influential parameters on the formation of machining-induced residual stress. However, little work has been carried out in determining machining-induced stress caused by milling, where turning has been opted for due to the simplicity in further modelling activities. It can also be noted that only a small amount of the work has been conducted to link the milling-induced stresses with final component distortions, where most are considered with the effects of surface integrity only.

Some authors have indicated that bulk stresses are the main cause of distortions in the final components. Yang *et al.* concluded that bulk stresses were the main cause of the distortions in their machined AA7075 test piece [113]. However, they did observe errors between simulated and experiment machining induced distortions results which could be attributed to machining-induced residual stresses. Huang *et al.* [114] also observed this, who undertook FEM and machining experiment on a similar pocket feature workpiece. They determined by FEM that the machining induced stresses only accounted for 10% of the distortions. Chatelain *et al.* [49] also concluded that bulk stresses primarily cause final part distortions. However, it has been shown that the thickness of the final machined component will affect the level of contribution

that the machining residual stress has on the final distortions. As previously discussed, the work of Sim [6] identified by flat plate machining trials that the machining-induced stresses started to have effect on distortions when the plate thickness was reduced to 3mm and below. The results of these trials are displayed in Figure 2-50 and it can be seen the diverging trend between the simulated results and plate distortion as plate thickness is decreased.

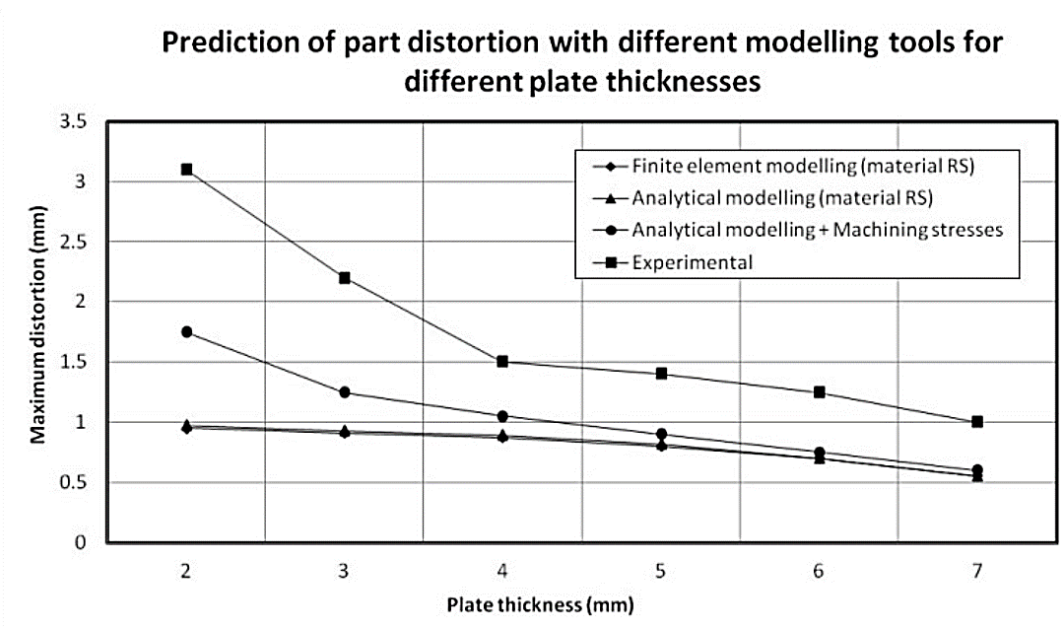


Figure 2-50: Influence of machining-induced stresses on flat plate distortion [6]

Haug *et al.* observed similar effects with respect to the increasing influence of machining-induced stress with decreasing component thickness [114]. Similarly, the effort of Masoudi *et al.* linked the decrease in wall thickness with increased distortion by machining-induced stresses in turning of AL7075 T6 thin wall components [72]. It was inferred that thinner components feel the increase in distortion by machining due to increased stress variation. Thus, it can be said that when considering components where regions of the part fall below a critical thickness, both sources of residual stress will influence the final distortion mode and magnitude, if these sections make up a significant proportion of the component question. However, there is no consensus on what governs this relationship between the bulk and induced stress on distortion. However, it can be determined that when considering wing rib component distortion, due to their complex design, both forms of stresses will need to be accounted for in modelling considerations, as identified by D'Alvise *et al.* [97] in Figure 2-51.

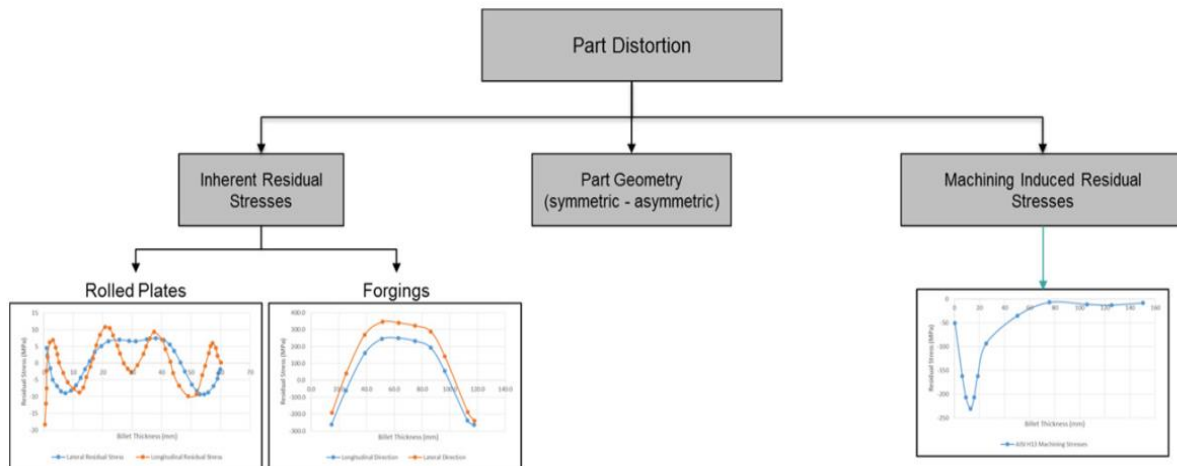


Figure 2-51: Important considerations for part distortion in aerospace components [97]

2.6 Modelling and simulation of residual stress and part distortion

Various modelling methods have been reported to study the formation of residual stresses and their impact machining related distortions; empirical, analytical, finite element and artificial intelligence [115]. All have benefits and limitations, as will be discussed. The following sub-sections will consider the models used to simulate the formation of bulk and machining-induced residual stresses and present models and methodologies developed to understand the influence of the aforementioned residual stress sources on part distortion.

2.6.1 Bulk Residual Stress generation

Numerous examples within the literature have used finite element simulation to model the bulk residual stress formation (Figure 2-52) due to quenching to; better understand its formation [114] and develop various state-of-the-art material processing techniques. As such, the literature regarding residual bulk stresses can be grouped into two general categories; 1. Bulk stress formation 2. Methods to limit the magnitude of bulk residual stresses. Firstly, using FEM to predict the bulk residual stress establishment by quenching operations is well established [116]–[121].

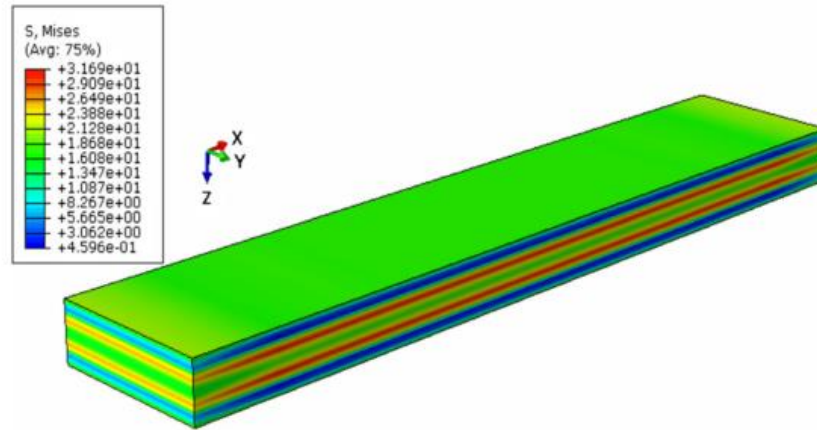


Figure 2-52: Bulk stress FE model [114]

Tanner and Robinson utilised a thermo-mechanical model to simulate the formation of residual stresses during the quenching of AA7010 using an uncoupled FE method [116]. The inherent material residual stresses were measured using hole-drilling and X-ray diffraction methods. Thermocouples were utilised to establish the surface cooling rate curvatures. This data was used to establish heat transfer coefficients utilised as inputs for modelling in Abaqus FE software. Although the FE approach in determining heat transfer coefficients proved advantageous, the experimental and simulated residual stresses lacked correlation. The lack of fit was put down to the use of non-exact material properties, which govern the plasticising behaviour of the material. Furthermore, the effect of precipitation hardening on residual stress development was assumed negligible.

In later work, Tanner and Robinson [117] would attempt simulating the bulk stress formation for AA7449 and the resulting distortions after machining. Again, non-exact material properties were used to rationale the lack of fit between measured and simulated stresses. Chobaut *et al.* would later develop an FE strategy that incorporates material information omitted by Tanner and Robinson through interrupted Gleeble tests [120]. The measured and simulated residual stress levels were in good agreement, highlighting the importance of highly accurate material parameters for effective modelling. As was presented, FEM can accurately predict bulk stress establishment caused by heat treatment. However, the simulation of bulk stress formation requires experimental data by measurement to validate the simulation results, as no universally accepted method has been established.

Other authors have employed FEM to optimise material processing parameters with respect to bulk stress reduction. The work of Jones [118] looked to model the effect of the uphill quenching method on RS formation within a workpiece and the subsequent distortion from machining operations. The paper

showed a promising distortion reduction strategy by uphill quenching material as opposed to the conventional heat treatment. Tanner & Robinson [117] utilised FEM to examine the effects of cold compression and stretch stress relieving on bulk stress formation in 7XXX aluminium. The reviewed literature shows that establishing the bulk residual stress via simulation is promising and suitable for sensitivity trials. However, these simulation results still must be validated via measurement.

2.6.2 Machining Induced Residual Stresses generation

Various methods have been reported in the literature to determine the machining-induced residual stresses [122]. The following sub-sections will consider empirical, numerical and artificial intelligence methods reported in the literature.

Empirical

The empirical method is well established where models are developed through curve fitting to experimentally determined data. The work of El-Axir considered the application of a polynomial function to describe the subsurface stress profile:

$$\sigma_i = c_{0i} + c_{1i}z + c_{2i}z^2 + c_{3i}z^2 + \dots + c_{ni}z^n \quad 2-5$$

where the coefficients (c_{ni}) are determined as separate or interacting functions of three inputs:

$$C_i = b_{0i} + b_{vi}v + b_{fi}f + b_{ti}t + b_{vfi}vf + b_{vti}vt + b_{vti}vt + b_{vti}vt + b_{fti}ft \quad 2-6$$

Where b_{xi} is the effect (or interaction) of x that are related to cutting speed, feed and material tensile strength determined via empirical testing [123].

Ulutan [124] presented the use of the sinusoidal decay function for modelling the machining-induced residual stress in turning of IN-100 nickel super-alloy:

$$\sigma = C e^{-\zeta\omega_0x} \cos(\omega_d x + \phi) \quad 2-7$$

The sinusoid function maps the stress (σ) over the length (x) where each variable is parameterized over a fixed range given in Table 2-3. These variables are optimised using particle swarm optimisation to fit the experimentally determined data.

Table 2-3: Sinusoidal variables ranges

Variable	Range
Amplitude (C)	[0, 10000] (MPa)
Damping coefficient (ζ)	[0.7, 1.0]
Damping frequency (ω_d)	[0, 0.06]
Undamped frequency (ω_0)	$\frac{\omega_d}{\sqrt{1 - \zeta^2}}$
Phase angle (ϕ)	$[-\pi, +\pi]$

Although these models are shown to be highly accurate, they can only describe the stresses for the specific narrow bandwidth of experimental data used to fit the models and are not based on the physics of the problem. On the other hand, analytical models have been developed to predict machining-induced residual stresses using mathematical expressions for imparted strain and temperature and workpiece material properties to describe the evolution of the non-uniform elastoplastic deformation and temperature fields. However, the current analytical models are generally oversimplified in expressing the cutting contact conditions and do not cover the three-dimensional cutting process well [122].

Numerical

The complex combination of thermal and mechanical loading caused by the cutting action of the machine tools makes finite element simulation a promising modelling approach. Although much development in analytical modelling of machining-induced stresses has been made, it is evident that due to the complexity of the tool-workpiece interaction, much of the proposed analytical models fall short of accurately predicting a wide variety of machining-induced stresses or machining responses [115]. When utilising the FEM method correctly, a much greater understanding of the mechanical-thermal tool-workpiece interaction phenomena and surface/sub-surface residual stress formation can be obtained. Many commercially available software platforms that employ different formulations well summarised in the review published by Outeiro et al. [119] can be utilised. Commercially available FEM software platforms have been extensively used to investigate machining-induced stresses, the most commonly used including; ABAQUS [69], [125]–[132], DEFORM [129], [133], [134], and AdvantEdge [132], [135]. These works include various machining processes, including turning and milling. Also, various materials have been modelled, with most of the work conducted on titanium, nickel and Inconel alloys.

The accuracy of any model is highly dependent upon the input data used. FEM of the machining action is highly sensitive to the thermo-mechanical input models and parameters used, which govern the behaviour of the simulation and the results obtained [20], [136]. These input models control the

constitutive material behaviour, friction, damage and chip formation, of which many varying models have been developed. The most notable of such models, which have been used extensively in the reviewed literature, is summarised well by Markopoulos [115]. Next, this review will consider the research undertaken in modelling the complex interactions of machining parameters, tool geometry and workpiece material properties in aluminium alloy machining to develop an understanding of induced residual stress formation.

The work of Denkena, Garcia & Köhler [77], as discussed in section 2.5.2, showed through FE modelling that corner radius has a prominent effect on the newly machined surface in aluminium alloy and a more significant influence on sub-surface residual stress formation than heat, cutting speed and feed rate for the experimental settings and parameter ranges they investigated. However, this work was limited by the size of the corner radius they could model due to the limitations of AdvantEdge 3D modelling capability.

Limited work has been carried out in modelling the machining of aluminium alloys and residual stress formation, including Huang *et al.* [53], who simulated face milling of simple plate geometry to establish the effects of bulk residual stresses on machining-induced stress formation. Ma *et al.*, using DEFORM FE software (Figure 2-53), studied the effect of bulk stress on the machining process variables and the induced residual stress [137]. The sign of the initial bulk stress caused variation in the cutting forces and temperatures, resulting in varying levels of induced stress. A more tensile initial stress in the wake of the tool strengthens the establishment of tensile residual stress in the newly formed surface, and the opposite is true of initial compressive stresses. The reviewed literature shows that although a good correlation between empirical and FEM results can be obtained, the modelling of explicit chip formation and the resulting residual stresses require highly complex finite element models with very refined meshes, high element densities and complex re-meshing algorithms, resulting in computationally expensive simulations.

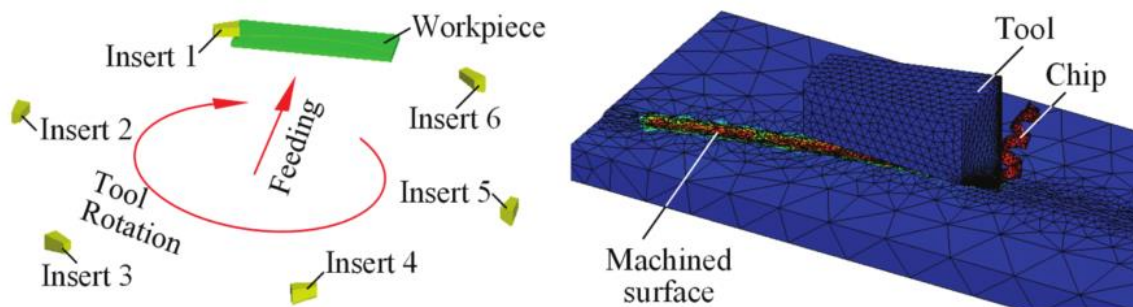


Figure 2-53: AdvantEdge face milling [137]

Artificial intelligence

Artificial intelligence (AI) models are becoming an increasingly popular tool in manufacturing due to their ability to optimise processes with multi-response input parameters that share complex interactions and cope with chaotic data sets due to variations arising from indeterminate engineering systems [138]. Numerous papers have explored the use of AI models in improving machining processes in areas such as tool wear prediction, machine health monitoring and surface integrity determination. Furthermore, AI methods are utilised in hybrid models, combining either empirical, numerical, analytical or AI approaches to improve the prediction capability. This literature review will briefly summarise current and relevant research on AI and hybrid models to predict machining-induced residual stresses.

The earliest work in this area was undertaken by Umbrello et al. in 2008 [139]. They presented a hybrid ANN-FEM approach to predict the machining-induced residual stresses during the hard turning of 52100-bearing steel. This methodology utilised 2D orthogonal machining FE models and empirically determined stress data to train the ANN, which was validated by experimental trials. A three-layer ANN was employed to predict the residual stresses where the input layers included tool geometry information, material properties and process parameters. Furthermore, the model optimised the required surface conditions by altering machining parameters by inverse process design. Preferential residual stress profiles could be attained by adjusting the machining and material parameters. The overall accuracy of the model predictions was reported to be between 4% and 16%.

In 2009 Zhang et al. [140] proposed using a fuzzy modelling approach to predict residual stresses in the milling machining of aluminium alloys. The modelling approach (shown in Figure 2-54) works on 'IF-THEN' rules with assigned membership functions related to some known variables instead of having some level of influence on the system under consideration. Two models were developed, one with 7 input parameters and the other with 14. Each developed fuzzy model was evaluated using the root mean square error (RMSE) index. These input parameters included cutting speed, feed per tooth, feed velocity, coolant type, rotational speed, macro tooling geometry, and measurement depth. Rule-sets were used to establish the residual stresses induced by machining by plotting the measurement depth variable output against the residual stress variable output. The results showed a good fit of the experimentally determined training set stress data with the predicted values, as seen in Figure 2-55. No additional validation experimental trials were performed. The authors proposed a multi-objective optimisation technique or "reverse engineering" where the task was to minimise given objective functions (i.e. mean absolute residual stress and machining cost).

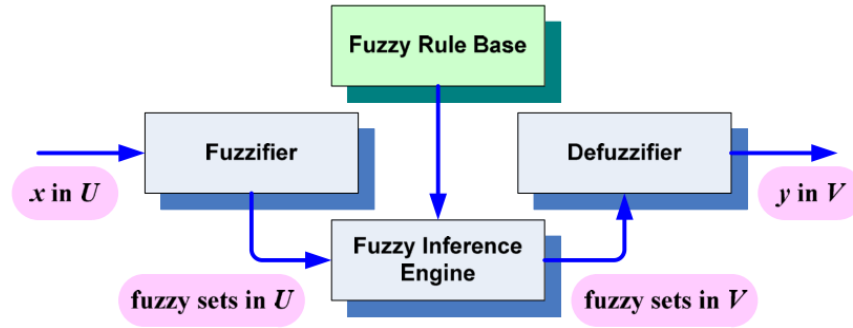


Figure 2-54: Schematic diagram of a simple fuzzy system [140]

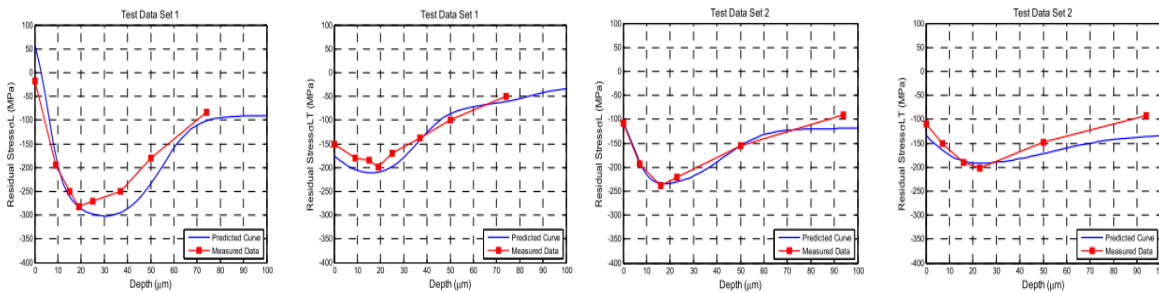


Figure 2-55: Results of the fuzzy model [140]

Following their initial work, Zhang et al. [141], [142] introduced a flexible model fusion method to collate the benefits of various AI modelling methods to predict machining-induced residual stress. The types of models used included artificial neuron network (ANN), linear regression and fuzzy systems all controlled by a higher-level master fuzzy system (Figure 2-56). For the optimal model with 15 input rules, an RMSE of 16.83 MPa was reported. The work presented in this paper improved upon the modelling capabilities of their earlier lone fuzzy system [140].

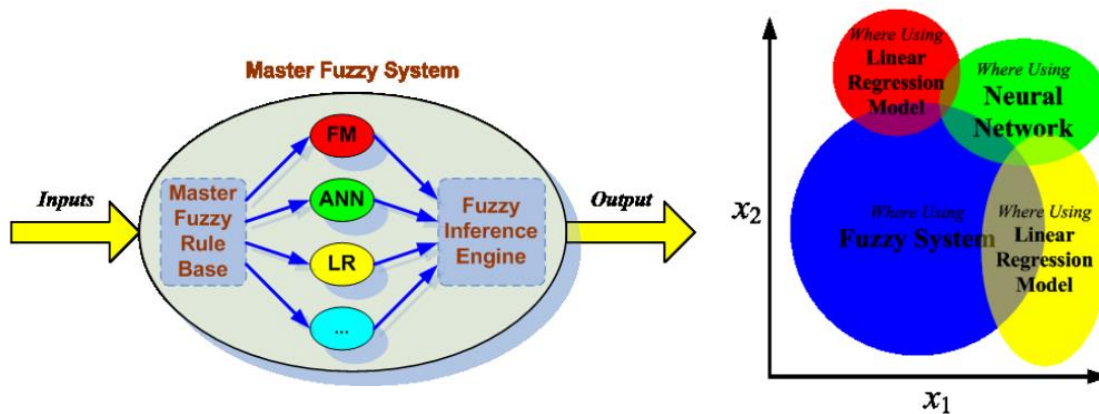


Figure 2-56: Master fuzzy system (left) modelling space (right) [141]

More recent work by Reimer & Luo [143] evaluated using two ANN models capable of predicting the machining stresses in ball end milling of AISI H13 steel. As in the work of Umbrello et al. [139], machining parameters were used to form the input layer in the ANN. The researchers validated the results of the ANN by FEM. The first type of ANN utilised was forward-facing. The second was a Radial Basis Function structure, as shown in Figure 2-57. This paper displayed the possibility of using a standard MatLab toolbox to establish residual stress prediction ANNs that produce satisfactory results.

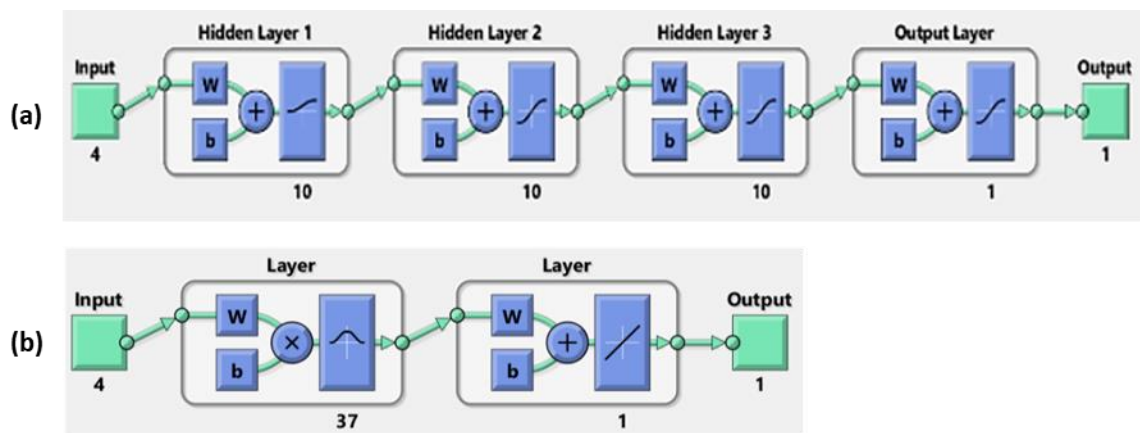


Figure 2-57: (a) Feed Forward and (b) Radial Basis Function ANN Structures (Matlab) [143]

2.6.3 Modelling residual stress-related distortions

As discussed in section 2.5.4, distortions in aluminium alloy aero structure components with complex geometries, including thin wall/web thicknesses, are believed to result from a combination of bulk and machining-induced stresses. As such, it would be advantageous for companies to develop modelling methodologies to predict and account for these residual stress-related distortions at the design or programming stage of manufacture so that final part distortion can be mitigated pre-machining [144]. There is no consensus on an approach to dealing with the issue of distortion by modelling, with researchers opting to use various methods. In this section of the literature review, the various methodologies for residual stress-related distortion modelling will be discussed, distinguishing between analytical, numerical and hybrid approaches. Additionally, for each modelling methodology, the sources of residual stress will be considered (i.e. bulk, machining induced or a combination).

2.6.3.1 Analytical

Analytical methods have been proposed for modelling part distortion due to residual stresses. For example, Llanos, Lanzagorta and Beristain [145] developed an analytical approach to model residual stress-related distortion caused by residual bulk stress based on the Euler-Bernoulli beam theory:

$$\rho = \frac{-I \cdot E}{M_b} \quad 2-8$$

Where the curvature of the part (ρ) is determined using the moment of inertia (I), Young's modulus (E) and bending moment caused by the residual stress redistribution (M_b). Where the bending moment is given as:

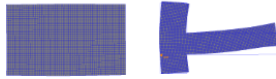
$$M_b = \sum_i \bar{\sigma}_i \cdot A_i \cdot k_i \quad 2-9$$

With the overall bending moment calculated through the summation of the products of average residual stress ($\bar{\sigma}_i$), cross-sectional area (A_i) and distance to the neutral fibre (k_i) of the discretised part. This technique provides a fast method for establishing distortion for simple flat plate geometries. However, this method cannot be applied to complex geometry, such as aircraft wing structural components [64]. Similarly, Fergani *et al.* [146] developed an analytical model to predict part distortion and residual stress caused by machining-induced residual stress and material removal, which they attempted to validate through experiments. Although the work showed some correlation between the analytical solution and the experimental results, errors of 30% were present. This error was believed to be due to the authors omitting the thermal and clamping effects, and the bulk stresses were omitted.

2.6.3.2 Numerical

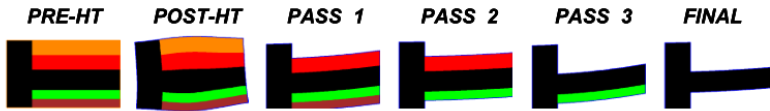
Researchers have widely adopted finite element modelling to simulate residual stresses' impact on part distortion. However, simulation methodology varies sustainably in the reported literature. It is possible to group the numerical approaches based on different categories. For example, models can be grouped based on the residual stress sources considered, i.e., bulk residual stress only or combined with machining-induced residual stresses. Modelling methods could also be grouped on the material removal technique described in [100], as depicted in Figure 2-58. To this end, the formerly mentioned grouping category (residual stress source considered) shall be used to collate the reported literature in this section, with attention given to the method of material removal.

1. "One-step" from heat treat shape to finished part shape



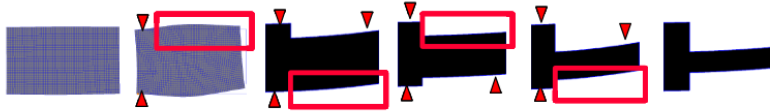
- **Method:** Material removal in one pass
- **Pros:** Simple, predicts trends
- **Cons:** Path-dependence and clamping ignored; inaccurate for large distortions

2. "Multi-step" procedure with predetermined material removal



- **Method:** Remove material in a pre-determined multi-pass sequence
- **Pros:** In-process distortion prediction
- **Cons:** Path-dependence and clamping ignored; inaccurate for large distortions

3. "Multi-step" procedure with path-dependent material removal



- **Method:** Multi-pass material removal; complete remeshing at each step
- **Pros:** More realistic; workpiece/tooling interactions considered
- **Cons:** Remeshing interpolation errors; more involved to set up model

Figure 2-58: Various material removal techniques

Bulk Residual Stresses Considered Only:

The following papers consider only the bulk residual stresses when simulating part distortion. Typically, the bulk stress data is either approximated through numerical modelling of the thermo-mechanical processes associated with manufacturing the stock material or determined by measurement and data fitting and implemented to the finite element model by way of mapping. Regarding the latter instance, Albino *et al.* [147] describe mapping empirical fit bulk stress data across a finite element mesh. Albino considered the impact of element shape (Tetrahedral and hexahedral) and the geometric order (linear and quadratic) on the solution accuracy and solve time of the FE method compared with the analytical plate bending formula. He concluded that specific element types should be employed to predict the distortion due to internal bulk residual stress accurately.

Chantzis *et al.* [66] proposed an industrial workflow incorporating an adapted on-machine layer removal method and finite element simulation to reduce part distortion after machining caused by bulk residual stress (Figure 2-59). It was suggested that through a guided user interface (GUI), machining planning engineers could account for machining distortions caused by bulk stresses through offset alteration by utilising the FEM tool having limited or no specialised knowledge of FEM. Open-source CalculiX FE software utilised an automated meshing procedure using second-order tetrahedron elements across the submitted CAD part. The paper proposes an attractive method for a fast and inexpensive method of

distortion control where limited input data is required. However, although quoted, no results were presented in the paper, so its verification cannot be determined.

Also, Chantzis *et al.* method proposed a single-step material removal method (see Figure 2-58) to simulate stock material machining. In reality, machining is a multi-step process where layers of material are removed in consecutive passes. As such, the material will undergo deformation by redistributing bulk stresses for each machining pass. This inter-process distortion potentially significantly influences the finished machined quality of the component.

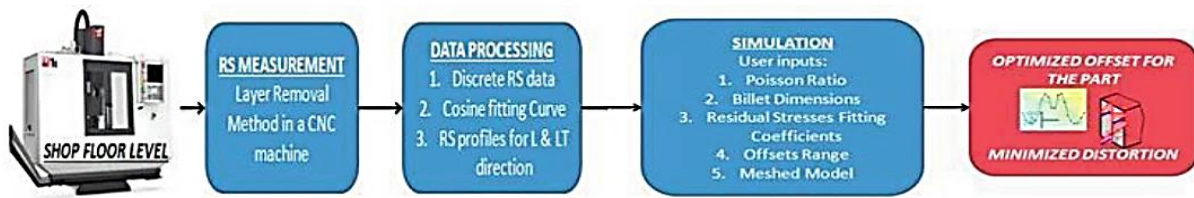


Figure 2-59: Work flow for distortion mitigation [66]

D’Alvisea *et al.* [97] developed this method by accounting for the multi-stage material removal sequence by the level set method to capture the evolution of residual stress redistribution. The extended finite element method (XFEM) simulated a 10mm axial machining pass without modelling the transient thermo-mechanical machining action. Because no thermal and mechanical action of the cutting process was modelled, a simple linear-elastic model could be utilised that required minimal material properties input (Young’s modulus and Poisson’s ratio only). The paper claimed this method could enhance the results obtained by the workflow proposed by Chantzis *et al.* Although the incremental material removal method proposes more realistic conditions than previous work, it does not account for the machining errors that occur by the gradual movement of the material by redistribution of the bulk stresses.

Cerutti & Mocellin [148] looked to overcome this issue associated with conventional “*element deactivation/deletion*” protocol by developing a robust Boolean deletion procedure, which is a multi-step material removal procedure with path dependant material removal as described by Ma *et al.* [100] Figure 2-58. A similar level set method to that introduced in [97] is utilised to systematically remove sections of the model that would represent machining level passes by mass removal. However, the principle does not target nodes/elements by predefined volumes but instead generates volumes to remove by the tool governed by the NC code after allowing for intermediate stages of part distortion. Parallelization of the code was required to improve the efficiency of the method. A single program, multiple data and message-

passing interface techniques were used to allow several subdomains of the model to be established and handled by separate CPU cores, speeding up the calculation time. An automatic mesh refinement procedure was created to increase the removal algorithm's accuracy. The results obtained for a test piece demonstrator showed a correlation between the simulation and experimental results when accounting for the experimental measurement boundary conditions.

Cerutti & Mocellin later utilised this method to investigate methods of quality improvements, including offset, machining sequence, fixture positioning and depth of cut on resulting distortions [48][63]. All of the parameters that Cerutti et al. explored exhibited some influence on component deformation. An essential feature of Cerruti's modelling methodology is the simulation of the fixturing conditions and how the residual stress field evolution would interact and deform according to the contact conditions. Using this method, Cerutti's model can account for under/over-cutting during machining due to part deformation caused by the interaction of residual stress deformation and applied to clamp condition constraints, as depicted in Figure 2-60.

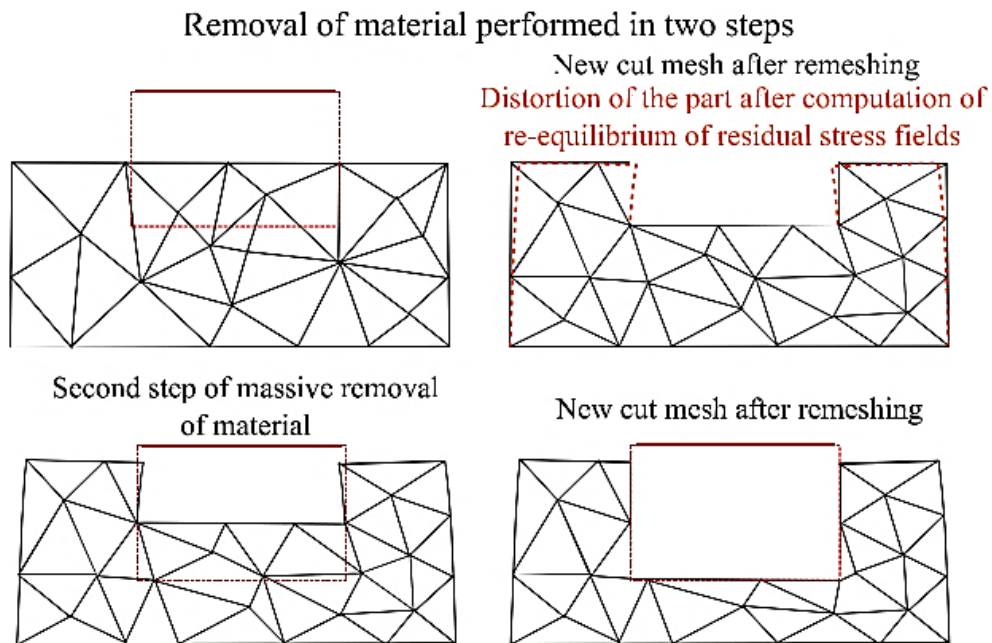


Figure 2-60: Boolean deletion procedure [148]

Bulk and Machining Induced Residual Stresses Considered:

In the previously reviewed literature, the distortions from the release of bulk stresses by machining are considered during modelling, and the effects of machining-induced stresses are neglected. This method is generally acceptable for components with thick structures. However, wing rib structures are complex geometries ranging from 5 mm stiffeners to 1.25 mm floor sections. Therefore, it can be assumed that distortion modelling for aircraft rib structures should consider the contributions of bulk and machining-induced residual stresses for increased accuracy.

The primary method researchers have taken in establishing distortions by induced and bulk stresses has adopted the ‘superimposition’ of machining-induced stresses as detailed in Madariaga *et al.* [99] and depicted in Figure 2-61. Madariaga *et al.* developed a model that accurately predicts the distortions for thin plate and inverted ‘T’ sections of 7175-T7351 series aluminium alloy. The material removal procedure followed the ‘one-step’ method as defined by Ma *et al.* [100] Figure 2-58. The main finding of this paper is that both the bulk and process-induced stress influence the final part distortions. More importantly, the machining-induced stresses were found to be more prominent further away from the newly established natural axis of the component. For the described modelling methodology, machining-induced stresses were applied homogeneously to the near-surface refined mesh because a singular direction tool path is used. However, it has been shown in order studies that machining-induced stresses applied in the machining feed direction are not equal to those applied in the feed-normal direction [27].

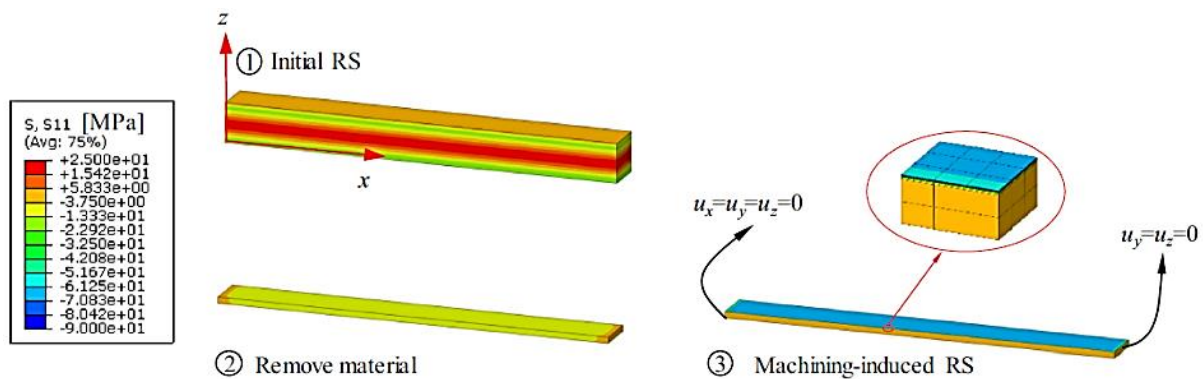


Figure 2-61: FEM model taking into consideration the bulk and MIRS [121]

To this end, Jayanti *et al.* [98] developed a modelling strategy (Figure 2-62 – left) considering the bulk and machining-induced stresses on resulting part deformation post-machining. Machining-induced stresses are determined in AdvantEdge finite element software by numerical calculations, which considers the thermo-mechanical loading by the machining action of the tool using Lagrangian formulation (Figure 2-62 – right). Machining-induced residual stress profiles are generated for varying process parameters and tooling geometries and stored within a database for residual stress mapping and redistribution simulations. The component geometry developed within the CNC software undergoes discretization by finite element meshing. Bulk and machining-induced residual stresses are mapped across the model surface, after which the FE model performs an equilibrium analysis. The simulated distortion is a function of the superimposed bulk and machining-induced residual stresses. Preliminary application to aerospace components, including fillet rib and pressure bulkhead, has been demonstrated. The modelling method utilised shell-type elements, whereas other researchers have opted for solid-type elements due to their accuracy in describing mechanical bending problems. The method is a one-step approach and only simulates the post-machining distortions.

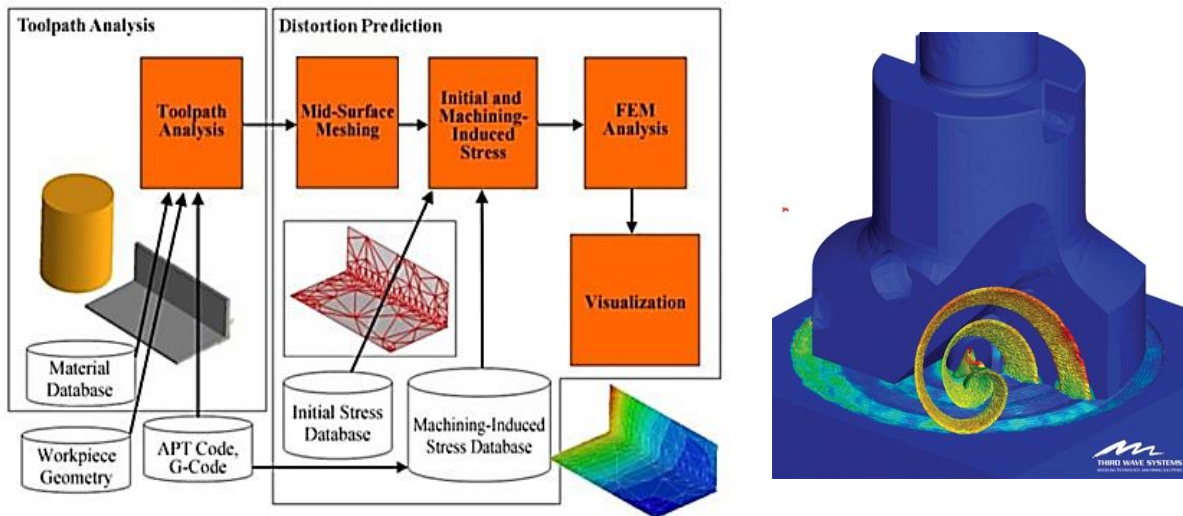


Figure 2-62: FEM strategy for coupled analysis (left) and AdvantEdge FEM (right) [98]

Dreier *et al.* [96], [149], [150] also proposed a one-step simulation strategy similar to that of Jayanti *et al.* [98] depicted in Figure 2-63 but developed the solution for 3D solid continuum elements opposed to shell elements as reported by Jayanti *et al.* Dreier *et al.* successfully predicted distortions caused by machining-induced and bulk residual stresses for a representative aerospace component made from AA7075-T651. Dreier's model considered establishing the machining-induced stresses as a function of the tool path

directionality and machining-induced stress biaxiality, as shown in Figure 2-64 (a). Furthermore, they used the model to suggest distortion improvements, including altering offset and the milling tool path strategy, as seen in Figure 2-64 (b). Dreier trialed various cutter path strategies, resulting in different machining-induced stress patterns and final distortion values. This variation in the post-machining distortion was determined to be due to the variation of machining-induced residual stresses in the feed and perpendicular direction of the machining tool path.

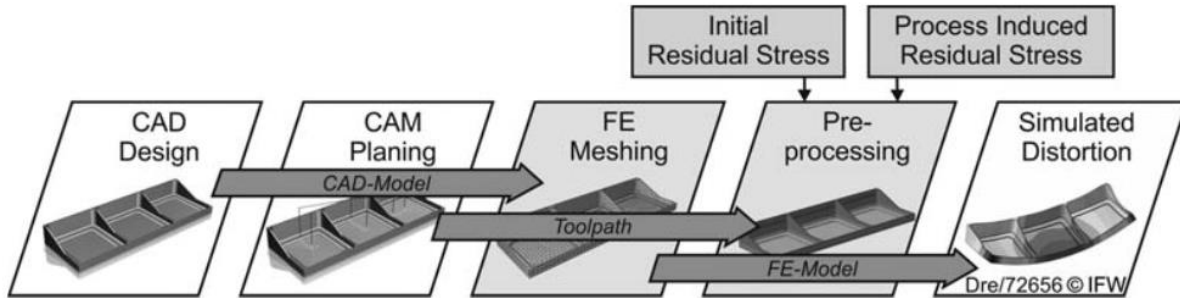


Figure 2-63: Distortion simulation structure [3]

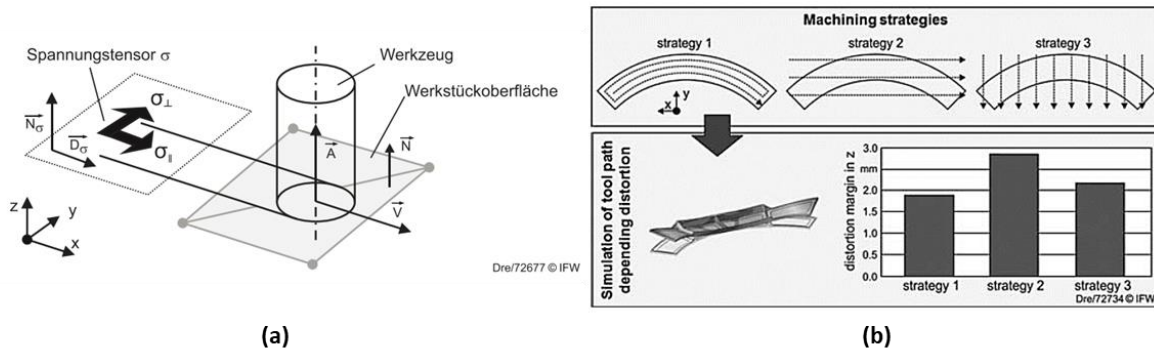


Figure 2-64: Tool path MIRS (a) and effect of machining strategy on component distortion (b) [3]

Weber *et al.* [151], [152] also utilised a one-step modelling approach with tool path-defined machining-induced stresses to simulate part distortion in a simple rib coupon, as shown in Figure 2-65. The results were validated through machining experiments and inspection of machined test pieces. The simulation and measured values were in good agreement. Weber *et al.* developed Dreier's machining-induced stress application protocol by including the shear residual stress values determined by fitting ICHD empirical data. Another important finding of Weber's modelling work was that certain features are more important to consider for MIRS application mapping to the surface area

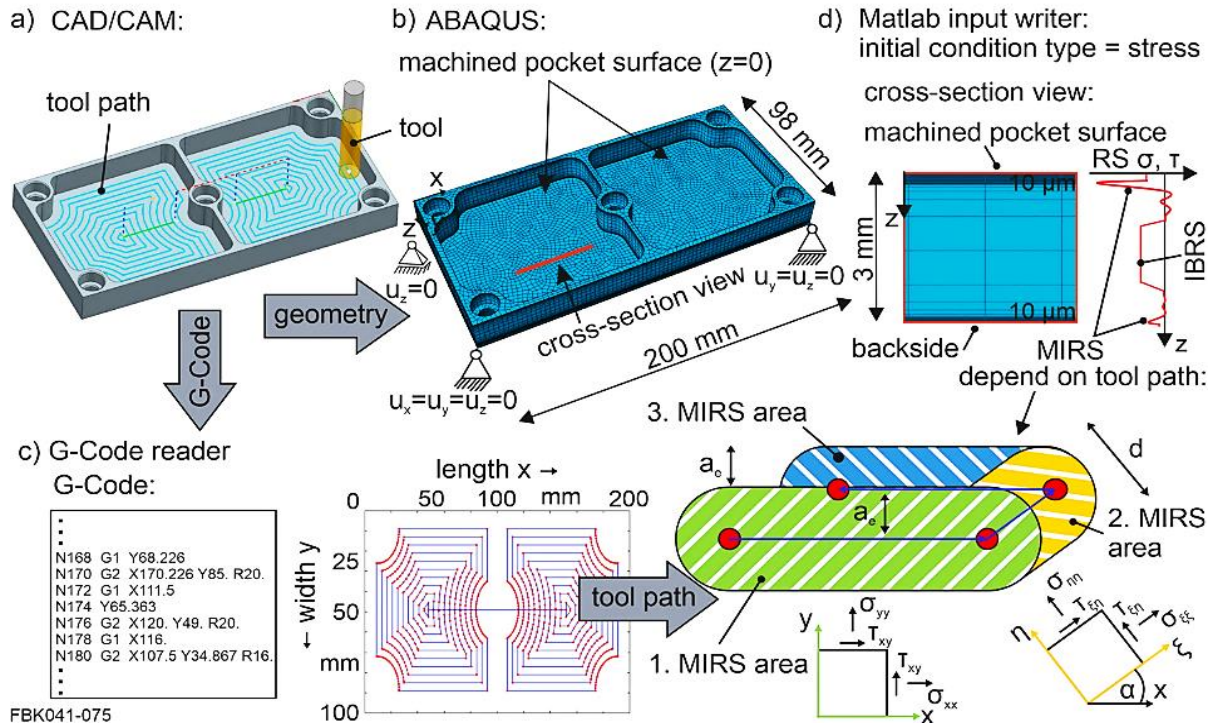


Figure 2-65: Modelling scheme from [145]

Raj & Xirouchakis [153] developed a system architecture capable of handling multiple inputs, including fixture layout, operation sequence, tool path and cutting variables in determining the final machined part quality concerning stresses and distortions. The model used an elastoplastic material definition and element ‘birth and death’ deactivation procedure to simulate material behaviour and removal, respectively. Bulk stresses are imposed on the part by mapping stress values (produced by fitting experimental data) according to curves representing the stress profile through the thickness of the component. Transient thermo-mechanical coupled loading is applied to the elements intersecting the tool path to calculate the machining forces and temperatures. The couple stresses are considered in the material removal sequence.

Relatedly, Ma *et al.* [101] employed the element deactivation approach based on tool path progression to simulate material removal in a distortion analysis simulation. Machining stresses were applied at the finishing stage of machining and determined by analytical means. Bulk residual stresses were mapped across the initial mesh using experimentally determined data. Although the model showed reasonable accuracy, the author based the error between simulation and experimental validation on the inaccuracies in measuring the bulk stress and the limitations of the analytical machining-induced stress model.

Tang *et al.* [154] accounted for multifactor coupling in modelling bulk residual stresses, clamping loads, milling thermo-mechanical loads and machining-induced residual stresses. Geometric simplification of chip formation was performed to apply equivalent cutting loads in DEFORM-3D. An adaptive mesh protocol was employed to allow refinement at the contact area.

Jiang *et al.* [155] performed distortion modelling in ABAQUS by mapping the simulated bulk and machining-induced residual stresses generated by numerical analysis in DEFORM and Third-wave AdvantEdge finite element software, respectively. The method proposes an appealing alternative to generating costly empirical data for model input. If it can be scaled up to larger, more complex part geometries and complex tool-workpiece machining conditions, this poses a promising alternative to generating residual stress input data for such models through costly experimental processes and measurement.

Ma *et al.* [144] produced a detailed body of work which included 2D modelling of the heat treatment and distortions by material removal of an engine disk forging as well as the 3D modelling of an airframe structure, utilising Boolean material removal procedure with local re-meshing to reduce the computation expense (Figure 2-66). The modelling procedure includes importing the cutter strategy data from the CNC program to generate detailed element deletion paths representative of the machining strategy. The paper also describes the development of a production model flow with GUI for “error-free” modelling.

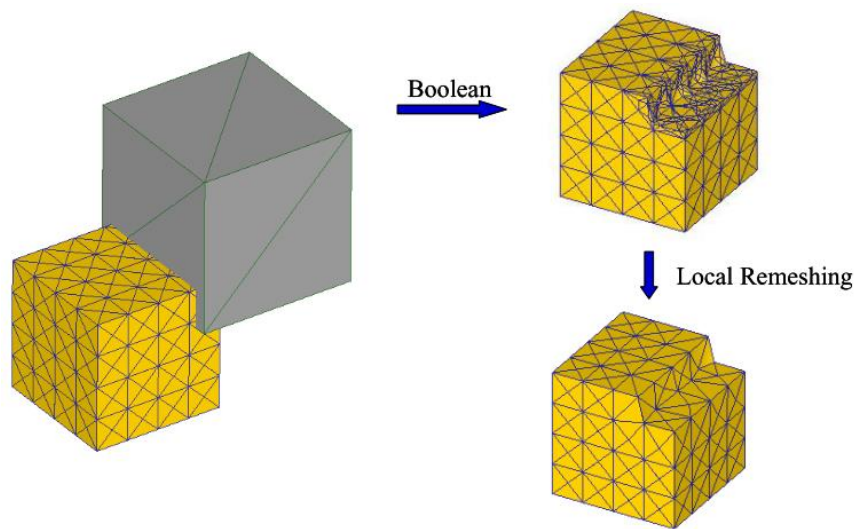


Figure 2-66: Boolean operations with the localised re-meshing procedure [144]

2.6.3.3 Hybrid

The modelling of residual stress-related distortion is not limited to singular model use, i.e., analytical or numerical methods. Other approaches in literature have been shown to provide a promising solution through hybrid modelling. Zhang *et al.* [156] reported using a fuzzy modelling approach coupled with finite element modelling to predict residual stress formation in the machining of aluminium alloys and then process related part distortion. The machining-induced stress modelling system is described in 2.6.2 and works on IF-THEN rules with assigned membership functions related to some known variables than have some level of influence on the system under consideration. The notable benefits of the model are that it can handle many complex variables that influence machining-induced residual stress and produce accurate models for relatively small sample sizes/training data. In this instance, up to 13 input variables were investigated. This rule set was used to establish the residual stresses induced by machining as inputs and utilised in a linear elastic FE model of the final component to model distortion, as shown in Figure 2-67.

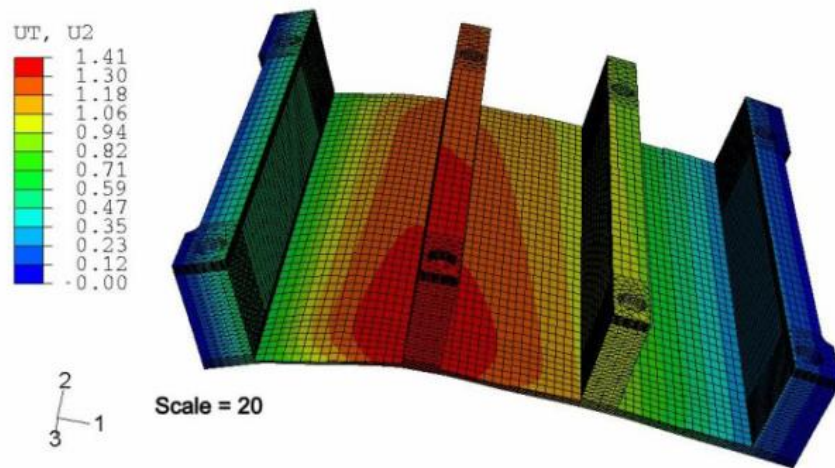


Figure 2-67: FEM distortion mapping by machining induced stress determined by fuzzy model [156]

2.6.4 Summary of modelling and simulation of residual stress and part distortion

The literature shows that finite element analysis is a highly valuable tool in modelling residual stress and part distortion. For the reported studies, it has been shown that FEM can be utilised to simulate the formation of bulk and machining-induced residual stresses and part distortion in representative part geometries to a reasonable degree of accuracy. The finite element strategy also allows for numerous scenarios to be simulated and large data sets to be acquired cheaply compared to the much more expensive and time-consuming method of experimental work. The numerical modelling approach also overcomes the limitations posed by analytical methods. Although it will never fully replace the need to produce empirical data sets (as models will always require validation), steps are being taken in developing a design for distortion modelling strategies to combat residual stress-related distortions.

It is important to note that no singular modelling methodology has been adopted to model residual stress-related distortion. Some have neglected the effect of machining-induced stresses and considered the manifestation of distortion solely by redistributing bulk material stress due to material removal. Others have considered the inclusion of machining-induced residual stresses with bulk stresses, including mapping of the machining-induced stresses as a function of the machining toolpath, whilst considering the variation in residual stresses in the feed and normal directions.

Table 2-4 summarises the key work regarding distortion modelling methodologies reported in literature. Some commonality between the methods exists. As can be seen, most models consider both bulk and residual stresses as sources of part-related distortion. Where the machining-induced residual stresses have been omitted, the author clearly states that they believe the test components are of a thickness where machining-induced stresses can be neglected [48]. Moreover, all models utilised empirically determined residual stress profiles as input to the modelling schemes. This literature review has shown that bulk and machining-induced residual stress can be determined by other means but are still relatively inaccurate or limited compared to empirically derived data. Where the models vary, includes the material removal approach, machining induced stress application technique (if applicable), fixturing representation and material model. The accuracy of the reported models also varies as captured in Table 2-5.

Regarding the reported error it should be noted that the measurement of distortion carried out using a mixture of coordinate measurement machine and laser interferometry. Furthermore, various modelling methodologies were reported. Therefore, direct comparison between modelling results cannot be drawn. Instead, the accumulation of the reported errors given in the literature provides an indication on what

level of accuracy is achievable using FE to predict residual stress related distortions. For all results reported in Table 2-5, modelling error is defined as the difference in max distortion between simulation and experiment. The range of the error reported was between 0 and 29% with the average error of 13%. The reasons for the error given by the authors include the accuracy of experimental data, complexity of geometry and limitations in the numerical procedure. Through reviewing the work, it is clear that modelling methodology and complexity of the machined geometry have strong influence of the recorded error i.e., errors reported include simple plate geometries to complex component demonstrators.

Table 2-4: A comparison of key distortion modelling research methods

	Dreier <i>et al.</i> [96], [149], [150]	Cerutti <i>et al.</i> [48], [63], [148], [157]	Ma <i>et al.</i> (Rib & Web Model) [144]	Madariaga et al. [99]	Weber et al. [151], [152]
Residual stress sources considered	Bulk + Machining induced	Bulk Stress only	Bulk + Machining induced	Bulk + Machining induced	Bulk + Machining induced
Residual stress data source	Empirical data	Empirical data	Empirical data	Empirical data	Empirical data
Material removal representation	One-step approach	Mass removal	Mass removal	One-step approach	One-step approach
MIRS applied as a function of tool path	Yes	N/A	Yes	No	Yes
Fixturing representation	N/A	Contact modelling	Nodal constraints	N/A	N/A
Material model	Linear elastic	Elastic-plastic	Linear elastic	Linear elastic	Linear elastic

Regarding the reported error it should be noted that the measurement of distortion carried out using a mixture of coordinate measurement machine and laser interferometry. Furthermore, various modelling methodologies were reported. Therefore, direct comparison between modelling results cannot be drawn. Instead, the accumulation of the reported errors given in the literature provides an indication on what level of accuracy is achievable using FE to predict residual stress related distortions. For all results reported in Table 2-5, modelling error is defined as the difference in max distortion between simulation and experiment. The range of the error reported was between 0 and 29% with the average error of 13%. Through reviewing the work, it is clear that modelling methodology and complexity of the machined geometry have strong influence of the recorded error i.e., errors reported include simple plate geometries to complex component demonstrators.

Table 2-5: Key distortion modelling research reported measurement methods and model accuracy

	Dreier et al. [96], [149], [150]	Cerruti et al. [45], [62], [148], [157]	Ma et al. (Rib & Web Model) [144]	Madariaga et al. [99]	Weber et al. [152], [153]
Methods of measurement	laser interferometry	CMM	laser interferometry	CMM	CMM (extracted line profiles for direct comparison)
Error on Max distortion	5% - 9.81%	15%	2-29%	12%	0%-22%

2.7 Concluding statements

This chapter is dedicated to reviewing the literature on residual stress and machining-related distortion to determine the research background themes and current state of the art. The following can be concluded from this review.

The redistribution of bulk material residual stresses and generation of machining process-induced residual stress drives distortion in machined aluminium aero-structure components. Finite element simulation can be utilised to model distortion caused by these sources of residual stress during and after machining. Furthermore, finite element models have been utilised to mitigate part distortion in aerospace components [96]. However, it can be deduced from the literature reviewed that the picture of residual stress and distortion is complex, with many variables contributing to its formation and redistribution during machining, affecting the magnitude and mode of component distortion. Based on this review and observations made on the current state of the art in machining-related distortions, the potential following work is suggested.

Bulk material residual stresses have been described as the leading cause of part distortion in thick-walled components, where the component wall and web thickness are greater than 3~4 mm [51]. Whereas for thin-walled components (< 3 mm), the combination of machining-induced and bulk residual stresses has been designated as the foremost reason for distortion. It has been observed that this critical thickness is not agreed upon between various authors. However, it has been noted that various authors have reported accurate simulations when machining-induced stresses have been considered.

It has been observed that the publications reporting upon machining-induced stresses have described trends between machining parameters (feeds, speeds, depth of cut) and varying induced residual stresses. However, most of the effort has been focused on single-point turning and hard-to-cut metals (i.e. titanium and nickel-based alloys). More research is required to understand the influence of high speed and aggressive machining operations on induced residual stresses when milling high-strength aluminium aerospace components, to understand better the influence of high speeds and feeds on machining-induced residual stresses.

Another consideration for further investigation is determining the influence of the chosen machining strategy in its contribution to final surface/subsurface machining-induced residual stress. The machining strategy is the variable of interest, including the chosen number of sequential machining operations and the tool path strategy. The research is contradictory when discussing the influence of sequential cutting

on MIRS generation. Some researchers suggest that only the last machining pass influences the final MIRS state in the machined component, as stresses imparted by previous cuts are removed upon machining. Others suggest that the previous machining passes influence the MIRS state within the final machined parts. The conclusion of the sequential cutting influence could have implications on the distortion modelling methodology where MIRS applied must be considered for each simulation machining condition when utilising a multi-step approach. Additionally, the literature review has shown that the choice of tool path could impact localised variations in the machined surface layer residual stresses. However, this area is less well-researched and more data is needed to understand the potential variance in high-speed machined components.

It is clear that work focused on developing a strategic and integrated modelling approach is required so that engineering professionals can make informed decisions on their machining processes regarding residual stress-related machining distortion. As proposed in [96], [98], [137], [153], a workflow should be developed that incorporates; actual CNC tool paths and machining process parameters, bulk stress and machining-induced stress results from testing and simulation so that accurate and agile distortion predictions can be made.

The extensive literature review presented in this chapter has highlighted the sources and causes of residual stress-related post-machining distortion. An evaluation of state-of-art distortion modelling methodologies has been provided, from which the modelling methodology developed in this work will be developed.

3. Objectives and methods

The conclusion drawn from the literature review supports that part distortion in machined thin-walled, monolithic, aluminium wing structural components derives from the redistribution of bulk residual stresses in the initial stock material after material subtraction and the introduction of machining-induced residual stresses at cut surfaces. State-of-the-art modelling of machining distortion due to initial and process-induced residual stress is conducted with finite element models that account for the material removal and introduction of the residual stress in the initial stock material and by the machining process itself.

Therefore, the main objective of this work is to produce a distortion modelling methodology capable of informing CAM programmers and manufacturing engineers of machining-related part distortion and quality errors at the production planning stage of manufacture to mitigate the impact of costly non-conformance due to residual stress-related distortion. To this end, the main research aim of this thesis is as follows:

“Creation of knowledge in residual stress-related machining part distortion through experiments and the generation of part distortion simulation methodology”

This work will build on the distortion modelling research area by proposing a modelling methodology that can account for the inter-process material removal sequence and tool path-related machining-induced residual stress. Based on these requirements, the main research objectives have been formed:

- A thorough literature review in residual stress and part distortion focuses on numerical methods for distortion modelling and machining-induced residual stress evaluation.
- Undertake a series of experimental trials to develop an understanding of machining-induced residual stress formation due to machining strategy selection.
- Conduct experimental trials to study the effects of machining strategy on bulk and machining-induced residual stress-related workpiece distortion.
- Develop a numerical simulation procedure to model the coupled influence of bulk material initial residual stress and machining process-induced residual stress on final part distortion with material removal sequenced based on the tool path progression.

The following sections of this chapter will detail the methodology and assumptions for the numerical modelling and experimental trials.

3.1. Numerical modelling

As discussed in Chapter 2, finite element modelling is a useful numerical method for modelling residual stress-related part distortion. It has been identified that there is not one generally accepted method for modelling this problem in machined aerospace components. Therefore, the simulation method proposed for this work is based on the perceived strengths and benefits of the previously defined methods found in the literature, reviewed in section 2.6.4. From the assessment of the undertakings mentioned above, it is believed two approaches can be discussed for their applicability in modelling residual stress-related distortion in aluminium wing structure components: Cerruti’s [157] Boolean or ‘mass removal’ approach and Dreier’s [150] single step and tool path model. The perceived strengths and weaknesses of both methodologies are given in Table 3-1.

Table 3-1: Strengths and weaknesses of FE modelling methods

	Cerruti’s Boolean method [157]	Dreier’s single-step method [150]
Strengths	<ul style="list-style-type: none"> + Considers the inter-process deformations caused by bulk stress re-equilibrium that cause quality issues (over/under-cutting) + Considers the influence of fixturing on final part quality + Reduced user-required model development (uses CAD/CAM planning data) 	<ul style="list-style-type: none"> + Simulates the influence of both bulk and machining-induced residual stresses on final part distortion + influence of machining tool path on MIRS accounted for + The computational cost of the problem minimised + Reduced user-required model development (uses CAD/CAM planning data)
Weaknesses	<ul style="list-style-type: none"> - It does not include MIRS influence - Remapping errors through stress interpolation - Requires paralysation and increased PC specifications for economic simulation times 	<ul style="list-style-type: none"> - In-process distortions and impact on machining error not accounted for (over/under-cutting)

Based on the described modelling methods and also the efforts discussed in the literature review, it can be observed that a gap exists where sequential material removal techniques and tool path-related machining-induced stress implementation has not been accounted for in the same model. Dreier [150] highlights this gap when providing an outlook on his work. The benefit of including the multi-step

approach in the simulation scheme would allow users to determine the influence of multiple part set ups in final distortion. Determining the optimal number of part set-ups in terms of productivity and distortion management in production would limit the costly and time-consuming change over of fixtures, therefore improving operational efficiency and productivity. Therefore, a simulation approach shall be developed to combine and build upon the benefits of the discussed methodologies. From this statement, the requirements for the simulation strategy are formulated:

- The model is to utilise bulk and machining-induced residual stress data to simulate part distortion. As highlighted in [150] both are important to consider for the components at the centre of this study. However, solutions for modelling either source of residual stress either lack general applicability, require high resources to develop or are of low accuracy. The modelling scheme should accept parametrised residual stress data by curve fitting as input from any of the previously mentioned sources. But for the context of this work the residual stress data will be experimentally determined.
- The modelling approach should, in theory, be deployable within the manufacturing planning stage of production and utilise the surrounding data/information generated from production planning software. Figure 3-1 shows the proposed modified digital process flow based on Figure 2-12, where distortion FE modelling has been incorporated. Furthermore, the models should be partly deployable by programmer engineers and such that a software interface be developed that controls the generation and execution of machining distortion simulations.
- Figure 3-2 focuses on data transfer between CAD, CAD/CAM and FEM software packages. The data format is industry generic and such that this method should stand to be deployable in a generalised way. The designed component generated in the CAD software package and the toolpath data generated in CAD/CAM software package should be transferable to the FEM software. The design data in .STEP format should include the geometric definition of the final machined part, the stock material and volumes to be removed via machining. The .aptsource data containing cutter location data defined for the machining coordinate system is also passed to the FE model. The machining-induced stresses are to be accessible in the format of fitted curves. Figure 3-2 also illustrates the feedback loop between CAD/CAM and FEM. This is represented as a dotted line to indicate no direct transfer of data occurs, but the distortion model results should provide information to the engineer on the influence of the designed CAM program. The output from the FEM is to be formatted in such a way that it is comparable to the inspection data generated to portray part distortion.

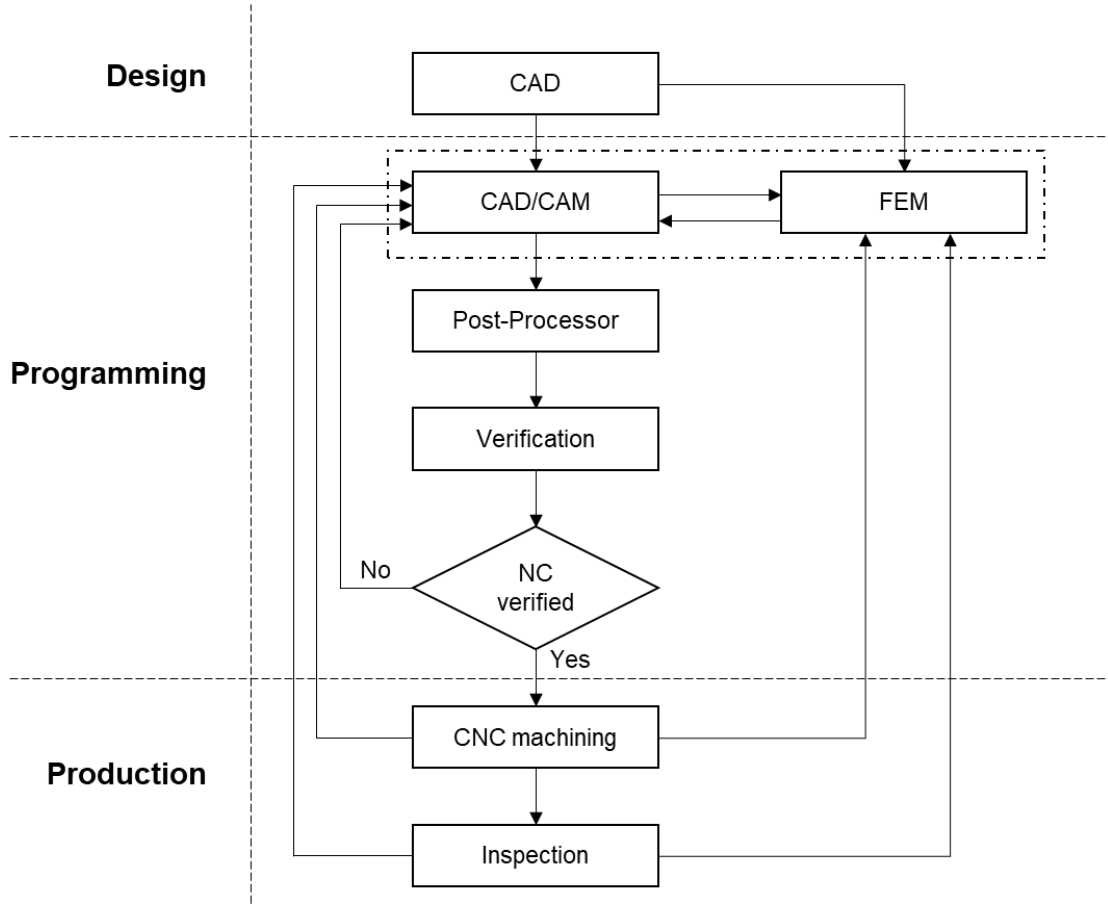


Figure 3-1: Proposed implementation of the FEM distortion model in the process programming phase

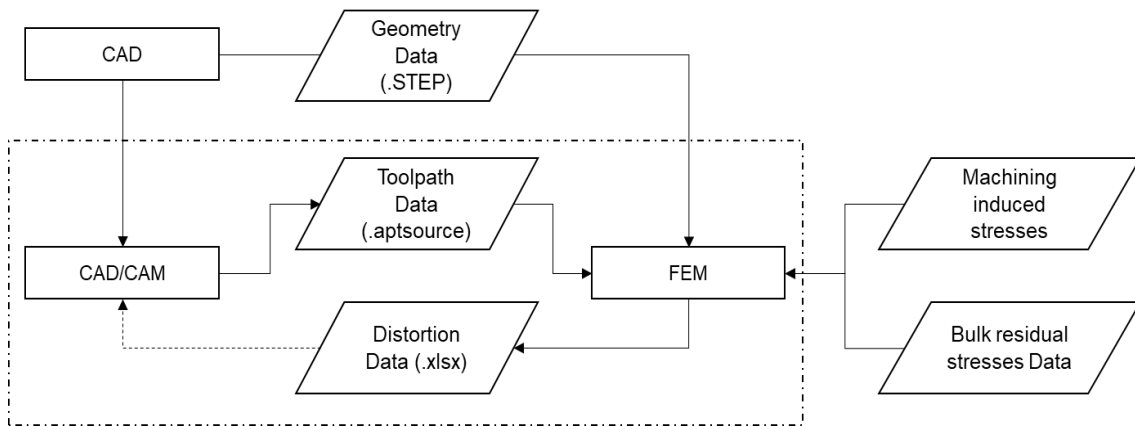


Figure 3-2: Data passing schematic for integrated process modelling

- Coordinate measurement machines (CMM) are used in the aerospace industry to inspect manufactured components by generating discrete measurement points on the component through tactile probing. Distortion data can be generated by comparing the intended designed CAD component to the discrete point measurements of CMM. Therefore, the FEM output is to be configured to be compared with CMM measurements. The feedback line from FEM to the CAD/CAM system is shown as a dotted line to represent that no input of virtual information occurs. Instead, the results should be interpreted, and modifications made by the programming engineer when trialling various manufacturing strategies to reduce part distortion.
- The distortion modelling procedure looks to generate novel capability in combining tool path related MIRS influence and Boolean removal procedures to capture machining strategy on inter and post process distortion, which is not currently offered by other modelling methods. The accuracy of the model is also important such that practically it could generate useful information to manufacturing engineers on the influence their programming stagey has on resulting component distortions. Therefore, the accuracy of the solution should aim to match or improve upon the accuracy reported by leading sources of literature in section 2.6.4
- In order to account for the inter-process distortion on final part quality, as described by Cerruti [157], and for tool path related machining induced stress effects, as described by Dreier [150], the model must be developed as a multi-step procedure where the bulk and machining induced stresses can be mapped accurately over an optimised mesh in terms of type and amount of elements. The ability to account for the influence of part set-up is considered important to industry as understanding the influence of using multiple fixturing stages during machining on component distortion prior to manufacture would yield competitive advantage (i.e., determining the optimal number of component set-ups steps to establish a balance between distortion management and productivity through simulation). Many of the modelling methodologies assume that MIRS is only introduced at the last stage. However, the progressive introduction of MIRS with successive material removal has not been studied for sequential milling operations. Therefore, further investigation is required.

3.1.1. Assumptions

The response of the distortion due to the re-equilibration of the residual stresses can be determined using a linear-elastic material model as described by other researchers [150]. It is assumed that the small deformation in the machined component is due to the elastic response of the bulk material stress and induced machining stresses. Therefore only the redistribution of the residual stresses arising from the thermo-plastic deformations caused by machining or heat treatment of the work piece material are accounted for. The actual in-process cutting loads and thermal effects are neglected. As such no plastic deformation is considered in the modelling scheme, which also reduces model complexity and computational efficiency requirements. Generally, the workpiece/tool deflection and thermal influence on workpiece and tool deflections can be mitigated in reality by careful selection of process parameters and cutting conditions. It is assumed that these are stable for the proposed simulation approach. Cerruti modelled plastic deformation due to the impact of clamping on the part locally [157]. Typically, clamping in production is designed to avoid over-constraining, and thus, the issue is negated. However, the interaction of fixture position(s) on the elastic deflection caused by residual stress-related part distortion can still be accounted for through the determination of appropriate boundary conditions under the elastic scheme.

3.1.2. Validating the modelling concept

To validate the modelling concept, experimental testing is conducted to generate a demonstrator component from which deformation data can be generated and compared to the simulation output. Industry-standard methods, tooling and parameters are used in the manufacture of the demonstrators such that important insight to these conditions can be derived. The design of the demonstrator is such that geometrical features from aero structural wing components have been reproduced to give the test validity in their study of the machining-related distortion phenomena and to increase the likelihood of distortion occurring after machining such that it can be measured accurately. Additionally, the concept methodology will be compared against the baseline methods identified in Table 3-1.

3.2. Experimental investigations

A series of experimental trials are considered in this work for three primary purposes:

1. To investigate the influence of machining sequencing and strategy on induced residual stress formation and part distortion due to bulk and machining-induced residual stresses.
2. To produce initial bulk and machining-induced residual stress as input to the distortion FE model.
3. To produce dimensional metrology data for validating the distortion modelling methodology.

Concerning the first statement, the research has shown that careful machining sequencing and strategy selection can reduce part distortion for aerospace components (see section 2.5). However, the research is not exhaustive or explicit when considering the complex interaction of machining-induced residual stresses with successive material removal techniques. Those researchers that have modelled the inclusion of MIRS as a function of the tool path have assumed that only the last machining pass needs to be considered for the application of MIRS in distortion finite element models. This assumption is based on the consideration that previously generated machining-induced stresses for inter-process machined surfaces are removed by additional machining passes. However, some researchers have shown that for specific machining processes, the previous machining steps must be considered in the residual stress evolution of the component, as identified in the literature review (see section 2.4.2).

Furthermore, another common consideration when modelling MIRS influence on machined component distortion is that the MIRS values are bi-directional but are homogeneous across the machined surface. However, it can be observed, according to the machining tool path strategy utilised and the geometry of the component being machined, that variable inter-tool path cutting conditions occur. Thus, it is possible that variation in the MIRS state also arises as a response to the variable mechanical-thermal loading state. This research space will be explored in this work.

Considering statement two, a series of test coupons with variable geometrical designs will be measured to determine bulk and machining-induced residual stresses. The coupons will be subjected to destructive and semi-destructive measurement methods to determine the bulk and machining-induced residual stresses. Therefore, stress measurements must be made in sacrificial coupons from the same material batch so that material properties and residual stress conditions are consistent, limiting the variation in the testing process.

For item three, the distortion measurement coupons will capture the challenge of machining aero structural components through demonstrator components that share features of typical wing structure components. These components will be measured to capture distortion data after machining and used to validate the distortion model and study the influence of sequential machining operations on final part distortion.

3.2.1. Assumptions

- Machining-induced stresses test measurement coupons will be taken from the same material condition of supply as the distortion measurement coupon and machined using the same process conditions as the distortion measurement coupons. Therefore, it can be assumed the measured process-induced stresses are consistent between the two types of coupons, as direct measurements cannot be made.
- The stress measurement coupons will be designed to be suitably thick so the induced residual stresses do not redistribute, as highlighted by [144][78].

3.3. Concluding statements

Within this chapter, the research theme and requirements have been defined. The main research aim was stated, and the objectives were specified to meet this aim. Secondly, the numerical modelling methodology was addressed. Two principal modelling approaches from the literature have been evaluated for their perceived strengths and weaknesses. From the evaluation and the literature review in Chapter 2, a gap in the modelling approaches was identified, where the requirement to develop models that can account for inter-process machining distortion and machining-induced stresses imparted as a function of the tool path is needed. The assumptions and validation method for the conceptualised modelling method have been provided. Thirdly, the experimental work and assumptions developed to address the gaps in knowledge on the influence of machining strategy on machining-induced residual stress formation were detailed. A series of machining trials will study the influence of sequential machining operations on machining-induced residual stresses in the final machined surface and the potential variation in machining-induced residual stresses that may arise due to variable cutting conditions relating to the tool path strategy.

4. Distortion Modelling Procedure

4.1. The finite element method

Finite element method is a numerical process of solving engineering problems mathematically. Problems including structural analysis, heat transfer, fluid flow, mass transport and electromagnetic potential can be resolved approximately using FEA [158]. The basic premise behind FEA is devising a system of simultaneous algebraic equations for a mathematical model representing the physical reality under consideration. FEM is valuable when considering parts with complex geometry or loading situations whereby achieving an analytical solution would be extremely complex or unattainable. The process of FEA is undertaken through a combination of procedures, as detailed in Figure 4-1 [159]. Firstly, a mathematical model is developed for the physical problem under investigation. This is done by conceptualising how best to represent the phenomena through a simplified model. Next, discretisation is undertaken, which is the process of taking the model of the physical reality and turning it into many representative elements interconnected by nodes. Local calculations for each element are accumulated into a global matrix equation to provide an overall approximation of the system response.

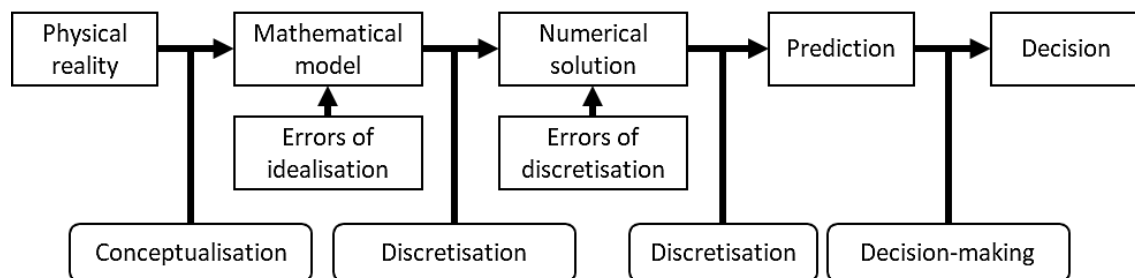


Figure 4-1: Processes associated with FEA [159]

FEA is widely used as an engineering decision-making tool [159]. Its use in the field of residual stress and part distortion is well documented in the literature (see section 2.6.3). The methodology outlined in chapter 3 produces the following requirements:

- Mapping of the bulk residual stresses in the initial stock model
- Impact of material removal on bulk residual stress redistribution and part distortion that can also account for in-process quality errors (over/undercutting)
- Mapping of machining-induced stresses according to the tool path direction
- Impact of machining-induced stresses on part distortion

Various software is available for FEM, with both meshing and solver provided separately or incorporated. However, as highlighted in [150], no standalone software is available that can map both the bulk and machining-induced residual stresses in an automated fashion. Therefore, the procedure must be developed in a pre-existing software package. ABAQUS [160] is a finite element analysis software package that includes ABAQUS/Standard and ABAQUS/Explicit solvers that use implicit and explicit integration schemes, respectively. The package includes the ABAQUS/CAE computer-aided engineering (CAE) module, an integrated pre-processor, a simulation submission manager and a results viewer. It is possible to import or generate geometry from the pre-processor, apply material properties, assign boundary conditions/loads, produce a mesh and specify the analysis type. The CAE environment is also scriptable using the Python programming to automate the previously described pre-processor tasks.

Furthermore, ABAQUS supports user-defined subroutines, which allow for customisation of the program for defining non-default properties such as material models, loading conditions and element types. ABAQUS user subroutines are generally written in FORTRAN programming language, and a dedicated compiler is needed to utilise this functionality. For this work, ABAQUS/Standard and ABAQUS/CAE, with Python scripting and Fortran user subroutines, have been employed to develop the modelling concept.

The physical phenomena of residual stress-related distortion can be framed as that of static structural stress analysis, such that the mapping and evolution of stress within the model can be exhibited without considering inertial or time-dependent effects. Within the finite element model, bodies can be considered either deformable or rigid. Due to the nature of the simulation, the machined component is considered deformable. The magnitude of deformation will be governed by the internal forces caused by residual stresses concerning the material properties that obey continuum mechanics material laws. As the material response being considered is linear elastic for this work, then only the elastic properties need to be defined; E = Young's modulus and ν = Poisson's ratio to describe the material behaviour. Although the material response is considered linear, the system's behaviour due to geometric and boundary conditions renders the model nonlinear. In order to solve and find a converged solution for the non-linearities, the Newtown-Rapson iterative solution is used, where the simulation task is split into small increments for which the approximate equilibrium condition can be found. Additionally, in ABAQUS, large-displacement formulation accounts for the large deformation that can occur.

Considering the 3D mechanical problem to be simulated, it can be given that the stress tensors acting at an arbitrary infinitesimally small material point within a solid (see figure 2-18) can be defined as a vector:

$$\boldsymbol{\sigma} = \begin{Bmatrix} \sigma_{xx} \\ \sigma_{yy} \\ \sigma_{zz} \\ \sigma_{yz} \\ \sigma_{xz} \\ \sigma_{xy} \end{Bmatrix} \quad 4-1$$

Considering strain at the same material point:

$$\boldsymbol{\varepsilon} = \begin{Bmatrix} \varepsilon_{xx} \\ \varepsilon_{yy} \\ \varepsilon_{zz} \\ \gamma_{yz} \\ \gamma_{xz} \\ \gamma_{xy} \end{Bmatrix} \quad 4-2$$

The strain can be defined in matrix notation as:

$$\boldsymbol{\varepsilon} = \mathbf{L}\mathbf{U} \quad 4-3$$

Where \mathbf{U} the displacement field vector is denoted:

$$\mathbf{U} = \begin{Bmatrix} u \\ v \\ w \end{Bmatrix} \quad 4-4$$

And \mathbf{L} the matrix of the partial differential operators:

$$\mathbf{L} = \begin{bmatrix} \partial/\partial_x & 0 & 0 \\ 0 & \partial/\partial_y & 0 \\ 0 & 0 & \partial/\partial_z \\ 0 & \partial/\partial_z & \partial/\partial_y \\ \partial/\partial_z & 0 & \partial/\partial_x \\ \partial/\partial_y & \partial/\partial_x & 0 \end{bmatrix} \quad 4-5$$

Where stress and strain can be linked by the generalised Hook's law:

$$\boldsymbol{\sigma} = \mathbf{C}\boldsymbol{\varepsilon} \quad 4-6$$

Where \mathbf{C} is relating the material constants Young's modulus, Poisson's ratio and shear modulus (G) that is given by:

$$G = \frac{E}{2(1 + \nu)} \quad 4-7$$

And so, for an elastic isotropic material, the stress-strain relationship can be defined as follows:

$$\begin{Bmatrix} \sigma_{xx} \\ \sigma_{yy} \\ \sigma_{zz} \\ \sigma_{yz} \\ \sigma_{xz} \\ \sigma_{xy} \end{Bmatrix} = \frac{E}{(1+\nu)(1-2\nu)} \begin{bmatrix} 1-\nu & \nu & \nu & 0 & 0 & 0 \\ \nu & 1-\nu & \nu & 0 & 0 & 0 \\ \nu & \nu & 1-\nu & 0 & 0 & 0 \\ 0 & 0 & 0 & 1-2\nu & 0 & 0 \\ 0 & 0 & 0 & 0 & 1-2\nu & 0 \\ 0 & 0 & 0 & 0 & 0 & 1-2\nu \end{bmatrix} \begin{Bmatrix} \varepsilon_{xx} \\ \varepsilon_{yy} \\ \varepsilon_{zz} \\ \gamma_{yz} \\ \gamma_{xz} \\ \gamma_{xy} \end{Bmatrix} \quad 4-8$$

The previous equations defined the governing principles of elasticity used in the continuum state. General solutions for these equations for complex problems rarely arise. The principle of FE is to find an approximation to these equations through procedures to reduce them from their continuum form to a series of linear systems of equations.

To achieve this discretisation, the part model must be split into manageable-sized domains in the form of meshing. The part domain is subdivided into smaller subdomains termed elements, connected to other elements via nodes. Various element types are available in ABAQUS, and their selection should be based on the analysis type to be undertaken and the resolution of the results sought. Elements vary in shape, number of nodes and Gauss/integration points. As the model under consideration is a 3D structural configuration, suitable elements are given in Figure 4-2.

Elements seen in Figure 4-2 (a) & (b) are linear (C3D8) and quadratic (C3D20) formulation hexahedral type elements, respectively. These elements are suitable for static stress analysis, where the quadratic type performs better in bending problems as the linear type is prone to hourglassing. Additionally, the quadratic formulation hexahedral element has more integration points than the linear type and can more accurately represent the mapped stress state. However, due to the inherent cuboidal shape, they are limited in the complexity of the part geometry they can discretise. Elements seen in Figure 4-2 (c) & (d) are of the type linear (C3D4) and quadratic (C3D10) formulation tetrahedral type elements. They are more suited to representing the complex geometry of machined aerospace components as they can conform to circular forms. However, a significantly higher number of tetrahedral elements would be needed for any given volume to accurately capture the same material response compared with hexahedral elements.

Nevertheless, the representation of the machined geometry is of high importance; therefore, the use of tetrahedral elements is chosen for the distortion modelling methodology. Figure 4-2 (e) & (f) displays linear and quadratic type 'wedge' elements, which are used to form boundary layer elements across specified regions of the model.

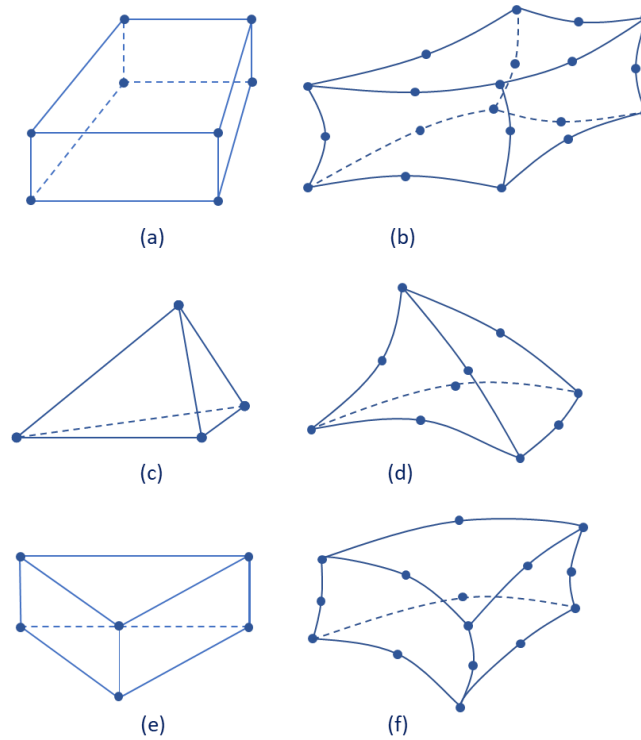


Figure 4-2: ABAQUS solid continuum element types [161]

Displacements within the elements are governed by the displacements of the adjoined nodes and inferred through interpolation governed by the shape function, typically in the form of a polynomial. Nodal displacements are given in the local coordinate system and defined generally by:

$$\mathbf{U}^h(x, y, z) = \sum_{i=1}^{n_d} \mathbf{N}_i(x, y, z) \mathbf{d}_i = \mathbf{N}(x, y, z) \mathbf{d}_e \quad 4-9$$

Where (\mathbf{U}^h) approximate displacement field vector, x, y, z the spatial coordinates, n_d is the number of nodes for the given element, (\mathbf{N}_i) the shape function and (\mathbf{d}_i) pertains to the individual nodal displacement. Therefore, (\mathbf{d}_e) is the vector of the nodal displacements for the given element. Substituting equation 4-9 into 4-3:

$$\boldsymbol{\varepsilon} = \mathbf{L}\mathbf{U} = \mathbf{L}\mathbf{N}(x, y, z)\mathbf{d}_e = \mathbf{B}\mathbf{d}_e \quad 4-10$$

Where, (\mathbf{B}) is the strain-displacement matrix. For static problems the mass-inertia effects are neglected, and the element displacement can be related to the element external forces (\mathbf{f}_e) by the element stiffness matrix (\mathbf{k}_e):

$$\mathbf{k}_e\mathbf{d}_e = \mathbf{f}_e \quad 4-11$$

Where \mathbf{k}_e given by:

$$\mathbf{k}_e = \int_V \mathbf{B}^T \mathbf{C} \mathbf{B} dV \quad 4-12$$

The individual element equations are assembled to create the global stiffness matrix (\mathbf{K}) and global nodal force vectors (\mathbf{F}) vector:

$$\mathbf{K}\mathbf{D} = \mathbf{F} \quad 4-13$$

The inverse of the global stiffness matrix is taken to resolve the vector of global nodal displacements (\mathbf{D}). The global nodal displacements within all elements within the specified domain can be determined by substituting equation 4-10 in 4-3, then subsequently 4-3 in 4-6.

As defined by [147] for mapping sources of stress such as the bulk and machining induced residual stresses, additional components can be included in equation 4-6 to define initial stress conditions, under the principle of superposition:

$$\boldsymbol{\sigma} = \mathbf{C}\boldsymbol{\varepsilon} + \boldsymbol{\sigma}_{IBRS}(z) + \boldsymbol{\sigma}_{MIRS}(bl) \quad 4-14$$

Where, $\boldsymbol{\sigma}_{IBS}$ and $\boldsymbol{\sigma}_{MIRS}$ are the initial bulk residual stress and machining induced residual stress vectors respectively. $\boldsymbol{\sigma}_{IBS}$ is defined as a function of the global spatial positioning and $\boldsymbol{\sigma}_{MIRS}$ as a function of the machining induced stress layer depth. Due to the nature of distortion under consideration for this work plane stress assumption is assumed for both residual stress sources ($\sigma_{zz} = 0$). This assumption has been made by other simulation methods reported for various reasons [151]. Including the fact that the residual stress in the Z principal direction is typically uniform, of small magnitude and do not contribute to the out-of-plane distortion, which is of primary interest in this work. Both stress vectors specify only the two principal direction stresses, such that initial bulk residual stress:

$$\sigma_{IBRS} = [\sigma_{xIBRS} \quad \sigma_{yIBRS} \quad 0 \quad 0 \quad 0 \quad 0]^T \quad 4-15$$

And machining induced residual stress:

$$\sigma_{MIRS} = [\sigma_{xMIRS} \quad \sigma_{yMIRS} \quad 0 \quad 0 \quad 0 \quad 0]^T \quad 4-16$$

4.2. Distortion modelling procedures

The section details the procedures required to realise the distortion modelling methodology outlined in Chapter 3. The initial model for characterising the bulk stresses is created and submitted using ABAQUS. This model forms the starting point for subsequent 'machining' steps to simulate the feature-based material removal and mapping of stresses. The residual stress state from the previous machined model configuration and the machining-induced residual stresses as a function of the tool path is calculated by the solver across the mesh defined for the current machining step. The machining steps can be grouped by machining stages. In reality, a machining stage refers to a specific part orientation setup within a work holding devices to machine all feature surfaces due to access and fixturing constraints. Typical wing rib components can undergo two to three stages with various fixturing configurations to obtain the required geometry. The number of stages can also be increased to aid with problematic parts experiencing distortion. Machining stages in the simulation space refer to a change of boundary conditions required to model the inter-stage process in physical reality. After all machining steps and stages are completed, the results are evaluated and exported for further analysis. The following sections discuss the modelling process steps in further detail.

4.2.1. Modelling the initial bulk residual stress state

Bulk residual stresses in high-strength aluminium rolled plate material are generated during the manufacture of the billet. The heat treatment cycle used to attain favourable material properties includes a high-temperature thermal soak and rapid quench that produces high thermal gradients across the thickness of the billet. This heat treatment process results in differential cooling and shrinking rates between the core of the plate and its extremities. This results in balanced regions of tensile and compressive stresses through the thickness. Stress relieving methods, such as stretching, are employed but do not fully remove residual stresses. It can be seen from the literature that residual stresses determined experimentally within a rolled plate exhibit different profiles and magnitudes in the

longitudinal and long-transverse billet rolling directions. Therefore, the application of bulk residual stresses within FE models must be able to describe the biaxiality of the bulk residual stress fields.

In the FE model, bulk residual stresses can be defined as a function of the initial billet model thickness coordinate (z), as shown in Figure 4-3. The bi-directional residual stress values are applied as a stress tensor at the corresponding element material integration point (equation 4-15). The billet is modelled and meshed in ABAQUS\CAE to represent the starting material condition before machining. SIGINI user subroutine can be utilised for this purpose. SIGINI is called at the start of the analysis for every integration point, where the stresses are calculated according to a polynomial expression. Two polynomial expressions describe the stress curves obtained through the experiment. The stresses attained through the thickness of the rolled plate material in the longitudinal and long-transverse directions. Both polynomials have the general form:

$$f(x) = p_n z^n + p_{n-1} z^{n-1} + \dots + p_2 z^2 + p_1 z + p_0 \quad 4-17$$

Where p_n are the coefficients of the polynomial expression determined through curve fitting. To fully describe the model material properties (see section 4.2.4), element shape and formulation (see section 4.1) and boundary conditions (see section 4.2.5) must be defined. A single static general analysis step is used to load the element integration points with the bulk stress data and resolve any stress unbalance across the model over the analysis step. The implementation of the SGINI user subroutine in the ABAQUS\standard process is covered in section 4.3.

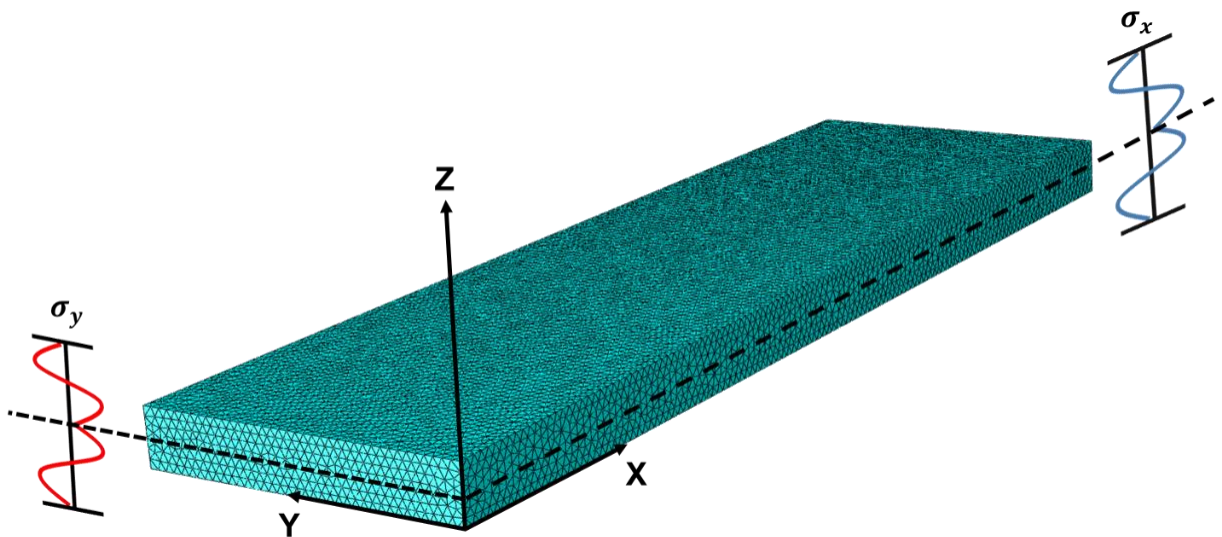


Figure 4-3: Bulk residual stresses applied to the billet with respects to coordinate system

4.2.2. Mesh import, Boolean removal and Part clean-up

To capture the influence of sequential material removal on the rebalancing of the internal residual stress field several machining simulation steps are required. To realise this 'multi-step' or 'Boolean' procedure, as described by Ma *et al.* [144], such that the inter-process part distortion can be modelled, a method has been developed in ABAQUS/CAE where the following sequence of tasks are carried out:

- Import deformed mesh from the previous analysis.
- Convert orphan mesh to part.
- Perform Boolean removal.
- Clean up cut part for accurate meshing.
- Mesh cut part instance.

With ABAQUS/CAE, importing the deformed mesh from the last step in a previous simulation as an orphan mesh is possible. The orphan mesh has no associated geometry but comprises orphan elements and nodes. It is not possible to work directly on the orphan mesh, such as modelling the material removal with a Boolean operation. Therefore, it must be converted to geometry first. Various methods in ABAQUS/CAE can be used to generate part geometry from an orphan mesh. However, to perform the conversion such that it can be automated via scripting, the mesh-to-geometry toolbox is used. The mesh-to-geometry process creates geometrical faces from the orphan mesh external element's faces and adds internal volume to obtain a solid part. It is then possible to perform Boolean cutting in the part module within CAE.

Cerruti describes the various levels of material removal modelling, including machining sequence discretisation [157]. In the simplest case described, the entire material removal sequence is simulated in one step. The one-step method is realised by applying the corresponding bulk residual stress profile to the mesh representing the final machined geometry, according to its offset position in the initial stock material. This method was utilised by Dreier [150] who demonstrated it is possible to capture accurate final part distortion for machine components but not distortion-related machining quality issues that are a function of the sequencing.

Further levels of modelling conveyed by Cerruti included the removal of material in a 'multi-step' approach by separating the machining sequence into key machining features (i.e., pockets, channels and datum faces). In turn, the removal of key features could also be discretised further such that the mass removal be broken down into smaller sub-volumes to represent single tool path passes. Increasing material removal resolution is associated with increased numerical processing time. Therefore, the degree to

After the newly cut geometry has been generated, the part must be meshed such that the simulation procedure can be achieved. However, the Boolean process intersects the edges of the faces on the surface of the old geometry generated by the mesh-to-geometry function. If the part is seeded without editing the intersected edges, a poor mesh results. A part 'clean-up' method has been developed using Python scripting and ignoring entities functionality in ABAQUS/CAE. The process can be seen in Figure 4-5.

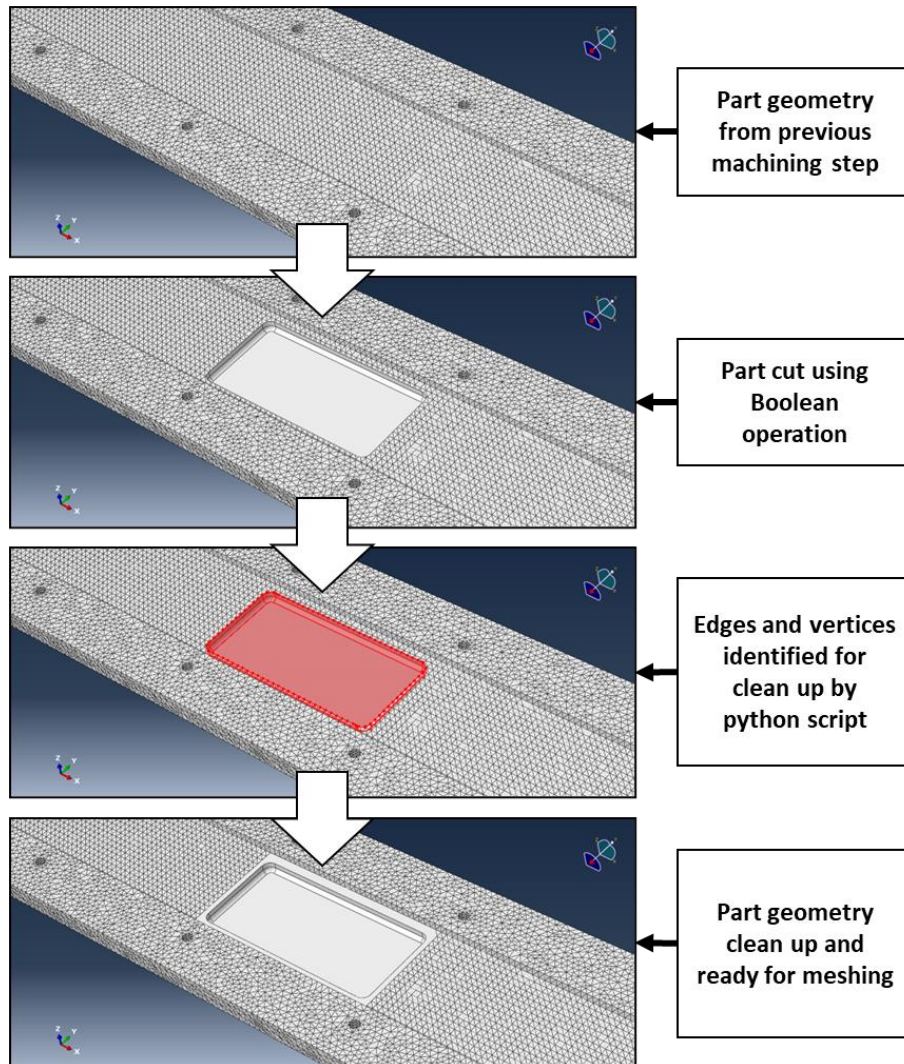


Figure 4-5: Boolean part clean up procedure.

After the part clean-up operation, the mesh is applied to the cut part instance. A ten-node quadratic tetrahedron element type is defined for the general part model. The application of the nodal positions is controlled by global seeding, which determines the element density in the model. The progression of the

meshing procedure in CAE follows: generation of a surface mesh by introducing nodal positions at the geometry vertex, generation of connected element edges along the part edges, and creation of triangular element faces approximately equivalent in the surface area across all geometric faces. Then the internal elements are grown from the surface element faces. Due to the selective clean-up procedure, seeding is generated to 'follow' the vertex on the surface left from the mesh-to-geometry process where no clean-up has been performed. This leads to the generation of elements of similar size and geometric position to the elements in the previous model, which aids with the solution mapping procedure discussed in detail in section 4.3. The meshing routine is controlled by ABAQUS/CAE automated meshing algorithm.

In order to accurately map machining-induced residual stress, a refined boundary layer element must be applied at the region of interest. The boundary layer is applied only to regions of the model where machining-induced residual stress (MIRS) will be defined. Otherwise, the unrequired refinement of the surface layer mesh at regions where MIRS is not applied will increase the computational cost of the model to the point of poor economic return [150]. With ABAQUS/CAE it is possible to assign linear and quadratic type 'wedge' elements, as shown in Figure 4-2 (e) & (f), respectively, as boundary layers to specified regions across the model surfaces. Figure 4-6 shows the selective boundary layer application across a meshed component. The boundary layer region assignment in this work is controlled by Python script to target specified floor sections of the model for refinement. When considering the mapping of MIRS across boundary elements, two important considerations arise: first, which of the machining processes should the MIRS be considered for mapping and secondly, what level of refinement is needed to accurately map the effect of the applied MIRS on part distortion.

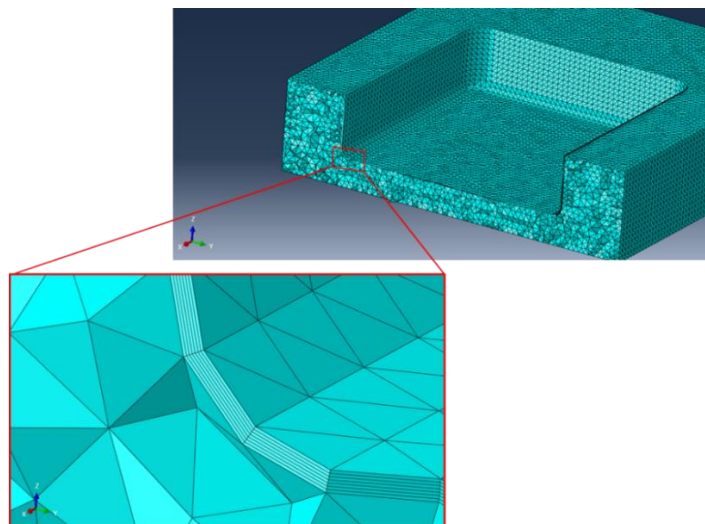


Figure 4-6: Mesh refinement of boundary layer

On the first consideration, as previously mentioned, it is advantageous to limit the amount of boundary layer refinement such that the most economical model can be generated in terms of computational expense vs solution accuracy. Therefore, based on their impact on part distortion, the targeted application of machining-induced stresses for influential machining processes should dictate the locations at which the boundary layer and MIRS are applied. It has been shown that for asymmetric models, the application of the MIRS at the pocket floor and component backside features, in combination with bulk residual stress, is the cause for the majority of the part distortion, and modelling MIRS across the surface of other areas of the geometric part only increases accuracy insignificantly [151].

Concerning the second point, Dreier has studied the influence of boundary layer depth and discretisation extensively [150]. He concluded that the boundary layer height should be prescribed based on the depth of the MIRS layer to be mapped and that the number of elements within the boundary layer can be optimised based on the convergence of the solution. The optimal number of boundary layer elements is subject to the shape of the empirical stress curve to be mapped such that an accurate representation of the machining-induced stress field can be achieved. Chapter 7 of the work considers the boundary layer's selection and application. The following section will discuss the selection procedure of the elements to be assigned MIRS.

4.2.3. Toolpath identification of elements for mapping MIRS

The modelling methodology for this work includes the application of empirically determined MIRS across boundary layer elements as a function of the CNC tool path progression. Machining-induced residual stresses can vary in profile and magnitude in the tool feed direction and normal to the feed direction. Therefore, the MIRS mapping method should apply process-induced residual stresses as a function of the tool path direction. To identify the boundary layer elements as candidates for MIRS mapping, according to the tool path progression, a number of Python scripts have been developed. Figure 4-7 shows the process flow and associated Python scripts with identifying MIRS target elements in the FE model: (1) Convert .aptsources file to ABAQUS usable format and (2) assign FE mesh target areas for MIRS mapping.

For the first script, the tool path data is converted from .aptsources format to data that is utilisable in ABAQUS/CAE environment. The .aptsources file includes information on the programmed machining process, including tooling, programmed feed/speeds and the tool centre point location in relation to the work coordinate system. The tool centre point defines the location of the tip of the tool in Cartesian coordinates in three-dimensional space with respect to the work coordinate system (WCS). The program

work coordinate system in CATIA environment is not consistent with the assembly coordinate system in ABAQUS/CAE environment, thus the script performs a coordinate system transform such that the tool path will intersect the meshed FE model. With the tool path information converted the data is passed to the second Python script that creates the element set for MIRS application based on tool path direction.

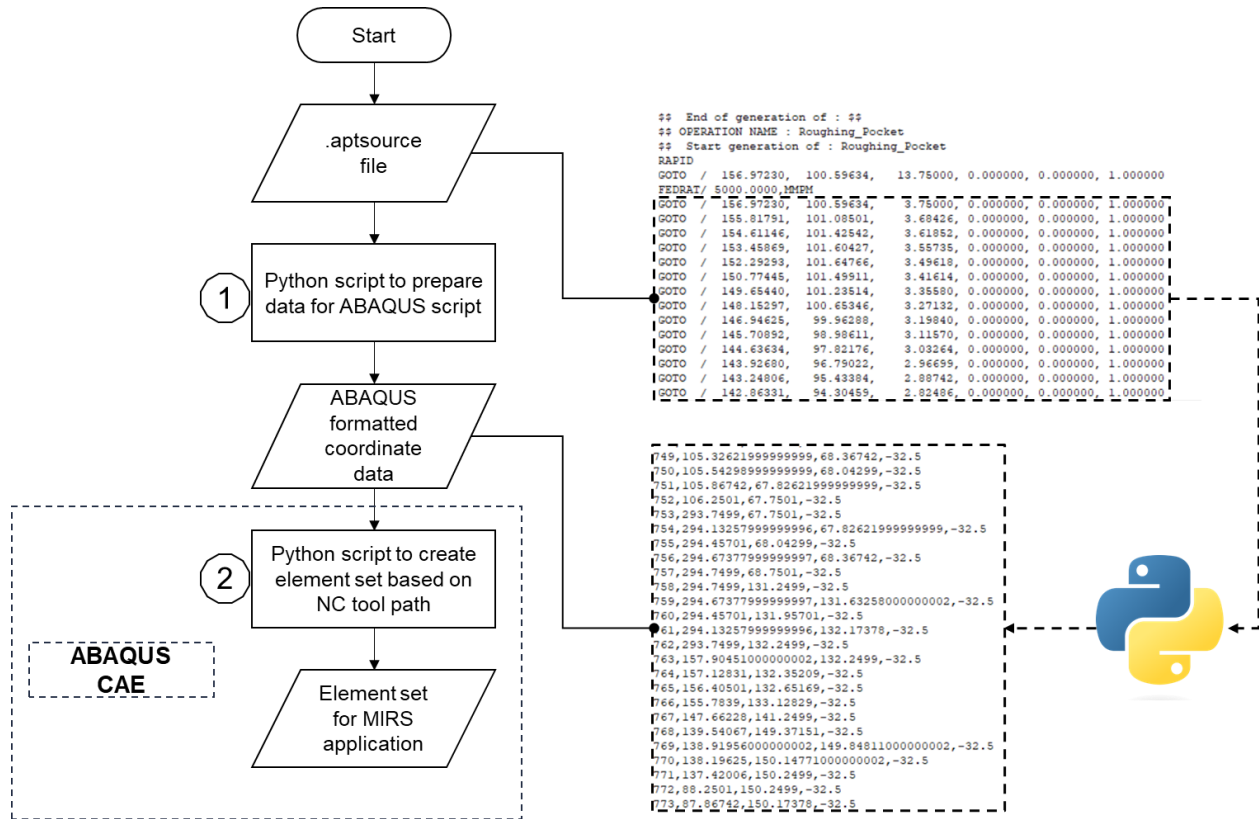


Figure 4-7: Process flow for generating MIRS element candidate set

As mentioned, ABAQUS/CAE interfaces with Python scripts such that CAE commands can be implemented in an automated fashion. Utilities within ABAQUS/CAE have been exploited to collate mesh nodes as a function of the machining tool path. The tool/mesh interaction is determined by the intersection of the tool-swept volume with the boundary layer nodes. The tool swept volume as depicted in Figure 4-8 (b) is simulated using the CNC tool centre point information generated from the previous Python script by expressing the geometry as a series of cylinders (C1 + C2) adjoined by a cuboid (B). The radius of the cylinders and the width of the cuboid is determined by the radius of the cutting tool (R) used in the physical machining process. The script is conditioned only to select nodes associated with wedge-type elements and ignore nodes that have already been selected in regions where the toolpath 'overlaps'. The directionality of the tool path can be calculated based on the orientation of the swept volume in the global

coordinate system such that when intersecting any given node the script can prescribe a user predefined field condition to that node set for application of stresses at the analysis stage of the procedure via user subroutine. The detail of MIRS application by subroutine is given in section 4.3.

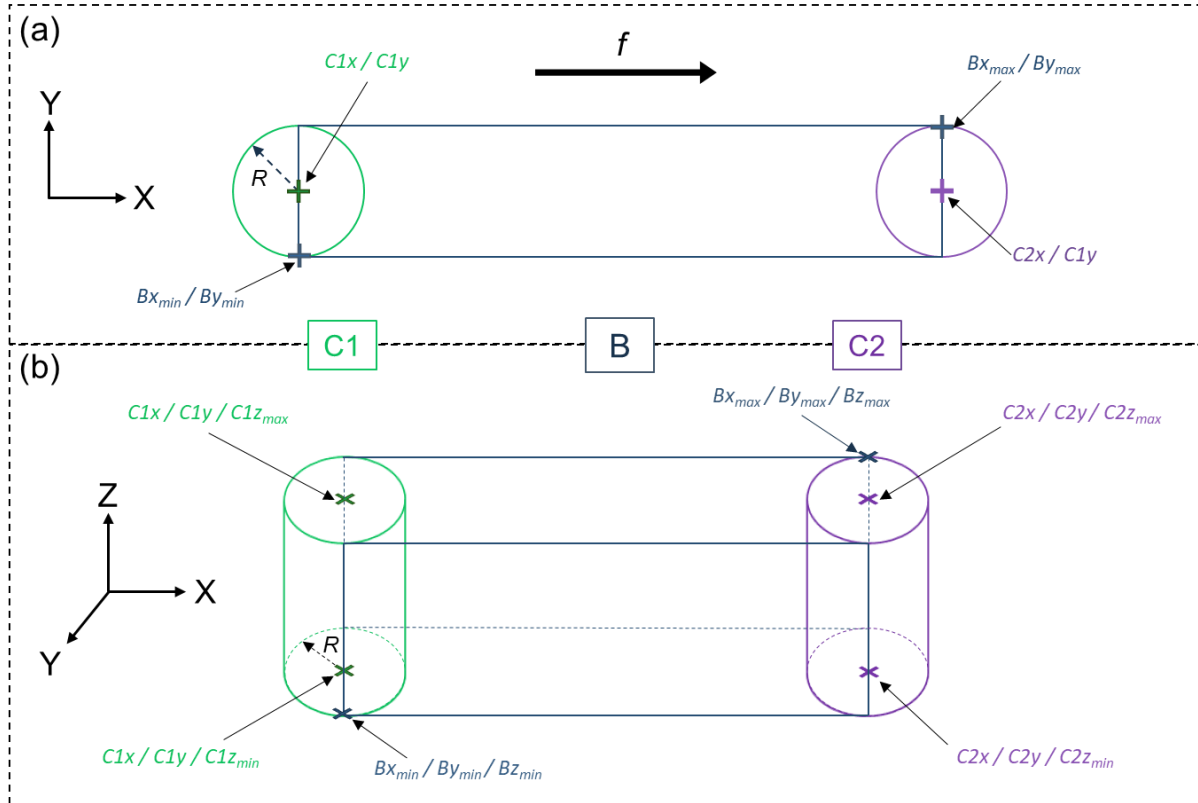
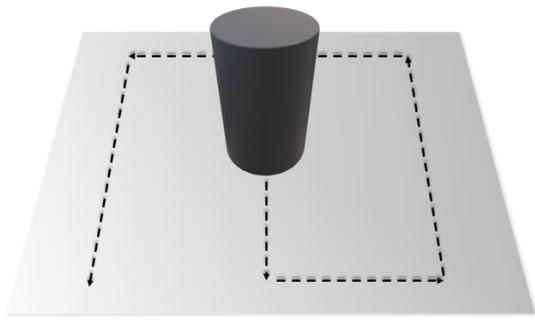
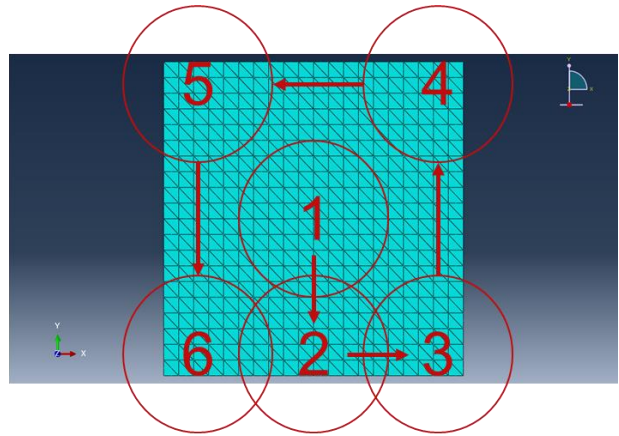


Figure 4-8: Swept tool volume

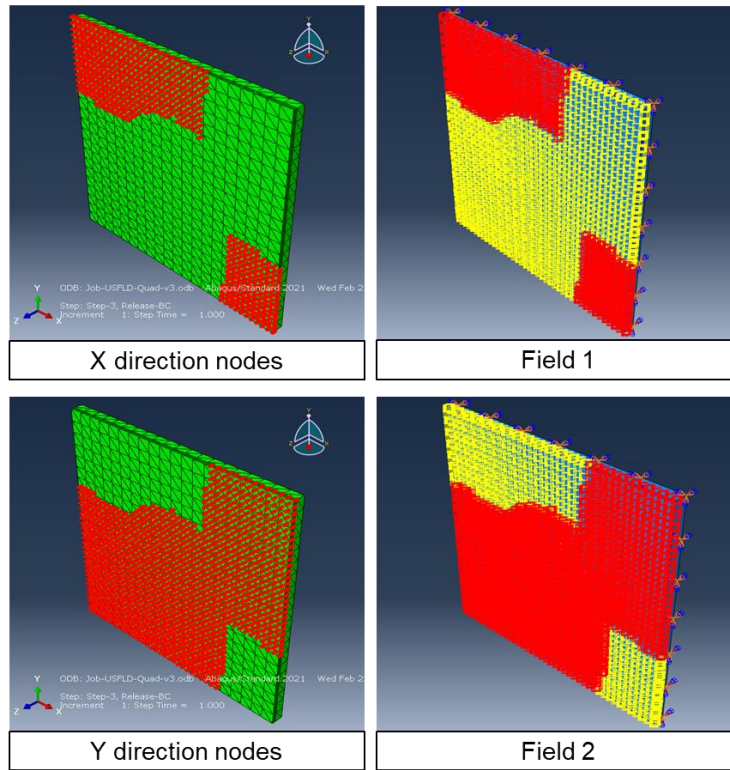
An example of the tool path mesh identification routine in practice is given in Figure 4-9. First the example given is that of a tool performing a helical spiral outwards tool path movement on plate material as seen Figure 4-9 (a). Figure 4-9 (b) shows the relative tool movements in ABAQUS which can be described by a series of computer numerical controlled (CNC) data lines i.e., relative tool vector coordinate points describing the movement of the tool in cartesian space with respect to the workpiece coordinate system. The script calculates the candidate nodes based on the tool path swept volume intersection. These nodes are assigned to a set and field value based on the tool path direction relative to the global coordinate system at the point of intersection, as illustrated in Figure 4-9 (c). The application of the MIRS is controlled via subroutine utilising the conditions implemented by the tool path routine and is discussed in section 4.3 of this chapter.



(a)



(b)



(c)

Figure 4-9: Tool path mesh identification routine

4.2.4. Material definition

The fundamental assumption of the modelling methodology is that distortion can be simulated by way of a linear elastic material response. Therefore, only the elastic material properties need defining for the model. All machining trials conducted in this work consisted of 7050 T7651 aluminium alloy. The elastic material properties taken from the condition of supply are given in Table 4-1.

Table 4-1: Elastic material properties

Young's modulus (E)	Poisson's ratio (ν)
72,000 MPa	0.33

The material behaviour for the models is specified by UMAT user subroutine, which defines the mechanical constitutive behaviour. UMAT requires a matrix definition of the Jacobian, which is based on equation (4-8) for a linear elastic material. The UMAT accepts input from the model, such as the elastic material properties and the current analysis model for each simulation iteration, including the current strain increment, strain tensor and stress state. The user defines the material values in the input file that is passed to the user subroutine at the start of the analysis. Its execution during the analysis stage is discussed further in section 4.3.

4.2.5. Simulating the machining fixture and boundary conditions

In the physical machining space, fixturing is used to locate and constrain the component to be machined in reference to the CNC work coordinate system. The accurate location of the workpiece allows for the desired material removal and generation of the intended design shape as programmed. It is also responsible for withstanding the loads imparted by the cutting action that would cause the part to deflect or relocate from its reference position in the machining centre, resulting in geometrical error. Additionally, the fixture method should impede in-process part deflection caused by the residual stress redistribution resulting from the sequential removal of stock material. Therefore, it can be seen that the importance of an appropriately designed and applied fixture system directly influences the quality of the final mainlined component. Figure 4-10 depicts various types of clamping and fixture methods used in the experimental trials for this work.

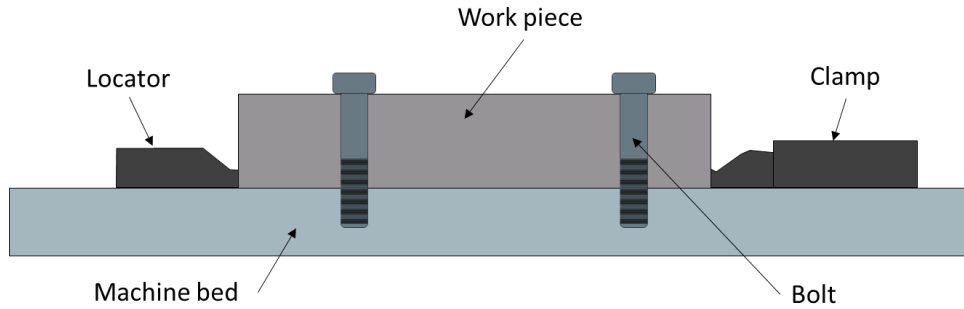


Figure 4-10: Types of work holding utilised in this work

The influence of fixture design on part quality due to distortion can be incorporated into the simulation approach as detailed in [157]. Various levels of modelling can be employed to represent the physical fixture. The finite element method requires that for static general analysis the model must be minimally constrained to prevent rigid body motion. In the single step modelling approach the use of 3-2-1 boundary constraints are utilised to allow for the free distortion of the model whilst preventing rigid body movements. The 3-2-1 principle is based on constraining the 6 translation and 6 rotation degrees of freedom that are present for any given prismatic body as shown in Figure 4-11. To constrain these degrees of freedom the 3-2-1 principle states that three locators be applied to the first face, two locators to the second and 1 locator to the third, as depicted in Figure 4-12. In the FE model this can be realised through blocking specific degrees of freedom at nodes such that the 3-2-1 principle is realised.

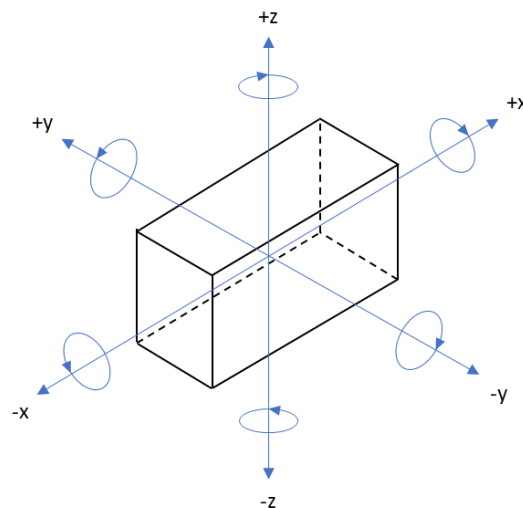


Figure 4-11: 6 degrees of freedom

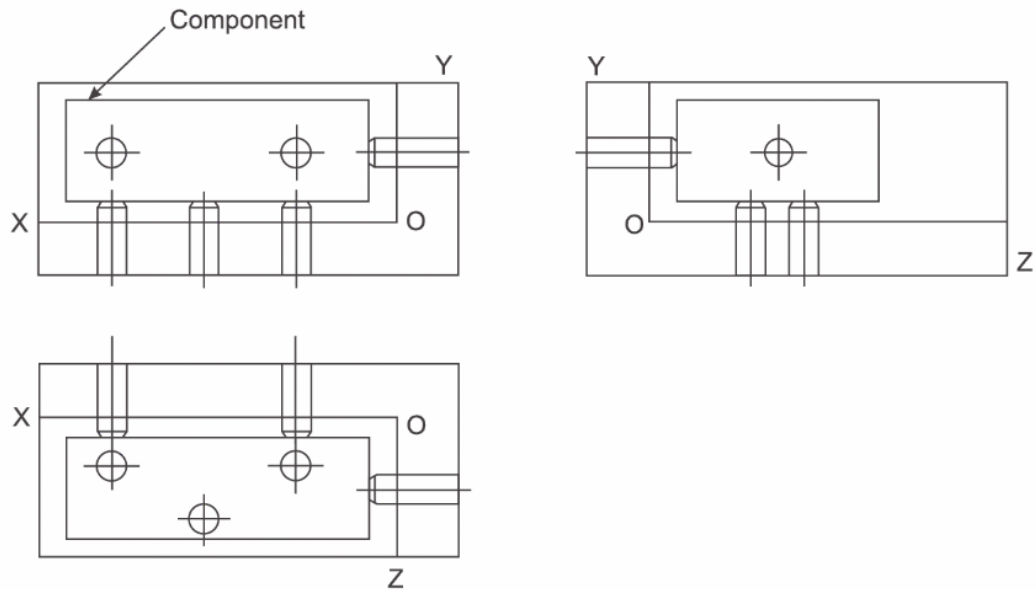


Figure 4-12: 3-2-1 constraint [162]

For the multi-step material removal model, it is necessary to develop boundary conditions that restrict movement so as to represent the clamping conditions in reality during material removal. There are two principal methodologies possible. The first method represents the constraint of the machined component in the model by restraining degrees of freedom and/or applying relative forces at nodes within the clamping zone in order to simulate the contact condition. Secondly, contact between the meshed part and deformable or rigid bodies representing the designed fixture(s) can be modelled.

The restraining degrees of freedom method can range from simplified conditions where nodes along arbitrary part features are selected for constraint to more realistic boundary conditions where the nodes constrained are selected based on their proximity within the contact surface area between the model and virtual fixture system. However, in certain instances these constraints are over simplified and do not provide a good solution to simulating the fixture conditions of the machining operation i.e. when the part becomes thin or the fixtures do prevent all movement in the component.

Comparatively modelling contact between bodies (the part model and fixtures) can be more representative of the physical workpiece/fixture system under consideration. However, modelling contact is highly nonlinear and is therefore more computationally expensive. ABAQUS/Standard has multiple contact interaction procedures available to the user including general contact, contact pairs and contact elements. For this work the use of general contact has been explored. General, surface-based, contact is considered to model the contact surfaces between the machined part model and fixtures. In the physical

machining trials fixtures cover the clamp, bolts and machine bed that all contact the workpiece in order to constraint and locate throughout the machining process. The general contact method is generally easier to define than the contact pairs method and therefore works well in the automated model definition of the machining simulations by scripting. Surface-to-surface and finite-sliding formulations are employed by the general contact algorithm by default.

The surface-to-surface formulation is a contact discretisation method describing how the nodes on contacting surfaces interact. Nodes on the surface of contacting bodies are linked depending upon which of the surfaces is defined as the main or secondary surface. This definition of main and secondary contact surfaces is depicted in Figure 4-13. Because the contact constraints are calculated for a primary node and also adjacent nodes that lie on the secondary surface, the contact condition is enforced in an average sense. For modelling machining fixture and part interaction, this provides a powerful contact control method that limits secondary node overclosures and, therefore, sources of numerical inaccuracy. Finite-sliding is a type of contact tracking approach describing the interacting surfaces' relative motion. Under this tracking scheme, contacting surfaces can slide, separate, and rotate relative to one another.

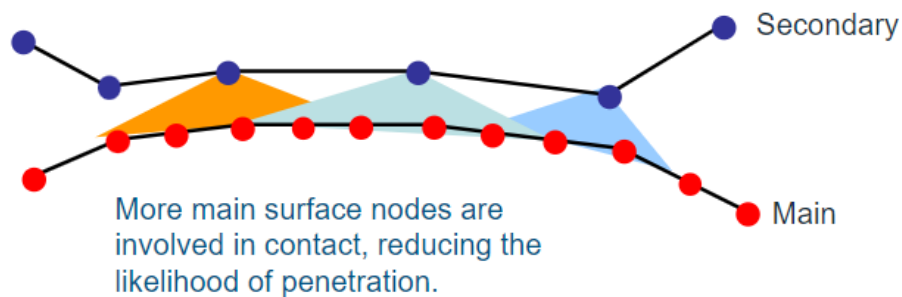


Figure 4-13: Surface-to-surface contact [161]

In addition to selecting the control algorithm that defines how the contact is enforced, the interaction properties that describe the contacting bodies' mechanical behaviour must also be defined. Complex contact interaction properties can be specified in ABAQUS, including pressure-overclosure relationship, friction, damping and cohesive behaviour. For this work, all contact interaction properties are defined by normal and tangential behaviour only.

Normal contact properties are described with 'Hard' contact pressure-overclosure behaviour which states are depicted in Figure 4-14. This is important as if excessive overclosure occurs where the nodes of the part mesh are allowed to penetrate the fixture mesh then the model would effectively be displaced from

the intended fixture position. This would result in a potential error in the machining simulation approach. Figure 4-15 illustrates this point. Figure 4-15 (a) shows a simple machining and work-holding arrangement to be modelled. Figure 4-15 (b) shows the model of the physical process outlined in (a), where the bolt contact force is modelled by boundary constraints on the top surface of the mesh, forcing it into the machine bed model. The machining removal of material is represented by a Boolean volume. Figure 4-15 (b) shows the idealised condition where no penetration occurs between the meshed part and the machine bed. Z_f is the floor thickness of the machined pocket feature where no penetration occurs and is equal to the starting height of the part minus the Boolean depth of cut. Figure 4-15 (c) illustrates the case of excessive penetration where Z_f is now the original height of the part minus the Boolean depth of cut plus the penetration. However, some penetration still occurs for the 'Hard' contact pressure-overclosure to aid with numerical convergence and this effect will be considered in results given in chapter 7.

Friction is a highly nonlinear behaviour to simulate and is recommended being modelled only if it is critical to the physical behaviour being considered. In the case of machining processes, clamps and fixture systems used to constraint parts are design optimised such that contact is maintained and part movement tangential to the contact surfaces is minimised. This is also consistent for the clamping and fixtures used in the experimental trials considered in this body of work. Therefore, to reduce the complexity of the simulation process and improve convergence attainment the tangential behaviour is specified as frictionless for contacting bodies under this modelling methodology.

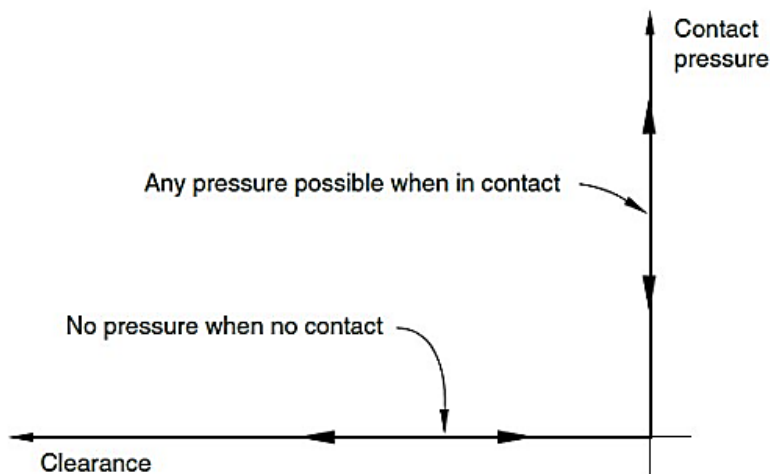


Figure 4-14: Hard contact behavior [161]

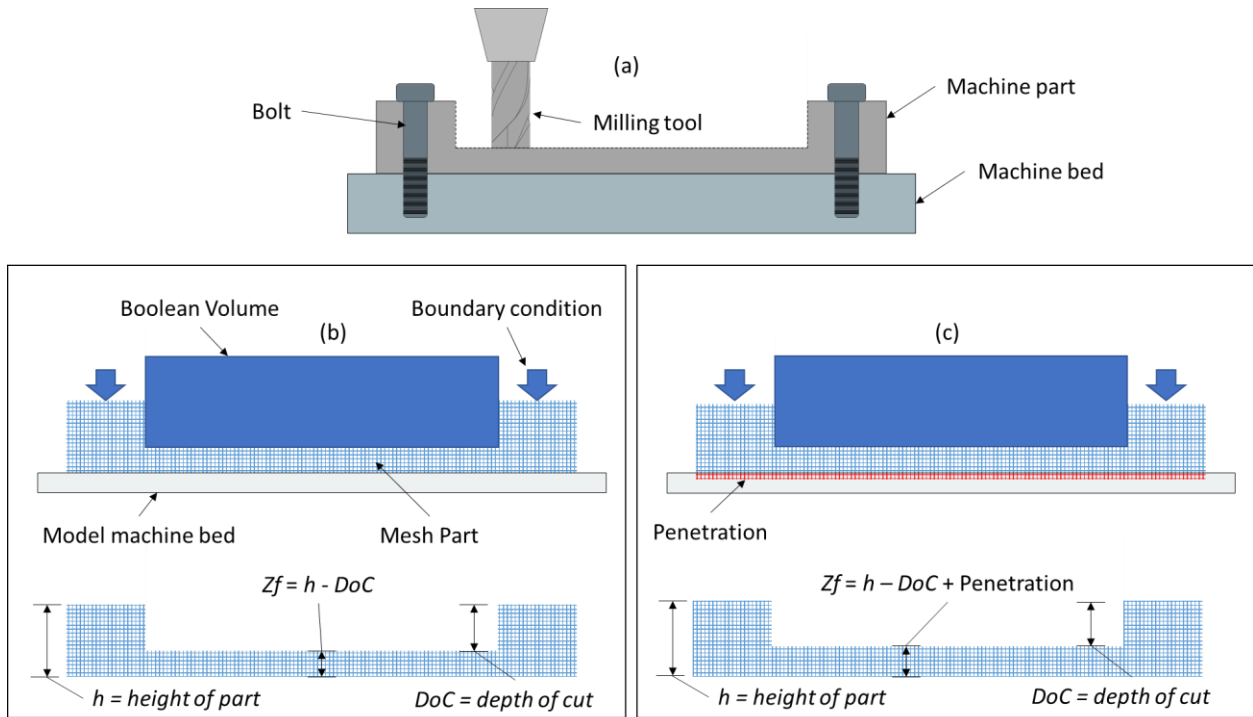


Figure 4-15: effect of contact overclosure on Boolean operation

As discussed, modelling fixtures by either nodal boundary conditions or contact between finite elements has specific drawbacks and advantages for each. The level of boundary condition of distortion modelling is highlighted well in previous research [157]. Therefore, the level of boundary condition modelling should be chosen based on the workpiece/fixture condition in reality. For instance, when it is reasonable to assume the clamping method is sufficient to restrain all relative movement between the part and fixture during machining, then the low computational cost of utilising nodal boundary conditions can be realised. However, when there is a possibility of movement of the part concerning the fixture during machining (i.e. the part moving away from fixture support, known as 'lift-up' in the industry), then more complex but representative fixture conditions should be modelled. The specific fixture modelling of the component under consideration for this work will be deliberated upon in section 7.3.2.

4.3. Distortion modelling execution

As highlighted in section 3.1, development of the simulation methodology in the production chain should include automated model generation and execution, such that the distortion modelling process is deployable in production. It is possible to utilise Python object-orientated programming language to automate the creation/modification of ABAQUS models and analysis jobs, the results of which can also be generated via scripting. Figure 4-16 shows the process flow of the simulation implementation. The input to the machining simulation process includes the deformed mesh and bulk residual stress data of the bulk stress model described in 4.2.1, the tool path information containing the transformed tool path coordinate data for MIRS application outlined in 4.2.3, and the Fortran file containing the UMAT user subroutine for material property and MIRS definition. A sequence of sequential machining models and analysis jobs are created and submitted via the Python control script where the output from one analysis is transferred to the start of the next.

At the start of each machining step, the ABAQUS Python 'Machining script' for the specific machining stage and step is created and executed to carry out the processes shown in Figure 4-17. The machining step CAE model file is generated from the initial bulk stresses model CAE file, which contains the suppressed Boolean removal volumes generated from the CAD design process. In the first instance, the deformed mesh from the initial bulk stress analysis is imported to the current model. The deformed mesh from the previous machining simulation is imported for all other machining steps. The Boolean procedure is then carried out, and the cut part is cleaned up as detailed in section 4.2.2. A global mesh is then applied to the part model using quadratic tetrahedral elements and localised refined boundary layer mesh consisting of quadratic wedge elements at the specified machined surfaces described in section 4.1. Next, the regions for the MIRS application are selected as outlined in section 4.2.3, and *INITIAL CONDITIONS, TYPE=FIELD is updated for the current machining model step. The boundary and external loading conditions depend on the current machining stage and virtual fixture representation. The material section is specified as user-defined for the 3D deformable component model, the definition of which is presented in section 4.2.2. The script then generates the .inp file that contains the analysis-specific information required by ABAQUS/standard solver. Finally, the Python script opens and edits specific keywords in the generated .inp file such that the *MAP SOLUTION procedure can be realised.

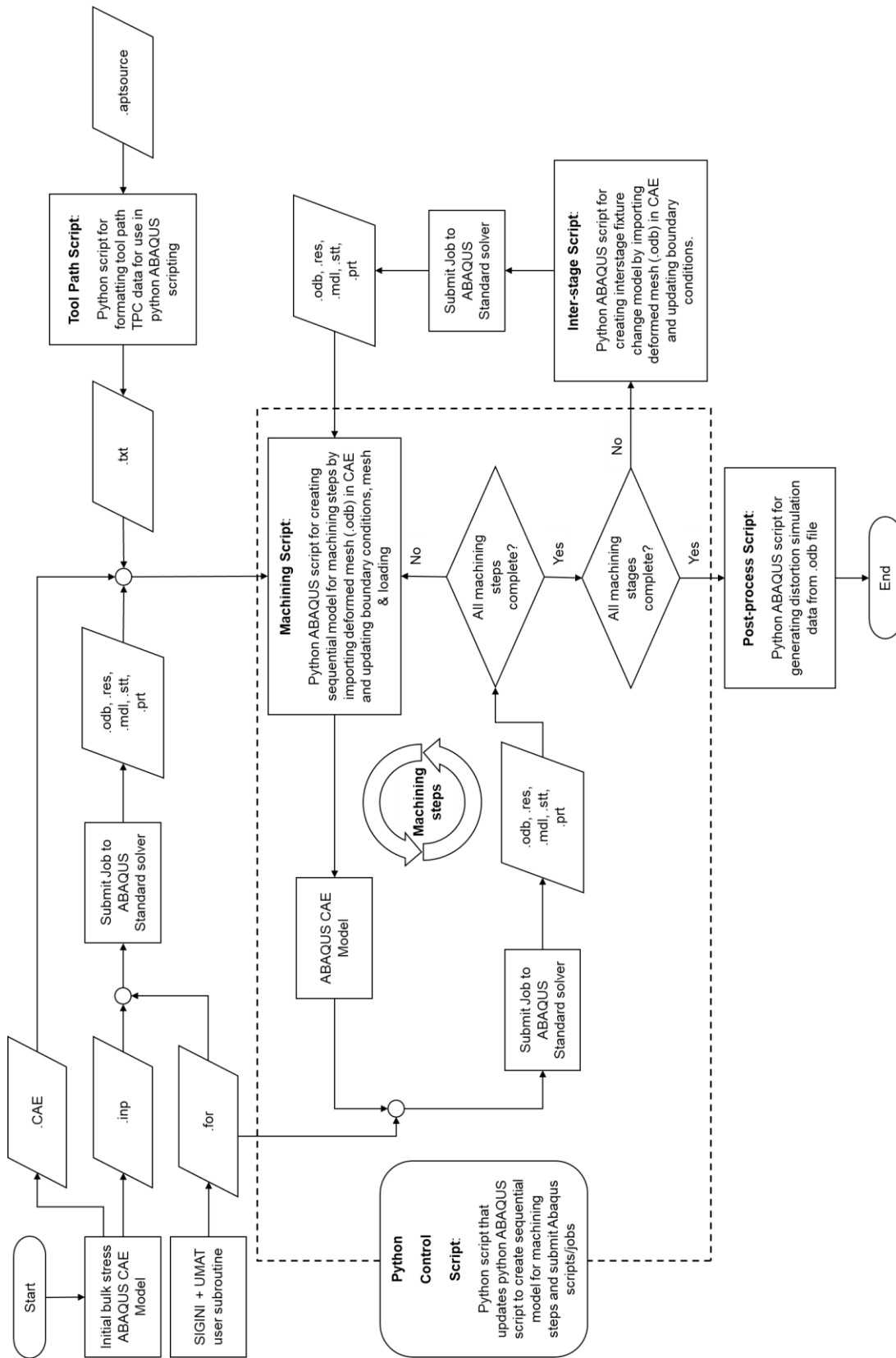


Figure 4-16: Distortion modelling process

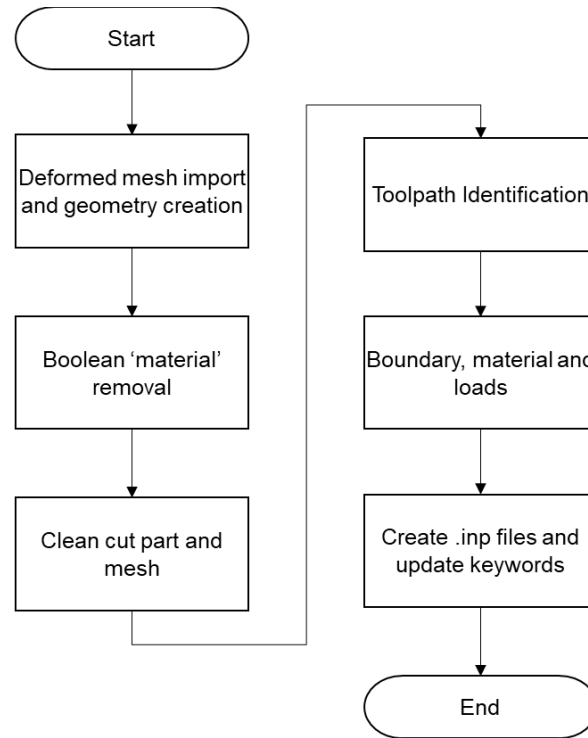


Figure 4-17: Machining simulation Python script processes

The machining simulation analysis file for the current machining step is submitted to ABAQUS\standard along with the Fortran user subroutine file for material and MIRS definition. For general machining analysis the simulation is carried out in three general static steps. In the first step the transfer of previous mesh stress field data is carried out. This mapped field stress data includes both the bulk stresses and any applied MIRS from the previous machining simulation step. The second step is utilised as a dummy step such that the MIRS tool path *INITIAL CONDITIONS, TYPE=FIELD is updated to allow for the targeted application of MIRS to boundary elements. The third step sees the application of MIRS in the boundary layer elements controlled by the UMAT subroutine. For the last machining step for a given machining stage, an additional step is generated by the machining Python script to update the boundary conditions to that of type 3-2-1. This is to allow for the free distortion of the simulated part under the current stress conditions. The following sections discuss key analysis features associated with the process flow given in Figure 4-16.

4.3.1. Mapping the residual stress state

The MAP SOLUTION procedure is responsible for the transfer of the stress field variables from the end state of the previous machined part model analysis to the start of the next analysis. The Boolean removal procedure results in a new model where sections of the old model no longer exist. Therefore, regions of

stresses that once contributed to the equilibrium state of the old model are not transferred and the stress state at the start of the new analysis is unbalanced after solution mapping. This drives the rebalancing process that causes distortion of the new part mesh. The solution mapping algorithm interpolates the results from the old to the new mesh in several steps:

1. Stress solution variable of the old mesh is extrapolated from the integration point to the node of each element.
2. The intersection of the new mesh element integration points within the old mesh is calculated.
3. The field values of the old mesh nodal locations are interpolated to the integration points of the new mesh as a function of the calculated position as shown in Figure 4-18.

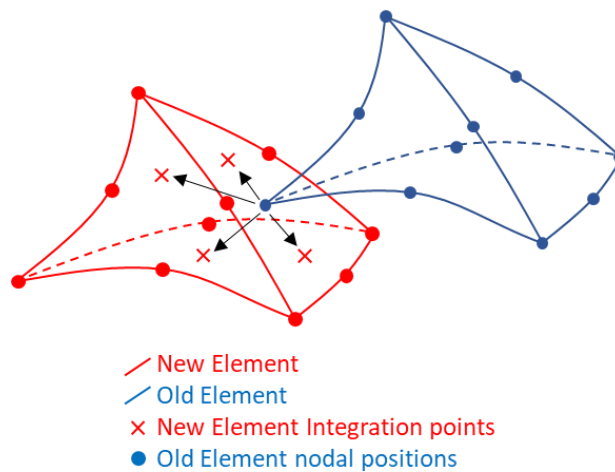


Figure 4-18: Solution transfer between elements

4.3.2. Application of the machining-induced residual stress

To apply the MIRS as a function of the tool path progression the predefined field values assigned to boundary layer elements by the toolpath identification module of the machining Python script (see section 4.2.3) are passed to the UMAT user subroutine. Under the developed modelling procedure, predefined fields have been specified for combinations of tool type (as each machine tool produces variable MIRS profiles) and tool feed vector direction with respect to the model's global coordinate system. As discussed, empirical trials employing representative cutting conditions have been used to generate bi-directional *descriptions* of the machining-induced residual stress for application to the boundary layer. These stress measurements are reported with reference to the tool path feed (σ_{\parallel}) and normal (σ_{\perp}) directions aligned with the sample coordinate system. To apply the MIRS data to the boundary layer mesh as a function of the tool path direction, these stress components must be transformed according to the tool path vector

given by the predefined field variable set by the tool path definition script. Figure 4-19 (a) depicts the progress of a cutting tool for a given machining test sample where the feed and normal tool path direction are specified. Figure 4-19 (b) illustrates how the process can be modelled to define stress direction values for selected elements. In the example provided, the red swept tool volume represents selected elements where the feed and normal direction stress can be applied to the element stress tensor with respect to the global coordinate system such that:

$$\sigma_{MIRS} = [\sigma_{\perp} \quad \sigma_{\parallel} \quad 0 \quad 0 \quad 0 \quad 0]^T = [\sigma_x \quad \sigma_y \quad 0 \quad 0 \quad 0 \quad 0]^T \quad 4-18$$

Where σ_x and σ_y are the principal stress directions for the given element in the defined set. The in-plane and all shear stress terms are not defined per the modelling assumptions.

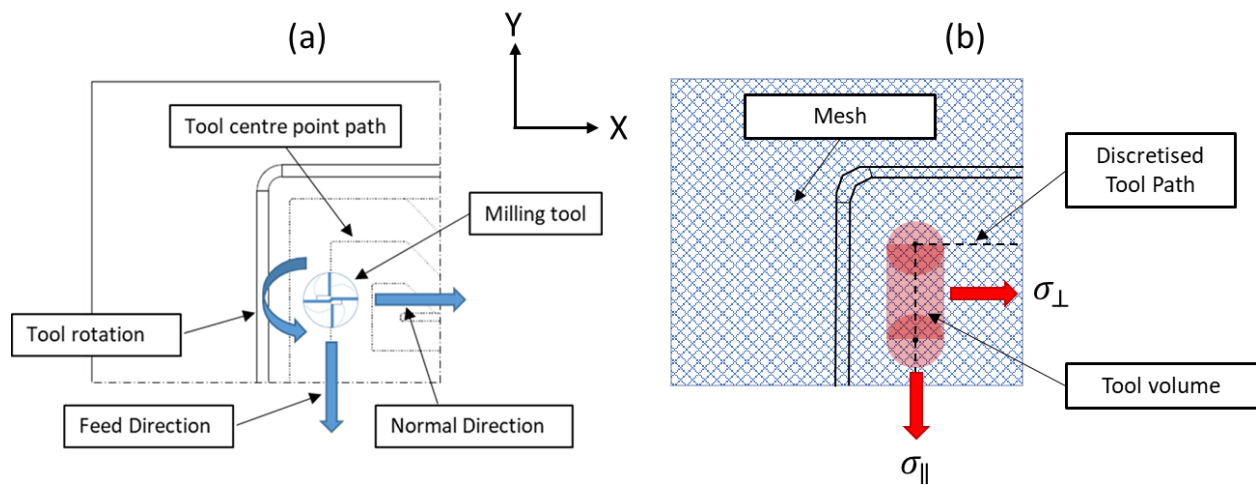


Figure 4-19: Application of MIRS as a function of the tool path progression

After the directionality of the MIRS application is determined, the MIRS value applied to the integration points through the depth of the boundary layer is defined using the sinusoidal decay function proposed by Ulutan [124] (see section 2.6.2.1 for more detail) fitted to the experimentally determined data conducted as part of the work undertaken. As per the work of Ulutan the particle swarm optimisation was utilised to condition the curve to the experimental data using regression principles, calculated using MATLAB [163]. The UMAT calculates the stress tensor to be applied to the boundary layer element integration points for a given machining process based on the assigned predefined field value of the current element for stress tensor orientation and the depth of the integration point from the 'machined' surface as illustrated in Figure 4-20. Each second-order wedge element uses 9 integration points for stress/displacement calculations and therefore provides a greater resolution of the MIRS than discretising

the MIRS curve as representative mean values in whole boundary layer elements as proposed by Dreier [150].

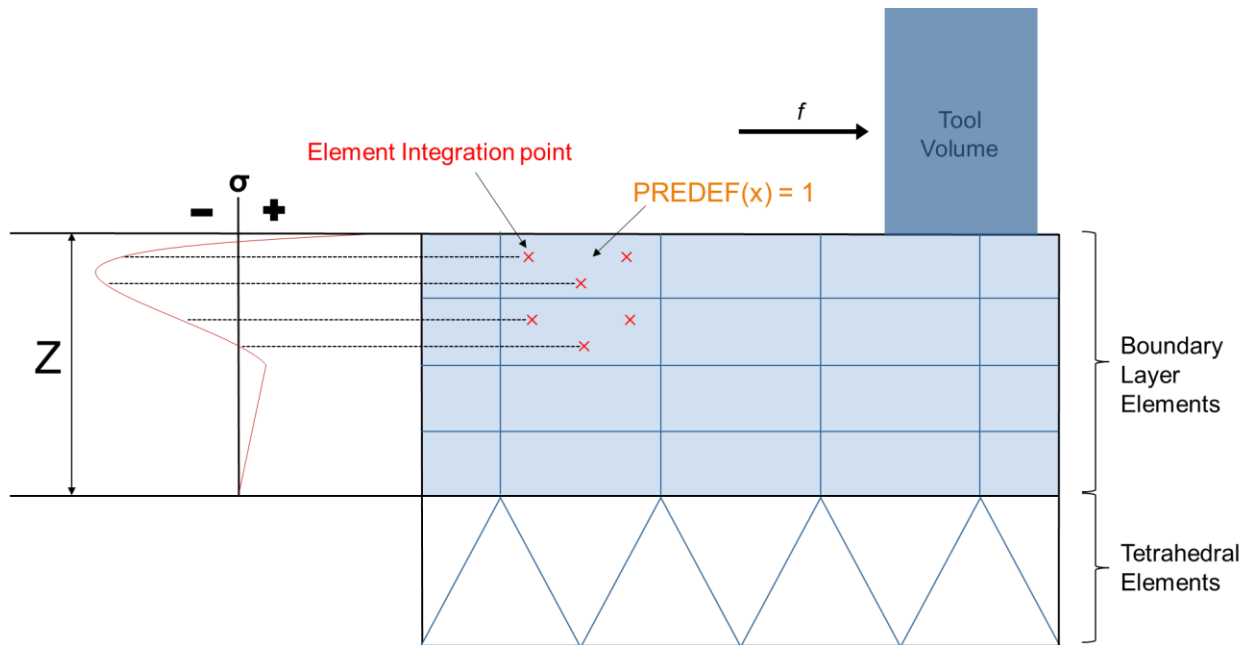


Figure 4-20: Assignment of the MIRS in the boundary layer

4.3.3. Execution of ABAQUS\standard

The process flow of ABAQUS\standard and the inclusion of utilised keywords and user subroutines is given in Figure 4-21. The SIGINI user subroutine is called only for the initial bulk stress analysis as shown in Figure 4-16. The initial conditions are used to reset the field variables used in the tool path identification Python script. The map solution is also called at the start of the analysis step. The UMAT is called at the stress calculation step of the increment for each integration material point during the analysis. The UMAT calculates the stress state according to the calculated strain in the model. The MIRS section of the UMAT is only called at a specified step and increment during the analysis as discussed at the start of this section.

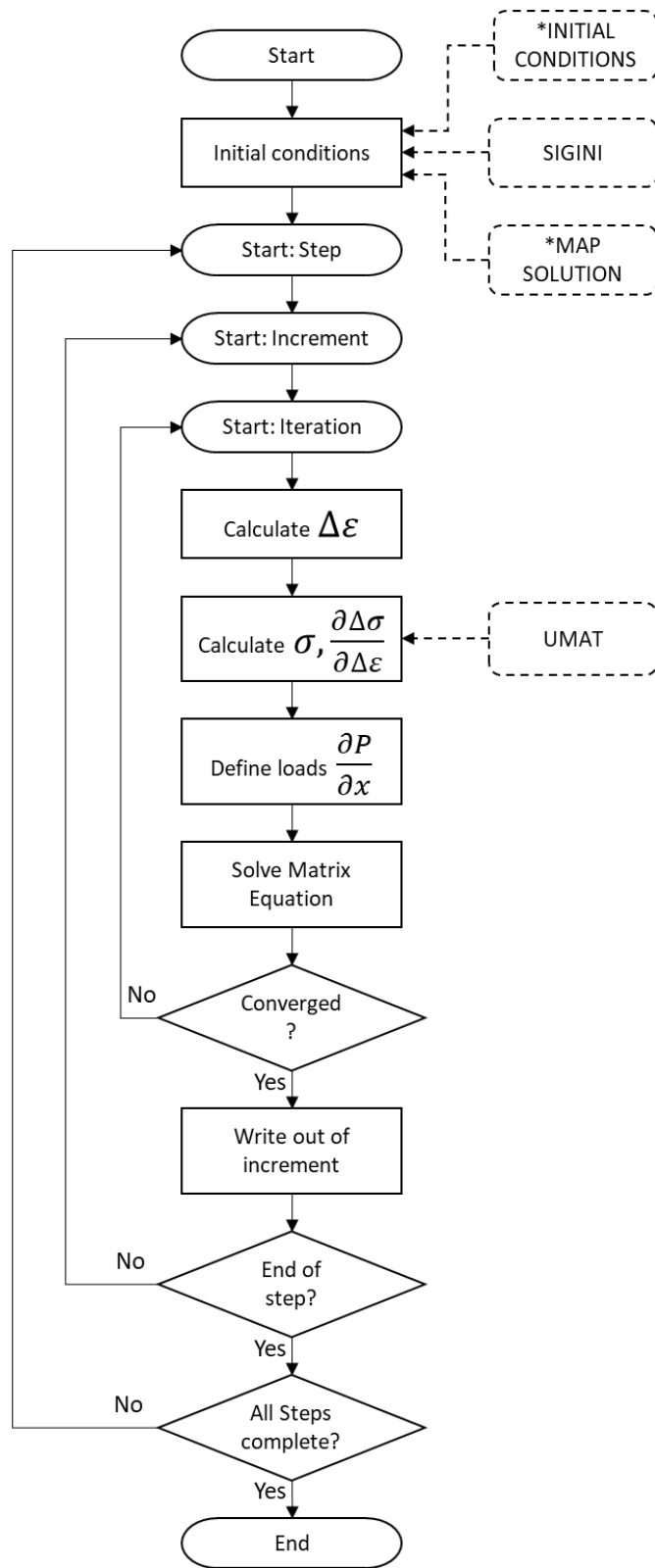


Figure 4-21: Application of user subroutines and key words in ABAQUS/standard execution

4.3.4. Inter-stage fixture modelling

In order to produce required design features on complex large aero-structural components, it is typically necessary to employ multiple machining stages for productivity, quality and access considerations. Machining stages are characterised by the features machined for a given work-holding configuration of the machined component in its current state of manufacture. Due to material removal across each machining stage, various fixture and location methods must be employed to suit the changing component structure condition. The fixture method must also constrain any distortion of the component during machining. After clamp release, the external forces resisting the part distortion are removed, and the part deforms due to the internal residual stresses reaching a new equilibrium state. The amount of distortion is a function of the magnitude and distribution of the inherent and machining-induced residual stress imbalance and the structural rigidity of the component. Furthermore, for subsequent machining stages, the fixture must remove any component deformation by introducing clamping force that elastically deforms the part back into the undeformed shape. Figure 4-22 illustrates a simple component machining process that employs two stages of machining where:

- (a) The part is located and constrained by side clamps in the stage 1 setup.
- (b) The part is machined in stage 1 (machine volume area identified by red diagonal stripes).
- (c) Stage 1 clamping is removed, and the part is allowed to deform (inter-process distortion).
- (d) The part is flipped and set up for stage 2 machining.
- (e) Stage 2 clamping was applied, and the part is forced back into its undeformed configuration and machined.
- (f) Stage 2 clamping is released, and the part can deform, revealing the final component's geometrical form and distortion response.

So that the modelling methodology can capture inter-process distortion-related quality issues, the release and re-establishment of boundary and contact conditions is conducted to simulate the inter-process fixture change as described previously. To simulate the in-process clamping effects, the 'machining' Python script re-establishes the boundary and contact conditions for each given machining step and adds a 'clamp release' analysis step for the last machining step of any given machining stage, such that all previous boundary conditions are deactivated and replaced by 3-2-1 constraint. The 3-2-1 constraint allows for the free distortion of the model without rigid body motion.

The specific application of the mentioned boundary conditions are discussed in more detail, with reference to the distortion validation machining trials in Chapter 7.

The Python 'Inter-stage script' has been developed to simulate the updating of the clamping method between machining stages. The script introduces boundary and contact conditions depending on the fixture solution for the current machining stage. In this work, a combination of surface node sets for the application of boundary conditions and the use of rigid bodies have been applied to simulate the clamping setups for various machining stages.

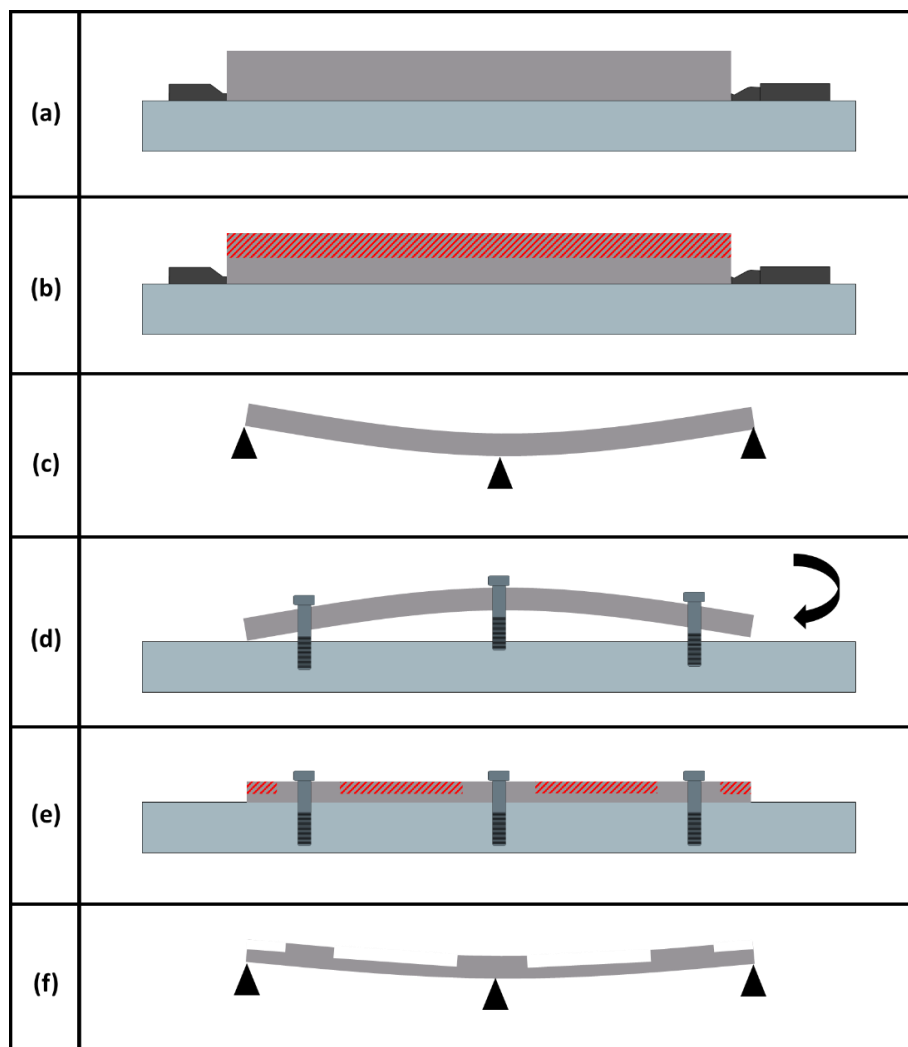


Figure 4-22: Process of inter-stage fixturing

4.3.5. Results post-processing

Coordinate measurement machines (CMM) are prominent in companies that manufacture aerospace components. CMM are highly accurate metrology equipment utilised to check part geometric quality in an automated fashion, typically through touch probe discrete contact stylus to general surface point data for machined components. The generated point maps are assessed against CAD models, geometric dimensioning and tolerancing (GD&T) standards, or to provide information about specific features in isolation. It is possible to capture part distortion of aero structural components by this measurement technique. In this work, the use of CMM data to evaluate distortion simulation results is proposed.

To generate comparative distortion data in a semi-automated fashion, a 'post-processor' Python script is developed to extract key information from the output database ABAQUS file (.odb) such that comparison can be made to the discrete CMM data and the simulation results. The script is defined to extract nodal displacements for defined nodal sets that represent the location of the discrete CMM distortion inspection points in reality. The nodal displacements for the features of interest are exported as tabular data and compared against the CMM data in secondary software (i.e., Excel, MatLab).

4.4. Concluding statements

This chapter outlines the distortion modelling method established to account for the influence of bulk and machining-induced residual stresses on inter-process and post-process distortion to address the gap in the current state-of-art modelling methodologies. The chapter is divided into three sections. The general finite element method and the formula for defining the system's mechanics concerning the machining-induced and bulk sources of residual stress are addressed in the first section.

Next, the distortion modelling procedure is covered. Consideration is given to applying bulk residual stresses to an initial mesh configuration through the SIGINI user subroutine. Then the numerical multi-step material removal process in ABAQUS is discussed. Following this, the tool path utility program and identifying boundary-layer elements for stress mapping are covered. The material definition is then covered. Lastly, the virtual representation of the machining fixture by model boundary conditions is deliberated in the section, including the boundary and contact conditions utilised under this modelling approach.

The third section of the chapter covers the execution methods for the proposed simulation approach. First, the semi-automated modelling procedure using Python and ABAQUS is covered. The developed control script manages the submission of ABAQUS Python scripts and analysis jobs submitted with user subroutines to achieve the multi-step simulation procedure in a semi-automated manner. Next, the stress field mapping between meshes for material removal simulation is discussed. Then detail is given for the machining-induced residual stress application procedure, where the boundary-layer element sets created using the tool path utility program are assigned stress tensor values, at integration points, according to the prevailing tool path direction. The execution routine for the ABAQUS/STANARD analysis is addressed before covering the boundary condition generation during the modelling process and generation of node sets for comparison to distortion measurement data, both executable by Python scripting.

The proposed novel modelling method addresses the shortcomings of other methods to date through the semi-automated multi-step modelling approach and inclusion of the bulk and machining-induced residual stresses. With this approach, it is theoretically possible to simulate the machining component quality issues associated with over/undercutting.

5 Experimental methods

5.1 Experimental Rationale

As set out in Chapter 3, the experimental objectives for this thesis include the investigation of machining-related residual stress and part distortion by way of three experimental trial objectives:

1. To investigate the influence of machining sequencing and strategy on induced residual stress formation.
2. To produce initial bulk and machining-induced residual stress as input to the distortion FE model.
3. To produce metrology data to validate the FE distortion modelling methodology and machining sequencing hypothesis.

The following sections will discuss the rationale behind each trial objective in detail.

5.1.1 Influence of Sequencing and Strategy on Machining-induced Residual Stress

CAD/CAM allows for creation of complex CNC milling tool paths to achieve process productivity and quality in machined components. The influence of machining parameter selection on machining-induced residual stresses in aerospace 7000 series aluminium is a well-researched area [26], [27], [77], [78]. From the literature review, it appears less effort has been placed on understanding the influence of machining sequence and strategy on machining-induced residual stress, including possible evolution of MIRS in sequential machining operations and variation in the depth and magnitude of MIRS across machined surfaces due to local cutting condition variations.

Sequential machining operations

In order to achieve final component geometry by machining, it is typical that several machining passes will be made to generate the final cut surface condition. Figure 5-1 illustrates a multiple depth of cut (DoC) machining processes where the red zones indicate roughing passes, and the blue zones indicate finishing conditions. Roughing machining processes are associated with aggressive machining conditions where the primary objective is efficient material removal. Finishing machining processes are typified by lower feed rates and DoC to generate suitable surface conditions. Therefore, a region of the part may be subjected to multiple machining passes of varying process conditions. The review of the literature identified research undertaken to investigate the impact of sequential machining operations on MIRS formation through experimental and FEM work. However, it seems there is not a shared consensus on the importance of sequential machining operation on the final surface MIRS condition. Some researchers

suggest that due to the complex interaction of the plastic deformation and material behaviour, the previous machining passes influence the MIRS condition below the cut surface of the last machining pass [102], [164]. Other researchers only deem it necessary to characterise the stress state from the final machining pass due to the depth of the influenced layer being smaller than the depth of cut [100].

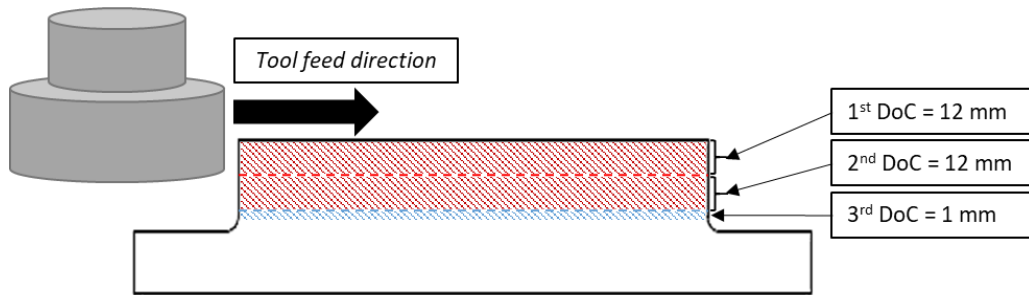


Figure 5-1: Example of sequential DoC machining

It may be a valid assumption when considering MIRS formation in machined aluminium components not to consider the previous passes due to the shallow affected depth compared to the axial depth of cut, as illustrated in Figure 5-2, where the DoC is greater than the machining-induced stress layer depth identified by the red hatch zone. However, there is not enough data to suggest either way categorically.

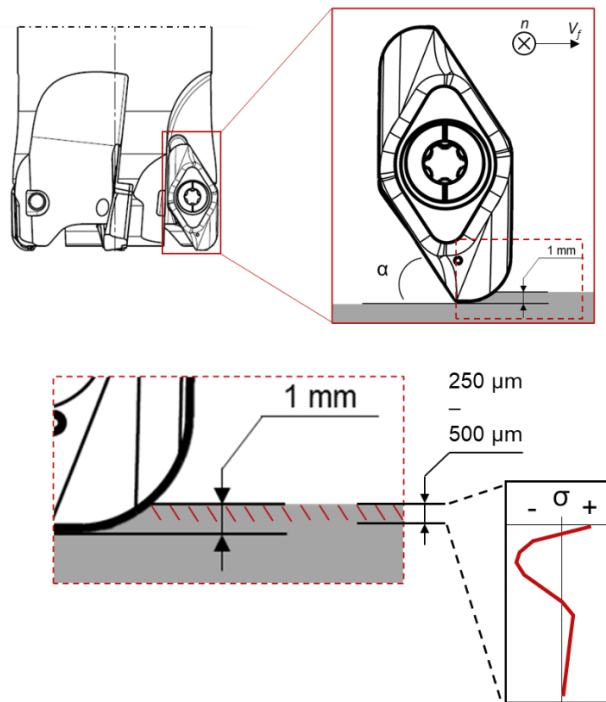


Figure 5-2: Depth of cut and MIRS affected zone

Furthermore, most research only focuses on one tool/workpiece contact condition and fixed machining parameters whilst altering the DoC. Few researchers have looked at the interaction between roughing and finishing passes. Some have looked at this in turning of steel [102], but not milling of aluminium. There is limited experimental data reporting the impact of sequential machining passes on final surface condition in 7050 aluminium and subsequent component distortion. It is, therefore, an important consideration to determine whether previous cutting passes impact the final machining stress state and if this influence needs to be accounted for in the distortion modelling approach.

Impact of local cutting conditions variations across a tool path

It is possible to utilise various milling tool path strategies when planning the machining of aerospace structural components. Typically, the governing factors for programmers when determining tool path choice are the structure's geometry to be machined, productivity and cutting force management. The research has shown that tool path selection also impacts final distortion due to the directionality of the applied MIRS [149], [151], [155]. However, what is not well understood is the influence of local variations in the cutting conditions driven by machining tool path choice on machining-induced residual stresses.

The primary and tertiary cutting zones generate MIRS by severe plastic deformation and thermal loading. The magnitude and depth of MIRS in high-strength aluminium is governed strongly by machining parameters, coolant medium and geometric design of the cutting tool [78]. Machining parameters are typically set as a constant value where cutting speed is given as:

$$V_c = \frac{\pi \times D \times n}{1000} \tag{5-1}$$

And feed rate by:

$$V_f = f_z \times n \times z_{teeth} \tag{5-2}$$

Where, D = cutting tool diameter (mm), n = spindle speed (RPM), f_z = feed per tooth (mm) and z_{eff} = effective number of cutting teeth. The influence of the cutting parameters on MIRS is linked by their effect on the mechanical and thermal loading. The variation of feed rate (V_f) for example alters the undeformed chip thickness and thus the amount of material to be removed, increasing the load on the workpiece material [152]. Chip thickness (h_{ex}) is a better indicator of mechanical load potential between the tool and workpiece than feed rate and is a function of the DoC, feed rate and tool geometry. Figure 5-3 illustrates the influence of radial engagement and feed rate of the max chip thickness where; EA =

engagement angle and a_e = radial engagement. In peripheral milling where the tool is engaged at 50% or above its effective diameter, the chip thickness is equal to the feed rate as shown Figure 5-3 (a). When the engagement drops below 50% chip thinning occurs where feed rate is no longer equivalent to the max chip thickness. In order to maintain chip thickness, the feed rate is increased as depicted in Figure 5-3 (c).

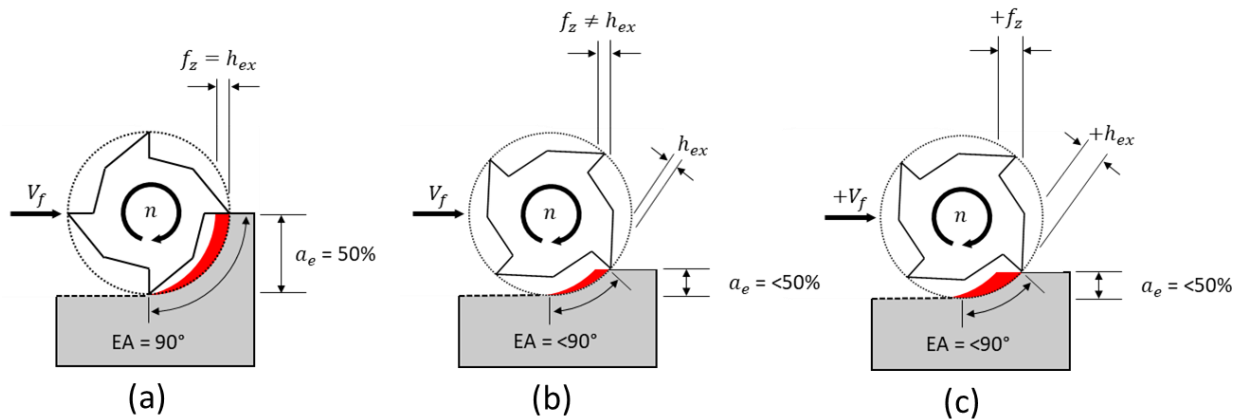


Figure 5-3: Chip thinning effect: (a) at 50% tool diameter engagement; (b) <50% tool engagement; and (c) increased feed rate to maintain chip load

Even for machining processes programmed with constant feed rate the undeformed chip thickness changes due to localised cutter workpiece engagement conditions. Figure 5-4 shows different tool workpiece engagement angle for (a) straight line cutting and (b) corner cutting. This increase in the engagement angles is associated with an increase in chip load and therefore cutting forces. For complex geometries that are present in aero structural components changing tool engagement with the workpiece is common.

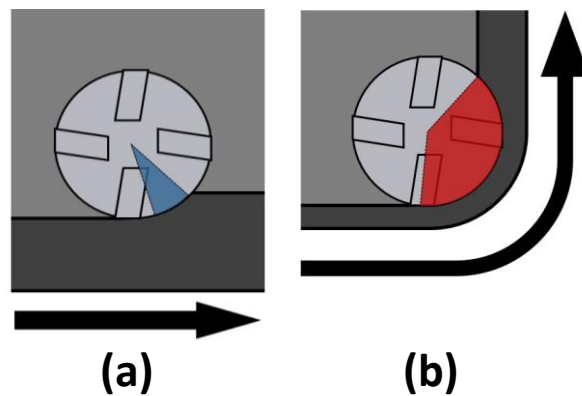


Figure 5-4: Variable cutter engagement: (a) straight line cutting; and (b) corner cutting

Pocket features can be found across various aerospace component designs and give rise to variable cutter contact conditions. Pocket feature designs include various shapes and depths but can be collectively defined as cavity regions within the primary geometry of a component and bounded by either open or closed boundaries. Pockets are typically machined using a combination of slotting and peripheral milling. The tool paths utilised are pocket geometry dependant. However, for a conventional cuboidal pocket (Figure 5-5) standard tool paths include unidirectional, zigzag and helical spiral as shown in Figure 5-6. These types of tool path have been used in machining of aluminium pockets in industry due to the ability to achieve high material removal rates and therefore, high productivity.

Dynamic milling is a relatively newer type of tool path that is fast being adopted by the industry. The machining strategy makes use of the phenomena of chip thinning (see Figure 5-3) and consistent effective radial engagement of cut to maintain consistent loading between the workpiece and cutting tool through the cutting process. A smaller radial depth of cut is typically taken that allows for a more considerable axial depth of cut to be exploited and therefore material removal rates are maintained comparable with traditional high radial low axial cutter/workpiece contact conditions. This benefits tool wear rates by maintaining consistent thermo-mechanical loading cycles and also results in more constant cutting force magnitudes.

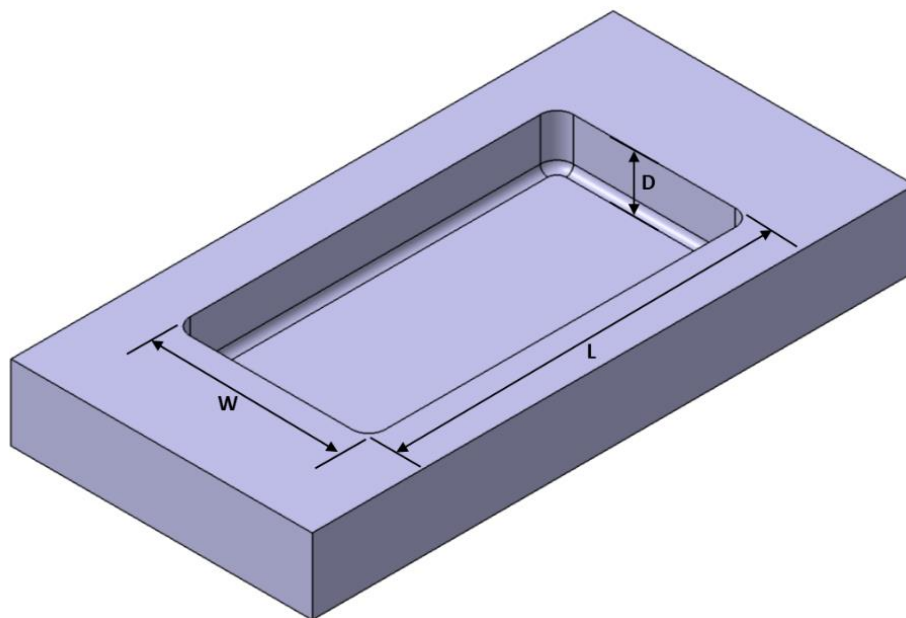


Figure 5-5: Pocket geometry where; W = width, L = Length & D = Depth

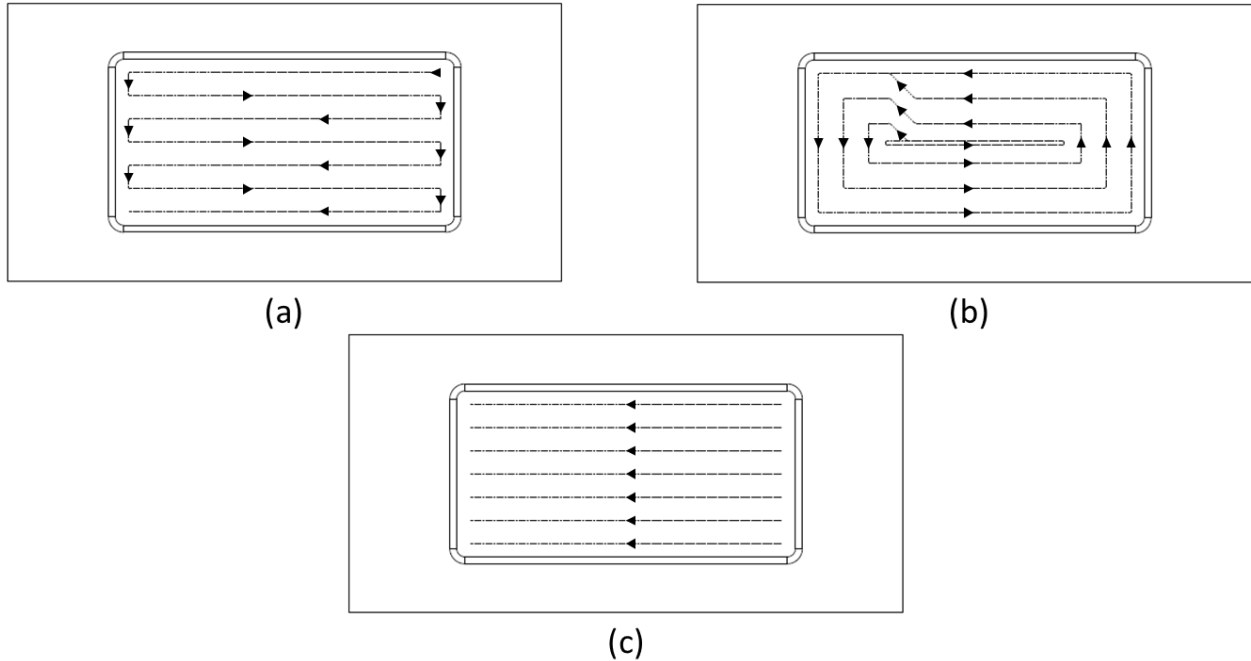


Figure 5-6: Conventional pocket milling tool paths; (a) zigzag, (b) helical spiral & (c) unidirectional.

Tool wear rates are less of a consideration in aluminium machining compared with harder-to-cut materials such as titanium, as tool life for carbide tools can be in the range of hundreds of minutes for processes without dynamic instability (chatter). However, managing the surface integrity and induced residual stress is important for fatigue performance [165] and residual stress-related distortion [96] in machined components. Therefore, a section of the experimental trials is given to developing an understanding on the impact of tool path strategy selection on milling machining process-induced residual stresses through:

1. Comparing machining-induced residual stresses imparted by various pocket milling strategies.
2. Developing an understanding of how machining-induced stresses form along selected tool path strategies.

5.1.2 Bulk and machining-induced residual stress measurement

The distortion modelling methodology requires bulk and machining-induced residual stress in the form of fitted experimental data as input to the simulation. Machining-induced stresses are produced in machined test coupons and analysed using semi-destructive measurement techniques. The machining conditions used to generate the test coupons are also used to generate distortion demonstrator test pieces and are representative of those used in industrial practice. This is achieved through replicating tooling, machining parameters and cooling conditions. Therefore, it can be assumed the measured machining-induced stresses are the same as those experienced in the distortion demonstrator test pieces and machined

aerospace components. Similarly, bulk residual stress coupons were generated for destructive measurement techniques. The coupons are generated in the same mother plate as the billets for the distortion demonstrator coupons such that the bulk stresses should be consistent. The material used in the trials is aerospace-grade aluminium roll plate product used in the manufacture of aero components. The rolled plates are generated using conventional aerospace treatment cycles to produce the required temper. Therefore, the generated bulk stresses are also likely consistent with those found in industrial practice.

5.1.3 Metrology data to validate the distortion modelling methodology and study machining sequencing

In order to validate the distortion modelling methodology and study the machining strategy's effect on part distortions, an experimental test demonstrator component is manufactured and inspected to capture post-machining distortion. The component was designed to share features consistent with aerospace wing structural components. Another design consideration was to generate a component that is susceptible to residual stress-related distortion such that the measured deformation is disenable from the measurement error associated with the inspection technique. As previously discussed, the use of CMM in metrology inspection of aerospace component features is well utilised in the industry and as such, is used to inspect the distortion of the machined demonstrator components.

5.2 Influence of sequential machining operations on machining-induced residual stress

Machining trials employing variable roughing strategies have been conducted to produce coupons for residual stress analysis to study the effect of sequential machining operations on MIRS. The trials aimed to study the effect of sequential face milling passes, of variable axial depth and machining parameters, on the MIRS state after a consistent finish machining pass.

5.2.1 Material

All coupons are aerospace-grade Aluminium 7050 T7651 alloy, typically used to manufacture aircraft wing structures. The material has good strength-to-weight characteristics whilst having low internal bulk residual stresses. The plates are cast and hot rolled down to the final thickness gauge, followed by homogenisation, quenching, stretching and final natural and artificial ageing. This material class is mainly provided at two temper conditions: T7451 and T7651, which are the over-aged and peak-aged temper

conditions. In the reported trials, peak-aged condition plates in the T7651 temper have been used. General material data is given in Table 5-1. Alloying composition weight % is provided below in Table 5-1.

Table 5-1: 7050 T7651 material properties

Ultimate tensile stress	Yield Strength	Density	Modulus of elasticity	Poisson's Ratio
552 MPa	489 MPa	2.7 g/cm ²	70,300 MPa	0.33

Table 5-2: 7050 T7651 alloy composition

Si	Fe	Cu	Mn	Mg	Cr	Zn	Ti	Zr
0.12%	0.15%	2.0 - 2.6%	0.1%	1.9 – 2.6%	0.04%	5.7 – 6.7%	0.06%	0.08 – 0.15%

5.2.2 Equipment

The stress coupon face milling machining trials were conducted on the Starrag Technology 'White tail' research and development NC machining centre with a Siemens 840D controller. The nominal spindle power for the White tail NC centre is 120 kW. Max torque is 83 Nm max. Max spindle speed is equal to 30,000 RPM. The spindle accepts HSK 63/80 tool holders. The machining utilises minimum quantity lubrication (MQL) system for heat management and was used across trials. A combination of roughing face milling passes of variable axial DoC and finishing face milling passes with a fixed axial DoC were carried out with industry representative machining parameters and strategies.

Face milling roughing operations were carried out using a Mitsubishi ADX7000 Monobloc face mill with XDGX227050PDFR-GL inserts. Finishing face milling operations were undertaken using an Iscar HSM90S FAL Monobloc face mill with HSM90S D50-4L126HSK-MQ-14 inserts.

Table 5-3 provides relevant information for both face mills. Table 5-4 contains insert geometry information which was consistent for both inserts used. The machining parameters used for each tool are given in Table 5-5 and Table 5-6, respectively. To limit the impact of tool wear on the induced stresses, the carbide inserts were changed every coupon for TPC1 and every other coupon for TPC2.

Table 5-3: Face milling cutters

	Inserts	No. teeth	Diameter	A_p Max
mitsubishi ADX7000- D50-126	XDGX22705 OPDFR-GL	3	50 mm	21 mm
ISCAR HSM90S D50- 4L126HSK- MQ-14	HSM90S APCR 140550R-P	4	50 mm	10 mm

Table 5-4: Insert geometry

clearance angle major	cutting edge angle major	Rake angle	Clearance angle	Cutting edge radius	corner radius (mm)
20°	30°	30°	10°	<3µm	5

Table 5-5: Mitsubishi tool machining parameters

n - Spindle speed	F_z - Feed rate	a_e Max - Radial DoC	a_p Max – axial DoC
2100 RPM	0.1 mm	30 mm	Variable

Table 5-6: Iscar tool machining parameters

n - Spindle speed	F_z - Feed rate	a_e Max - Radial DoC	a_p Max – axial DoC
2100 RPM	0.15 mm	30 mm	Variable

5.2.3 Test Piece design

The machining-induced stress coupon design is shown in Figure 5-7. The max dimensions of the test pieces are 260 X 200 X 50 mm and were extracted from 620 X 410 X 50 mm rolled plates by band saw. As per reference [78], the test pieces are designed to remain thick after machining so that distortion which may impact the machined surface stresses measured, is minimised. The test pieces were prepared using a combination of profile milling and to drill through holes to allow rigid bolting of the test piece to the machine bed. The test pieces have been extracted from the rolled plate in line with the longitudinal rolling direction. Work holding during machining was achieved using four off M12 bolts, as seen in Figure 5-8 (b). The bolting was carried out in a crisscross sequence for each test piece, as shown in Figure 5-8 (a). Each bolt was torqued to 81 Nm with a calibrated torque wrench.

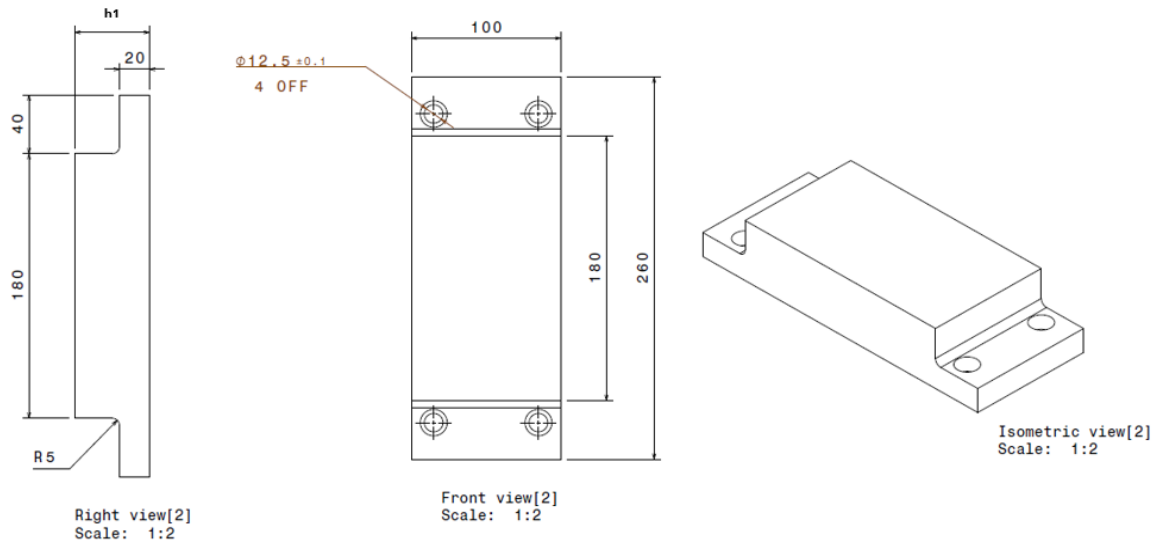


Figure 5-7: TPC1 test piece design

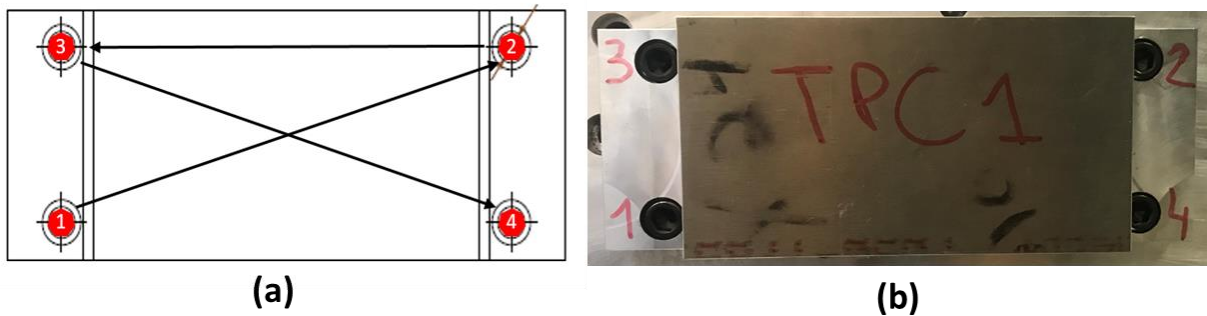


Figure 5-8: TPC1 bolting sequence diagram (a) and bolted to machine bed (b)

5.2.4 Test design

Five tests were conducted with the testing configuration outlined in Table 5-7. A zigzag milling tool path was consistently used across all test configurations, as shown in Figure 5-9. This type of tool path is typical of the strategy used to manufacture flat datum surfaces for aero-structural components. Test number 1 consisted of one machining DoC to generate machining-induced stress data for the roughing pass. Tests 2 to 5 consisted of variable roughing machining passes followed by a single machining pass to determine the influence of variable roughing strategy on the final MIRS state in the final surface. Additionally, for TPC1-4, additional ICHD measurements were made to make an understanding of the repeatability of the measurement procedure.

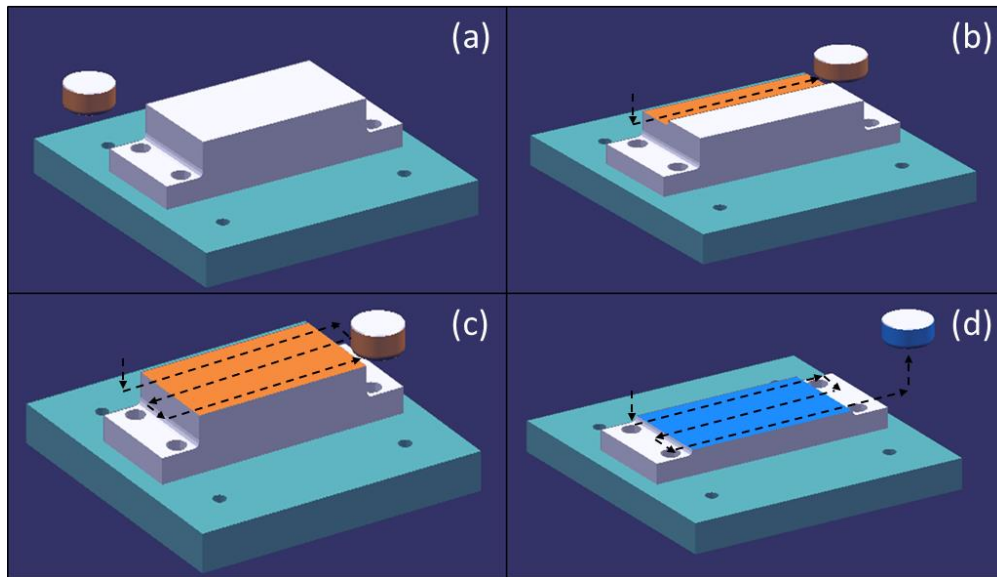


Figure 5-9: Sequential machining coupon (a) initial configuration (b) first roughing pass (c) n roughing pass (d) after finish machining

Table 5-7: TPC1 Test Matrix

Test #	Test ID.	R1 DoC (mm)	R2 DoC (mm)	R3 DoC (mm)	R4 DoC (mm)	F1 DoC (mm)
1	TPC1-3	12	-	-	-	-
2	TPC1-4	6	6	6	6	1
3	TPC1-5	12	12	-	-	1
4	TPC1-6	12	6	6	-	1
5	TPC1-7	9	6	6	3	1

residual stress state at the centre point of the drilled hole was developed by Kirsch [168] and can be resolved to give equation 5-3.

$$\varepsilon_r = \bar{A}(\sigma_{max} + \sigma_{min}) + \bar{B}(\sigma_{max} - \sigma_{min}) \cos 2\beta \quad 5-3$$

Where:

- σ_{max} & σ_{min} are the max and minimum principal stresses
- \bar{A} & \bar{B} are calibration constants
- β is the angle between the max principal stress and the axis of the strain gauge

Figure 5-11 shows how the orientation of a 45° strain gauge is set up and how it relates to the measured relieved strain.

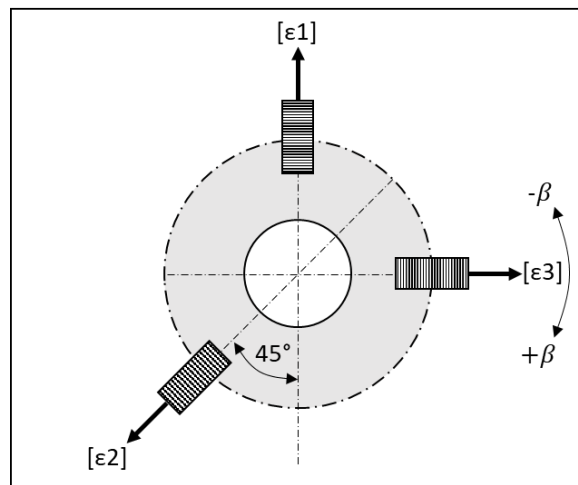


Figure 5-11: 45° Strain gauge rosette schematic with respects to the relieved strain orientation

The three measured relaxed strains (as seen in Figure 5-11) can be related to the Cartesian stress components and calibration constants, defined in matrix form as defined in equation 5-4.

$$\begin{bmatrix} \bar{A} + \bar{B} & 0 & \bar{A} - \bar{B} \\ \bar{A} & -2\bar{B} & \bar{A} \\ \bar{A} - \bar{B} & 0 & \bar{A} + \bar{B} \end{bmatrix} \begin{bmatrix} \sigma_1 \\ \tau_{13} \\ \sigma_3 \end{bmatrix} = \begin{bmatrix} \varepsilon_1 \\ \varepsilon_2 \\ \varepsilon_3 \end{bmatrix} \quad 5-4$$

Where σ_1 , τ_{13} & σ_3 are the residual stresses that relate to the relieved strains ε_1 , ε_2 & ε_3 respectively. A & B refer to the infinitesimal strains devised by the Kirsch solution [168] and are governed by strain gauge geometry, material elastic properties and drilled hole radius. In actuality the measured relieved strains

are variable over the finite gauge area. Therefore, coefficients A & B must be integrated over the gauge area becoming \bar{A} & \bar{B} . For a through hole thin plate solution \bar{A} & \bar{B} can be derived analytically [167]. For blind hole \bar{A} & \bar{B} must be determined empirically by performing hole drilling measurements on a uniaxially loaded sample with a known stress distribution. To remove the material dependency Schajer [169] introduced coefficients \bar{a} and \bar{b} as defined in equations 5-5 & 5-6.

$$\bar{a} = \frac{2E\bar{A}}{(1 + \nu)} \quad 5-5$$

$$\bar{b} = 2E\bar{B} \quad 5-6$$

It stands that for ease of analysis, the stress-strain relationship given in matrix 5-4 can be decoupled to provide the transformation stress variables as detailed in equations 5-7, 5-8 and 5-9 below.

$$P(H) = \frac{(\sigma_3(H) + \sigma_1(H))}{2} \quad 5-7$$

$$Q(H) = \frac{(\sigma_3(H) - \sigma_1(H))}{2} \quad 5-8$$

$$T(H) = \tau_{13} \quad 5-9$$

Where $P(H)$ is the mean 'pressure' of the residual stress evaluated at a distance H (nondimensional depth from the surface) on a plane parallel to the surface. $Q(H)$ and $T(H)$ refer to the shear components of the 'pressure' stress. Likewise the relieved strains can also be expressed in the form of transformed 'volumetric' strain variables, provided in equations 5-10, 5-11 and 5-12 below.

$$p(h) = \frac{\varepsilon_3(h) + \varepsilon_1(h)}{2} \quad 5-10$$

$$q(h) = \frac{\varepsilon_3(h) - \varepsilon_1(h)}{2} \quad 5-11$$

$$t(h) = \frac{\varepsilon_3(h) + \varepsilon_1(h) - 2\varepsilon_2(h)}{2} \quad 5-12$$

Where $p(h)$ is the 'volumetric' strain determined by the relaxed strains recorded by the gauges at h (nondimensional hole depth). $q(h)$ and $t(h)$ are the shear strain equivalent. The transformation allows

for the individual strains and stresses to be evaluated individually. Therefore the integral method detailed by Schajer [169] can be defined for $p(h)$ as given by equation 5-13.

$$p(h) = \frac{1 + \nu}{E} \int_{h_0}^h \hat{A}(H, h) P(H) dH \quad 0 \leq H \leq h \quad 5-13$$

Where $\hat{A}(H, h)$ is the strain relaxation per unit depth caused by a unit stress at depth H when the hole is h deep. $\hat{A}(H, h)$ is determined using finite element modelling [170] and $p(h)$ through strain gauge measurements. Therefore $P(H)$ can be determined by solving the integral equation 5-13. Where the strain measurements are made at n increments to hole depths of h_i then equation 5-13 can be written in the discrete form defined by equation 5-14.

$$\sum_{j=1}^{j=i} \bar{a}_{ij} P_j = \frac{E}{1 + \nu} p_i \quad 1 \leq j \leq i \leq n \quad 5-14$$

Where:

- \bar{a}_{ij} = strain relaxation due to a unit stress within increment j of a hole i increments deep
- P_j = equivalent uniform stress within the j th hole depth increment
- p_i = measured strain relaxation after the i th hole depth increment
- n = number of hole depth increments

The relationship between the coefficient and strain relaxation function is given by equation 5-15.

$$\bar{a}_{ij} = \int_{H_{j-1}}^{H_j} \hat{A}(H, h_i) dH \quad 5-15$$

Then the discrete equation relating strain relaxation coefficient, equivalent 'pressure' stress and 'volumetric' strain can be written in matrix form as defined in equations 5-16, 5-17 and 5-18.

$$\bar{\mathbf{a}}\mathbf{P} = \frac{E\nu}{(1 + \nu)} \mathbf{p} \quad 5-16$$

$$\bar{\mathbf{b}}\mathbf{Q} = E\mathbf{q} \quad 5-17$$

$$\bar{\mathbf{b}}\mathbf{T} = E\mathbf{t} \quad 5-18$$

By resolving the transformed stresses the Cartesian stress components can be determined as defined 5-19, 5-20 and 5-21:

$$\sigma_1(H) = P(H) - Q(H) \quad 5-19$$

$$\sigma_3(H) = P(H) + Q(H) \quad 5-20$$

$$\tau_{13}(H) = T(H) \quad 5-21$$

Machining induced stresses that are generated by milling of aluminium alloys typically form near-surface up to depths of 500 μm . The strain gauge rosettes were orientated to record bi-directional strain relief so that stresses can be calculated in the direction of the tool feed (longitudinal) and normal to the tool feed direction (transverse).

The preparation of the surface was achieved by cleaning the surface with acetone followed by iterative applications of acid and neutraliser. Vishay Measurements Group Ltd strain gauge rosettes of type EA-06-031RE-120 have been used and the specifications are given in Figure 5-12. The back of the strain gauge was treated with a catalyst and appropriate time allowed for it to dry. Glue was applied to the back of the strain gauge and pressure applied with the gauge in situ to allow the product to cure. The gauges were connected to the strain recording system in a quarter Wheatstone bridge configuration. It is important to fixture the test piece in alignment with the drilling equipment during measurement without introducing additional external stresses from clamping, which could affect the measurement results. Support material was placed around the test piece as can be seen in Figure 5-13 (a) & (b). A numerically control orbital drill, as shown in Figure 5-13 (c), was utilised to remove material to predefined depths at which point the relaxed strain is measured. Post measurement the residual stresses over the depth of the drilled hole have been calculated using hole drilling software for depths given in Appendix A.

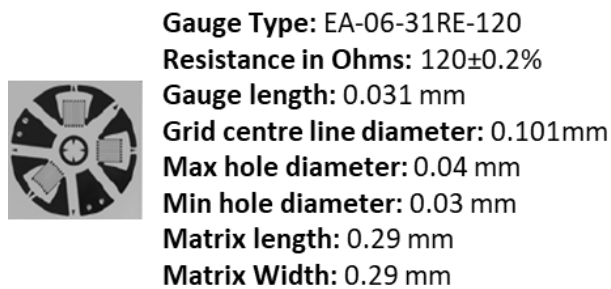


Figure 5-12: ICHD strain gauge specification

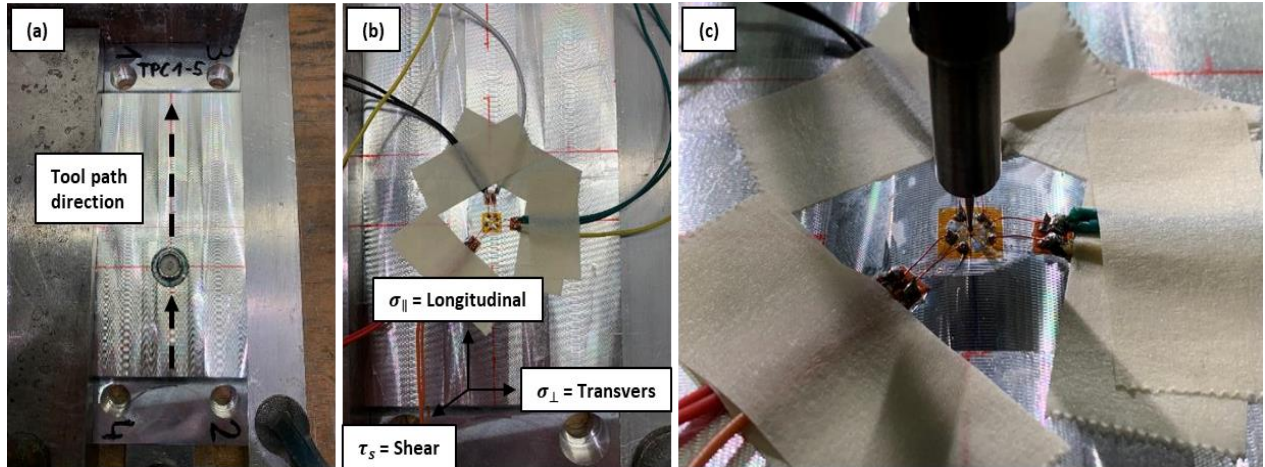


Figure 5-13: ICHD drilling: location of the measurement position (a), application/alignment of the strain gauge rosette (b), and locating the zero depth (c)

5.3 Influence of local cutting conditions variations on MIRS

To assess the influence of tool path strategy on MIRS variation across the machined component sub-surface layer a number of stress measurement coupons have been machined with variable process conditions. Four stress measurement coupons were machined in total as defined in Table 5-8. Two coupons were machined to the 'as roughed' condition where finish machining was not performed. This was to assess the depth and magnitude of MIRS imparted by each roughing operation. The roughing strategies used in these trials included a conventional spiral outward tool path (Figure 5- (a)) and a concentric circular dynamic tool path (Figure 5- (b)). The dynamic tool path poses an interesting tool path alternative to the conventional machining process as it is possible to limit and maintain consistent machining forces and therefore elicit a different MIRS condition in the machined component surface.

A further two test pieces were machined using the aforementioned conventional outward helical roughing process and finished using a conventional spiral outward tool path, as seen in Figure 5- (c). The amount of material left post-roughing for finishing operations was 1 mm all over. All tool paths were programmed in CATIA V5 advanced machining workbench.

Table 5-8: Machining coupon manufacture detail

Coupon ID No:	Roughing tool path:	Finished machined:
2	Concentric – Dynamic	No
4	Outward helical	No
7	Outward helical	Outward helical
8	Outward helical	Outward helical

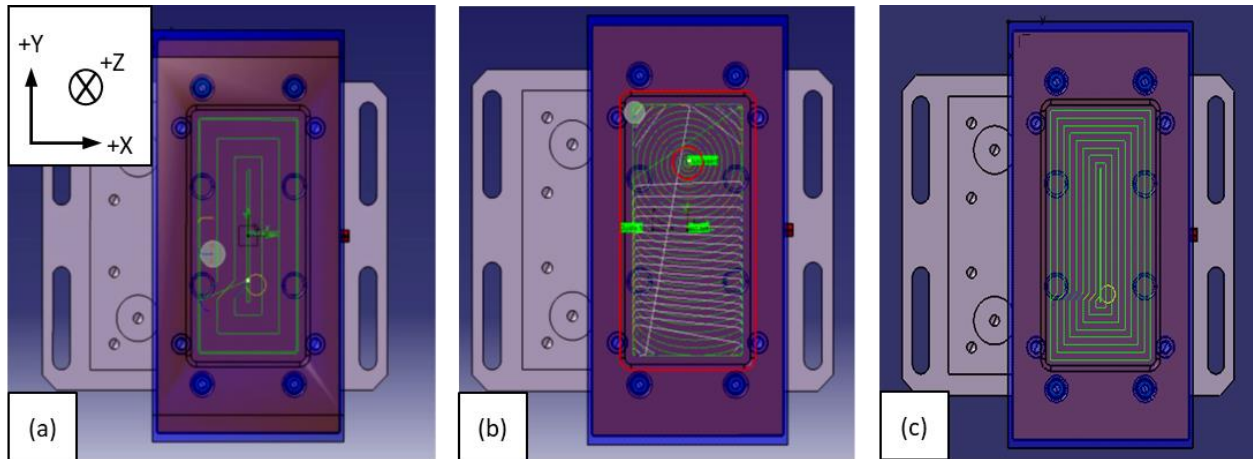


Figure 5-14: helical roughing (a) Dynamic Roughing (b) and helical finishing tool paths (c)

5.3.1 Material & test Piece design

Aluminium alloy 7010 T7651 billets were prepared to the stock condition before the experimental trials (see Figure 5-15). The pocket design is given in Figure 5-16. The material condition is the same as that given in section 5.2.1.

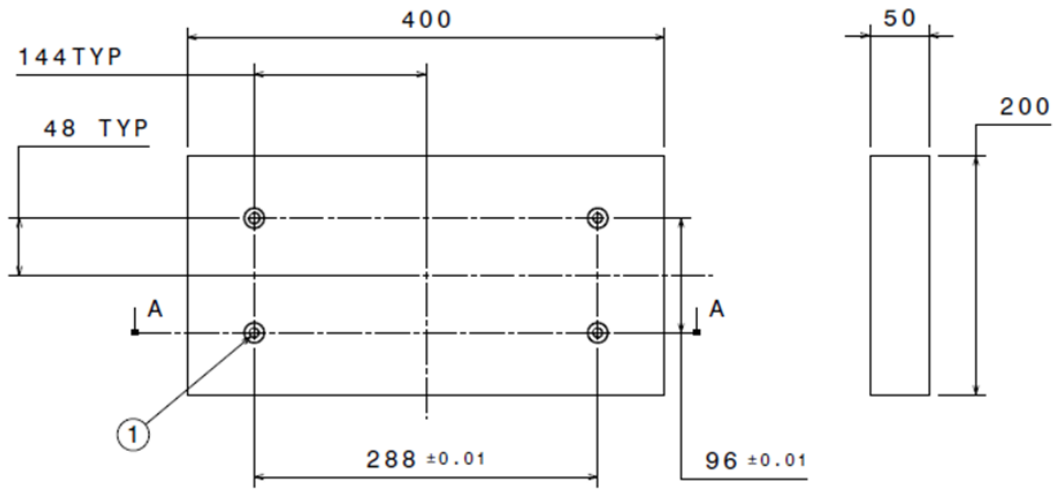


Figure 5-15: MIRS pocket coupon stock condition

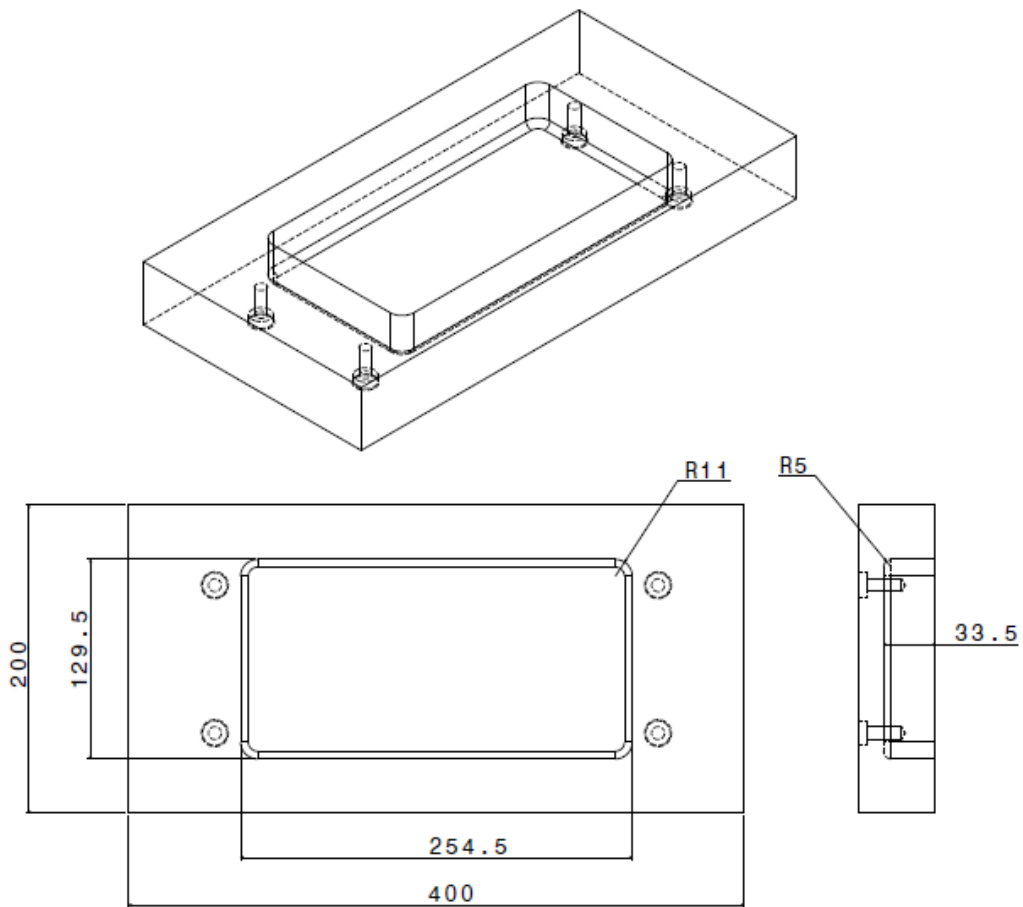


Figure 5-16: MIRS pocket coupon design

5.3.2 Equipment

The coupons were machined on a Starrag Eco-speed five-axis CNC machining centre. The Eco-speed's max spindle power is 120 kW with a max spindle speed of 30,000 rpm. MQL coolant delivery system is utilised and flow rate defined for each tool. Two standard carbide shoulder/slot milling cutting tools and one dynamic tool were used in the experimental trials. Walter solid carbide end mills MB265 (Figure 5-17 (b)) and MB266 tools (Figure 5-17 (c)) were used in the conventional roughing and finishing pocketing strategies, respectively. Kennametal Kor 5 dynamic milling cutter (Figure 5-17 (a)) was used in the trials for producing in the dynamic milling tool path coupons. The machining parameters used to all tools are displayed Table 5-9.

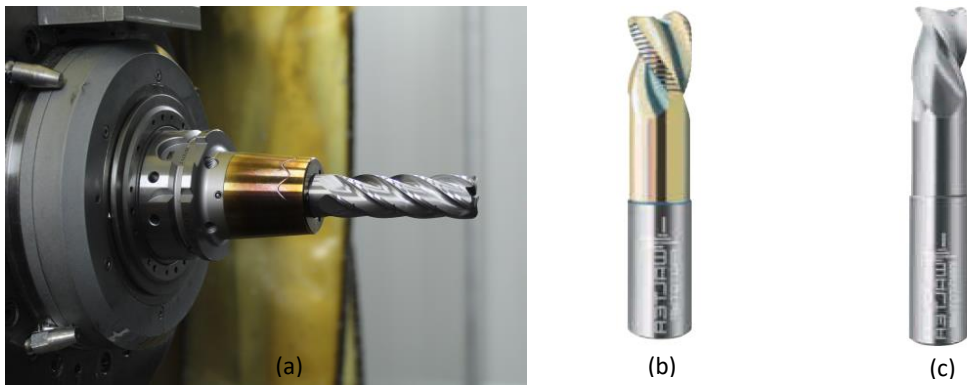


Figure 5-17: Kennametal Kor 5 solid carbide (a) Walter roughing (b) and Walter finishing tool (c)

Table 5-9: Machining parameters for tools used in trials

	Kennametal Kor 5	Walter MB265	Walter MB266
Diameter (D)	20 mm	25 mm	20 mm
Number of flutes (z_{eff})	5	3	3
Axial DoC (a_p)	32.50 mm	16.25 mm	Variable
Radial DoC (a_e)	4.00 mm	Slot / 18.00 mm	Variable
Feed per tooth (f_z)	0.12 mm (Hex)	0.13 mm	0.1 mm
Cutting speed (V_c)	1700 m/min	2258 m/min	1433 m/min
Spindle speed (n)	27056 RPM	28750 RPM	22800 RPM

As the MIRS formation is heavily influenced by the mechanical loading imparted by the cutting action a 9255C type Kistler dynamometer was used to record the milling cutting forces. 20 KHz frequency was used as the sampling rate for the cutting trials. The workpiece billet was connected to the dynamometer via a Lang Zero-Point Clamping System (see Figure 5-18). The Lang plate has been adapted so that it could be directly bolted to the dynamometer. The billet is connected to the Lang system by four locking studs. Due to the work holding and stock condition, the test billet overhangs the Kistler Dynamometer. However, the pocket machining is done over the dynamometer within the working envelope. The fixture set up was aligned to the machine bed using a dial test indicator (DTI) to within 20 μm . A sampling rate of 20 kHz was used to record the forces using the Kistler equipment.

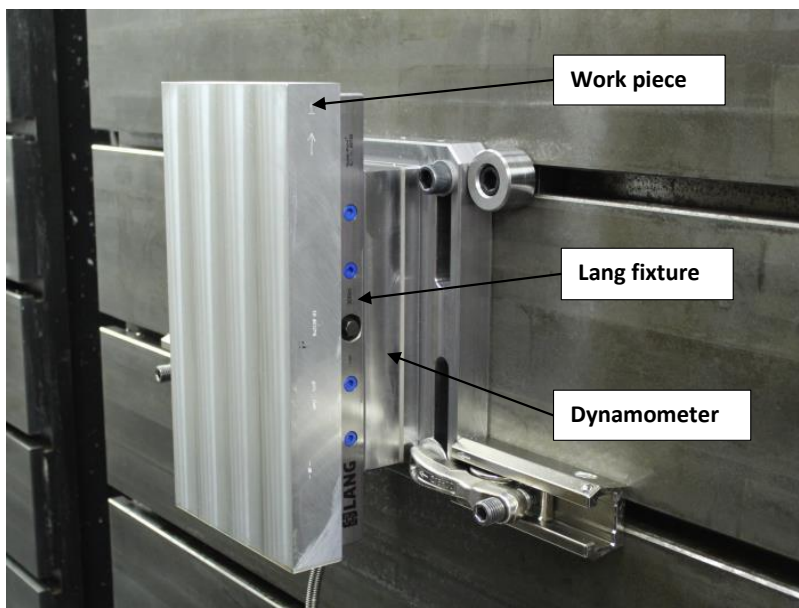


Figure 5-18: Experimental setup

5.3.3 Machining induced stress measurement of pocket coupons

To measure the MIRS in the pocket coupons a combination of incremental hole drilling and x-ray diffraction measurements have been carried out. Unlike the fine ICHD measurements outlined in section 5.2.5 conventional ICHD measurement technique was used to capture MIRS in the machined pocket coupons. The conventional method incurs a loss of stress information close to the machined surface compared with the fine ICHD technique [171]. To determine the induced residual stresses closer to the surface x-ray diffraction measurement was employed. Both sets of measurements were carried by VEQTER LTD. The following two sections will discuss both measurement methods in relation to the inspected coupon.

Incremental hole drilling

Incremental hole drilling (IHD) has been used to measure machining induced residual stresses at various positions along the tool centre path trajectory. See section 5.2.5 for detail on the measurement technique. The surface of the measurement site was cleaned using a chlorinated hydrocarbon solution and neutralised using an ammonia-based solution. Vishay Measurements Group Ltd strain gauge rosettes of type EA-06-31RE-120 were bonded to the surface using 'M-Bond 200' product. The specifications of the strain gauge are given in Figure 5-12. Wire EDM machine has been used to remove the pocket walls for access of the IHD equipment to the machined surface. The gauges were connected to the strain recording system in a quarter Wheatstone bridge configuration.

A numerically controlled orbital drill, as shown in Figure 5-19, was used to remove material at 0.025 mm increments up to a depth of 0.50 mm. At each increment, the computer system recorded the strain values for each orientation automatically. Post measurement the residual stresses over the depth of the drilled hole have been calculated using the method determined by ASTM-E837-13a.

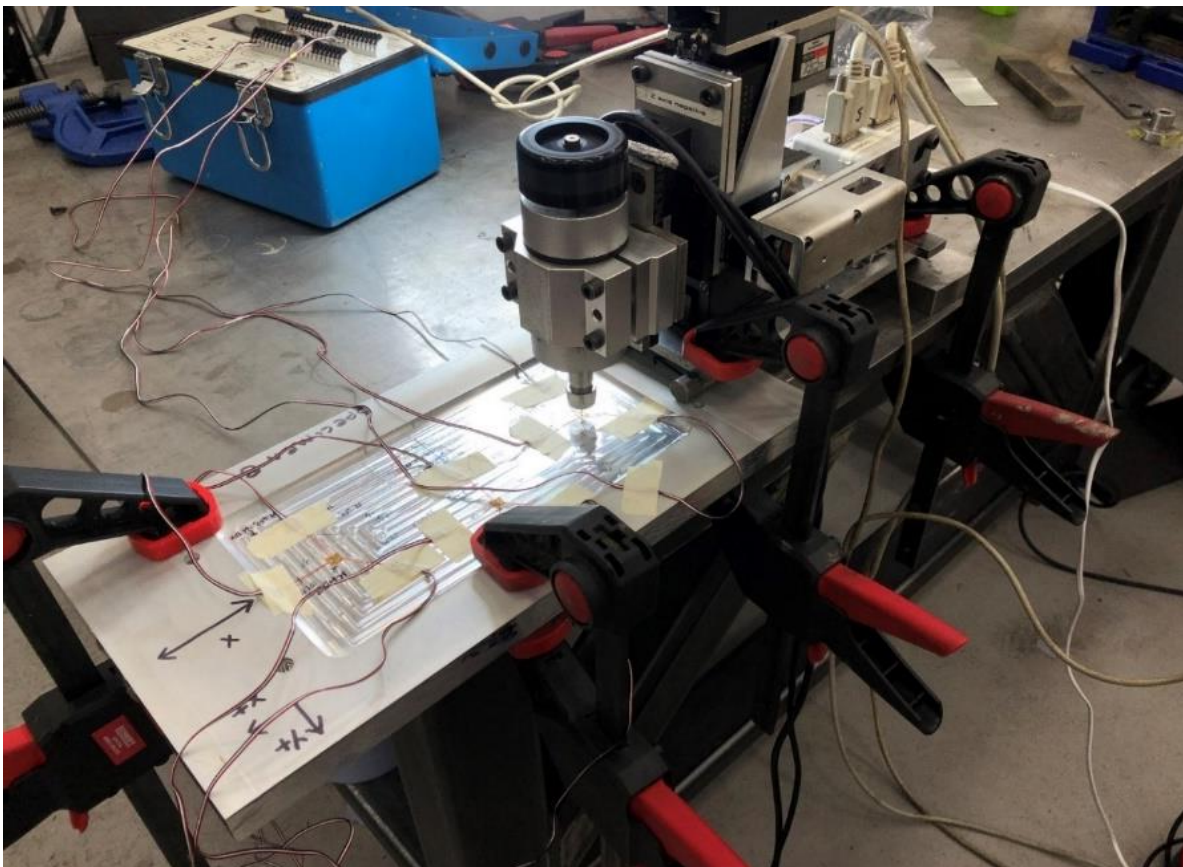


Figure 5-19: IHD drilling rig

X-ray diffraction

The x-ray diffraction method was introduced in section 2.4.3 as a semi-destructive method of measuring residual stress. The principle behind the method is that for a material with internal residual stress state the inter-planar atomic spacing will differ from that of an unstressed sample. Therefore, by measuring the difference between the stressed and unstressed sample the strain can be determined. From the strain, stress can be calculated using the mechanical principles of elastic materials.

To measure inter-planar spacing x-rays are used with wavelengths of the same order of magnitude as the inter-atomic spacing of the polycrystalline material. Incident x-rays backscattered will therefore constructively interfere resulting in a diffracted beam for which the angle is used to determine the inter-planar spacing using Bragg's law:

$$n\lambda = 2d \sin \theta \quad 5-22$$

Where; n = number of waves, λ = x-ray wavelength, d =inter-planar spacing and θ = angular position of the diffraction lines produced by the stressed sample with respect to Bragg's Law. The strain is given with respect to the inter-planar lattice by the following equation:

$$\varepsilon = \frac{\Delta d}{d} = -\cot \theta \Delta \theta = -\cot \theta_0 (\theta_0 - \theta) \quad 5-23$$

Where θ_0 = is the diffraction angle produced by the stress-free sample. The 'Cos α ' method was used in this work to determine residual stress by x-ray diffraction. With this method the diffracted x-rays are recorded by way of a 2D sensor generating a Debye-Scherrer (D-S) ring. The diffraction angle is related to the D-S ring by its radius by:

$$2\theta = \pi - \tan^{-1}(r_\alpha/L) \quad 5-24$$

Where r_α = the radius of the D-S ring at angle α and, L = distance between the 2D sensor and the specimen. From equations 5-23 and 5-24 the strain in relation to the azimuthal angle (α) is given as:

$$\varepsilon_\alpha = \frac{\cos^2 2\theta_0}{2L \tan \theta_0} (r_\alpha - r_0) \quad 5-25$$

Where r_0 = is the radius of the D-S circle for the stress-free sample. To determine the in-plane biaxial stress state of the sample a set of four strains are used to demine the following strain parameter:

$$\varepsilon_{\alpha 1} = \frac{1}{2} [(\varepsilon_{\alpha} - \varepsilon_{\pi+\alpha}) - (\varepsilon_{-\alpha} - \varepsilon_{\pi-\alpha})] \quad 5-26$$

And is related to the normal stress (σ_x) by:

$$\sigma_x = \frac{E}{1 + \nu} \cdot \frac{1}{\sin 2\eta} \cdot \frac{1}{\sin 2\psi_0} \cdot \left(\frac{\partial \varepsilon_{\alpha 1}}{\partial \cos \alpha} \right) \quad 5-27$$

Where η = angle between the incident beam and diffracted beam with respect to the diffraction vector, and ψ_0 = tilt angle.

Machining induced residual stresses were measured at selected points along the tool centre path with a Pulstec μ -X360n XRD residual stress analyser, as seen in Figure 5-20. The radiation source was Chromium ($K\alpha$). The X-ray power output of the equipment is 30 kV & 35 mA. The Pulstec μ -X360n records the Debye ring of diffracted x-rays emitted from the 311 {hkl} atomic lattice plane using a 2D detector. The residual stress is calculated from the difference in Debye between a stress-free sample and the measured workpiece using the 'Cos α ' method. Stress-free Iron Powder sample values are derived by the supplier.

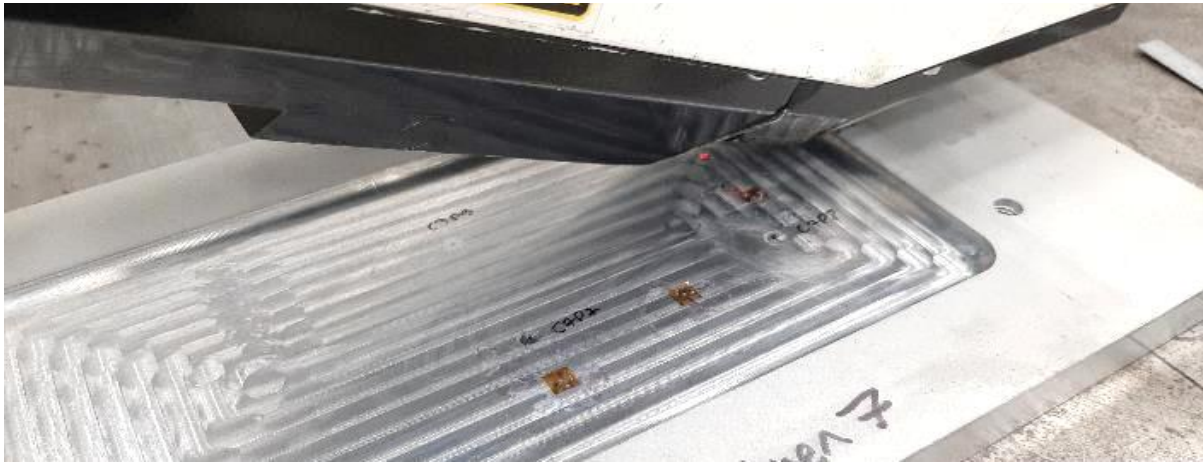


Figure 5-20: Measurement of surface stresses by XRD

XRD technique has a max penetration depth of $\approx 11 \mu\text{m}$. To measure subsurface residual stresses, electro-polishing was used to expose sub-surface regions. Electro-polishing displayed in Figure 5-21 (a) was used to layers of material so that stress below the surface could be measured by XRD technique. The depth of the holes were checked using CMM, as can be seen in Figure 5-21 (b). The accuracy of the CMM equipment is valued at $\pm 3 \mu\text{m}$.

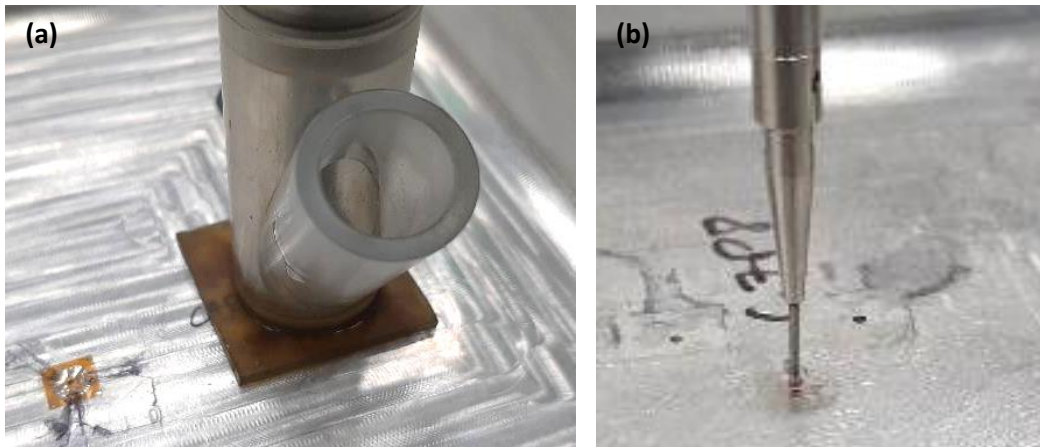


Figure 5-21: Electro-polishing (a) and CMM measurements (b)

5.4 Bulk residual stress layer removal method

Bulk residual stresses are locked in and balanced stresses that form during the manufacture of rolled plate material. Heat treatment processes are used to attain favourable properties in 7050 aluminium alloy. The rapid quenching required to lock in strengthening precipitates also causes differential cooling rates between the core and extremities of the plate material. This differential cooling results in compressive and tensile regions of residual stress that are in balance within the material. During machining these bulk stresses are unbalanced and after removing the constraints of clamping they redistribute to reach a new equilibrium state. This redistribution causes internal bending moments and subsequently part deformation.

Layer removal method was introduced in section 2.4.1 as a destructive measurement technique which utilises material removal to elicit distortion due to residual stress redistribution in a sample [57]. The resulting distortion or strain can be measured and used to inversely calculate prior internal stresses based on elastic material principles. For these trials a partial layer removal technique was carried out by Kaiser aluminium for use in distortion modelling. Figure 5-22 (a) shows the setup of the test sample, with a given through thickness residual stress profile, in between two clamps and a dial test indicator (DTI) gauge placed at one end of the beam to measure deflection. The DTI is rated with an accuracy of $\pm 5 \mu\text{m}$ and repeatability of $0.5\mu\text{m}$.

Figure 5-22 (b) displays the slotting performed on a Bridgeport 2 axis CNC milling machine by an end milling cutter. Part of the internal through thickness residual stress profile is relieved by the milling process and the remaining bulk stresses are unbalanced.

Figure 5-22 (c) shows the specimen after a single DoC and clamp release where the internal stresses redistribute to find a new unknown equilibrium. This in turn results in bending moments about the newly generated neutral axis. The deflection measured is measured and then the sample is re-clamped into the starting configuration. Process (b) & (c) are repeated for a number of machining passes until half of the specimen thickness is removed.

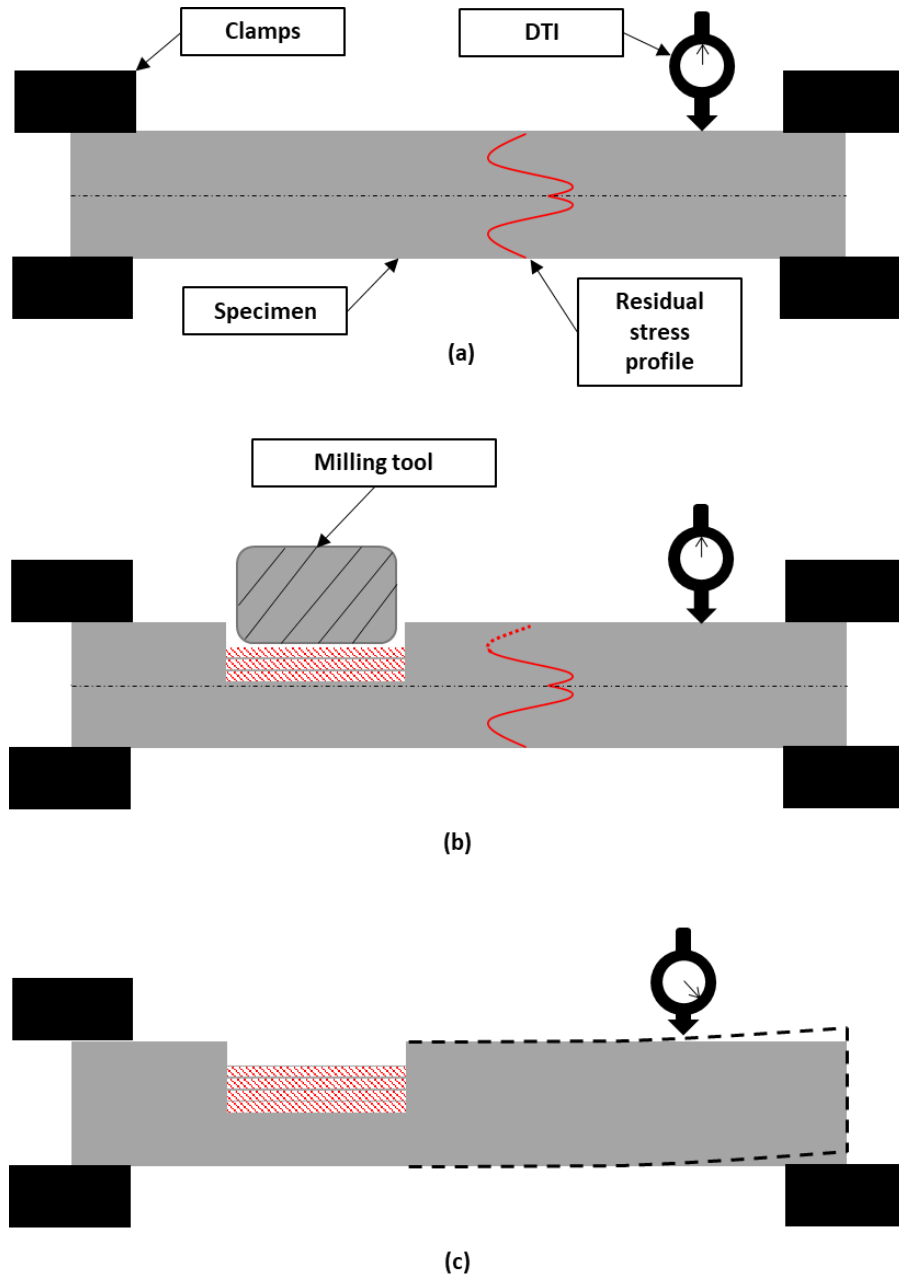


Figure 5-22: Diagram of layer removal method: (a) test setup; (b) milling of the test sample; and (c) process of clamp release and beam deflection measurement.

The equation generally used to relate measured deflection to the surface residual stresses based on geometric material removal and elastic properties of the coupon is defined as follows [172]:

$$\sigma_e(e) = -\frac{4}{3} E \frac{e^2}{l^2} \cdot \frac{df}{de} \quad 5-28$$

Where:

- $\sigma_e(e)$ = stress acting along the surface perpendicular to the plane
- f = deflection of the beam
- e = current thickness
- E = Young's modulus
- l = beam length

The main assumptions of the above equation are as follows:

- the coupon with residual stress is homogeneous and isotropic
- principal stresses align with the axis of the specimen
- Through thickness, stresses are considered negligible
- Transverse stresses are initially considered negligible (although accurate solutions can be determined by considering the Poisson effect)
- The residual stress profile is constant along the whole length of the beam

The stress $\sigma_e(e)$ relates to the stresses in each discrete layer during machining. These stresses are not the residual stresses in the material prior to material removal. The stress variation at the removed layer caused by the previously removed material is defined by equation 5-29.

$$\Delta\sigma = -\frac{8Ee}{l^2} \int_h^e df + \frac{8E}{3l^2} \int_h^e e' df \quad 5-29$$

Where h is the height of the sample, therefore, the residual stress within the specimen before machining is the summation of equations 5-28 & 5-29 given by equation 5-30.

$$\sigma(e) = \sigma_e(e) + \Delta\sigma \quad 5-30$$

Layer removal provides uniaxial stresses in the orientation of the measurement coupon in the original plate material. In large plates such as the ones utilised in the distortion demonstrator experiments (see

section 5.5), it is typically expected that stresses in the longitudinal and long transverse directions will give rise to deformation. Therefore, a minimum of two coupons orientated in the longitudinal and long transverse rolling directions are needed to determine the residual stresses in the two principal directions.

The stock condition for the distortion demonstrator machining trials has been extracted from a larger plate. The location of the machining stock 'blank' material and the layer removal samples in the mother plate is depicted in Figure 5-23. It can also be seen that stress measurement coupons are identified in the waste material between the 'blanks'. A total of four samples have been subjected layer removal method (samples 301 and 302 with L and LT direction configurations). The number of samples provides two stress measurement data sets for the two principal directions. Therefore, an average residual stress profile can be calculated for both directions for the four samples.

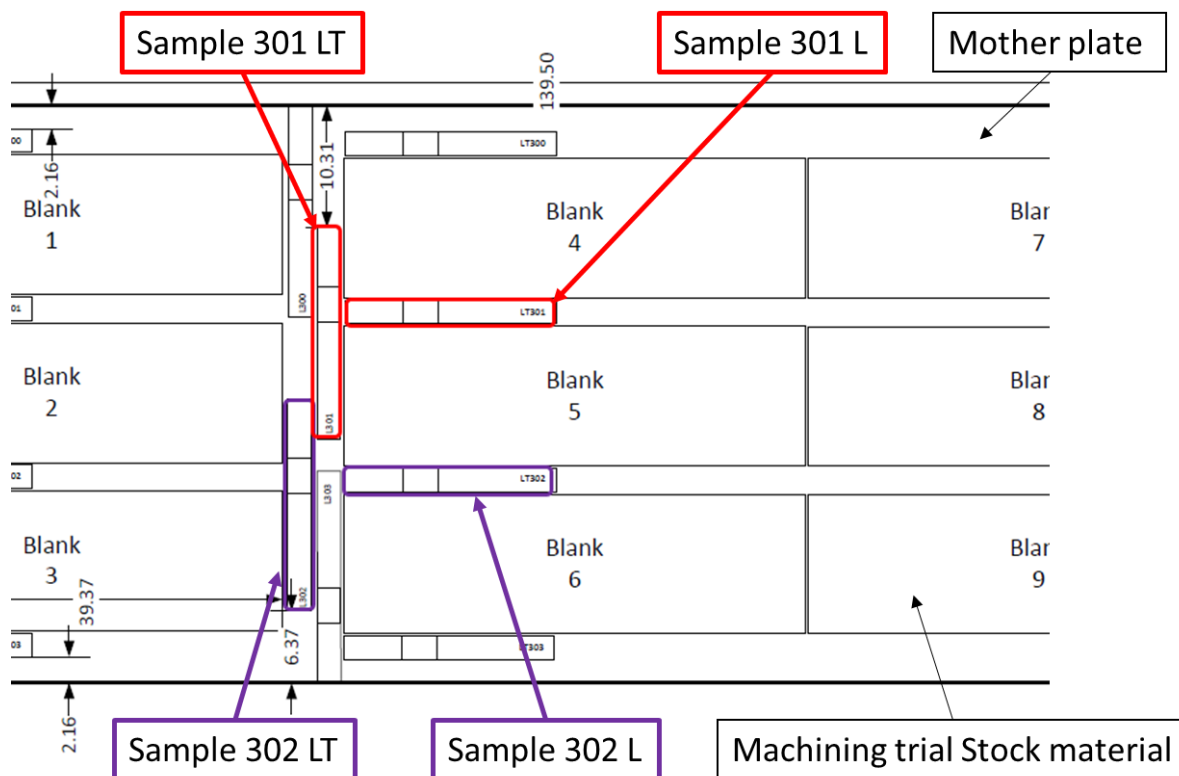


Figure 5-23: TPC2 stock material and stress measurement coupons map (all dimensions in ")

5.5 Distortion demonstrator machining trials

The machining of a test piece demonstrator (see image Figure 5-24) to validate the distortion modelling method and investigate the influence of machining strategy on part distortion has been carried out. These machining conditions were replicated from the machining of MIRS coupons discussed in sections 5.2 & 0 such that the measured induced stresses are assumed comparable to those found in the machined distortion demonstrators. To this end, the machining induced stresses are also used as input to the distortion model.



Figure 5-24: Distortion demonstrator

5.5.1 Material & test Piece design

In order to assess the effect of sequential cutting on machining-induced residual stress-related part distortion, a demonstrator component has been machined from 1000 mm x 300 mm x 50 mm rolled aluminium billet. The initial 'stock' condition is shown in Figure 5-25. The dimensions of the designed part are given in Figure 5-26. The material condition is consistent with the properties given in section 5.2.1.

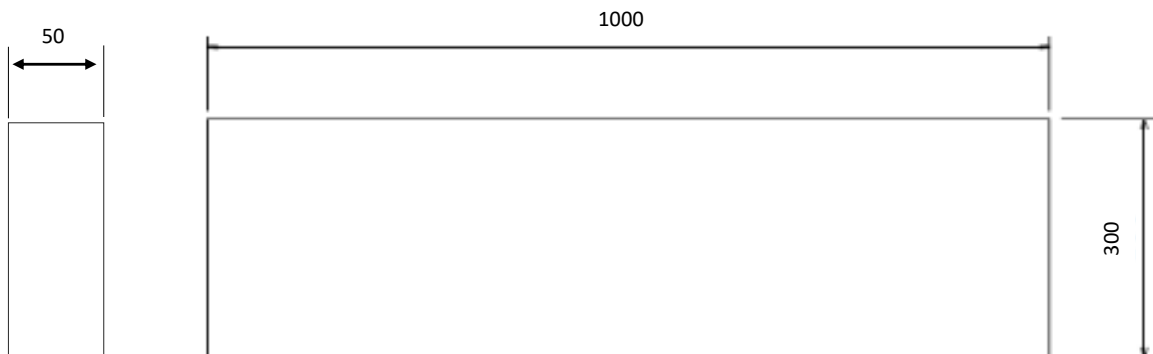


Figure 5-25: Demonstrator stock condition (all dimensions in mm)

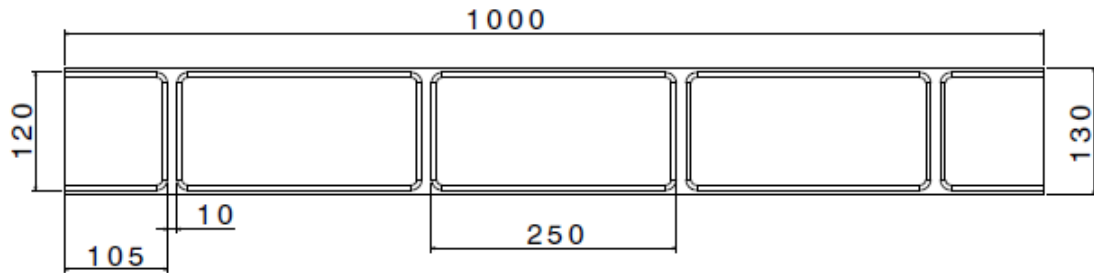


Figure 5-26: Demonstrator design dimensions (all dimensions in mm)

5.5.2 Test design

Machining of the distortion demonstrator part occurs in two stages. Stage one encompasses roughing (Figure 5-27 (a)) and finish (Figure 5-27 (b)) face milling of the initial plate to bring the overall thickness of the test piece down from 50 mm to 25 mm thick. The face milling process utilised a back-and-forth tool path and machining parameters consistent with those used in the sequential machining operation trials (see section 5.1). Drilling of through holes for stage two work holding was carried out last. For stage one, a series of test samples were produced using variable DoC sequences, replicated from the sequential machining trials (see section 5.2.4) and detailed in Table 5-10.

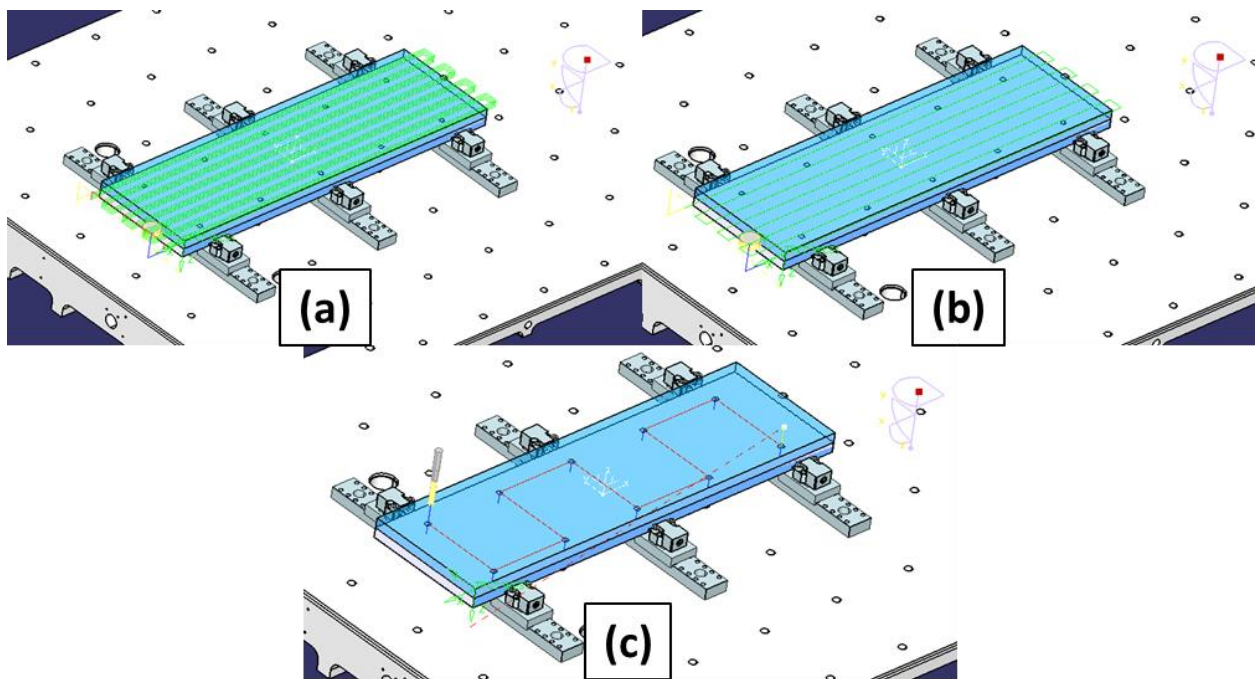


Figure 5-27: Stage 1 machining of distortion demonstrator component; (a) rough face milling; (b) finish face milling; and (c) drilling stage 2 bolt holes

Table 5-10: Stage 1 test identification and machining DoC

Test #	Test ID	R1 DoC (mm)	R2 DoC (mm)	R3 DoC (mm)	R4 DoC (mm)	F1 DoC (mm)
1	TPC2-S1-1	6	6	6	6	1
2	TPC2-S1-2	12	12	-	-	1
3	TPC2-S1-3	12	6	6	-	1
4	TPC2-S1-4	9	6	6	3	1
5	TPC2-S1-5	6	6	6	6	1
6	TPC2-S1-6	12	12	-	-	1
7	TPC2-S1-7	12	6	6	-	1
8	TPC2-S1-8	9	6	6	3	1

Four plates machined to the stage one configuration were taken to Stage 2 machining, as detailed in

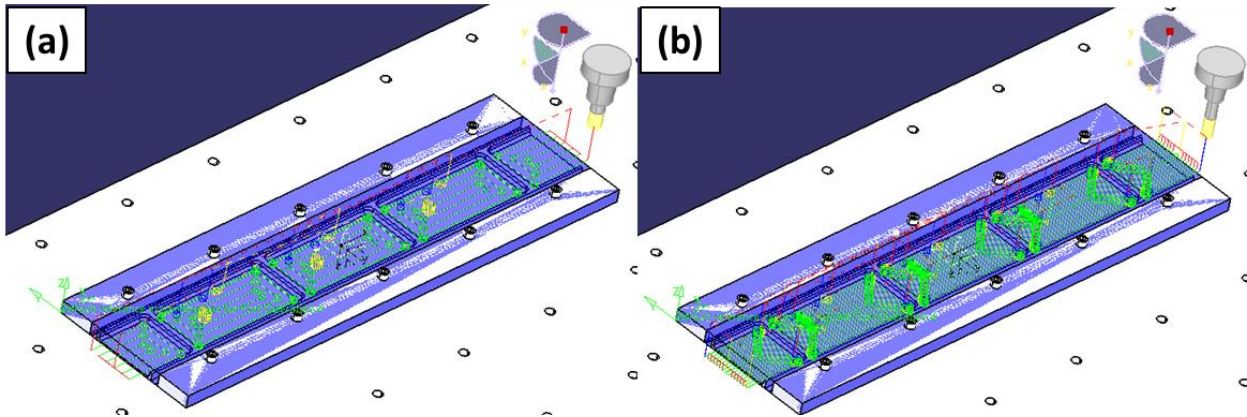


Figure 5-29: Stage 2 pocket milling; (a) roughing and (b) finishing

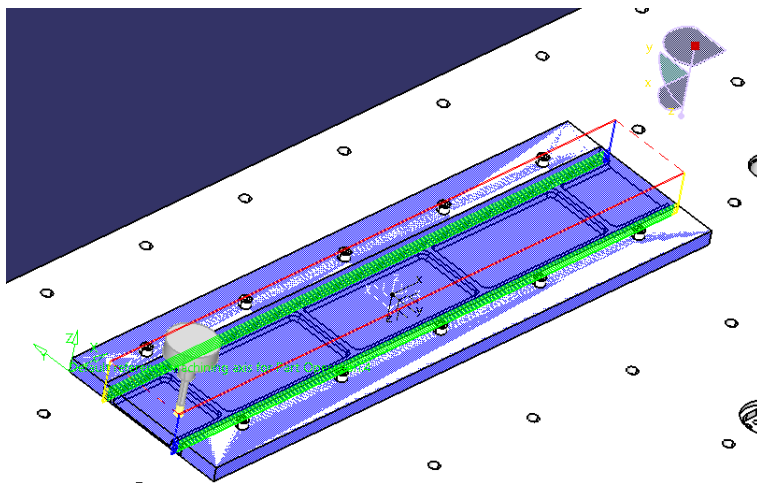


Figure 5-30: Stage 2 machining of break-off tabs

Table 5-11. Before stage 2 machining, stage 1 parts were flipped about the longitudinal axis and fixed to the machine bed via bolting. Stage 2 involves roughing and finishing face and pocket milling to produce the final part geometry. Firstly, face milling (utilising the tooling and machining parameters from stage one - section 5.2.2) was used to remove plate material to reach the designed component height, as shown in Figure 5-28. Then the demonstrator component pocket geometry is machined using the conventional roughing and finishing helical spiral tool paths (defined in section 5.3.2), as shown in Figure 5-29 (a) & (b), respectively. The final operation in stage 2 was to machine two channels on either side of the component, as shown in Figure 5-30, to generate break-off tabs to release the component from the waste material post-machining.

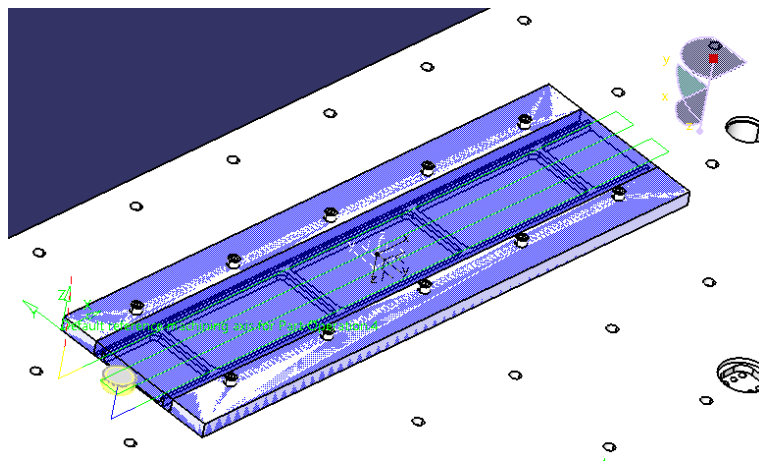


Figure 5-28: Stage 2 face milling operation

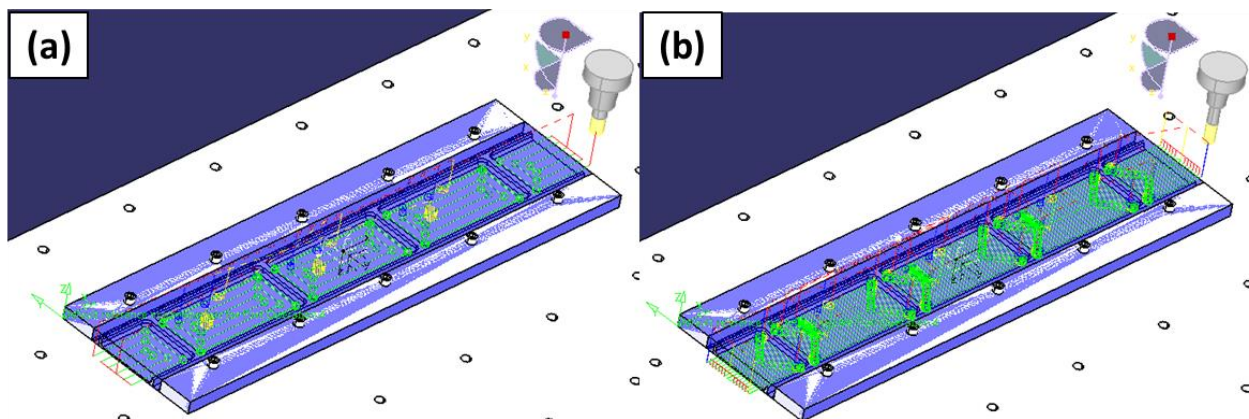


Figure 5-29: Stage 2 pocket milling; (a) roughing and (b) finishing

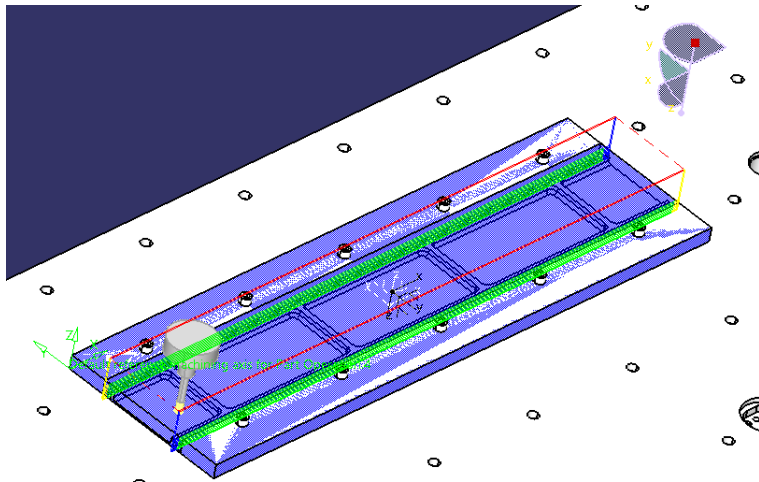


Figure 5-30: Stage 2 machining of break-off tabs

Table 5-11: stage 2 test identification numbers

Test #	Test ID.	Previous stage
1	TPC2-S2-1	TPC2-S1-1
2	TPC2-S2-2	TPC2-S1-2
3	TPC2-S2-3	TPC2-S1-3
4	TPC2-S2-4	TPC2-S1-4

5.5.3 Equipment

The distortion demonstrator machining trials were conducted on the Starrag Technology ‘White tail’ NC machining centre, as detailed in section 5.2.2. The tooling and machining parameters were duplicated from the MIRS trials, as highlighted in sections 5.2.2 & 5.3.2. During stage 1, coupons were constrained to the machine bed using a combination of fixed and adjustable Kopal side clamps. The positions of the clamps and the repeated order of tightening between all tests are provided in Figure 5-31. The clamps were torqued to 12 Nm, providing 10 kN of resulting clamping force. Figure 5-32 shows the plate set on the machine.

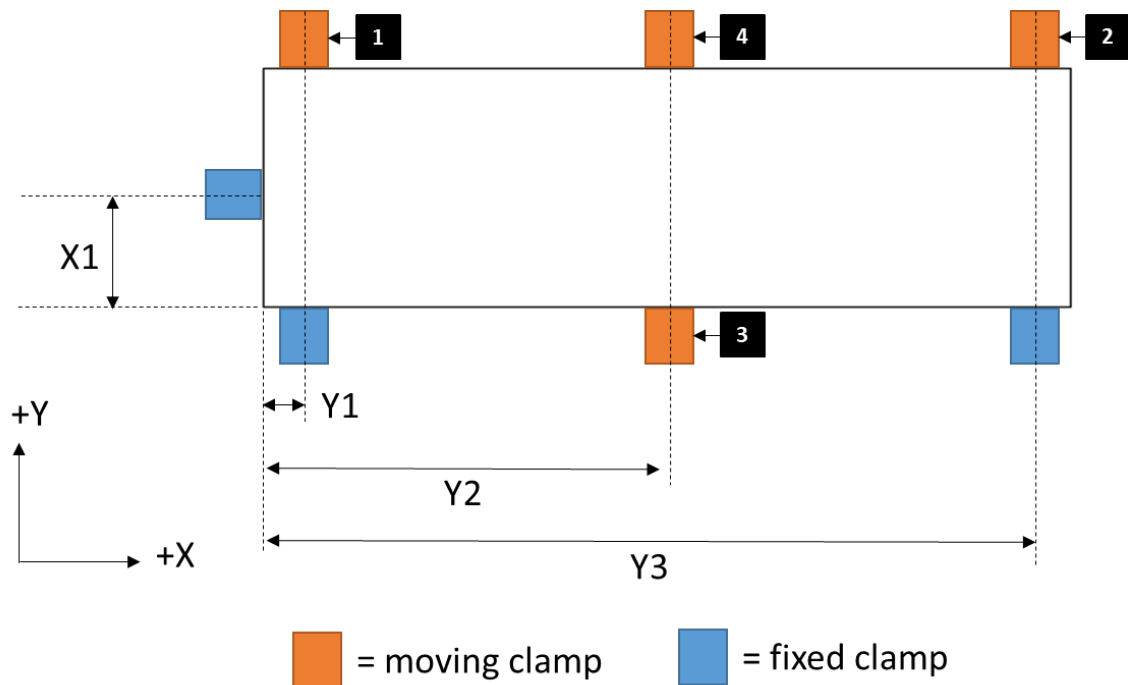


Figure 5-31: Stage 1 fixture configuration diagram



Figure 5-32: TPC2 stage 1 work holding on machine

TPC2 stage 1 parts were flipped over about the longitudinal axis and fixed to the machine bed via bolting. The use of 'break off' tabs have been employed as in industrial applications, the direct fixture of the part to the machine bed is typically not possible. The break-off tab locations are shown in relation to the final part, as seen in Figure 5-33. Break out of the part was performed manually post-machining. Figure 5-34 (a) shows TPC2 bolted to the machine bed before stage 2 machining. Figure 5-34 (b) identifies the bolting sequence used to attain consistent work holding for all TPC stage 2 test pieces. The part after machining and before removal from the machine bed is visible in Figure 5-35.

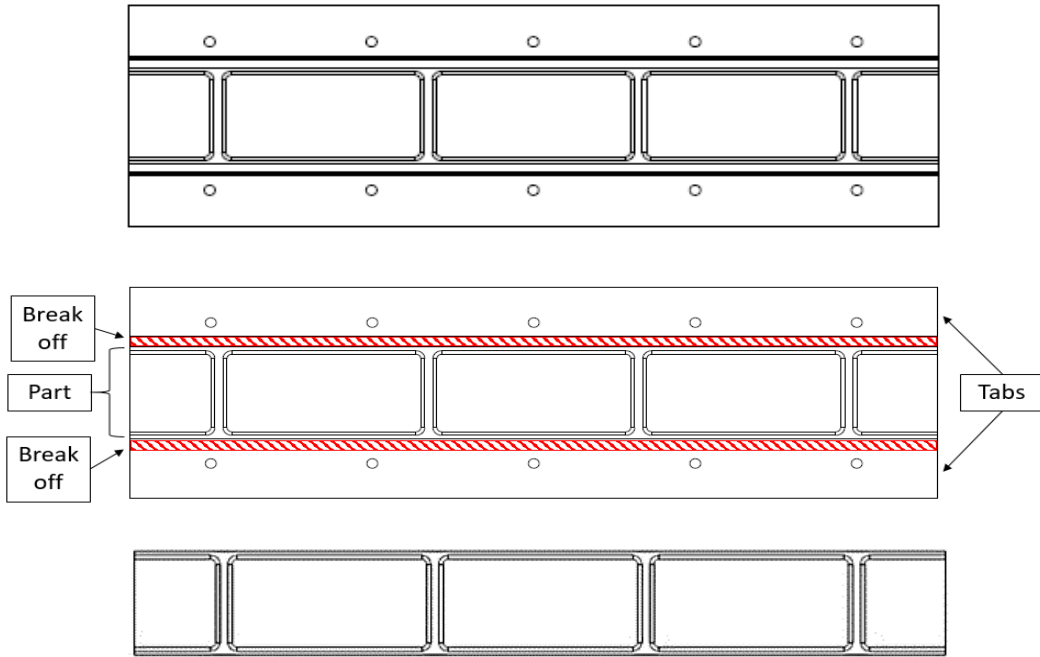


Figure 5-33: TPC2 stage 2 part design

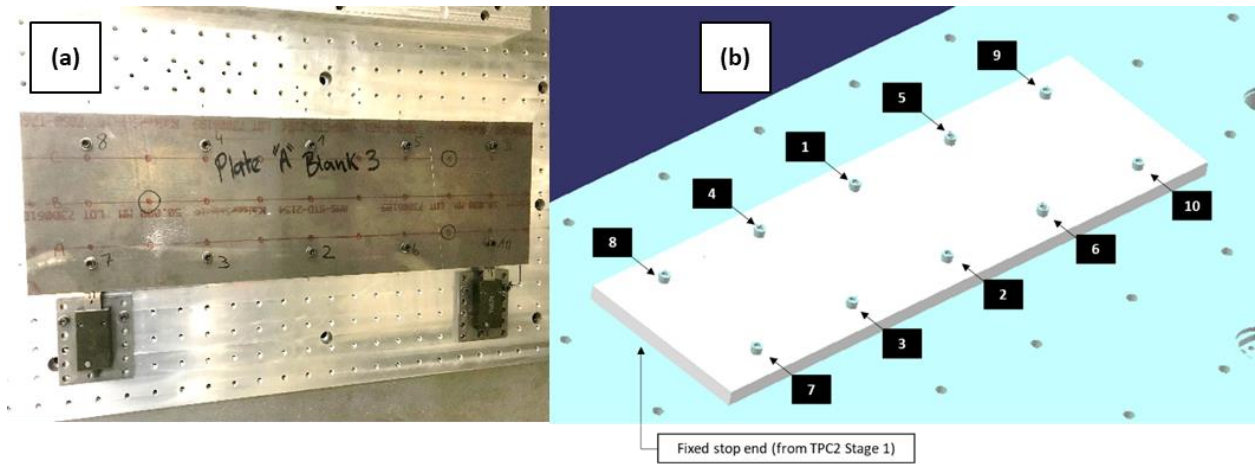


Figure 5-34: Bolting of TPC2 stage 2 (a) and repeat bolting sequence (b)



Figure 5-35: End of TPC2 stage 2 machining

5.5.4 Distortion measurement

Deflection measurements were made of the distortion demonstrator component after stage 1 and 2 machining to quantify residual stresses related distortion. The following sections detail the measurement processes.

Stage 1 CMM

For the experiments undertaken within this work, distortion is classified as the vertical displacements deviating from a calculated reference plane caused by plate bending. A Leitz 122610 Trax high precision coordinate measuring machine (CMM) has been used to determine the vertical displacement after stage one for eight components (as defined in Figure 5-10). The bridge-style CMM uses a trigger-type tactile stylus to make precision point measurements on the machined surface of the component. The system has a traceable accuracy of $1.9 \mu\text{m} + L/400$. CNC determines the motion of the machined, and such repeat

measurements between components can be made. A CMM system is depicted in Figure 5-36 with the representation of the general setup of the distortion measurement procedure.

Measurements were made along three lines denoted 'A', 'B' and 'C' spaced 32.5 mm apart on side 'B' of the rolled plate, as shown in Figure 5-37. The first and last points on each line were measured 10 mm from the ends of each plate. All other point measurements were made along each line in 100 mm increments. This point spacing equals 11 points per line, totalling 33 points per test piece. The physical part being measured can be seen in Figure 5-38, where 3-2-1 work holding is evident so that the part can be measured in a near-free state.

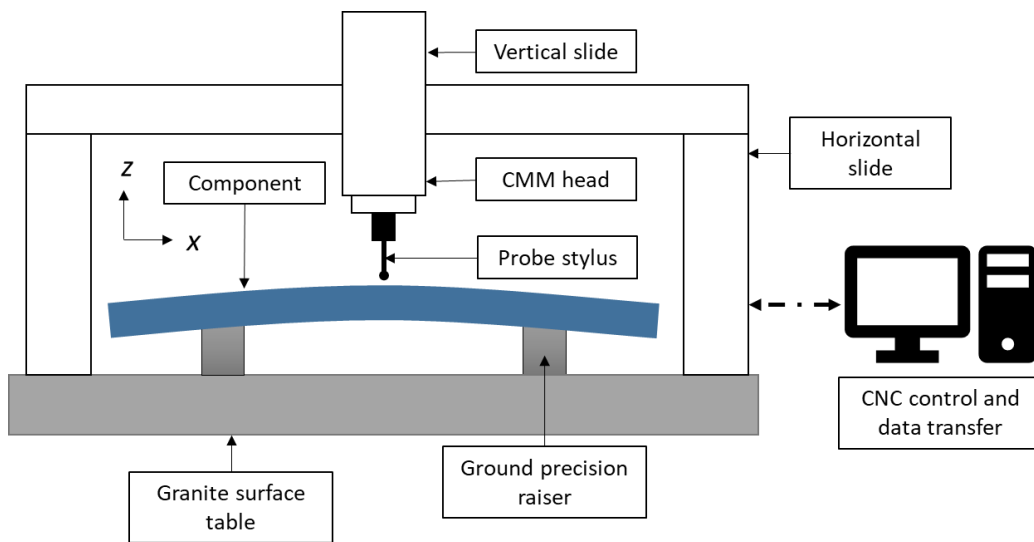


Figure 5-36: DDI distortion measurement schematic diagram

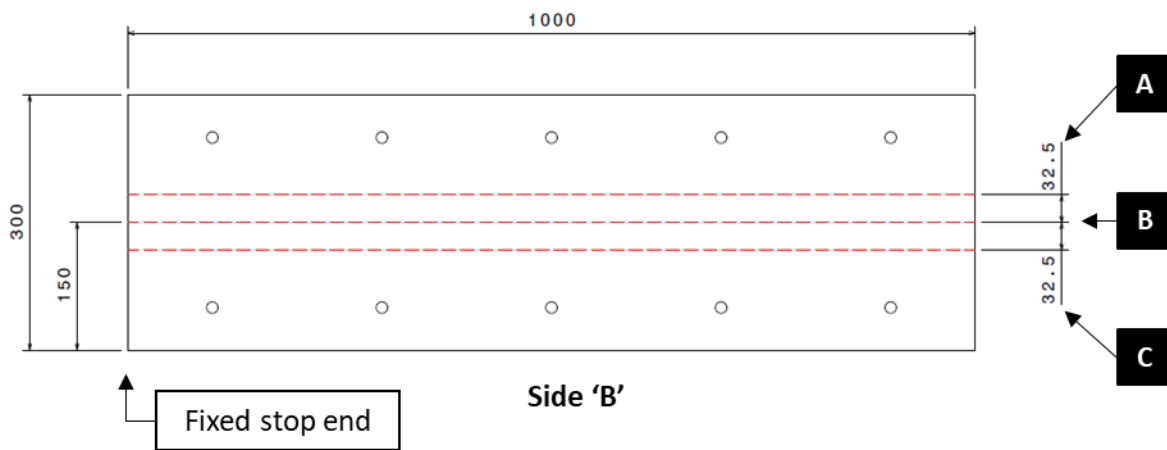


Figure 5-37: Position of TPC2 stage 1 distortion measurement locations

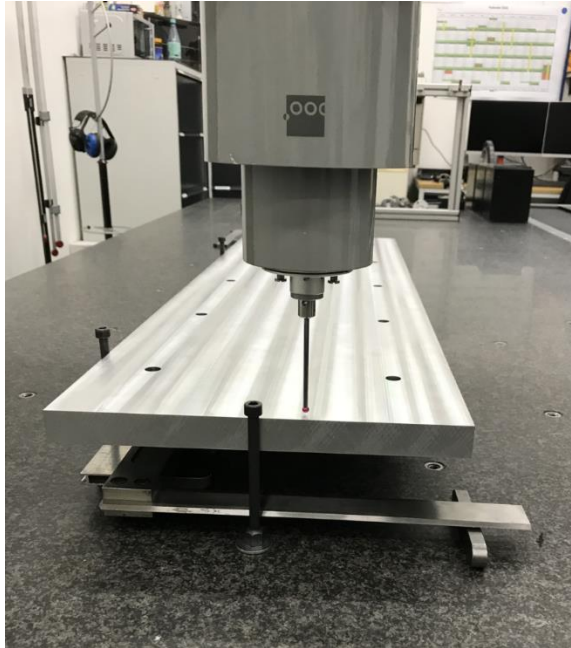


Figure 5-38: TPC2 stage 1 distortion measurements on CMM

Stage 2 CMM

After stage 2, distortion was measured using the same CMM system discussed in section 5.1.3. As per the stage one measurement procedure, 11 points were measured across three lines on surface side 'B' for four test pieces as defined in Table 5-11. Measurements lines were spaced 32.5 mm apart, as shown in Figure 5-39. In order to measure the part in a 'free' condition, 3-2-1 boundary conditions were utilised. Figure 5-40 (a) shows the location of the boundary conditions, and Figure 5-40 (b) the ground precision blocks used to create the constraints in the XY plane.

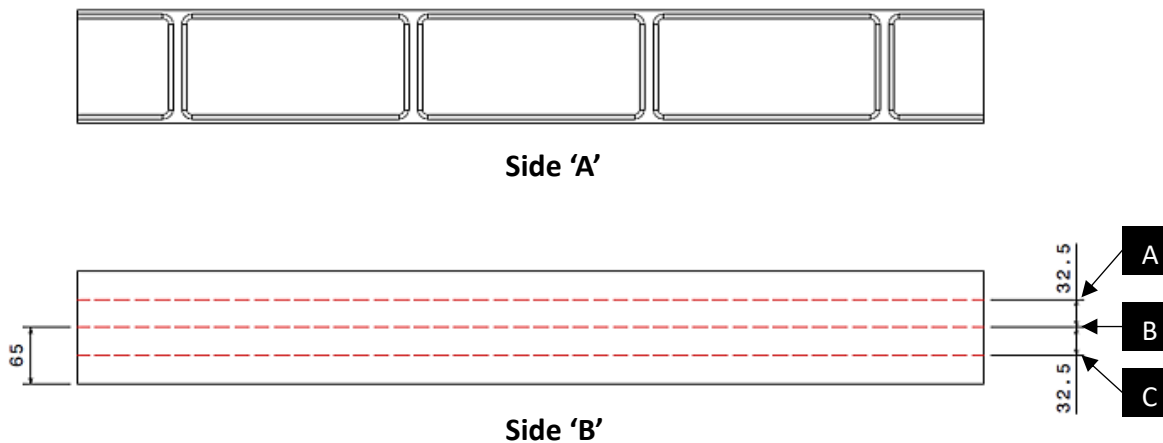


Figure 5-39: TPC2 stage 2 CMM measurement lines

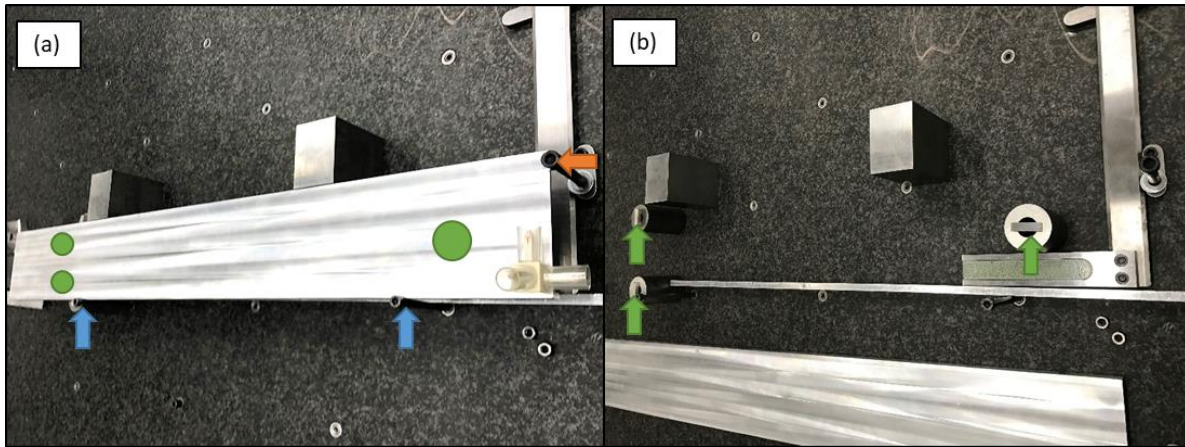


Figure 5-40: TPC2 stage 2 measurement 3-2-1 boundary conditions (a) and location of ground blocks providing Z displacement boundary conditions (b)

5.6 Concluding statements

This chapter has been earmarked to clarify the experimental methods used to study the influence of machining strategy on the formation of machining-induced residual stresses in coupons made of aerospace-grade aluminium alloy, utilising industry-standard machining techniques, tooling and parameters rather than arbitrary machining conditions used in the reviewed literature. The generation of experimental data for simulations to model the machining-related distortion (see Chapter 4) has also been covered. Section one of the chapter provides a rationale for each experimental study. Section two covers the sequential machining tests proposed to address the ambiguity of the influence of sequential machining processes on the machined product's final surface machining-induced stress state. Section three describes the machining trial and measurement techniques used to study the influence of inter-process machining-induced stress variations. The third section covers the layer removal method measurements for generating data for distortion simulations. The final section covers the distortion demonstrator component trials to produce a component for CMM measurements so that the influence of machining sequencing on part distortion can be studied and data generated to validate the developed modelling procedure. The component is designed to share geometrical features of aero wing structural components that give rise to machining-related distortion challenges and also such that machining processes studied in sections two and three can be reproduced on a distortion coupon.

The experimental trials detailed in the chapter look to address gaps in the current state of understanding in machining-induced residual stress measurement applications, which have the potential to have broader implications in modelling the influence of machining-induced residual stress on part distortion and to provide experimental data for use in the simulation of residual stress related part distortion.

6 Experimental Results & Discussions

As outlined in section 5.1 a series of experiments have been undertaken to determine the influence of machining sequencing and strategy on MIRS formation, bulk residual stresses in rolled plate aluminium and the machining of demonstrator coupons for the measurement of post machining distortion. To aid the discussion on the influence of machining technique on MIRS, a conventional stress profile is parameterised as illustrated in Figure 6-1 and described below:

- σ_0 – First depth residual stress value
- σ_{max} – Max compressive residual stress value
- d_{max} – Depth at which the maximum compressive stress occurs
- d_0 – MIRS influence layer depth

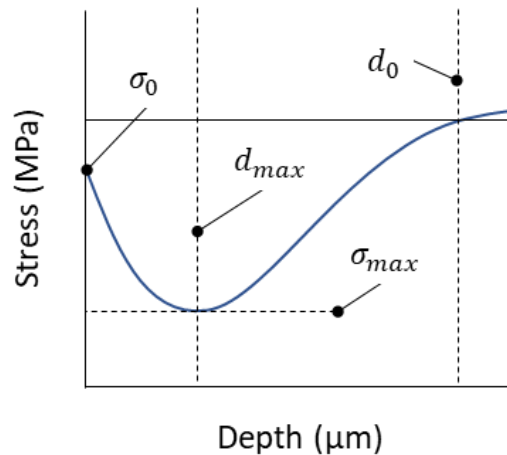


Figure 6-1: MIRS profile description

6.1 Sequential machining influence on MIRS

To understand the repeatability of the MIRS measurement method, three ICHD measurements were made on sample TPC1-4 in three different positions identified in Figure 5-10 (section 5.2). The three ICHD locations were chosen such that the MIRS was captured for surfaces that have undergone consistent machining conditions. Figure 6-2 shows the MIRS measurement plots. In general, the trends of the MIRS measured profiles agree well, showing the conventional near-surface compressive MIRS moving towards d_0 at around 112 μm . However, it can be seen that for the first two depths at which the stresses are reported, the individual MIRS stress magnitudes vary significantly. The averaged stress data profiles for the repeat measurements are also included in Figure 6-2 and used to determine the standard deviation

against each reported depth measurement presented graphically in Figure 6-3. The standard deviation of both the feed and normal direction measurements are worse in the first depth increments at approximately 78 MPa and 88 MPa, respectively. This reduces to approximately 26 MPa and 45 MPa at the second depth measurements. After the Third depth increment, the standard deviation drops below 23 MPa to the final reported measurement depth (512 μm). The uncertainty closer to the surface is inherent for this type of mechanical stress measurement technique, and it can be explained by the difficulty in determining the ‘zero surfaces’ position owing to the fact that the surface is not perfectly flat and, therefore, partial material removal occurs impacting the measured relaxed strain and calculated stresses [166], [173], [174]. This information should be considered when comparing ICHD measurements made across several positions.

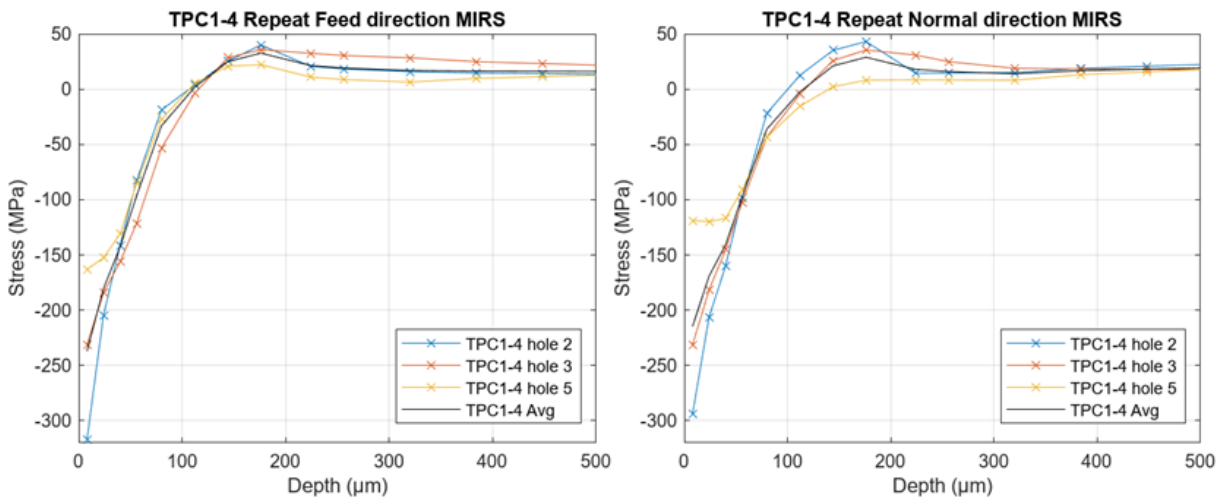


Figure 6-2: TPC1-4 repeat measurements.

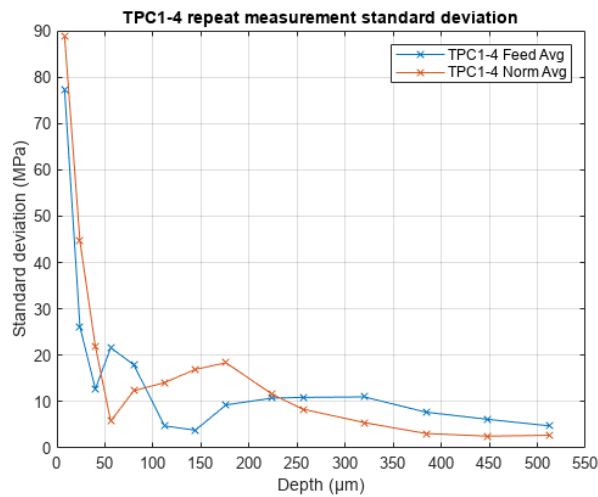


Figure 6-3: Standard deviation of the ICHD repeat measurements versus depth.

For reference, a single roughing machining pass has been conducted (TPC1-3). Figure 6-4 shows the stress profile generated after a single roughing pass of 12 mm DoC. For the roughing, MIRS σ_{max} occurs at the same depth as σ_0 . The σ_{max} values are -235.5 MPa in the feed direction and -211.1 MPa in the normal direction, d_0 occurs at $\approx 80 \mu\text{m}$. This profile follows the case 1 type MIRS as described by Jacobus *et al.* [75] and shown in figure 2-38. Therefore, it can be stated in this machining instance that the plastic strain is the primary cause of the MIRS formation mechanism where the near-surface thermal strains are minimal.

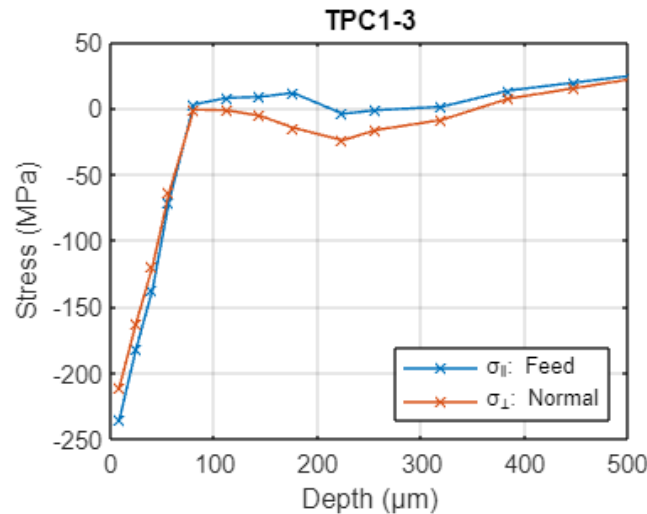


Figure 6-4: Roughing MIRS

TPC1-4 & TPC1-5 represent standard face milling DoC sequences utilised in industry, where TPC1-4 is considered a more conservative machining process. TPC1-6 is a combination of TPC1-4 & TPC1-5 with an initial 12 mm roughing depth of cut followed by two 6 mm roughing depths of cut. TPC1-7 is a conservative roughing sequence, where the DoC is reduced progressively from an initial 9 mm DoC to 3 mm DoC. All test pieces were finished machined with a final depth of cut of 1 mm. Figure 6-5 displays the measurement results for the aforementioned test piece conditions in the feed and normal directions, respectively.

For the finished coupons all measurement results showed similar trends. For the most part the typical square root or tick 'v' profile can be observed. Again, based on the study of Jacobus *et al.* [75] it can be suggested that these profiles were heavily influenced by the mechanical plastic strains imparted by the cutting process, but thermal plastic strain also influenced the MIRS formation to a less extent (the profiles therefore fall between case 1 and 2 as reported by Jacobus *et al.*). For all feed and normal measurements, the peak compressive stresses (σ_{max}) occurred between the second and third measurement depth ($24 \mu\text{m} \leq d_{max} \leq 40 \mu\text{m}$). Only for TPC1-4 feed direction and TPC1-7 normal direction MIRS measurements

was the peak compressive stress not observed in this interval, where the σ_{max} occurred at the first measurement depth ($d_{max} = 8 \mu\text{m}$) increment for σ_0 . Both the feed and normal stress profiles had a tendency tend towards the tensile residual stress region reaching d_0 between 112 and 176 μm .

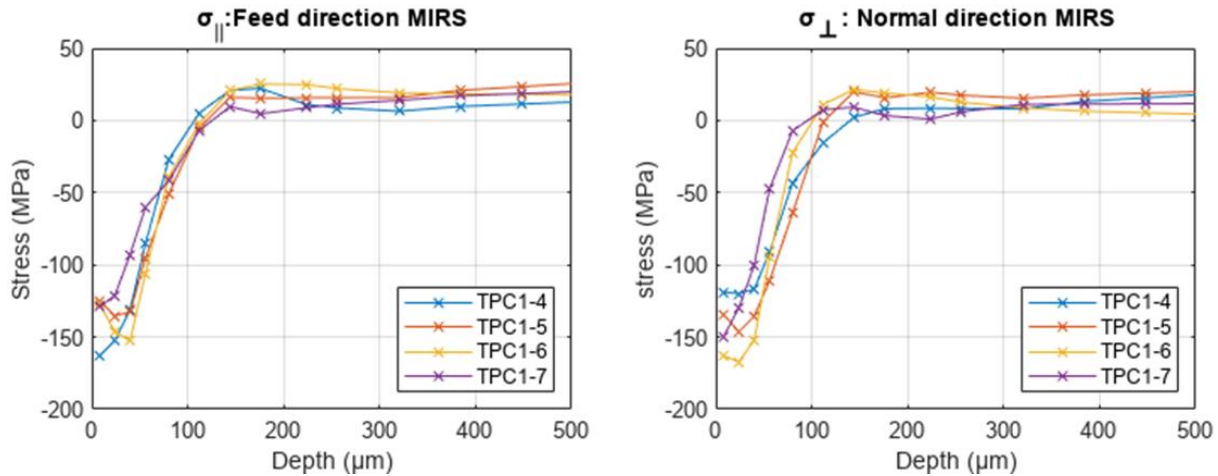


Figure 6-5: Variable machining DoC MIRS

6.1.1 Summary of sequential machining operations influence on MIRS generation

The impact of sequential machining operations on the generated machining induced stresses and part distortion has been considered due to the potential implications on the choice of machining sequence on MIRS and distortion control, and the required discretisation of the distortion modelling approach. Based on the variability of the MIRS profiles it appears that no trend exists supporting the influence of DoC sequence on final near surface MIRS using industry standard machining techniques. When considering that the d_0 of the roughing MIRS profile (shown Figure 6-4) is 80 μm compared with the finishing pass DoC of 1 mm, it can be determined that the tested strategies of MIRS from the roughing passes could be removed in the finishing pass, which do not impact the formation of the final surface MIRS.

6.2 Influence of local cutting conditions variations on MIRS

6.2.1 Cutting forces

Cutting force response was captured during roughing and finishing machining processes of the pocket test coupons. Cutting forces F_x , F_y & F_z have been measured with respect to the Kistler coordinate system (shown in Figure 5-14 in section 5.3) when machining the floor of the pocket coupon only. The cutting forces captured for drilling and machining of the pocket walls are not addressed as they do not influence on the MIRS within the coupon floor. The cutting forces reported coincide with the newly generated floor surface across, which residual stress measurements have been made.

6.2.2 Conventional & Dynamic roughing machining forces

Roughing procedures are characterised as the removal of the bulk of the stock material. Figure 6-6 shows an example of cutting forces generated during conventional roughing milling of the test pocket geometry, as defined in section 5.3.1 and described in section 2.1.1. The absolute max and average cutting forces are summarised in Table 6-1.

Table 6-1: Conventional roughing tool path absolute max and average forces

	Fx (N)	Fy (N)	Fz (N)
Max Cutting Force	2408	3029	1211
Average Cutting Force	550	440	227

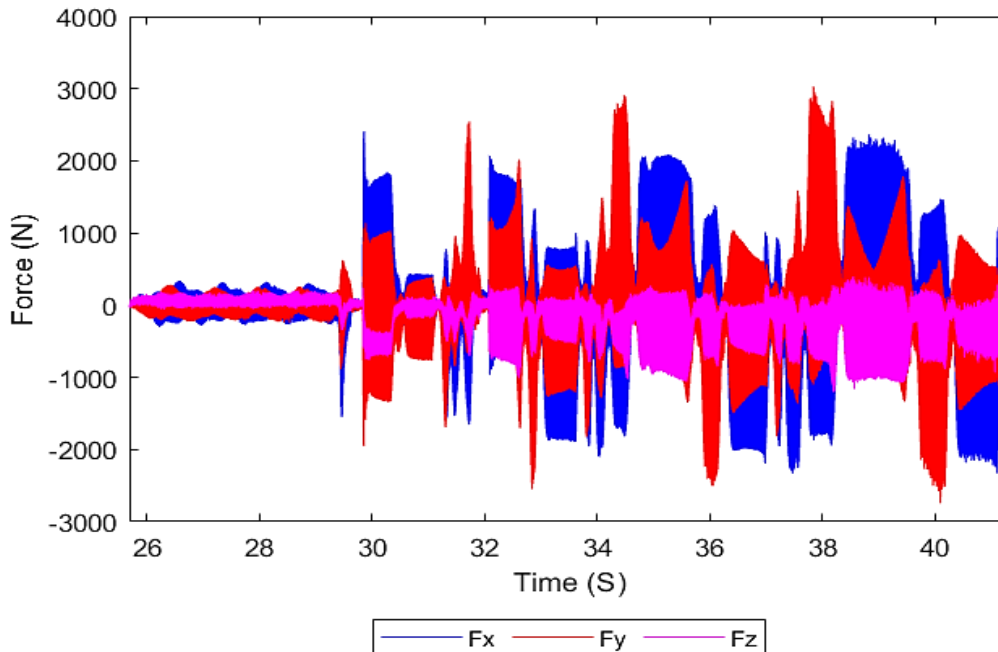


Figure 6-6: Conventional roughing cutting force

Cutting forces are typically higher in the Fx and Fy compared with Fz as these force components relate to the peripheral cutting that occurs in the feed vector. The magnitudes of the primary force component traces change periodically, this is because as the tool feed vector switches between alignment with the X and Y-axis of the dynamometer measurement coordinate system during the spiral milling tool path. The irregularity in the cutting force is caused by the spiral motion of the tool path such that the tool is regularly transitioning between a straight line and corner cutting, as illustrated in Figure 6-7. During the transition between straight line and corner cutting, the tool feed motion is subjected to acceleration and

deceleration. Additionally, the tool cutting contact angle is intermittently increasing/decreasing. Therefore, the changing local cutting conditions arise as variable mechanical loading between the tool and workpiece is experienced. The Fz cutting force is caused by the thrust force or the end cutting contact between the bottom of the tool and the machined surface, and it is also impacted by the variable cutting conditions.

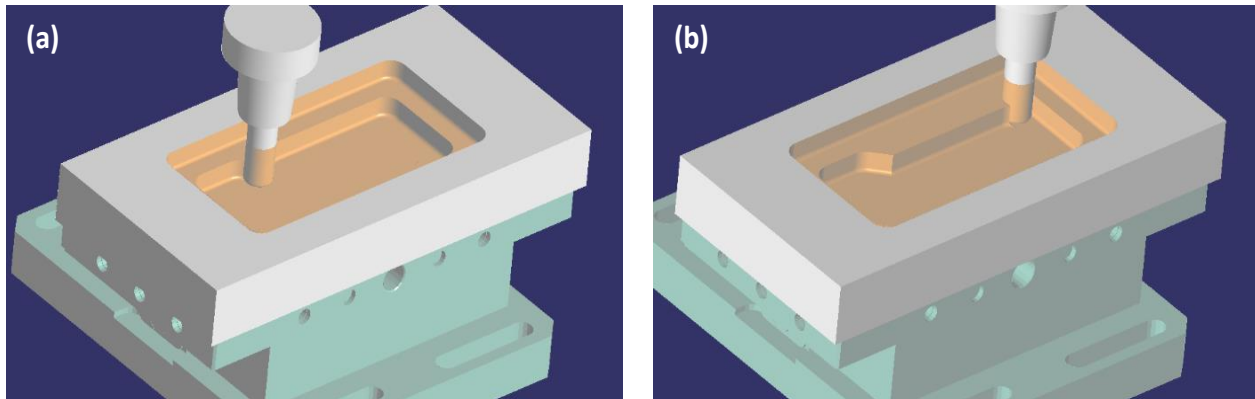


Figure 6-7: Conventional roughing tool path cutting at a corner (a) and a straight pass (b)

Figure 6-8 displays the cutting forces during the dynamic roughing strategy. The dynamic milling forces indicate a more consistent cyclic loading compared with the conventional spiral out milling tool path. As displayed in Table 6-2, the dynamic strategy results in lower absolute max and average cutting forces across all measurement directions. The max cutting forces are 37%, 41% and 15% lower for the dynamic milling tool path in Fx, Fy and Fz measurement directions, respectively. The average cutting forces are 39%, 20% and 34% lower in Fx, Fy and Fz measurement directions, respectively. The dynamic technique maintains a consistent radial tool loading arch as discusses in section 5.1.1. As such, the process forces remain relatively uniform.

Table 6-2: Dynamic roughing tool path absolute max and average forces

	Fx (N)	Fy (N)	Fz (N)
Max Cutting Force	1510	1785	1032
Average Cutting Force	333	354	148

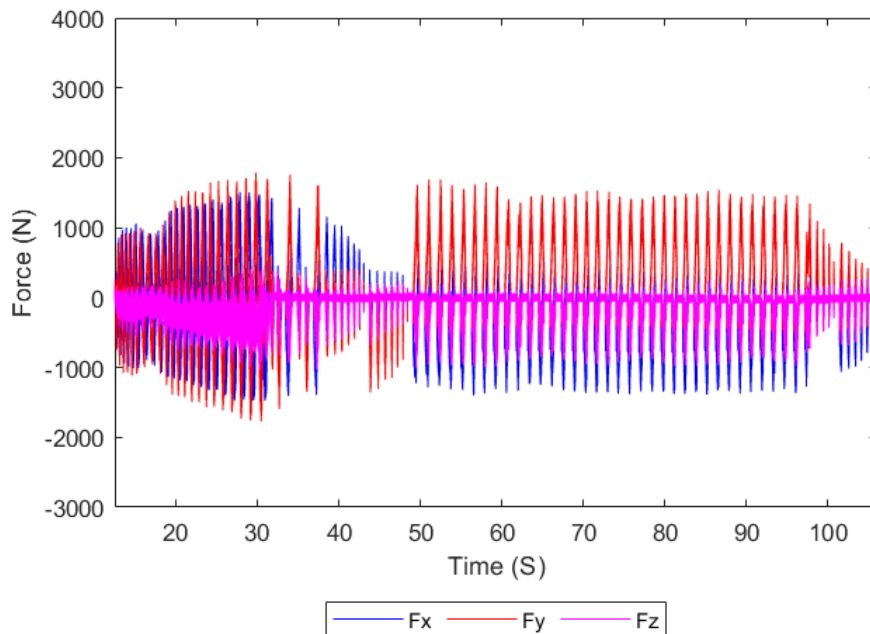


Figure 6-8 Dynamic roughing cutting force

6.2.3 Finish milling cutting forces

The outward spiral finishing tool path generates significantly lower cutting forces than those generated during both roughing procedures. The reduced cutting forces are due to the difference in the amount of material being removed through reduced undeformed chip thickness. The finishing procedure aims to attain precise geometric and surface profile conditions that are required of integral aerospace components. Therefore, light machining parameters and small DoC are utilised to achieve acceptable geometric accuracy and surface finishing condition by reducing the thermo-mechanical loading on the workpiece material. Coupon 7 & 8 absolute max and average cutting forces are presented in Table 6-3. Figure 6-9 and Figure 6-10 displays the cutting forces in Fx, Fy & Fz for coupons 7 & 8, respectively. The maximum and average cutting forces measured between the coupons are very consistent with a maximum variation of only 7% between the average forces (in Z direction).

Table 6-3: Dynamic roughing tool path absolute max and average forces

		Fx (N)	Fy (N)	Fz (N)
Coupon 7	Max Cutting Force	284	427	212
	Average Cutting Force	47	36	20
Coupon 8	Max Cutting Force	282	370	155
	Average Cutting Force	44	34	18

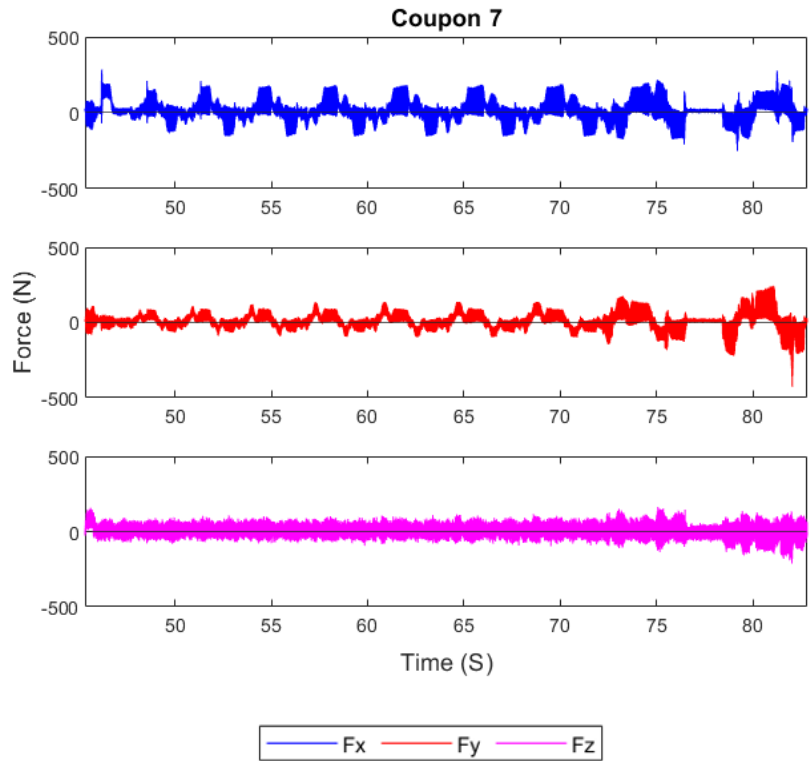


Figure 6-9: Coupon 7 floor machining cutting forces

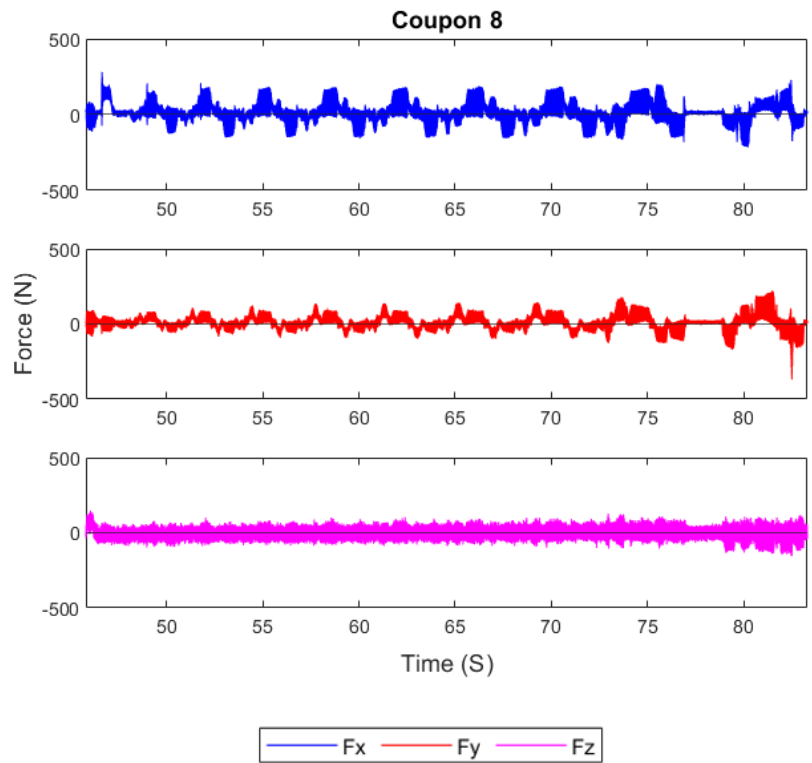


Figure 6-10: Coupon 8 floor machining cutting forces

6.2.4 Symmetry assumption and reproducibility

The geometry of the test pocket is designed such that planes of symmetry exist about the X-Z and Y-Z planes. All tool paths in this study exhibit symmetrical cutting conditions about these planes. Therefore, the machining conditions and thermo-mechanical loading are consistent, then machining induced stresses should also be consistent. Therefore, analysis can be made only on a quarter or half (depending on the tool path) of the plate.

The symmetry assumption was checked by measuring stresses at 4 points on coupon 8 (Figure 6-11), which lie on the centre of a straight-line tool path. Points C8V2 and C8V5 share symmetry about the X-Z plane. Where points C8H2 and C8H8 share symmetry about the Y-Z plane. These locations were chosen as they lie on straight line cuts and exhibit the same cutting conditions. The points were repeated on coupon 7, which allowed for direct comparison between measurements about the two geometrical symmetry planes, as shown in Figure 6-11. The results of the ICHD measurements are displayed in Figure 6-12. From the graphs it can be seen that the feed and normal direction stress profiles measured at the vertical and horizontal symmetry points are comparable. From the results, it can be seen that variation between the first measurement depth exists between points. This variation could be caused by the increased error inherent with the ICHD measurement technique, as highlighted in section 6.1. For incremental hole drilling, in the first 20% of the drilled hole depth strain relaxation is low and determination of 'zero-depth' is problematic, which increases the signal to noise ratio and overall uncertainty [173].

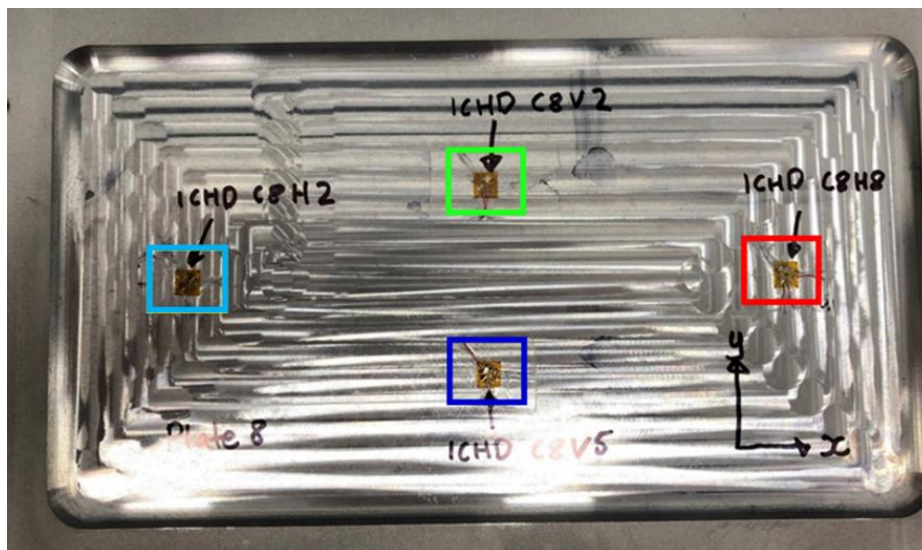


Figure 6-11: Coupon 8 symmetry check measurements

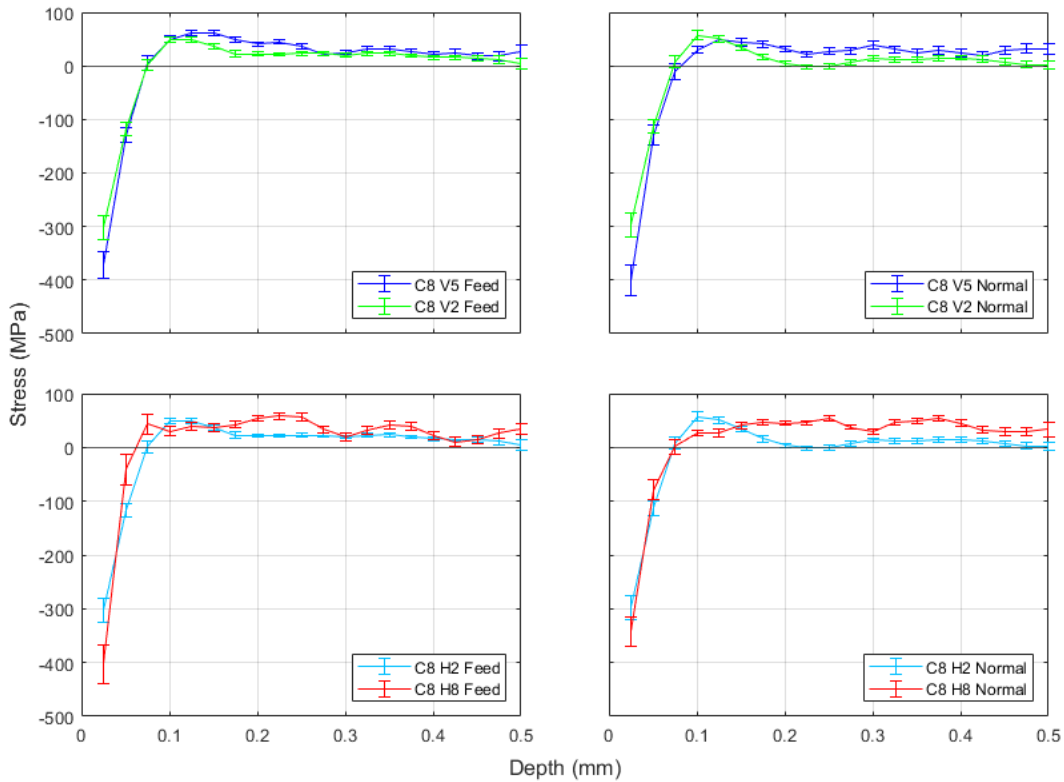


Figure 6-12: Coupon 8 machining induced residual stress profiles

To assess the variability of the ICHD procedure, stress measurements have been made at the same coordinates for test pieces 7 & 8. These coordinates are labelled ICHD P1 and ICHD P5 as shown in Figure 6-13. Figure 6-14 shows feed and normal stresses for two representative points. C8V5RS and C8H8 correspond with C7P1 & C7P5, respectively. Again, the first measurement depth produces the largest variance between measurements, but all repeat measurements are within the uncertainty band of one another (average error of 25 MPa in both feed direction and normal peak compressive stress measurements) suggesting the machining process and MIRS generation is reproducible.

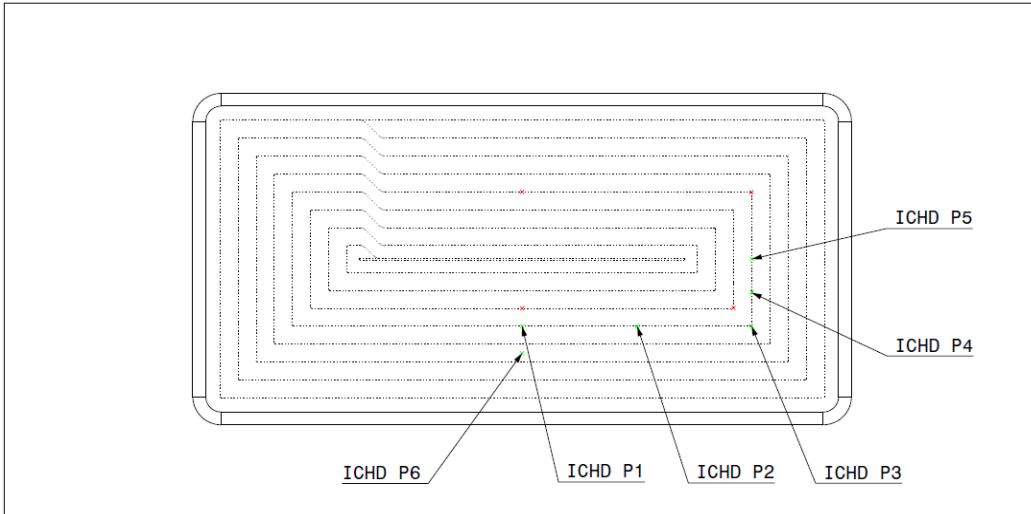


Figure 6-13: ICHD measurement points for coupons 6, 7 & 8

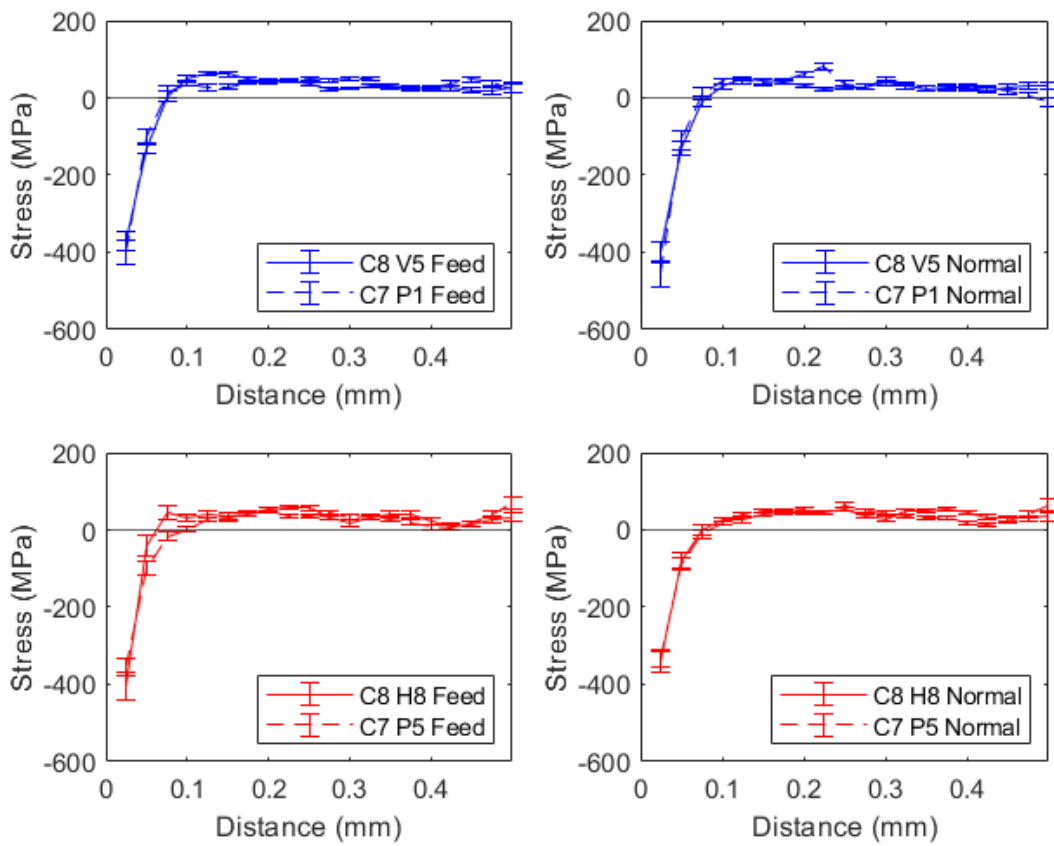


Figure 6-14: Replicate measurement results

6.2.5 Conventional roughing machining induced residual stress

To investigate machining induced residual stress profile generation as a function of the tool path progression, ICHD measurements have been made at various points along tool centre point paths machined using variable strategies. As highlighted in section 6.2.2 of this chapter, process conditions are regularly changing as the milling tool workpiece contact regime is also changing. Figure 6-15 displays the ICHD measurement positions and the corresponding stress profiles.

ICHD positions 1 to 5 follow the centre point path of the milling tool. For comparison, ICHD 6 measures the process induced stresses in a tool path 'step over' region where the cutting paths overlap as the tool spirals out from the centre of the work piece. It can be seen that stress profiles generated by the conventional roughing strategy exhibits a consistent trend in the peak compressive stress position, which occurs at the first measurement depth for all measured profiles. The MIRS profiles the trend towards zero and switches to tensile stress at around a depth of 80 μm to 100 μm . The mean compressive peak residual stress is -343 MPa and -410 MPa in the feed and normal direction, respectively. However, the magnitude of both feed and normal direction measured compressive peak stress varies significantly from point to point. The feed direction MIRS for points 1 & 2 is approximately - 200 MPa. Whilst points 3, 4 & 5 are approximately - 400 MPa in the feed measurement direction. The normal MIRS measurements for points 1 to 5 fall within approximately - 350 to - 450 MPa range. The standard deviation of the peak compressive stress is ± 147.12 MPa in the feed direction and ± 74.41 MPa in the normal direction. ICHD P6 feed and normal compressive peaks are noticeably lower than points 1 – 5. There is no observable variation between stresses measured at the straight line or corner tool path positions under roughing machining conditions. It should also be noted that beyond a depth of 400 μm stresses become increasingly more tensile or compressive, but this is more pronounced for points P4 and P5. The diverging stress values towards the final depth of the hole drilling is attributed to the measurement uncertainty caused by the signal-to-noise ratio associated with the hole drilling method, which is more significant for measurements made in the first and last 20% of the overall drilled hole depth [175]. This is also identifiable by the larger error bars for measurements in these regions. These findings are also consistent with those seen in literature [152]. The more extreme shift in stress values at lower measurement points at locations P4 and P5 could be credited to possible set up variations in the measurement procedure.

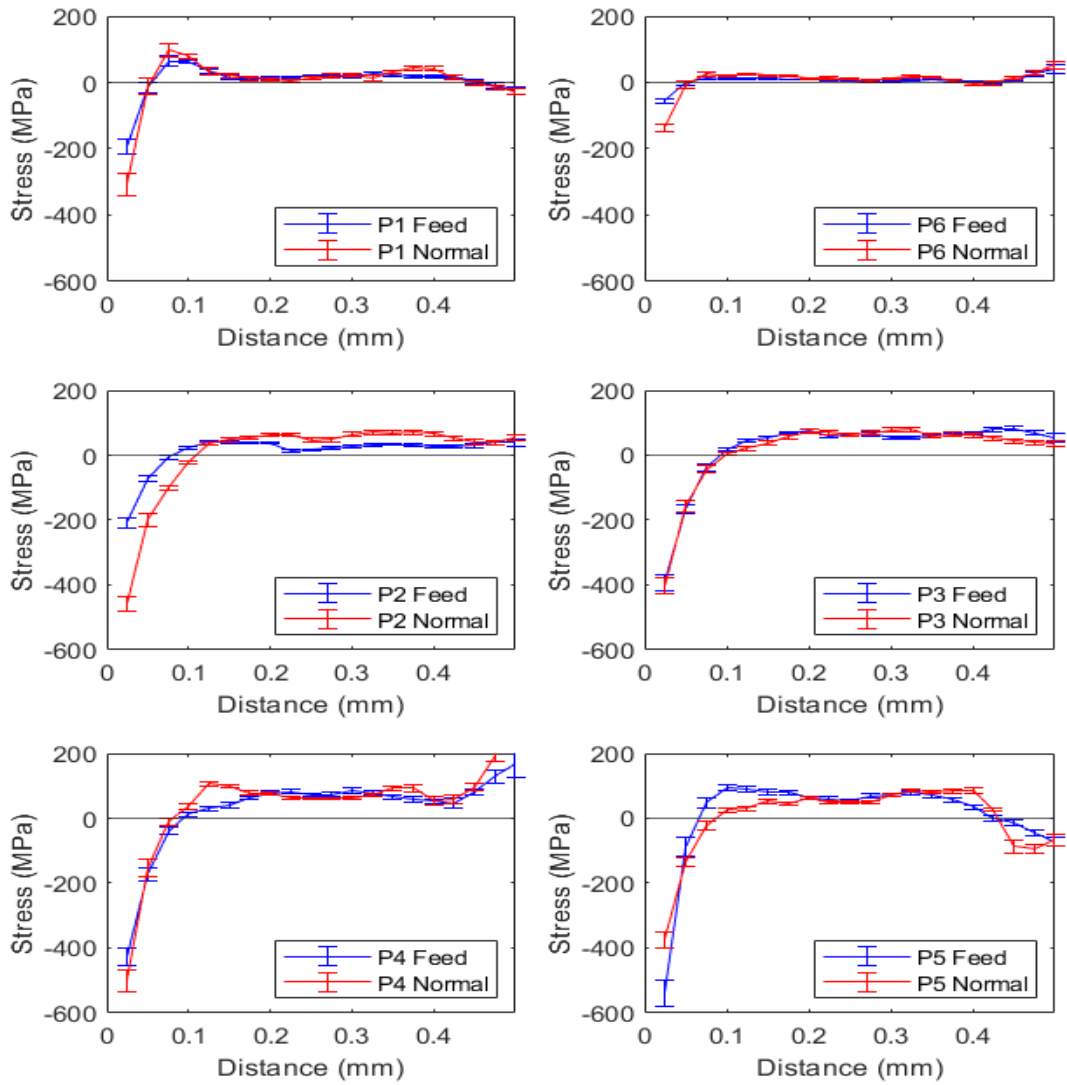
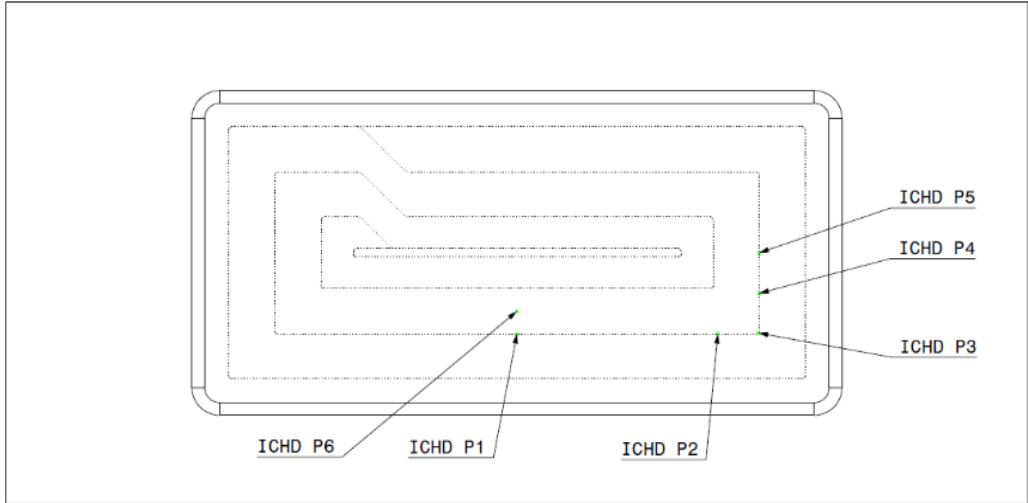


Figure 6-15: Coupon 4 outward helical roughing machining induced residual stresses

6.2.6 Dynamic roughing machining induced residual stress

Figure 6-16 displays the dynamic concentric tool path measurement locations and measured stress profiles. Firstly, it was noted that ICHD P5 seemed to be an outlier with recorded peak compressive stresses of -550 MPa and -460 MPa in the feed and normal direction, respectively. Therefore, ICHD P5 was left out in the further analysis. Mean peak compressive stress was determined as -264 MPa and -234 MPa in the feed and normal cutting direction. It can be seen that significantly lower peak compressive stress values were generated when compared with the roughing outward helical spiral milling process. That is a 25% lower mean peak compressive stress in the feed direction and a 43% reduction in the normal direction. The lower max compressive subsurface stress peak is attributed to lower mechanical plastic deformation inferred through lower machining forces.

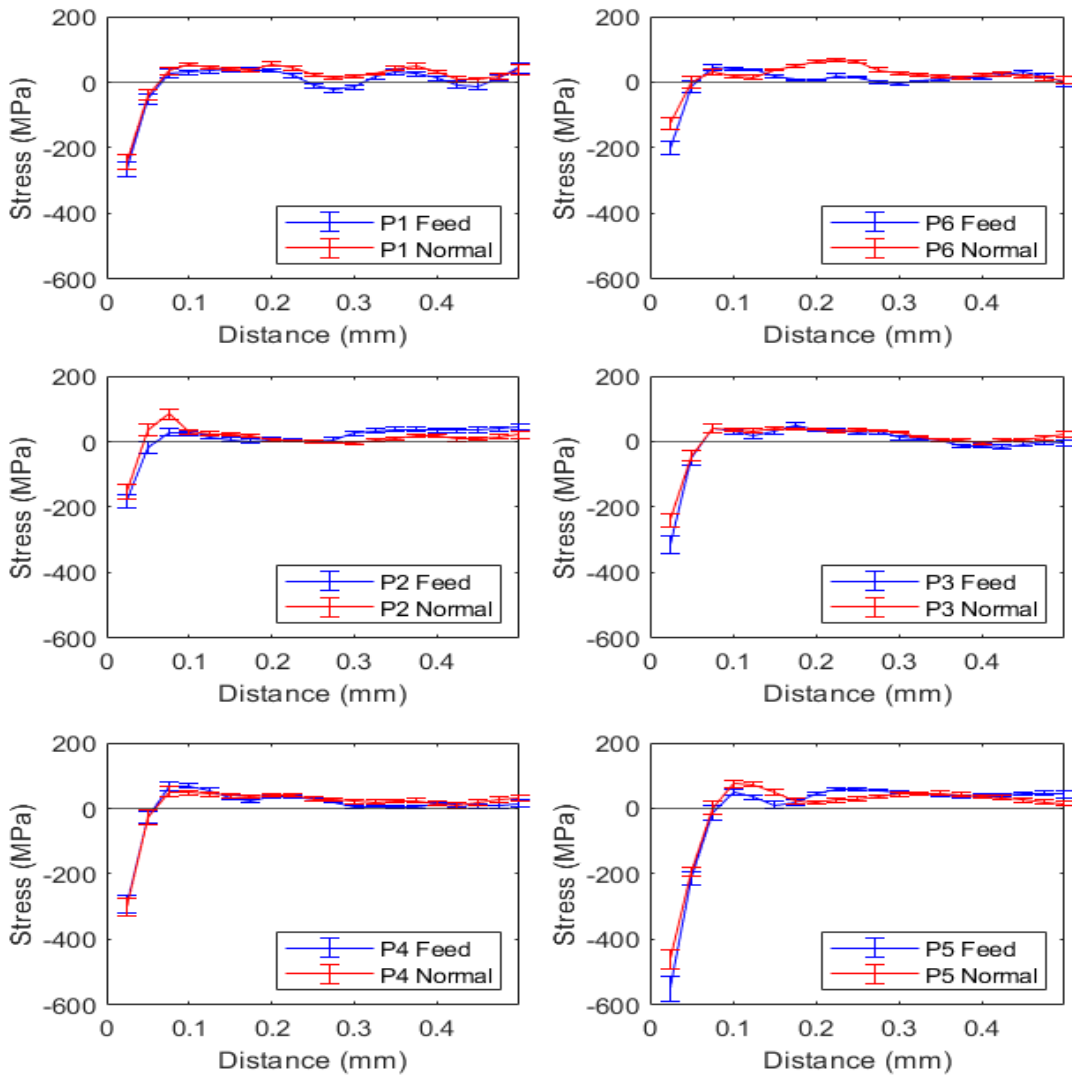
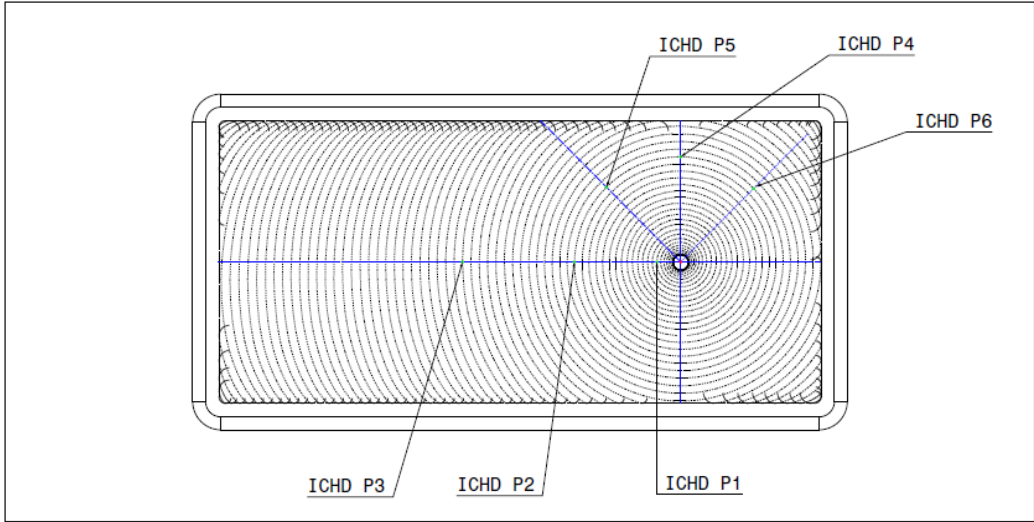


Figure 6-16: Coupon 2 Dynamic roughing machining induced residual stresses

6.2.7 Finishing machining induced stresses after roughing.

Coupons 7 & 8 were rough, and finish machined with an outward helical tool path strategy (see section 5.3.1). The stress measurement locations and stress profiles for coupon 7 are shown in Figure 6-17. The average peak compressive stresses for coupon 7 were measured as -376 MPa in the feed direction and -352 MPa in the normal direction. The finishing process is considered to be less aggressive than the roughing process as can be observed in the difference in cutting forces (see sections 6.2.2 & 6.2.3). However, an increase of 34 MPa in the average peak compressive residual stress value is observed between the conventional roughed and finished feed direction measurements. A reduction of 58 MPa in the average peak compressive MIRS value is observed in the normal machining direction. It should be stated again that the standard deviation of the conventional roughing peak compressive stress measurements is ± 147.12 . In contrast, the finish peak compressive stress measurement standard deviation is ± 36.83 MPa. Additionally, the max overall MIRS value recorded in the feed and normal directions was at points P5 and P4 on coupon 4 (conventionally roughed), respectively. Again, as with the conventional roughing MIRS measurement values, measurement uncertainty is greatest from 0 to 100 μm and 400 μm to 500 μm for reasons highlighted in section 6.2.5. Therefore, it appears the roughing process generates greater sub-surface compressive MIRS; however, it is difficult to draw definitive insight into this comparison due to the considerable measurement uncertainty.

The peak compressive stresses measured at the corner (ICHD P3) measurement for the finished machined component were almost half of the average peak compressive stresses measured along straight-line passes. The reduction in peak compressive stress could be explained by the deceleration of the cutting tool feed, and an increase in radial engagement between the tool and workpiece as the tool is fed into an internal corner [86]. However, this change in MIRS profile is very localised to the corner measurement as the measurements made at straight line feed sections of the tool path immediately before and after the corner are consistent with other straight line measurement points after orientating with respect to the tool vector feed and normal directions.

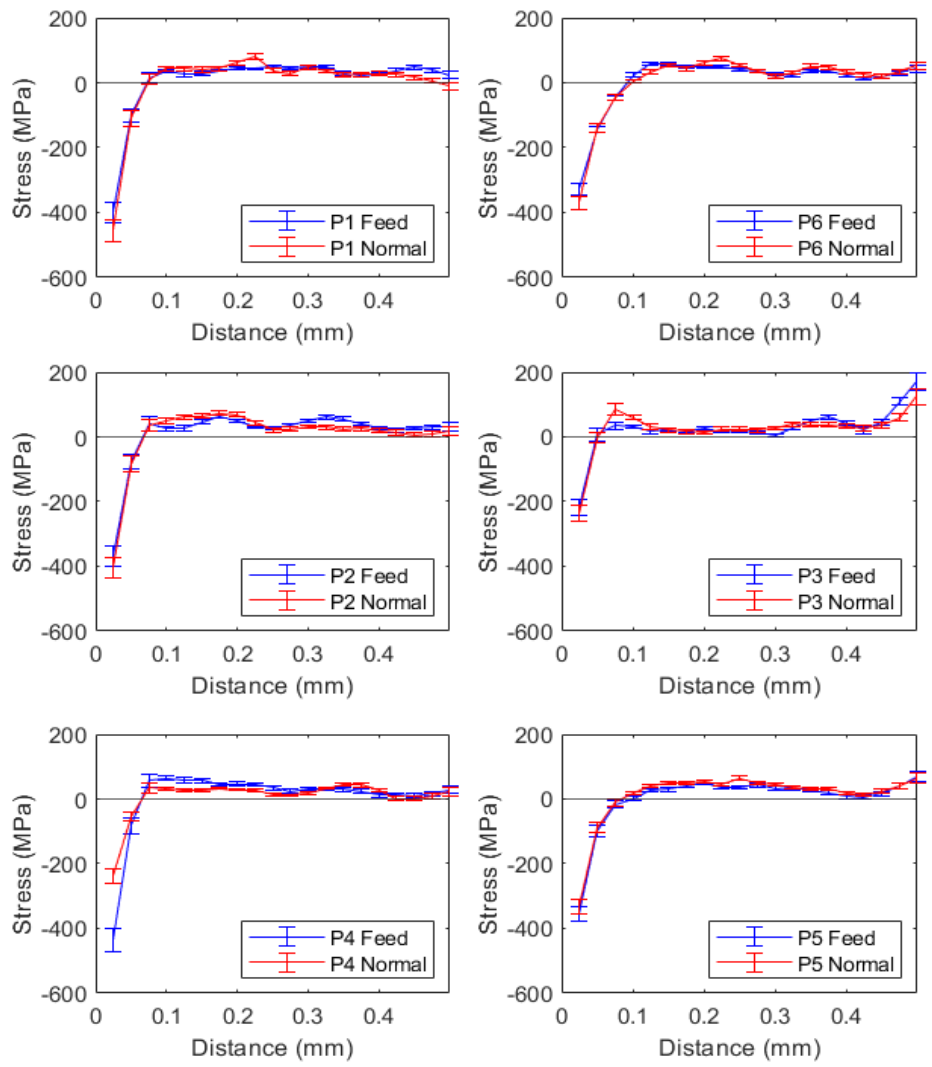
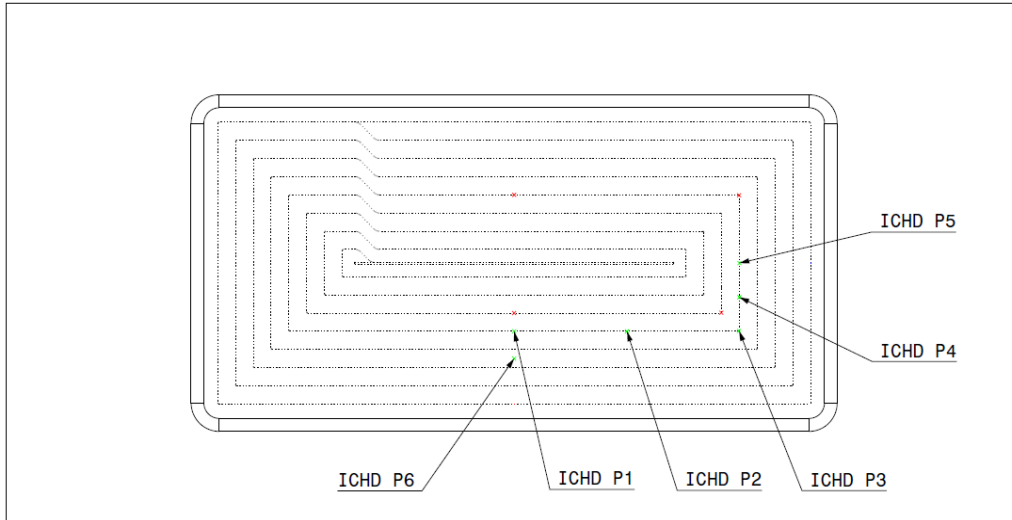


Figure 6-17: Coupon 7 machining induced residual stress measurement locations and profiles

6.2.8 XRD & ICHD

Conventional ICHD measurements used in the determination of sub-surface MIRS are limited to measuring MIRS from 25 μm and below the surface. To generate residual stress data from the near surface to 25 μm below an alternative measurement technique was required. XRD measurements were carried out to obtain near-surface residual stress profiles on coupon 7 using the $\cos\alpha$ method. Three Bi-directional measurements were made at variable depths; one at the surface and two subsurface at $\approx 12.5 \mu\text{m}$ and $\approx 25 \mu\text{m}$. The XRD measurement locations on coupon 7 are shown in Figure 6-18. XRD measurement points 7 & 8 were made at straight, and corner tool path points respectively located on the tool centre path a step in from the path on which ICHD measurements were made. Measurement points 9 & 10 again were made at straight and corner points on the TCP path respectively but on the same radial step over as the ICHD measurements in mirrored positions about the pocket geometry.

P7 and P9 show similar initial compressive surface stresses $\approx 10 - 45 \text{ MPa}$ at the surface in both the feed and normal direction. P7 feed and normal stresses show a similar trend in becoming more compressive around the depth of $\approx 12 \mu\text{m}$ before returning more tensile at the final measurement point. For P9 the feed stress peak compressive stress occurs at $\approx 25 \mu\text{m}$ deeper into the material. P9 normal trend follows that of P7 feed and normal stress profiles showing a peak compressive stress at the mid-depth measurement before turning less compressive at the deepest measurement point. It can be seen that XRD measurement results are inconsistent between equivalent straight line measurement locations P7 & P9.

Stress measurements at P8 & P10 locations show that normal direction stresses are in reasonable agreement. Both display initial tensile stress of $\approx 48 \text{ MPa}$ at the first measurement depth, which becomes increasingly more tensile at the next measurement depth at $\approx 14 \mu\text{m}$ with a value of 114 MPa for P8 and 116 MPa for P10. The Feed direction stress shows little similarity. P8 feed direction surface stress was recorded as -94 MPa. P10 feed stresses were measured tensile at 60 MPa. Measurements below the surface at P8 were compressive just below switching to tensile at the last measurement point. P10 sub-surface measurements remained tensile.

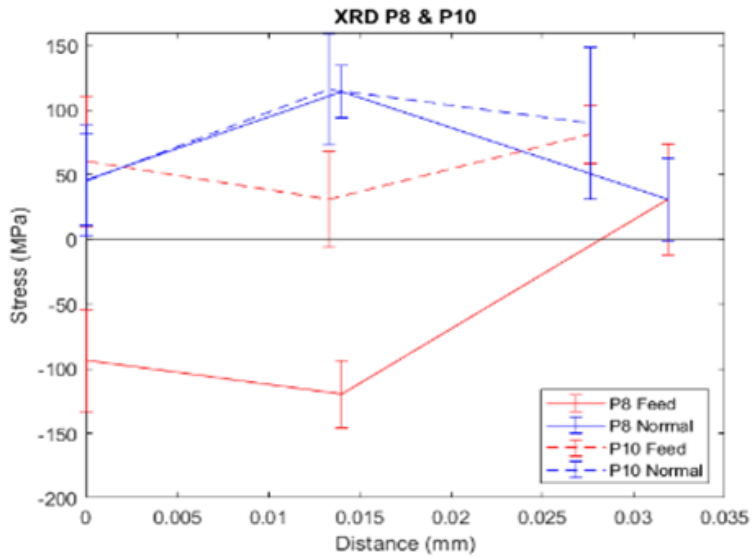
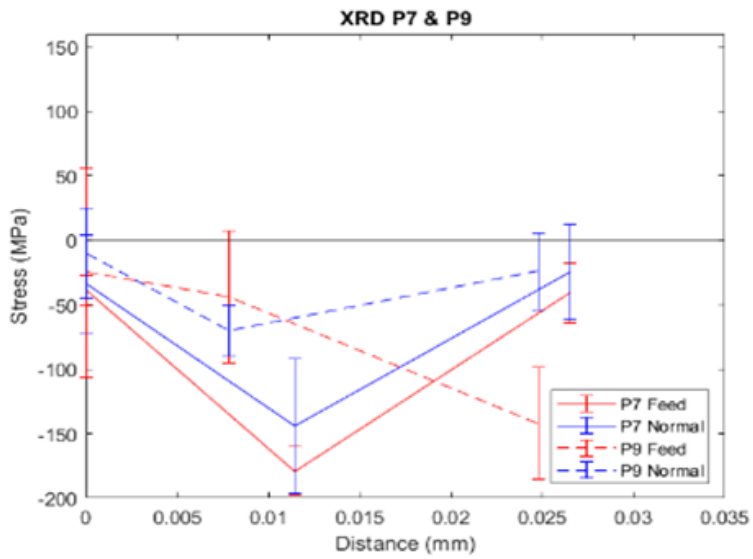
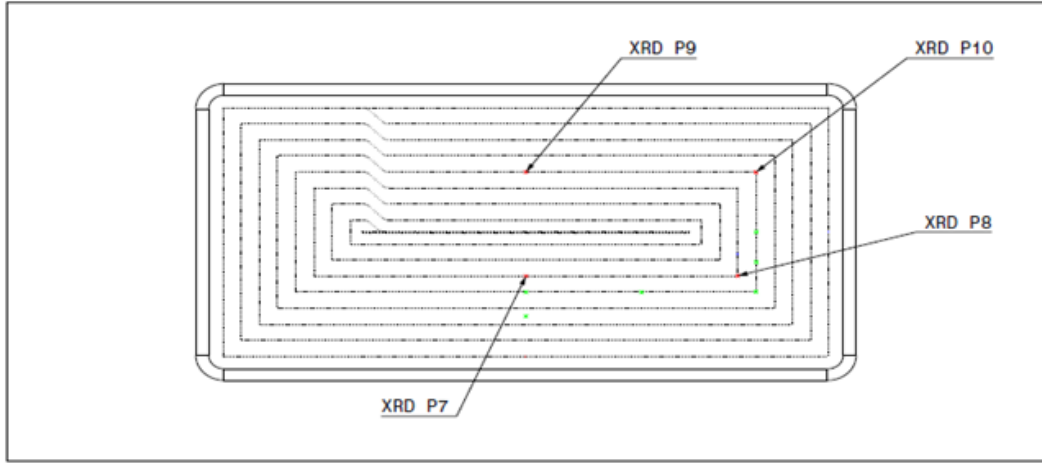


Figure 6-18: XRD measurement locations and stress profiles for coupon 7

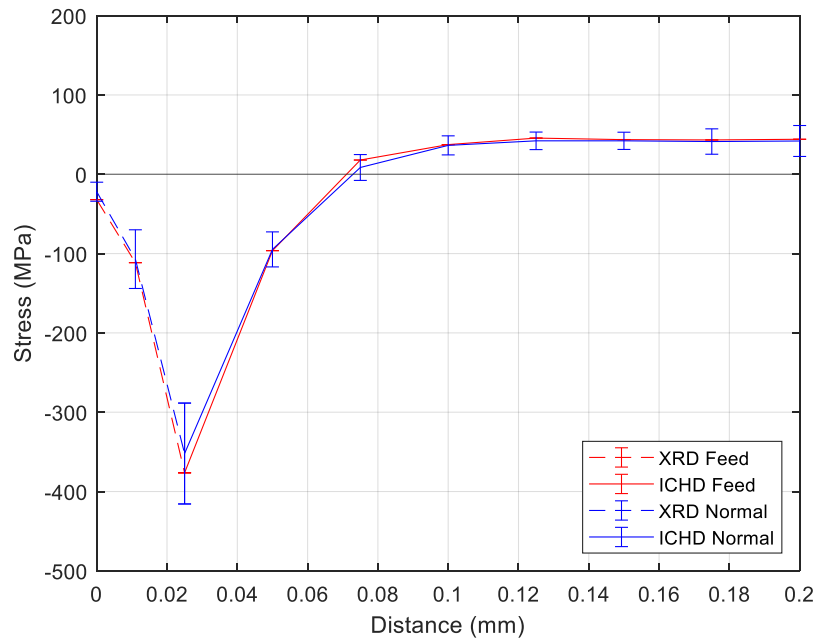


Figure 6-19: Straight line composite curve finish machining

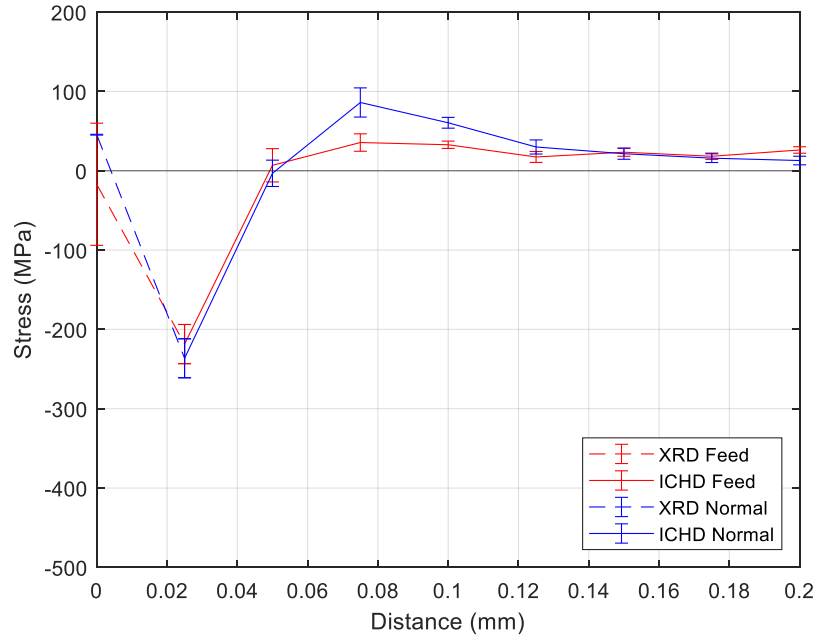


Figure 6-20: Corner point composite curve finish machining

Since performing the XRD measurements using the $\cos(\alpha)$ several studies have been conducted concerning near-surface residual stress determination in aluminium alloys. One notable paper compared techniques for attaining MIRS data for finite element distortion modelling [173]. They compared ICHD, Slotting, XRD $\sin^2(\psi)$ & XRD $\cos(\alpha)$ methods for determining MIRS in milled AA7050-T7451 plate. Their research concluded that all methods apart from the XRD $\cos(\alpha)$ showed a reasonable degree of conformity. The authors described the issue with $\cos(\alpha)$ noting that the Debye rings produced from measurements made on the machined aluminium alloy samples displayed poor signal quality, thus impacting the calculated stress. Figure 6-21 (a) shows the Debye diffraction pattern for a good signal response (made on mild carbon steel 1018), and Figure 6-21 (b) displays a poor response from measurements made on aluminium 6061 [176]. For the steel sample, the peak centre is consistent, whereas the aluminium sample displays an inhomogeneous intensity peak. The difference between the two materials is the grain distribution and morphology. The 1018 steel has a more homogeneous grain structure than the rolled AA6061 plate, which is highly textured.

The variable Debye intensity peak in the AA6061 measurements was consistent with the previous XRD $\cos(\alpha)$ measurements in AA7050 from [173]. The impact of the unfavourable texture of the rolled aluminium on the diffracted X-rays could also be exaggerated by the elongated grains, distorted in an anisotropic manner due to the machining-induced shear strain [177]. Thus, the aluminium grain orientations impact the X-ray diffracted beam through increased scattering, driving a poor signal response at the detector. Figure 6-21 (a) and Figure 6-21 (b) show example Debye rings of non-uniformity and improved uniformity taken from measurements of MIRS in milled samples [173]. Figure 6-21 (c) gives a representative Debye from the work conducted to determine MIRS in the near-surface layer for the pocket machining coupons. This Debye ring is representative of all XRD measurements made in the pocket samples. As can be seen, the peak intensities are inconsistent for all images and, therefore, can be used to explain the inconsistencies of XRD subsurface MIRS measurements.

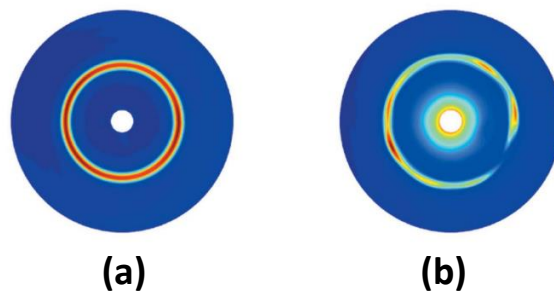


Figure 6-21: Debye 2D diffraction patterns for (a) mild carbon steel 1018 and (b) aluminum 6061 [176]

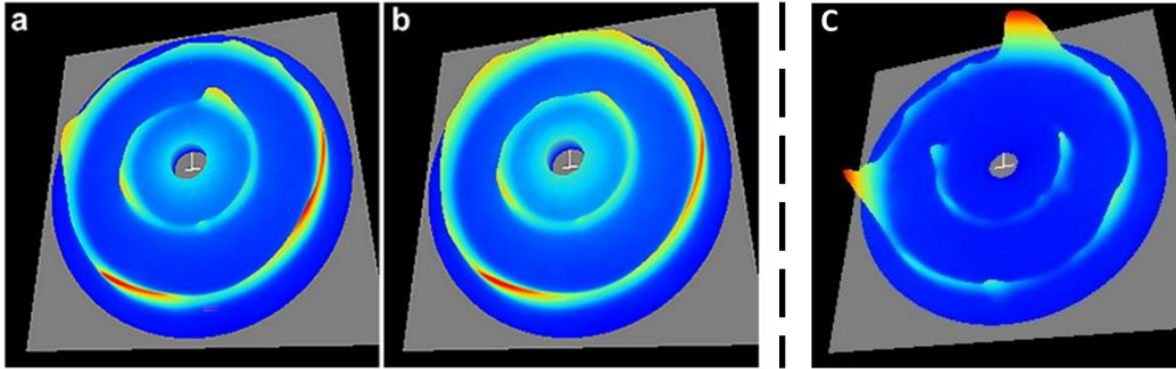


Figure 6-22: Example Debye rings of (a) non-uniformity and (b) improved uniformity from [176] and (c) Debye ring from pocket machining experiment coupon measurement (location C7 P10 – see figure 6-18)

To establish MIRS profiles for use in numerical modelling of residual stress related distortion, a combined profile of XRD and ICHD measurement data has been generated. Figure 6-19 and Figure 6-20 show the composite stress profiles generated to model the stresses observed at tool path straight line and corner points. The data utilised includes the XRD surface measurements and ICHD subsurface measurements made on coupon 7 & 8, which were subjected to conventional machining processes. The pocket machining conditions are reproduced when manufacturing the distortion demonstrator component (see section 6.4) against which the distortion modelling method will be validated (see section 6.4). Thus, the machining stress profile shall be used in future finite element analysis by fitting the data using a numerical expression such that it can be mapped across the simulated machined component where pocket machining has occurred.

6.2.9 Summary of the influence of local cutting conditions variations on MIRS

This experiment aimed to study the impact of tool path strategy selection on generated cutting forces and machining induced stresses as a function of the toolpath progression. The main conclusions are as follows:

- The dynamic roughing strategy utilised in this study generated significantly lower but more consistent peak cutting forces compared to the conventional helical spiral out roughing tool path. Max cutting forces for the dynamic strategy were 37%, 41% and 15% lower for the dynamic milling tool path in F_x, F_y and F_z measurement directions respectively. In terms of the average cutting forces, they were 39%, 20% and 34% lower in F_x, F_y and F_z measurement directions respectively.
- Stress profiles generated by conventional roughing utilising a helical spiral tool path exhibit more significant peak compressive subsurface stresses; 25% greater mean peak compressive stress in the feed direction and 43% increase in the normal measured direction compared to dynamic roughing.

Additionally, the compressive region formed under conventional roughing strategies extends deeper into the part than those generated by dynamic milling. This signifies that the increased loading from conventional rough machining process compared with the dynamic process causes a higher degree of plastic deformation driving the MIRS to form deeper and more compressive in nature [152].

- The subsurface stresses in the conventional helical spiral finished machined components on average showed slightly less compressive residual stresses peaks when compared with those generated by the conventional roughing process. But peak compressive stresses were also measured lower in the component generated with dynamic milling than the finishing procedure (once outliers were dropped from the analysis). The reduced compressive peak stresses cannot be explained only by the cutting forces alone as the conventional finishing tool path yielded lower average and max cutting forces than the dynamic tool path, indicating that other variables are influencing the MIRS generation [26].
- No discernible variation in max compressive stresses occurred between straight-line cutting and corner passes for the conventional spiral-out roughing procedure. However, for the finish machined test pieces the peak compressive induced stresses measured at the corners were 50% lower than the stresses measured at the straight-line cutting tool path regions. The reduced peak stress from corner measurement would indicate local variation in thermo-mechanical loading along the tool path, although this change in the MIRS is very localised to the region of tool path directional change.
- Discrepancy between ICHD and XRD subsurface measurements in the finished component was observed. It is suggested that the source of the discrepancy can be attributed to the stress measurement technique, as this has also been observed in the literature [173].
- The repeat XRD and ICHD measurements have been averaged with respects to the machining direction to generate a combined stress profile, to be fit and used in finite element to determine its contribution modelling of the residual-stress related distortion.

6.3 Bulk residual stress measurements

Figure 6-23 shows the layer removal measurement results made on samples 301 and 302 extracted from the rolled plate. The samples were extracted from similar positions in the mother plate (see section 5.4), so measured stresses are expected to be consistent across samples and with those found in the blanks used to generate the distortion modelling demonstrator. The residual stress profiles determined by the layer removal method exhibit a typical 'M' shape profile as described by Prime *et al.* [35], where tensile stresses exist and the centre of the plate balanced by compressive stresses towards the edge of the plate. The sample and magnitude of the bulk stresses are consistent with bulk residual stresses that form post quenching and stretch stress relieving. Local maxima and minima stresses occur at expected regions where one balances the other so that the whole stress field is in equilibrium. The repeat measurements between test samples 301 and 302 (see section 5.4) show good a correlation in both the longitudinal (L) and long-transverse (LT) principal directions.

Differences between longitudinal and long-transverse stress profiles can be identified. A shallower stress minimum at the centre of the plate and greater minima stresses towards the edges of the plate are found in the long-transverse direction compared with the longitudinal direction. This can be credited to the absolute difference in stress magnitudes between the two directions as described by Denkena *et al.* [57], who also found differences between the longitudinal and long-transverse directions when performing layer removal on samples extracted from 7075 T7651 rolled plate. Also, variable stress states arise closer to the surface when comparing the two measurement directions. The long-transverse stress profiles change from a compressive stress state at the local minima towards the edge of the plate switching to a tensile state at the surface. The longitudinal stress profiles also show similar trends going from compression to tension from the local stress minima to the surface until approximately 1.5 mm from the surface, where a sharp switch back to compression can be observed. A suggestion for this change in stress sign could be the effect of rolling and/or stretch stress relief inducing plastic deformation which occurs along the longitudinal direction.

The measured longitudinal and long transverse direction maxima stress for both samples $\approx 11 \pm 2$ MPa at ≈ 18 mm and ≈ 32 mm through thickness. The minima stresses differed according to the orientation of the samples measured. The minima stress for the samples extracted in the longitudinal direction exhibit minima stresses $\approx -10 \pm 1$ MPa at ≈ 8 mm and ≈ 42 mm through thickness. Minima stress for both samples extracted in the long transverse direction $\approx -14 \pm 1$ MPa at ≈ 6 mm and ≈ 44 mm through thickness. The

stress measurements were averaged with respect to the plate direction and used in the generation of fit models used in the FE distortion model.

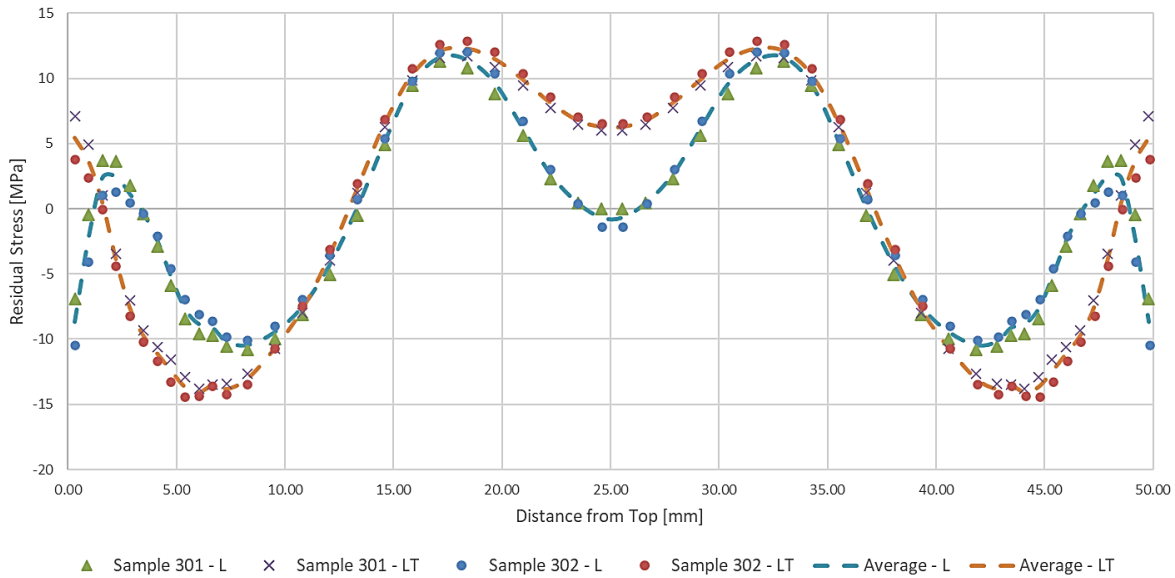


Figure 6-23: Residual stress in Kaiser 7050 T7651 plate

6.4 Distortion demonstrator machining trials

6.4.1 Stage 1 CMM measurement results

Figure 6-24 shows the averaged coordinate measurement machine (CMM) distortion measurements recorded along each of the measurement profiles of the distorted plates (see section 5.5.4.1) for each test and repeat. After stage 1 machining and release from clamps all plates distorted with the same bending trend. The plates all exhibited a negative sagging bending mode. Note the results are presented in a positive bending mode as the plates are flipped prior to measurement. Figure 6-25 displays the averaged peak distortion for each test configuration trailed, where the variable altered was the machining depth of cut sequence (see section 5.5.2). The averaged peak distortion between test is 0.420 mm. The standard deviation for each test configuration is such that the average peak distortion passes through all but test 4, which only slightly deviates from this trend (0.017 mm difference from lower standard deviation band to the average peak distortion).

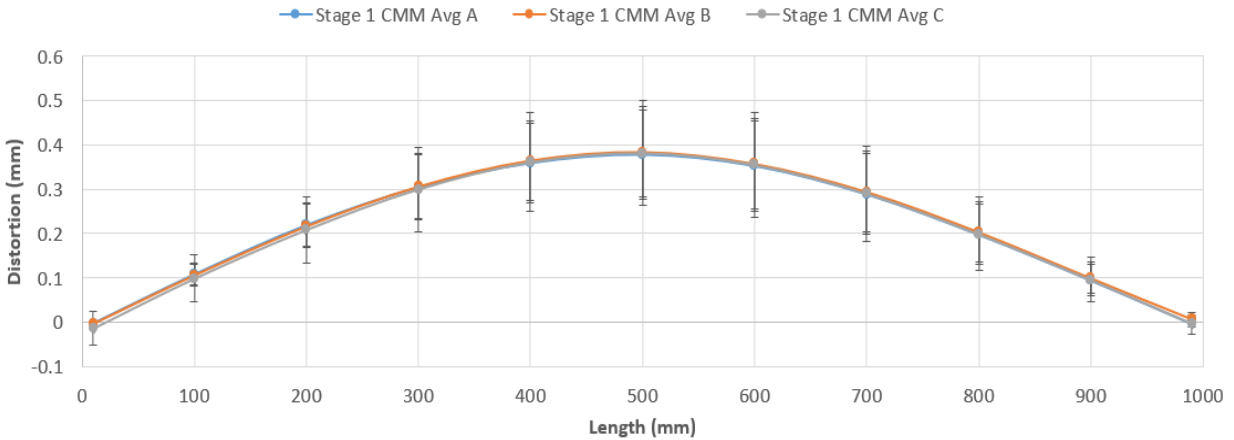


Figure 6-24: Average stage 1 measured deflection profiles

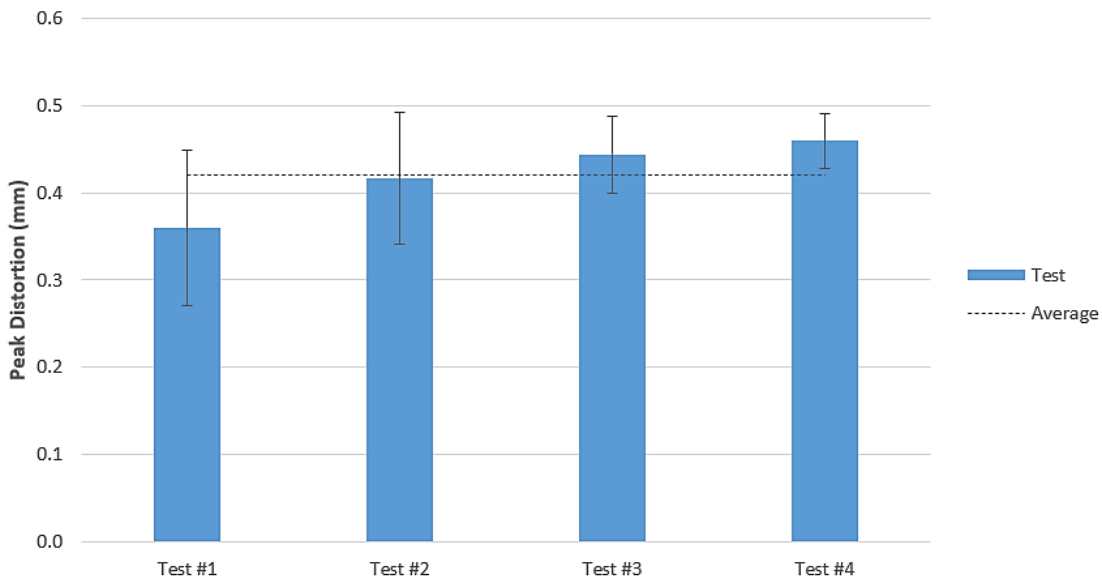


Figure 6-25: TPC2 Stage 1 peak distortion

6.4.2 Stage 2 CMM measurement results

Figure 6-26 shows the measurement profiles for all stage two machined components. As per stage 1, all coupons after stage 2 machining distorted after clamp release with the same trend, although the bending mode was opposite to stage 1 mode ('hogging'). Figure 6-27 displays the peak distortion values for the measured stage 2 components. The average and standard deviation is plotted for reference. A max peak distortion of 1.181 mm was observed for TPC2-S2-2. The minimum peak distortion of 0.751 mm was measured in TPC2-S2-3. Average peak distortion was calculated at 1.061 mm, which occurred at the centre of the plate. Measured peak distortion was very similar for TPC2-S2-1, TPC2-S2-2 & TPC2-S2-4, with a

standard deviation of ± 0.012 mm between measurements. TPC2-S2-3 shows a lower peak distortion of approximately 0.25 mm below average. This is considered an outlier within the test range.

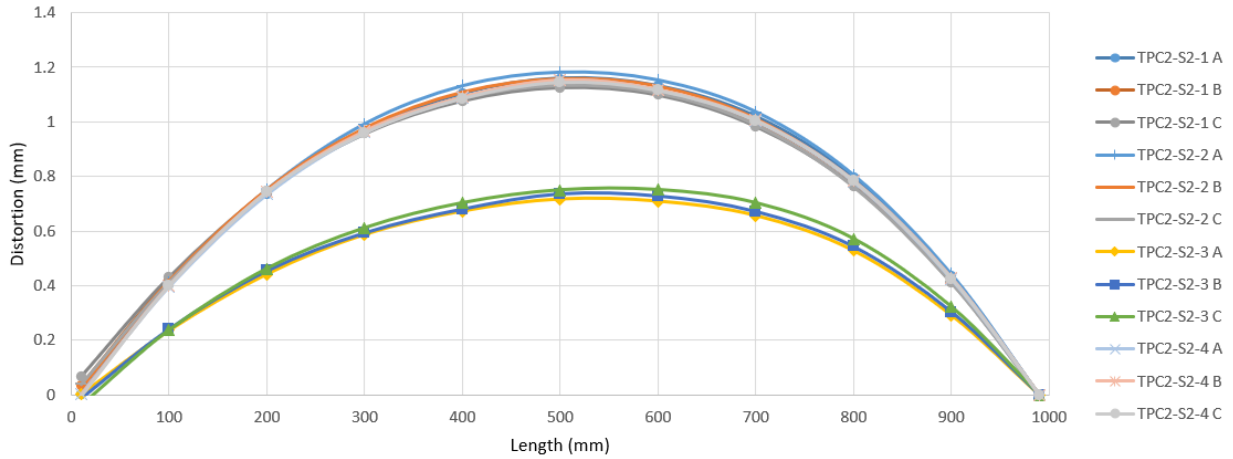


Figure 6-26: TPC2 stage 2 distortion measurements

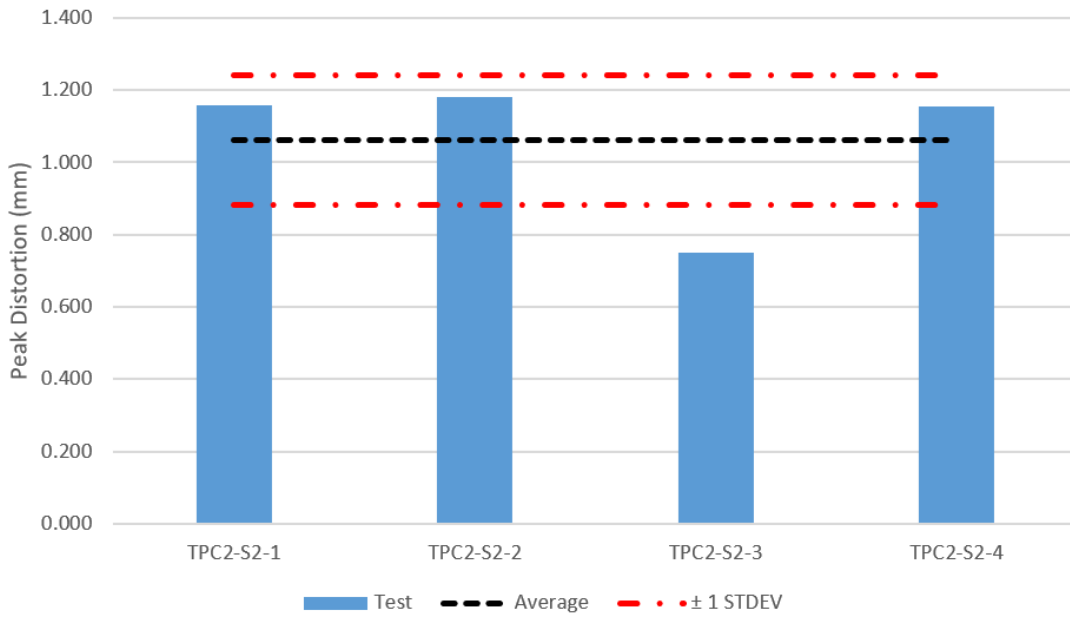


Figure 6-27: TPC2 Stage 2 peak & average distortion

6.4.3 Distortion demonstrator discussion

The stage one CMM measurements indicate that varying the axial DoC between roughing machining passes does not influence the distortion response. For most of the test variations, the peak deflection measurement falls within \pm one standard deviation from the average peak deflection, apart from test four which only slightly sits outside of this band. The post-stage one machining deflection measurements indicate that for the configuration of the test piece geometry and material removal scheme, the redistribution of residual stresses is independent of the machining DoC sequence. From stage 2 CMM measurements, the same conclusion can be drawn. When dismissing TPC2-S2-3 as an outlier, it can be stated that stage one machining sequence variation has no significant impact on the final post-machining distortion. This finding is consistent with the summary given for the sequential machining DoC MIRS trial (see section 6.1.1), where no significant variation in the resulting MIRS in the final machined surface was found when altering the depth of cut in the preceding machining passes. If it is assumed that the bulk residual stress is released consistently across that varying Z-level material removal sequences trial coupled with the same MIRS imparted at the finished surface, then the residual stress condition across the test pieces is similar and, therefore must be the distortion recorded. The next paragraphs consider the redistribution of the bulk stresses versus the machining DoC sequence in more detail.

Figure 6-28 displays a diagram depicting the redistribution of bulk residual stress upon machining of the stage one billet. Before machining the stock condition, global bulk residual stresses are in equilibrium, Figure 6-28 (a). For stage 1 machining, half of the plate material is removed by various DoC sequences. To generate the same distortion response across all test pieces, the bulk residual stress state in the remaining material must be consistent prior to clamp release (it is assumed that the MIRS has little impact on distortion during stage 2 due to the thickness of the plate material (see section 2.5.4). Figure 6-28 (b) shows the removal of the material and the remaining residual stresses, which are unbalanced about the position of the new centroid axis. The part is still clamped at this point in the machining process, which constrains the moments generated by the unbalanced internal stresses. Figure 6-28 (c) shows the direction of bending generated by the internal moments after release from clamps.

Regarding stage 2 distortion, it was considered that the residual stress impact is twofold. First, the remaining bulk residual stresses (which have reached a new equilibrium state after stage 1 machining) will again be unbalanced and will redistribute after stage 2 machining, upon release of work holding. Secondly, the thickness of the part is significantly reduced, and therefore the influence of the machining induced residual stresses will impact distortion to a greater extent. As the machining strategy did not

change during stage 2 machining, the bulk residual stress release and redistribution should be similar across all tests. Part of the hypothesis was to understand if the machining-induced residual stresses are variable when machining side 'B' (face milling stage) and elicit a variable distortion response post-stage 2 machining. Due to no observable difference in distortion magnitude and MIRS formation (see section 6.1), it can be said that sequential cutting sequencing has no impact on machining induced residual stresses imparted during stage 1 machining and final distortion.

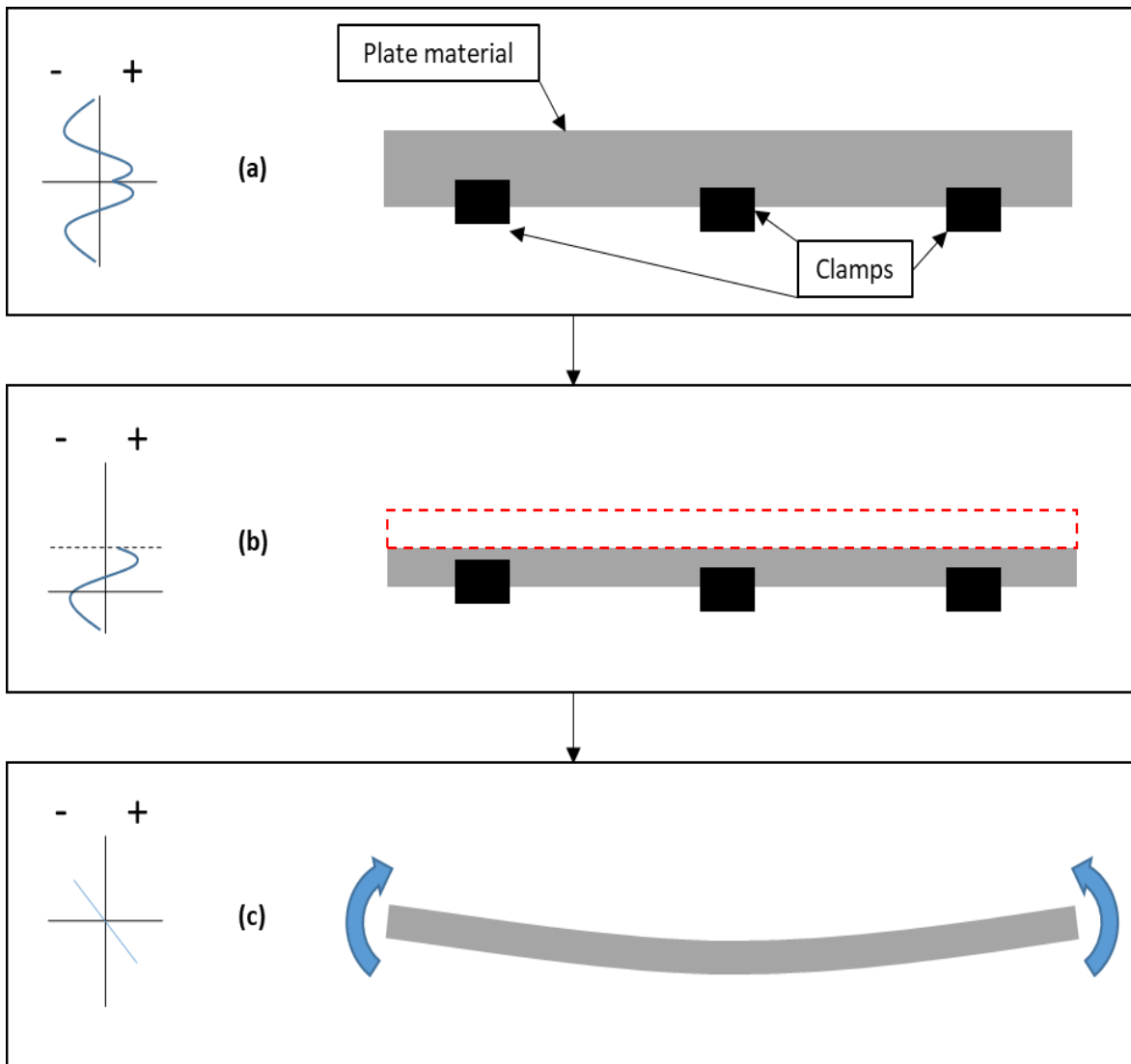


Figure 6-28: Stages of bulk residual stress release during stage 1 machining; (a) initial clamped condition; (b) the material removed in the clamped condition; and (c) residual stress redistribution after clamp release.

6.5 Concluding statements

In this chapter, results from a series of experimental trials have been presented. Machining trials have been conducted to study the influence of sequential machining processes and machining tool path strategy on MIRS generation. The characterisation of bulk residual stress by layer removal method measurements is also presented. Moreover, the results of the distortion demonstrator machining trials are given.

In section 6.1, the impact of sequential face-milling machining operations on the generated machining-induced stresses in the final component was studied through machining trials and residual stress measurement. It was determined that for the variable sequences trailed and machining parameters, no evident influence of the depth of cut sequencing on the final machining-induced residual stress was found. The final machining-induced residual stresses in the test coupons were consistent for the test range. Thus, it can be said that for the machining conditions trialled (based on industrial practices), the sequential machining strategy does not influence machining-induced residual stress in the final surface layer. Therefore, the assumption that subsequent passes remove the MIRS generated by previous machining passes holds for trialled material removal sequences. Therefore, based on the observations made, it can be suggested that the assumption only to consider the final machining pass when measuring stresses for use in finite element models predicting machining-related distortion is valid. The stress data generated in these trials will be used in the numerical modelling of process-induced distortion.

Secondly, a set of pocket-milling machining experiments were designed to investigate the impact of tool path strategy selection on generated cutting forces and machining-induced residual stresses. The experiments were created to observe how machining-induced stresses vary as a function of the tool path progression for variable strategies. Two coupons were machined using conventional and dynamic roughing strategies that were then subjected to near-surface residual stress measurements. The measurement locations were positioned concerning the tool centre point progression for each tool path. It was found that the dynamic roughing process generated lower cutting forces than the conventional roughing process. This trend was also observed in the machining-induced compressive residual stress values, where the dynamic milling process produced much lower peak magnitudes than the conventional roughing strategy. This influence can be ascribed to the mechanical loading, which is known to influence the compressive MIRS magnitude, where the dynamic tool path imparts lower cutting forces and, therefore, compressive MIRS magnitudes to the workpiece near surface material compared with the more aggressive conventional roughing process. Two additional coupons were produced using the conventional

spiral-out roughing and finishing strategies. The stresses measured in the finished coupon as a function of the tool path were shown to vary between straight-line cutting and corner cutting. However, this variation was only seen locally in the corner region where surrounding measurements along the tool path was consistent. These findings inform the representation and use of MIRS data as input to the distortion model. Furthermore, It may also be advantageous to explore the use of dynamic milling in roughing and finishing of aerospace components, where reducing the magnitude and depth of compressive stresses would help manage the inter-process and post-process MIRS related distortions.

The third set of experiments consisted of layer removal method measurements for bulk residual stress characterisation of 50 mm thick rolled aluminium billets. The residual stresses were determined in the longitudinal and long-transverse rolling directions, which showed directional dependence in the through-thickness stresses. The bulk residual stresses measured were comparable to those reported in the literature for similar materials [35].

The fourth set of experimental trials involved machining distortion 'demonstrator' components to (1) study the influence of a sequential machining process on component distortion and (2) validate the developed numerical modelling approach. The depth of cut sequences studied in the first set of machining trials was replicated in stage 1 machining of aluminium plates, which were then measured for deflection post-machining. No apparent influence of the depth of cut sequencing on final distortion was observed. This influence also carried through to stage 2 machining. This finding could have industrial practice ramifications where the depth reduction perceived to manage final part distortion is not based on scientific fact and thus acts as an unnecessary source of process inefficiency.

7 Modelling Results & Discussions

7.1 Validating the MIRS concept against a different modelling methodology

To evaluate the introduction of MIRS within boundary layers in the modelling concept, a comparison study has been made to a similar technique to determine applicability. The case in question is taken from Dreier's EngD work [150], where the example considers a simple cantilever beam bending problem. It is possible to derive analytical expressions for the distortion caused by imbalanced internal stresses for the simple cantilever beam, making it a suitable candidate to explore and validate the modelling methodology. In the case of Dreier's modelling approach, MIRS is applied to refined surface layer elements according to their position from the 'machined' surface. The stress tensor for a given element in the boundary layer is determined by subdividing the sinusoidal curve fit according to the considered depth length in the discretised boundary zone, and expressing the MIRS as a mean value of the fit at the element centroid using the following integral:

$$\sigma = \frac{\int_a^b \sigma(x) dx}{b - a} \quad 7-1$$

Where a and b denote the upper and lower limits of the discretisation layer dept. The MIRS application method, developed in the work presented in this thesis, defines discrete MIRS tensor values at element integration points for a higher resolution definition of the internal residual stress state as highlighted in [147], [151]. Therefore, the comparison will be drawn for this simple case so that the modelling approach is verified.

Dreier's modelling method made use of ABAQUS quadratic formulation tetrahedral elements (C3D10) in both the refined boundary layer and the bulk of the part with variable edge lengths. The method developed for this work, presented in section 4.2.2 of this thesis, uses ABAQUS boundary layer quadratic type wedge elements (C3D15) and UMAT user subroutine. From here, this developed procedure will be referred to as the 'UMAT' method of MIRS application. The performance of the boundary layer wedge elements in describing the MIRS state and driving distortion is compared with the tetrahedral solution posed by Dreier in the following section. Figure 7-1 (a) details the cantilever beam parameters, considering the mechanical problem to simulate. It is possible to calculate the bending moment and the resulting distortion of the beam caused by stresses contained within a discrete layer (in Figure 7-1 - denoted by σ_L). To test the subtlety of the modelling method in simulating distortion compared with two analytical

expressions for beam distortion. The beam bending moment (M_b) for both analytical expressions is given by the following formula:

$$M_b = \sigma_M \times h_r \times b \times h_l \quad 7-2$$

Where the stress driving the bending moment (σ_M), acts over the area defined by the stress-affected boundary layer height (h_r) and width of the beam (b) positioned from the natural fibre of the beam (n) by the lever arm length (h_l). For both analytical expressions, the second moment of area or area moment of inertia (I) of the beam is used:

$$I = \frac{bh^3}{12} \quad 7-3$$

Where the height of the beam (h) is required. The two analytical methods utilised by Dreier are the Euler-Bernoulli and Timoshenko beam theories. The Euler-Bernoulli method calculates distortion (w) at a discrete point along the beam (x) using the formula:

$$w(x) = \frac{M_b l^2}{2EI} \left(\left(\frac{x}{l} \right)^2 - \left(\frac{x}{l} - 1 \right) \right) \quad 7-4$$

Where Young's modulus (E) and the length of the beam (l) are referenced. The main limitation of the Euler-Bernoulli method is that shear deformation is not accounted for. The Timoshenko method accounts for the impact of shear deformation on overall distortion by including a shear modulus term (G) and a shear correction factor (A_s):

$$w(x) = \frac{M_b l^2}{2EI} + \frac{M_b}{2GA_s l} \quad 7-5$$

Where shear modulus:

$$G = \frac{E}{2(1 + \nu)} \quad 7-6$$

Giving that Poisson's ratio as ν . The shear correction factor is defined:

$$A_s = \mathcal{X}A \quad 7-7$$

Where \mathcal{X} is the shear correction factor given as 5/6 for a rectangular beam. Considering the radius of inertia (i) has the following relationship:

$$I = i2A \quad 7-8$$

Then equation 7-8 can be rewritten in the form:

$$w(x) = \frac{M_b l^2}{2EI} \left(\left(\frac{x}{l} \right)^2 - \left(\frac{x}{l} - 1 \right) \right) \left(1 + \frac{6(1+\nu)i^2}{xl^2} \right) \quad 7-9$$

Where the radius of inertia for the beam:

$$i = \frac{h}{2\sqrt{3}} \quad 7-10$$

The beam dimensions considered in the constant stress layer analysis using both the analytical and numerical calculations are as follows; Length (l) = 100 mm, width (b) and height (h) = 10 mm. The boundary layer height (h_r) was taken as 0.2 mm for the beam case study. For the analytical solutions, the elastic material properties were given as; Youngs' modulus (E) = 70,000 MPa and Poisson's ratio (ν) = 0.34. For the numerical analyses, Poisson's ratio (ν) was set to = 0 as the analytical solution considers the contraction of the beam only in two dimensions. Therefore, including this term in the three-dimensional numerical solution influences the longitudinal distortion results by accounting for the transverse contraction. The beam is considered fixed at one end. In the numerical solution, this is applied by setting Encastre boundary conditions at the end of the beam. The distortion of the beam (Δz) is characterised by the displacement in the z-direction, as shown in Figure 7-1 (b). To compare the numerical results against the analytical solutions, nodal displacements are extracted from the bottom of the deformed beam model designated by the blue dotted line in Figure 7-1 (b). The nodal positions are aligned with the coordinates centre of the beam length ($z = 0$ & $b/2$).

Attempts were made to reproduce Dreier's [150] beam bending ABAQUS model as detailed in [150] to compare MIRS introduction methods in the numerical analyses. The beam model was created in ABAQUS, with 1 mm edge length C3D10 elements for the bulk of the beam and refined elements in the near-surface zone with shorter edge lengths according to the discretised depth (0.2 mm). Residual stresses were introduced to the boundary layer elements using ABAQUS *INITIAL CONDITIONS, TYPE = STRESS keywords. The model was then reproduced using the 'UMAT' MIRS method developed in this work, including the affected zone mesh refinement and MIRS introduction detailed in section 4.2. Two boundary layer stress conditions presented in Dreier's work are considered here. In the first instance, Dreier applied a constant stress tensor value of -100 MPa uniformly in the σ_{11} direction throughout a refined layer depth

of 0.2 mm. Second, a representative stress profile is used to map a complex stress gradient across multiple elements comprising the boundary layer.

For the constant stress boundary layer case, the analytical and numerical results are compared in Figure 7-2, where it can be seen that all are in agreement. The analytical results match those reported by Dreier, where max distortion for the Euler-Bernoulli and Timoshenko were calculated as -0.0840 mm and -0.0847 mm, respectively (difference of $7\mu\text{m}$). Both numerical models generated a peak distortion of -0.0842 mm. This is an error of 0.6% compared with the Timoshenko analytical result. However, Dreier's work reported a peak distortion of -0.0823 mm with his stress application and mesh refinement modelling method. Therefore, a difference of 2.2% in peak distortion between the reproduced numerical beam bending model and that reported by Dreier is obtained. This slight difference is suggested to be caused by the non-exact method of reproducing Dreier's near-surface mesh refinement technique. Therefore, exact element distribution density may not have been achieved, influencing the calculated distortion. However, the slight difference suggests that the method was closely replicated, and the results can be compared. Therefore, it can be stated that in the case of constant stress applied across the boundary layer, each method performs equally well.

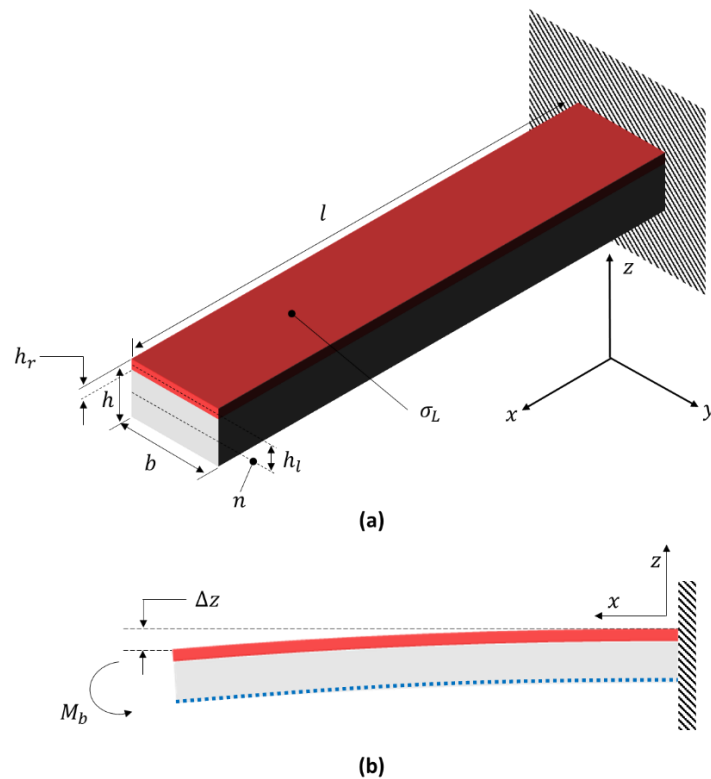


Figure 7-1: Cantilever beam [150]

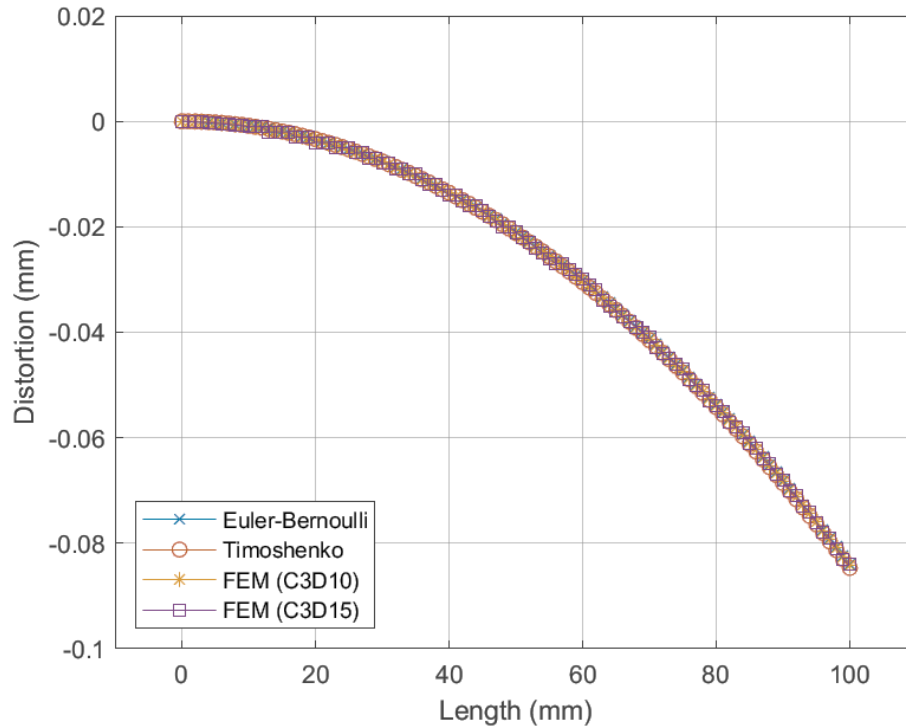


Figure 7-2: Comparison of the analytical and numerical MIRS modelling methods [150]

In the second case considered, Dreier applied arbitrary representative stress profiles across a refined boundary layer mesh to determine the ideal boundary layer discretisation with regard to the through-layer element density. The stress profiles are defined using the sinusoidal decay formula (given by equation 2-7 in section 2.6.2) [150]. One of the profiles (denoted ‘function 1’) has been reproduced from the cited work and used to compare the MIRS application methodologies. Function 1 stress profile is shown in Figure 7-3. The sinusoidal decay parameters used to define function 1 are given in Table 7-1. To maximise the influence of the stressed layer on bending moments, Dreier reduced the thickness of the bending beam to 2 mm. Dreier’s method of MIRS application defines arithmetic mean stress for each number of discretised element layers using the integral given by equation 7-1. This work calculated the arithmetic mean stress numerically using MatLab software.

Table 7-1: Sinusoidal fit parameters for function 1 [150]

c	ζ	ϕ	ω_d
1200	0.780	85°	14,000

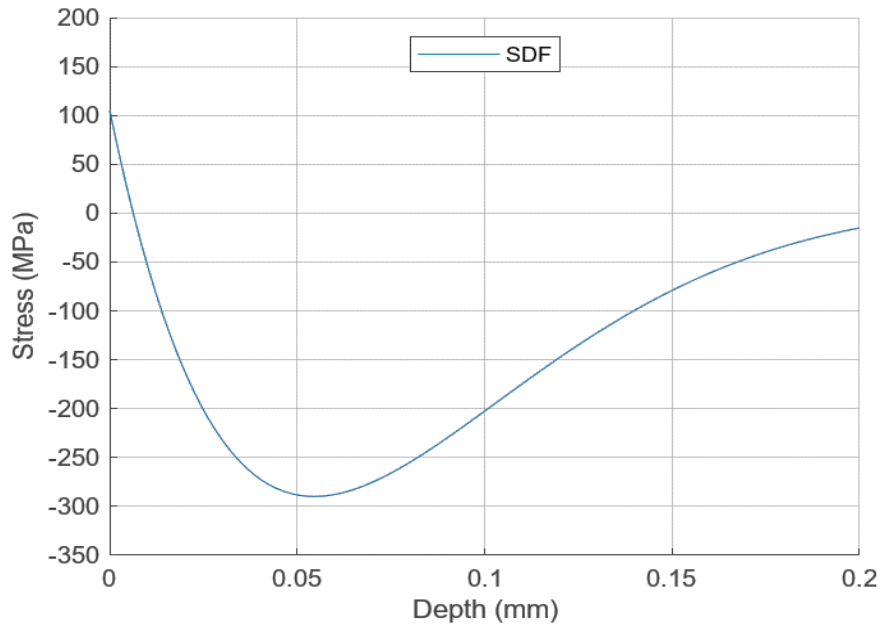


Figure 7-3: Dreier's function 1 MIRS profile [150]

Figure 7-4 shows the simulated distortion results for the cantilever beam with function 1 applied across various refinements of the surface boundary layer height using Dreier's MIRS application methodology. It can be seen that the beam distortion converges due to the boundary layer mesh refinement. In this case, peak distortion converges after three boundary layer element refinement with a difference of 0.23%.

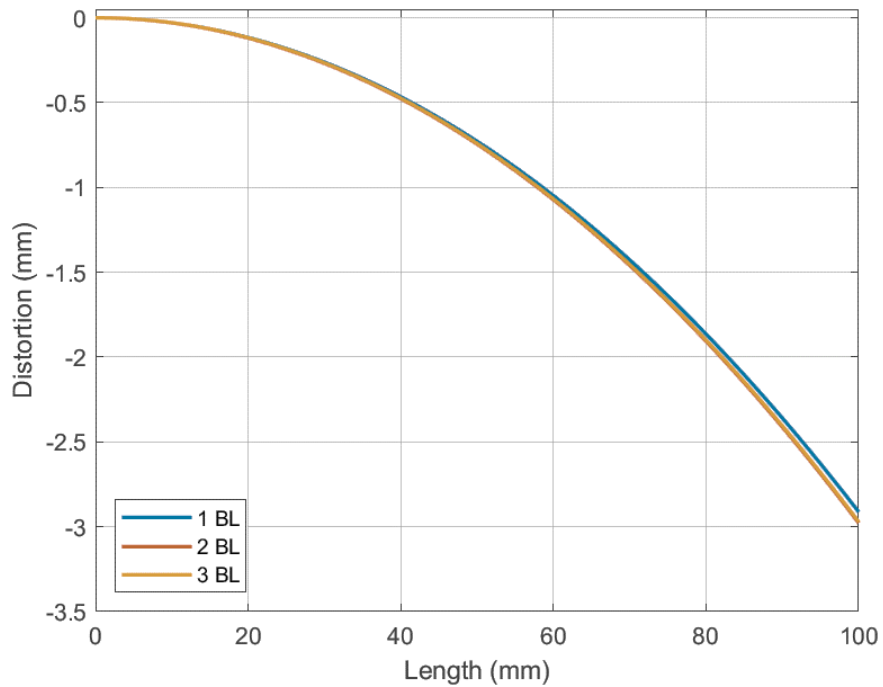


Figure 7-4: Beam bending due to MIRS using the Dreier method of stress implementation.

Figure 7-5 highlights the arithmetic mean MIRS values calculated for various spacing intervals according to the boundary layer height discretisation. These stresses are mapped across the boundary layer mesh (constant height of 0.2 mm) using *INITIAL CONDITIONS, TYPE = STRESS keywords. The sinusoidal decay function fit used to determine the mean stress values has also been plotted for reference. It can be seen that numerous refinement levels are needed to approximate the MIRS function values. Therefore, the challenge is sufficiently representing the MIRS values when a steep stress gradient is exhibited close to the machined surface.

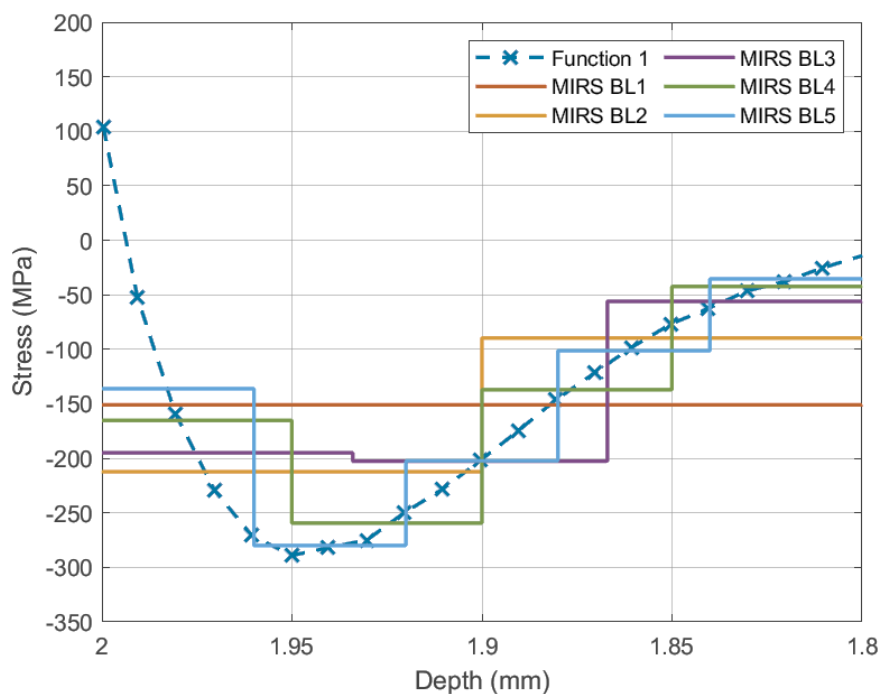


Figure 7-5: Dreier method applied MIRS values extracted from the FEM model.

Figure 7-6 presents the FEM bending beam results when applying MIRS using the 'UMAT' method. After the third mesh refinement, the percentage difference in the peak distortion from the previous mesh refinement is 0.24%. Figure 7-7 displays the MIRS values obtained from the boundary layer elements. Compared with Dreier's method, an improved representative stress profile is obtained, even with a refinement of just three elements through thickness.

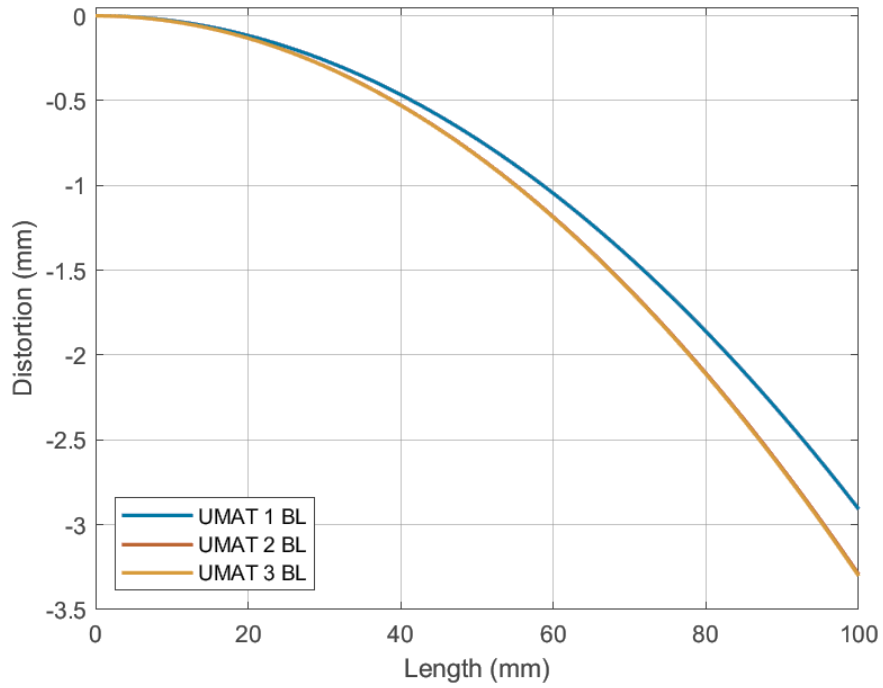


Figure 7-6: Beam bending due to MIRS using the UMAT method of stress implementation developed in this work.

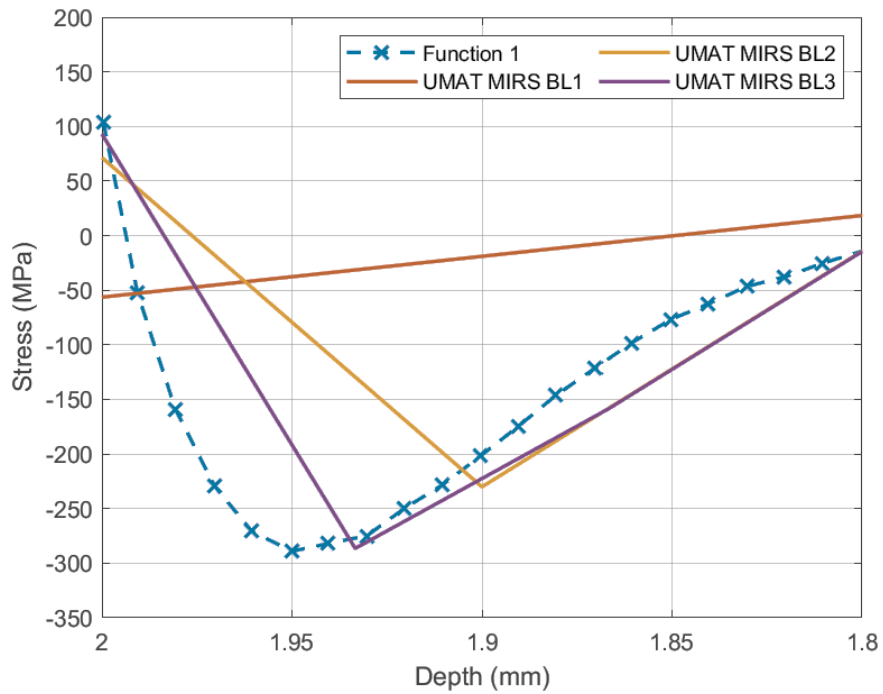


Figure 7-7: UMAT applied MIRS stress values extracted from FEM model.

It should be noted that the method of element stress retrieval from ABAQUS is conducted such that the stress values at integration points are extrapolated to nodes based on the shape functions used by the given element and averaged according to the proximity of a given node to the integration points within the element. Therefore, an accurate representation of the MIRS in the element defined using this method is not given in Figure 7-7.

However, due to the structure and formulation of the C3D15 boundary layer elements and the method of stress application developed in this work, it is possible to describe a stress gradient across even one element. Thus, high gradient stress profiles that occur over small depths can be described accurately using the developed method, compared to methods that apply constant mean stress values over one boundary layer. Hence the difference in peak distortion was observed between the methods.

7.2 Modelling residual stresses

This section concerns using experimentally determined residual stress data to define empirical models for distortion modelling.

7.2.1 Bulk Residual stress

The distortion demonstrator designed and manufactured to validate the modelling methodology has been machined from 50 mm thick rolled billet 7050 aluminium alloy. The layer removal method, as described in section 5.4, determined the bulk residual stress data. The measurement results are presented in section 6.3. Figure 7-8 shows half of the averaged experimental longitudinal and long-transverse bulk residual stress data and polynomial fits used to parameterise the stress data in the *SIGINI user subroutine. It is possible to map the stress about the centre of the plate model such that only half the stress profile needs to be described. A ninth-order polynomial expression was used to fit the bulk stress data in both L and L-T directions with the form:

$$\sigma_{bulk} = p_1 x^8 + p_2 x^7 + p_3 x^6 + p_4 x^5 + p_5 x^4 + p_6 x^3 + p_7 x^2 + p_8 x + p_9 \quad 7-11$$

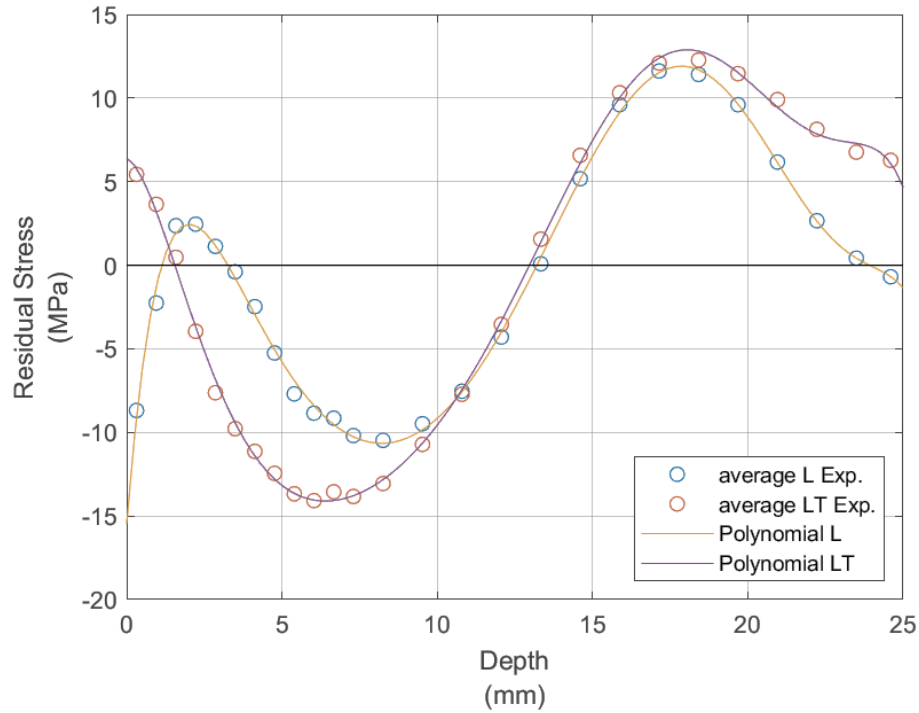


Figure 7-8: Longitudinal and long-transverse bulk stress data and fits

Where p_n = coefficients for the polynomial fit depending upon the direction. Table 7-2 and Table 7-3 contain the coefficients for longitudinal and long-transverse bulk residual stress polynomial expressions. Figure 7-9 displays the results of applying the bulk stress in the longitudinal direction corresponding to the S11 in the FEM. Figure 7-10 shows the long-transverse stress applied in the S22 direction. Consideration for the mesh density for bulk stress mapping and distortion is given in section 7.3.

Table 7-2: Longitudinal polynomial coefficients (to 2 DP)

p_1	p_2	p_3	p_4	p_5	p_6	p_7	p_8	p_9
-1.87e-07	1.94e-05	-8.29e-04	0.02	-0.26	2.19	-10.61	23.24	-15.47

Table 7-3: Long-transverse polynomial coefficients (to 2 DP)

p_1	p_2	p_3	p_4	p_5	p_6	p_7	p_8	p_9
-1.79e-07	1.76e-05	-7.02e-04	0.01	-0.17	1.15	-3.45	-0.97	6.41

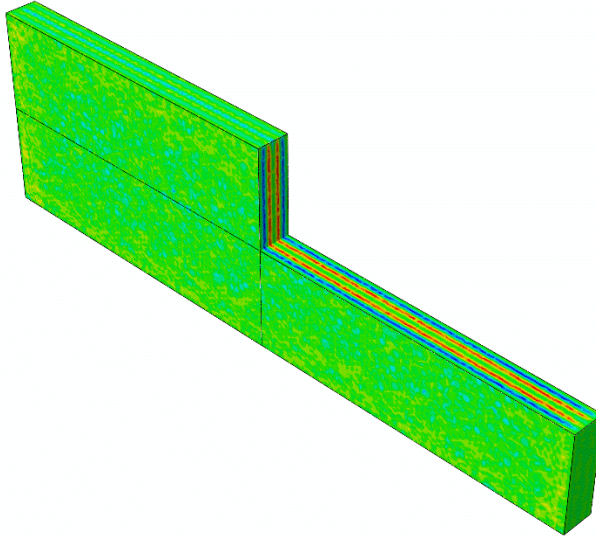
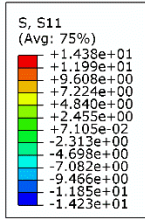


Figure 7-9: FEM longitudinal bulk stress

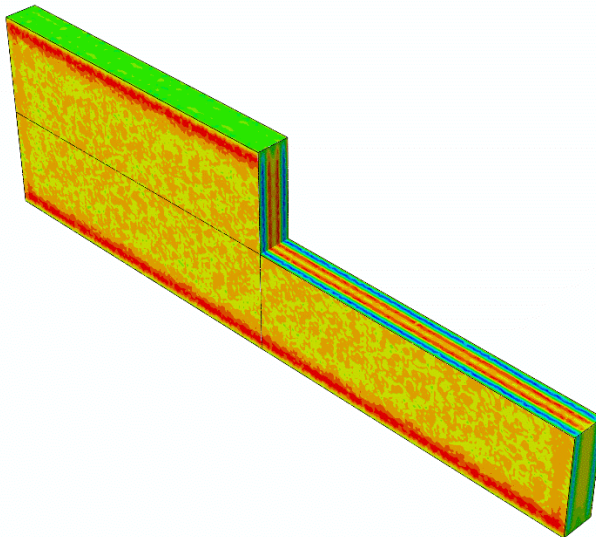
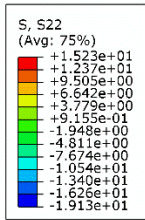


Figure 7-10: FEM long-transverse bulk stress

7.2.2 Machining-induced residual stress

Induced residual stresses at the component surfaces, caused by the machining process, has been shown to influence the final distortion of components post-manufacture. Therefore, when modelling machining-related distortion, it is essential to accurately represent these stresses within a boundary layer simulating the machining-affected zone. However, there must be a trade-off between solution accuracy and simulation efficiency as the element number increase will ultimately result in a much longer computation time.

As with the bulk residual stress, the empirically determined MIRS data must be described by a function such that the application via user subroutine can be realised. Traditionally, polynomial fits have been used to describe MIRS in previous work. Ulutan presented the uses of the sinusoidal decay function in modelling the MIRS [124]. Since this work, other researchers have employed the function in fitting experimentally determined MIRS and applying process-related residual stresses throughout finite element models when simulating machining-related distortion [150]. In this work, the sinusoidal decay function is used to describe the MIRS when assigning stress values at element integration points.

Fitting the data

In this work, two types of machining are considered for their influence on MIRS-related distortion. These are the face and end milling processes subjected to an experimental investigation within this work (see section 5.2 & 5.3). Both types of machining have been utilised extensively across the machined demonstrator component. Face milling was used to generate the datum face of the demonstrator component, and end milling was used for producing the pocket features. The residual stresses determined by a combination of incremental hole drilling and x-ray diffraction (see sections 6.1 and 6.2) have been subject to curve fitting using various methods.

Figure 7-11 displays the data and fits for the face milling MIRS, and Table 7-4 contains the parameter values for both feed and normal direction MIRS profiles optimised for using the particle swarm optimisation function in MatLab. The data was taken as the average of the MIRS profiles in Figures 6-5. Figure 7-11 (a) shows the feed direction MIRS measured data, the polynomial and sinusoidal decay functions (SDF) used to characterise the stress. Figure 7-11 (b) displays the same information but for normal direction MIRS. It can be seen that the polynomial Figure 7-1 approximation in both cases seems to overpredict the MIRS at the surface and suffers from oscillations after passing through the stress transition point (compression to tension) due to Runge's phenomena. Additionally, the stresses reported

after 0.2 mm are considered to be influenced by the bulk residual stress in part because the effective MIRS depth has been shown in the literature to extend the range considered [27], [78] and partly due to the stress magnitude being in the range of the measured bulk residual stress ($\approx \pm 15$ MPa). The sinusoidal decay function performs better when fitting the data than conventional polynomials as it does not suffer from the overestimation of the surface MIRS and oscillations exhibited by the polynomial and reduces to zero past the considered MIRS affected zone.

Table 7-4: Face milling SDF parameter values (to 2 DP)

-	c	ζ	ϕ	ω_d
Face mill feed (σ_{\parallel})	244.237	0.999	177.511	23.014
Face mill normal (σ_{\perp})	249.126	0.633	177.512	23.016

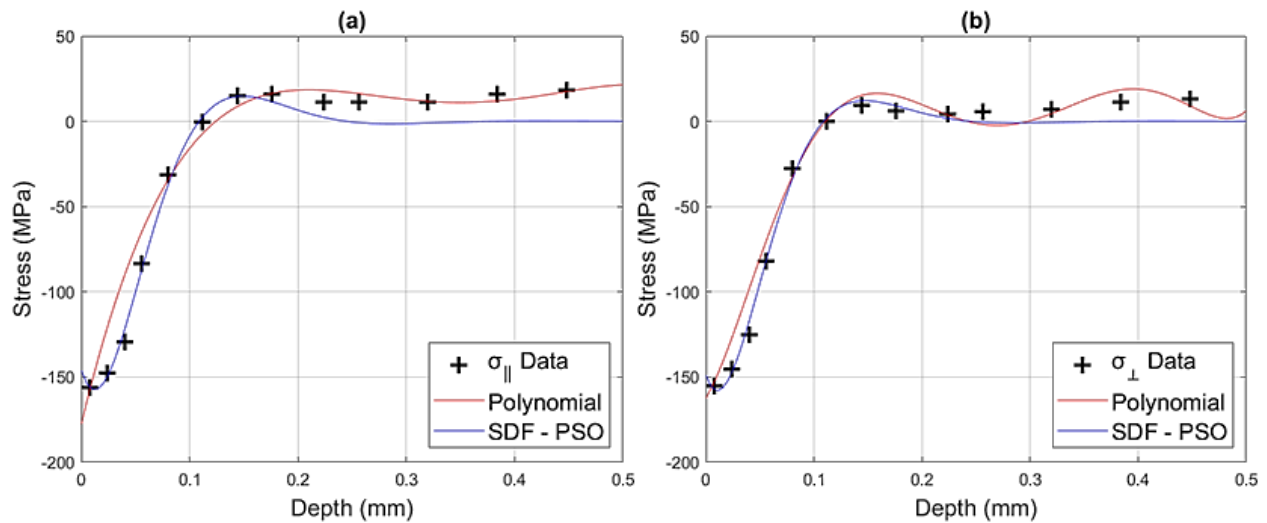


Figure 7-11: face milling MIRS data and fits in (a) feed direction; and (b) normal direction.

The process of fitting experimental data has been repeated for the end milling MIRS discussed in section 6.2. The MIRS profile for end milling was taken as the combinational curve presented in Figure 6-22 (see section 6.2.8). The results of the pocket milling trials showed that different MIRS conditions occurred at the corners than for the straight-line cutting locations. However, these variations were very localised. Therefore, for the case considered, the local variations of MIRS were not considered in the application of MIRS. Again, it can be seen in Figure 7-12 that the sinusoidal decay function performs better in both the feed (a) and normal (b) directions than the polynomial for the reasons outlined with the face milling fits. Table 7-5 contains the sinusoidal parameters for the end milling MIRS curves. However, it can be seen that both fits underpredict the stress data point occurring at a depth of $\approx 0.025\text{mm}$ for both measured directions. As this point corresponds to the first conventional ICHD measurement depth, the uncertainty of the data point is at its highest compared with deeper measurement locations. However, the trend of the near-surface measurements and sub-surface elements is likely such that the compressive stress point occurs in this region. Therefore, the point is used qualitatively to build the SDF curve for use in FEM.

Table 7-5: End milling SDF parameter values (to 2 DP)

-	c	ζ	ϕ	ω_d
End mill feed (σ_{\parallel})	874.61	0.70	45.55	37.10
End mill normal (σ_{\perp})	833.35	0.70	133.50	36.86

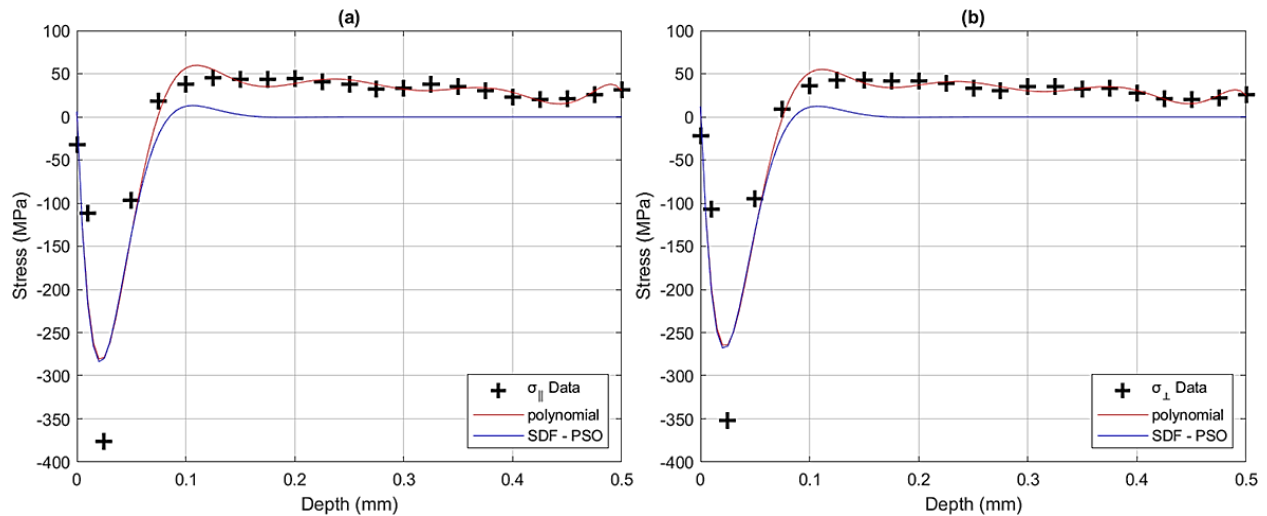


Figure 7-12: end milling MIRS data in (a) feed direction; and (b) normal direction.

Applying MIRS fit to the boundary layer mesh

The proposed 'UMAT' method routine was tested on a simplified plate model to determine the required mesh refinement for the mapped MIRS profiles. The process is to determine the point at which refining the boundary layer no longer influences the distortion response of the plate. The plate was dimensioned so that the length was equal to the width at 20 mm × 20 mm. The thickness of the plate was set at 1 mm. C3D10 elements are used in the bulk of the mesh, and C3D15 boundary layer elements are applied at the top surface. Boundary conditions are set such that the plate is rigidly work held during the MIRS application analysis step and then 'released' by changing the boundary condition to a 3-2-1 approach applied at the corners of the plate. The stresses have been plotted through thickness, and the peak nodal displacement was recorded at the centre of the plate model. Only fit values from the surface (0 mm) to 0.25 mm are used in the mapping of MIRS in the plates and demonstrator component as this range is equivalent to as the max settling depth for all MIRS curves used. See Figure 7-13 for plate design and distortion case.

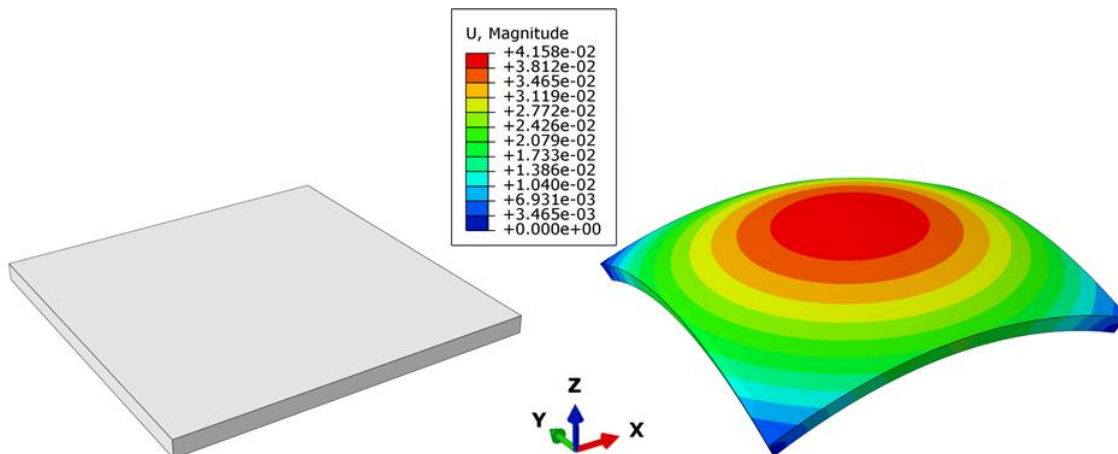


Figure 7-13: Flat plate boundary layer test (left) plate design and (right) deformed plate due to MIRS (deformed scale = 100)

Figure 7-14 shows the face milling MIRS extracted from the plate model (prior to relaxation by boundary condition update) against the SDF profile used as the preferential method to express the measured MIRS. After a refinement of 2 boundary layers, a good approximation of the stress curve is achieved. This is reflected in the peak distortion shown in Figure 7-15. After an initial percentage change of approximately 11.3% from refining the boundary layer from one element thickness to two, a difference of less than 1% is observed for the remaining refinements (0.12%, 0.19% and 0.02%). Therefore, it can be stated that for this model and MIRS profile, a layer of 2 elements is enough to achieve mesh independence of the distortion response.

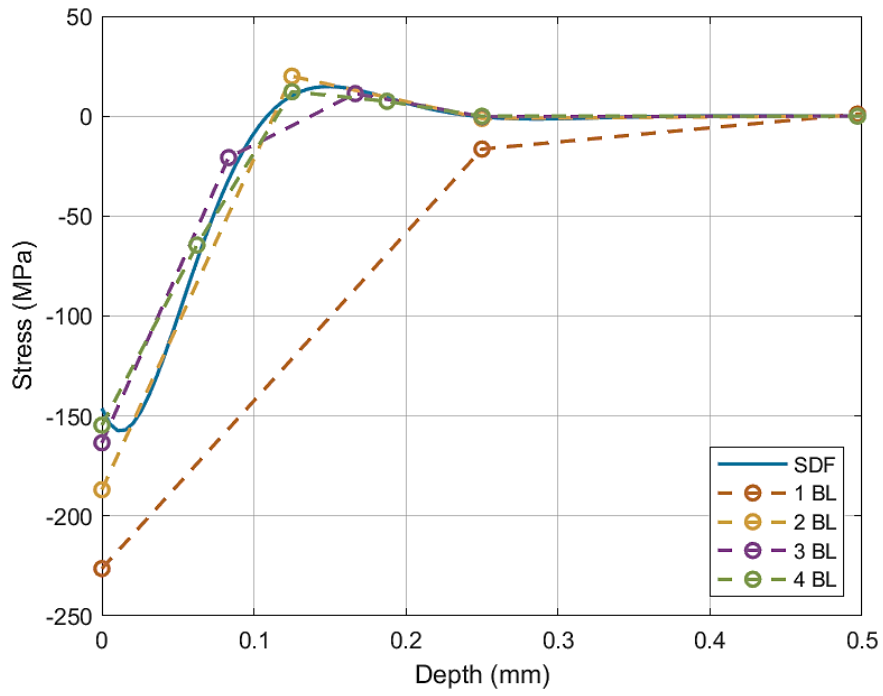


Figure 7-14: FEM vs Fit face milling MIRS

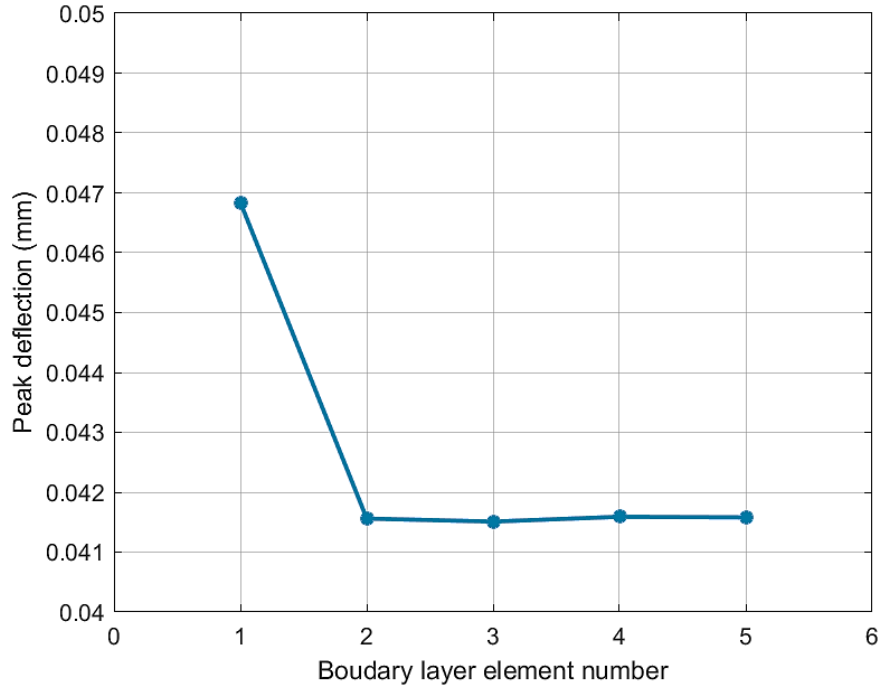


Figure 7-15: Peak distortion vs boundary layer discretisation for face milling MIRS

The process of determining boundary layer refinement was repeated for the end milling process MIRS. Figure 7-16 shows the SDF curve for the endmill vs the applied MIRS in the plate mesh with various refined boundary layers. The end milling MIRS profiles prove more challenging to represent in the near-surface boundary layer than the face milling MIRS due to the steep stress gradients from 0 to ≈ 0.025 mm and then ≈ 0.025 to ≈ 0.05 mm. Although the MIRS function appears to be underrepresented for the number of layers investigated, the response of the plate peak distortion vs the number of through-thickness boundary layers would suggest otherwise. Figure 7-17 shows that, similar to the face milling results, peak distortion is not significantly influenced by the mesh's refinement after two boundary layers.

The method of extracting stress values from FEM used in this work will also likely understate the stress condition in the boundary layer elements. The stress values are obtained only at extreme corner nodal positions to which the stress values stored at material integration points are extrapolated. The element shape function determines this process of extrapolation. Additionally, the reported stresses are averaged for shared nodes between elements according to the extrapolation scheme. Therefore, a more detailed stress distribution within the C3D15 element is probable.

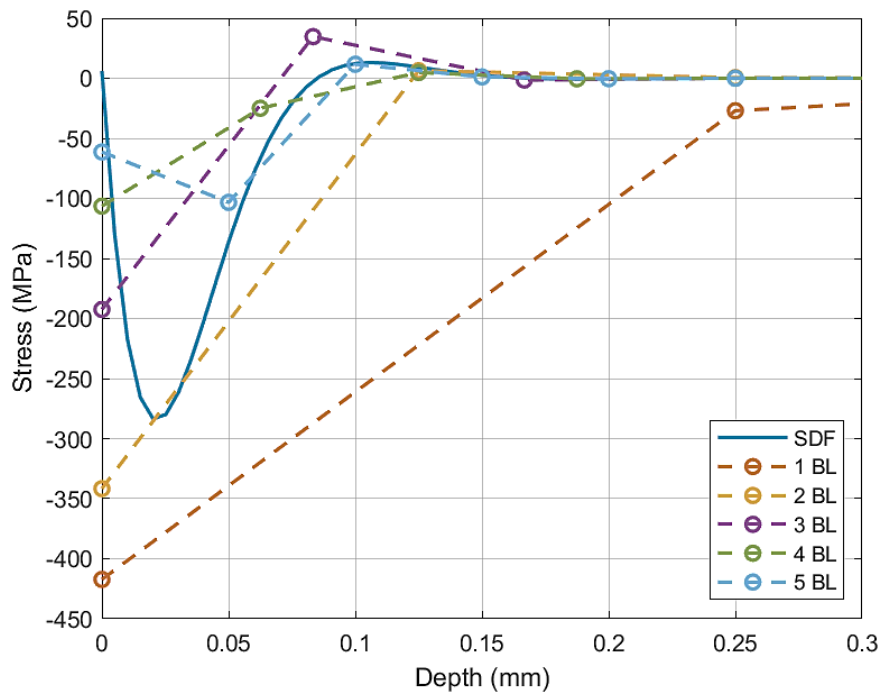


Figure 7-16: FEM vs Fit end milling MIRS

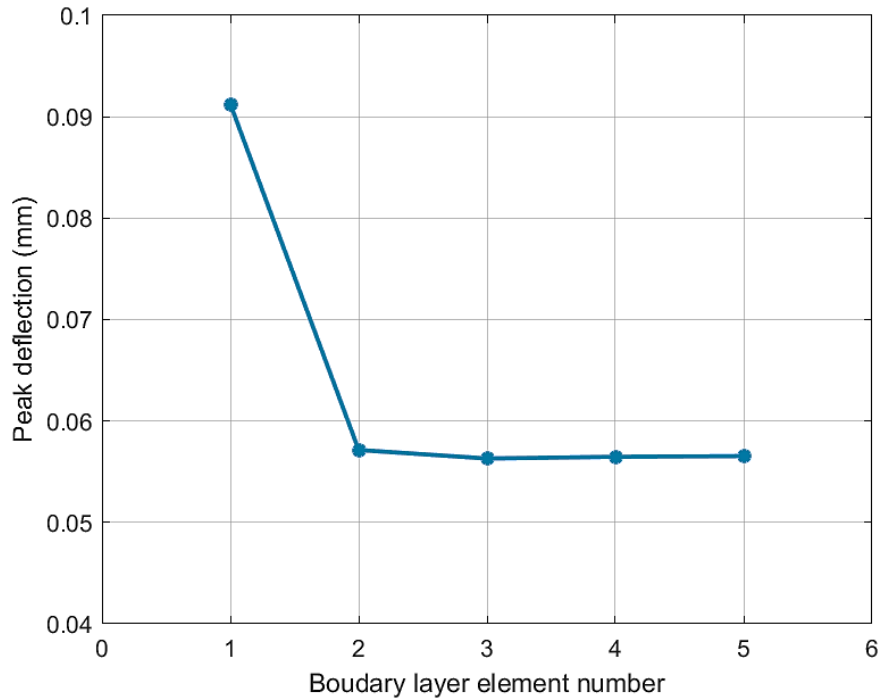


Figure 7-17: Peak distortion vs boundary layer discretisation for end milling MIRS

Conclusion

Based on the distortion response of the theoretical plates when mapping face and end milling MIRS values by the developed 'UMAT' method, a refinement of 3 elements is deemed suitable for capturing the influence on distortion. The increase in the boundary layer element through thickness value would only increase the simulation's computation time.

7.3 Modelling Component Distortion

As discussed in section 5.5, the distortion component was designed to share key features from problematic aero-structural machined components regarding residual stress-related distortion. The design has been considered to make the component susceptible to bulk and machining-induced residual stress-related part distortion. These features include:

- High length-to-width ratio (over 6:1)
- Low floor thickness (3 mm)
- Asymmetric (single-sided pocket features)

The demonstrator component has been machined from a 50 mm thick roll aluminium billet in two stages utilising two different fixture setups. After each machining stage, distortion was measured by CMM.

7.3.1 Simulation process

The distortion simulation process incorporates material removal and MIRS mapping at key modelling stages, representing the manufacturing process. The starting configuration for the model is a mesh representing the stock material geometry (length 1000 mm × width 300 mm × thickness 50 mm) with longitudinal and long-transverse bulk residual stress defined (see section 7.2.1). The mesh density should be considered when modelling the influence of bulk residual stresses on part distortion. The aim is to generate a mesh density such that the bulk stress can be mapped accurately and the calculated distortion is independent of the mesh refinement while keeping the numerical cost of the model as low as feasible. In ABAQUS, the global mesh seed (GMS) is defined to control the general mesh element size.

Figure 7-18 shows the coarsest and most refined mesh densities trailed for mapping the bulk stresses identified in section 7.2.1. Figure 7-19 and Figure 7-20 show the longitudinal and long-transverse bulk residual stresses extracted from the model after mapping against the data from which the bulk stresses are defined. As shown in both stress mapping directions, the more refined the mesh, the closer the modelled stress profiles follow the applied fit. However, even for the finest mesh iteration, the longitudinal numerical stress curve between 0 > 3 mm and 47 > 50 mm does not fully converge with the applied data fit.

This discrepancy can be explained by the variation in the stress state over a small area. The stress gradient moves from compressive to tensile and back to compressive stress within a 5 mm distance with a 30 MPa stress swing. For even the most refined mesh, the number of elements within the near-surface region is not enough to capture the stress variation and as such, numerical averaging at material points occurs. This averaging could be overcome by increasing the refinement of the mesh size. However, the trade-off between mesh size and run time must be considered. Because these mismatches occurred in areas far away from the location of the final component in the stock material in this instance, refinement of the mesh would increase the computational expense significantly with a marginal gain in accuracy.

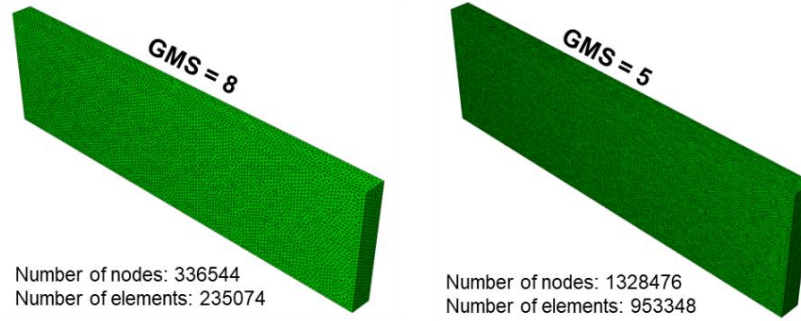


Figure 7-18: Various mesh densities trialed for the mapping of bulk residual stresses

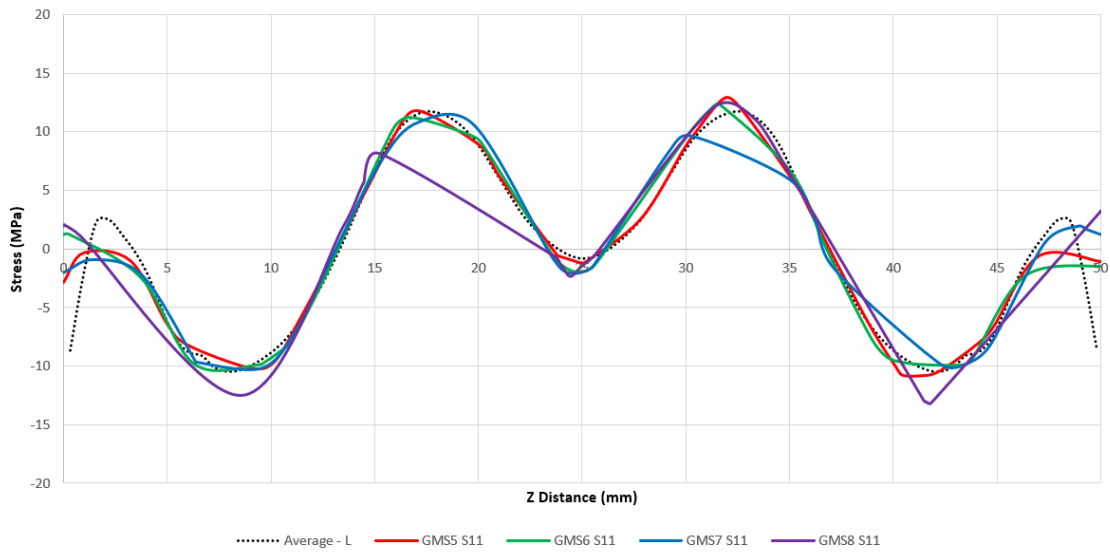


Figure 7-19: Longitudinal residual stresses extracted from various mesh refinements against the data set

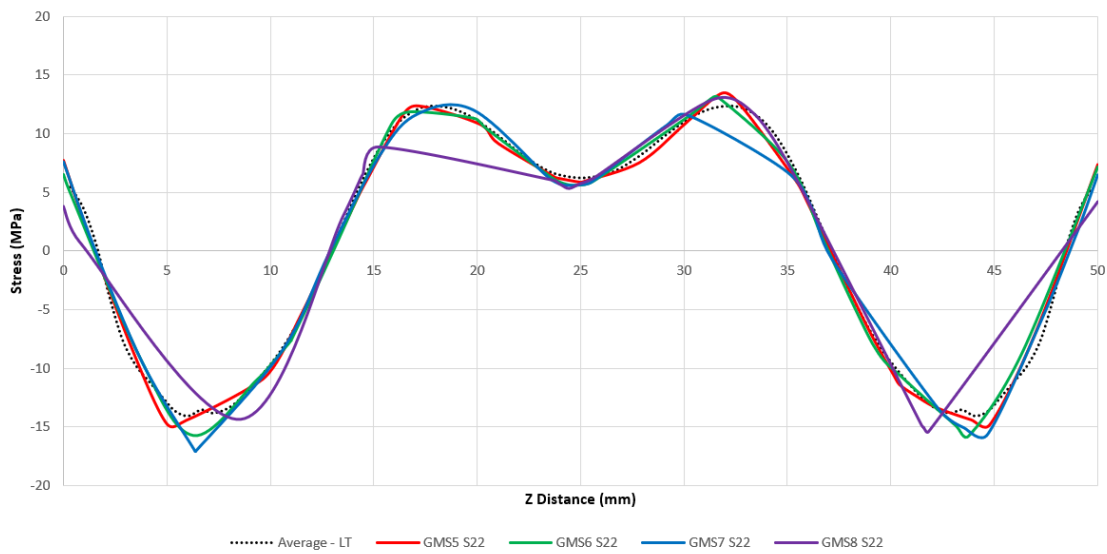


Figure 7-20: Long-transverse residual stresses extracted from various mesh refinements against the data set

Figure 7-21 shows the baseline material removal strategy performed in stage 1 face milling. The stage one process includes two roughing machining passes (1) & (2) and one finishing machining pass (3). Figure 7-22 shows the peak distortion values for various mesh refinement levels after performing the stage 1 material removal sequence. It can be seen that for increased mesh refinement, the peak distortion also increases. From global seed size 6 mm to 5 mm, this equates to a 4% increase in peak distortion (0.009 mm). Refinement of the mesh further was considered only to gain marginal change in the resulting distortion whilst increasing the time required to execute the simulation due to an increased element count.

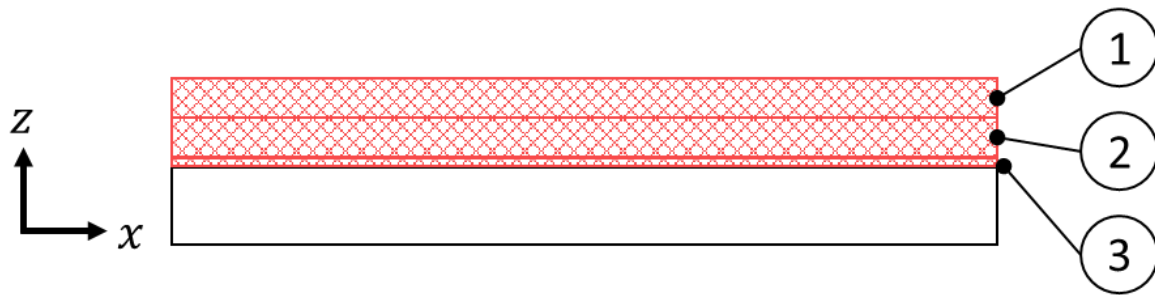


Figure 7-21: Boolean removal for stage 1 machining operations

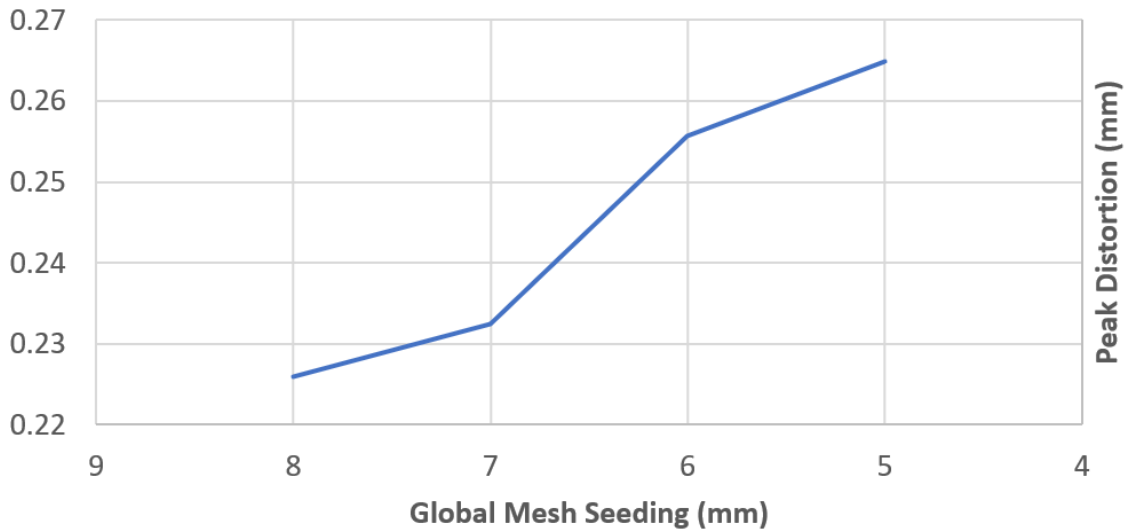


Figure 7-22: Peak distortion vs global seeding size

Figure 7-23 displays the 9 Boolean operations conducted in stage two. The first removal (1) is made by face milling to reduce the material height over the component to the final height. The five pockets are removed in sequence (2 – 6). Then the channels to the side of the component used to generate the break-off tabs are machined (7) & (8). Before finally, the remaining material is removed, simulating the break-off operation (9). The inter-process distortion caused by the stage 2 Boolean material removals is displayed in Figure 7-24 for reference.

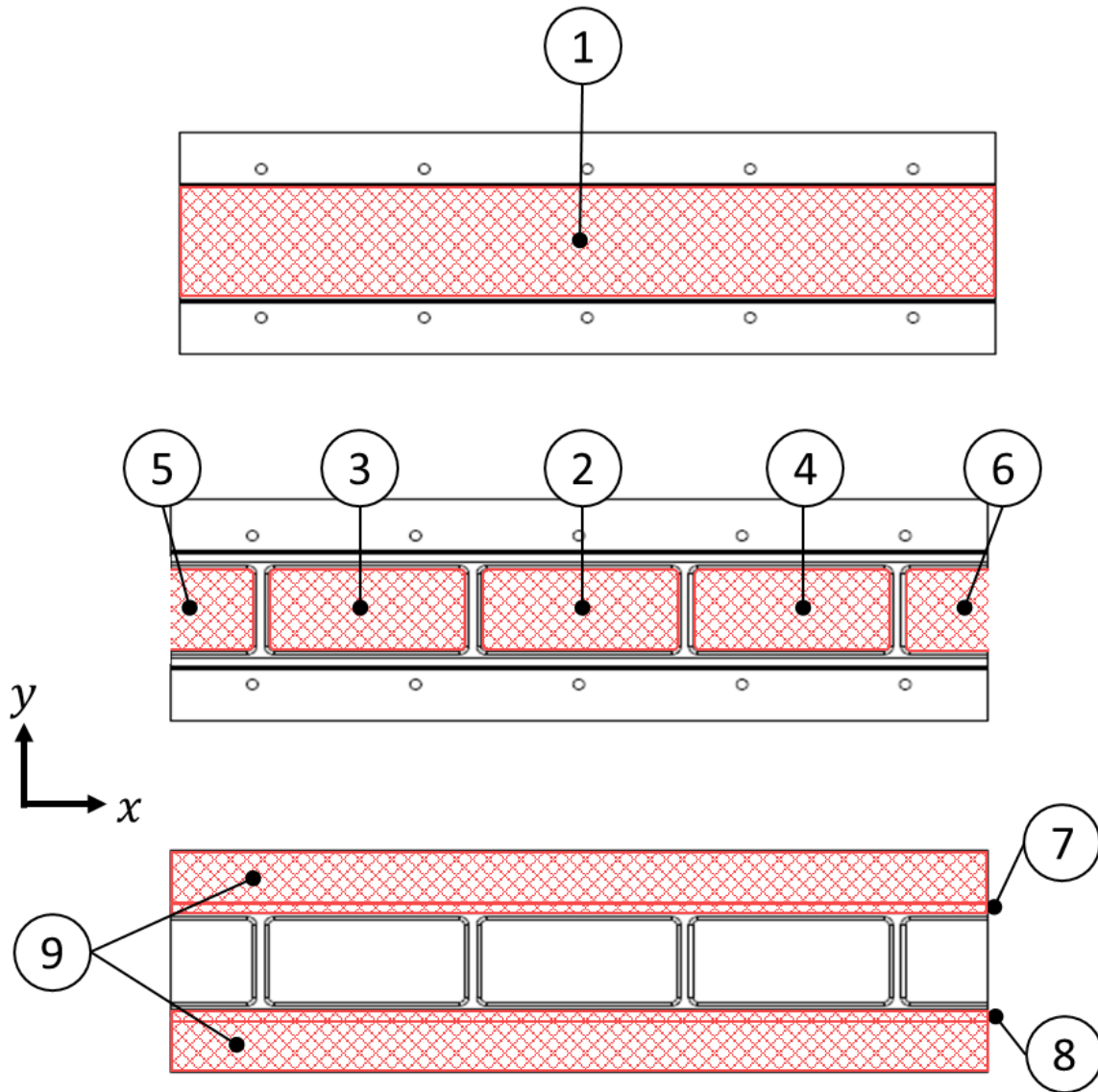


Figure 7-23: Boolean removal for stage 2 machining operations

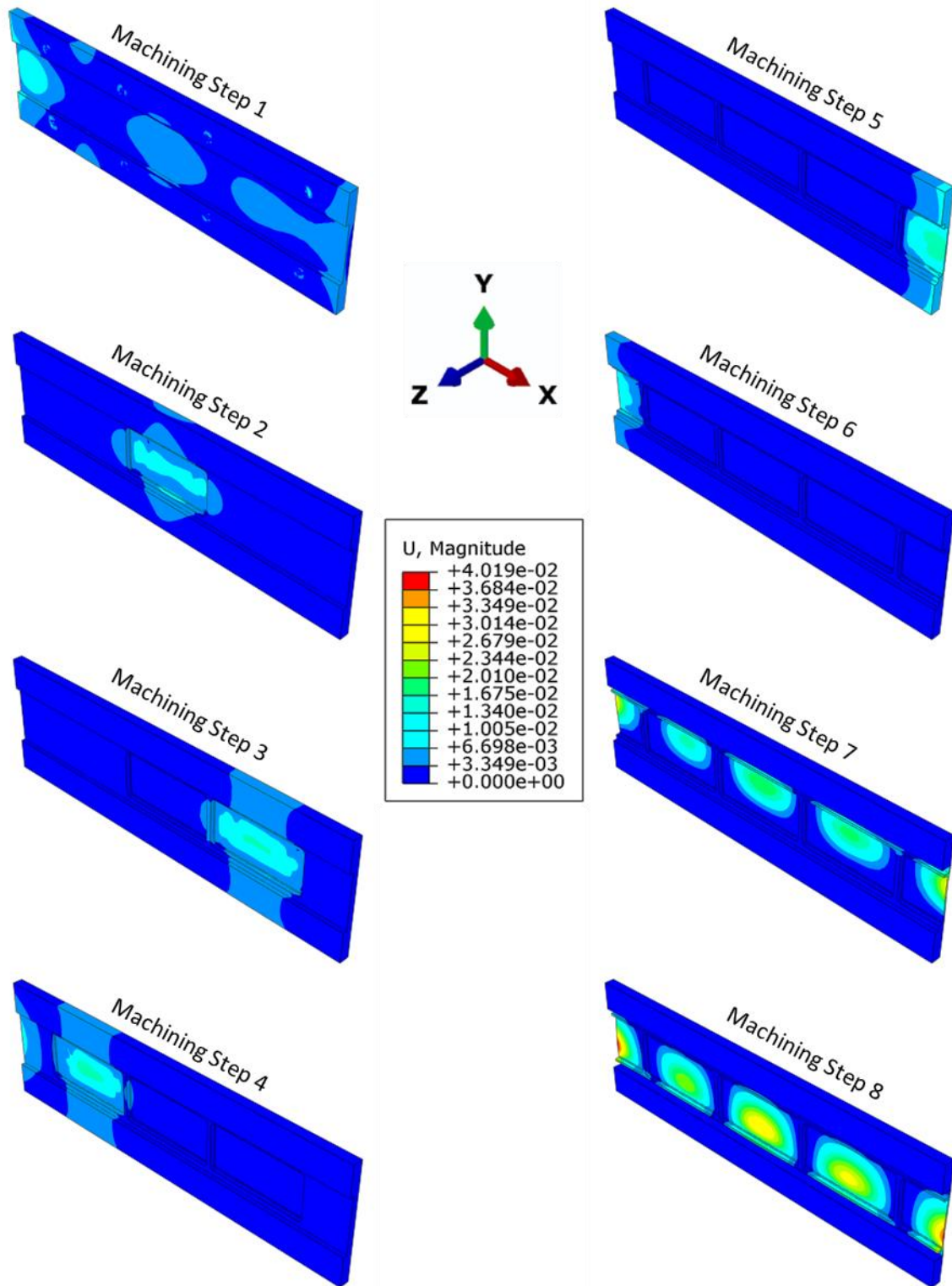


Figure 7-24: Development of the component displacement post-material removal

Machining-induced stresses are incorporated by the tool path Python script and UMAT subroutine after Boolean operations relating to the generation of critical machined surfaces. These include the Boolean operations (1) to (3) in stage one that concern the datum side face milling and operations (2) to (6) in stage 2 for the generation of the pocket geometry. These machining operations contribute to the machining of the component floor and apply process-induced residual stresses. The MIRS imparted within the floor of the component are considered to contribute most to the MIRS-related distortion of the component post-machining. All other simulated machining operations are not considered for MIRS application as modelling these process stresses has shown to be unbeneficial [151].

Figure 7-25 displays the tool path feed directions for the machining demonstrator component considered when applying MIRS during stage one (a) and stage two (b) modelling. The red arrows define the tool path when the tool feed vector is aligned with the x-Cartesian axis. The green arrows indicate when the tool path direction is aligned with the y-Cartesian axis. This information is identified by the Python utility script from which the information is passed to the UMAT subroutine for correct stress tensor application. Thus, the MIRS is applied such that the feed and normal direction tensor values are orientated based on the tool path progression. Figure 7-26 shows the nodal selection procedure for stage 1 face milling operation, where Figure 7-27 displays the process employing the tool path nodal selection for pocket milling simulation during stage 2 operations.

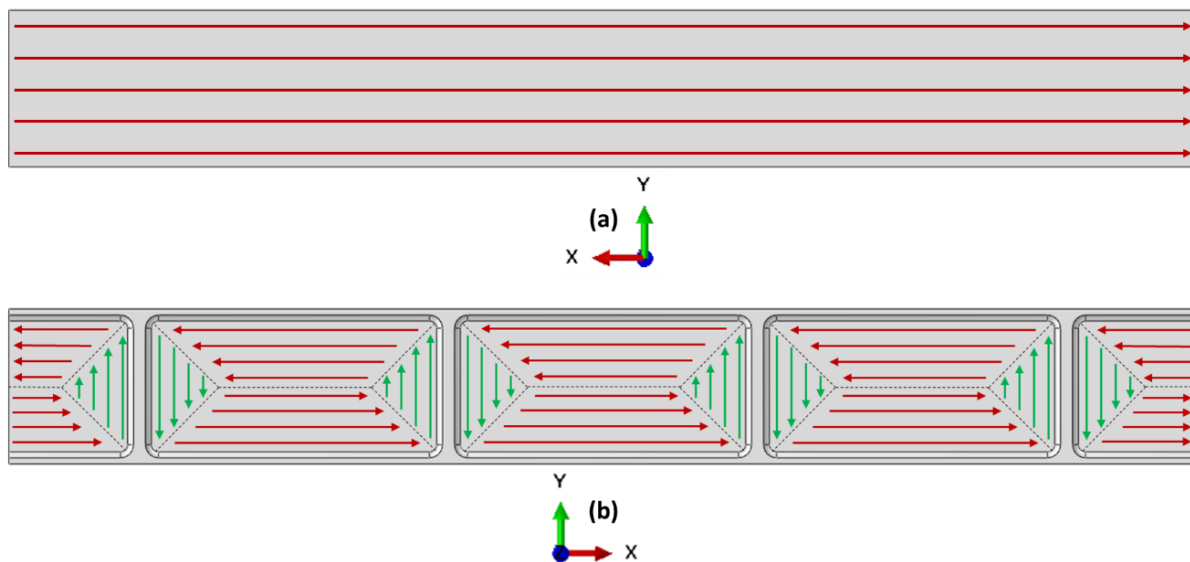


Figure 7-25: Tool path MIRS applied in the distortion modelling.

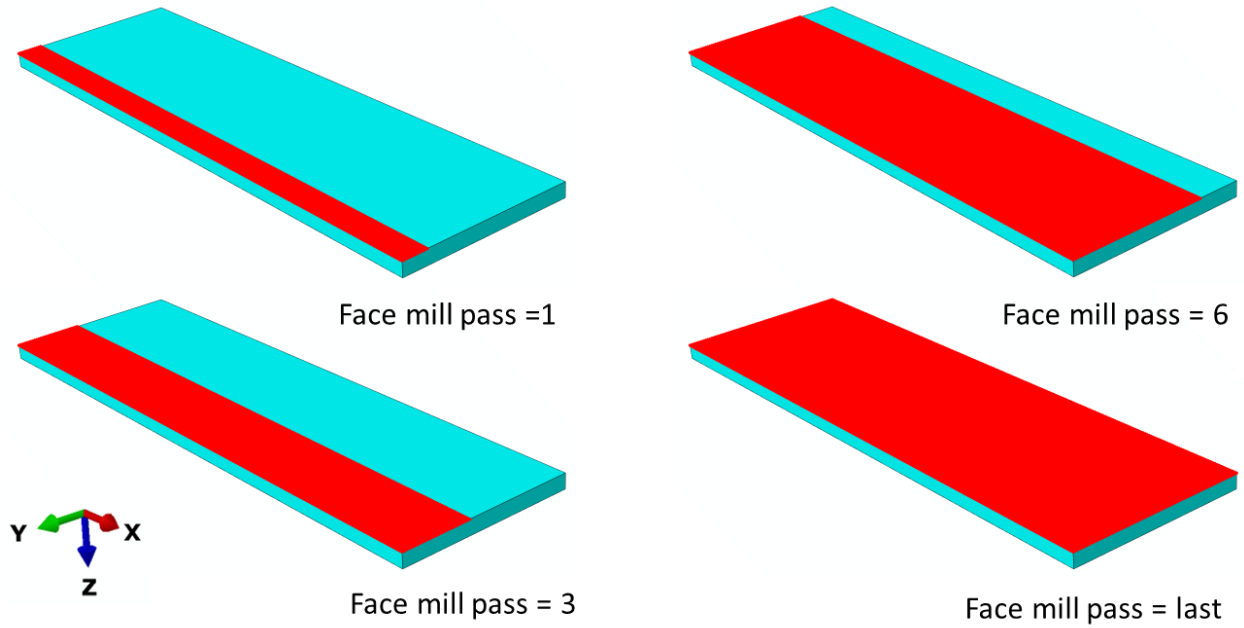


Figure 7-26: Nodal selection following stage 1 face milling simulation.

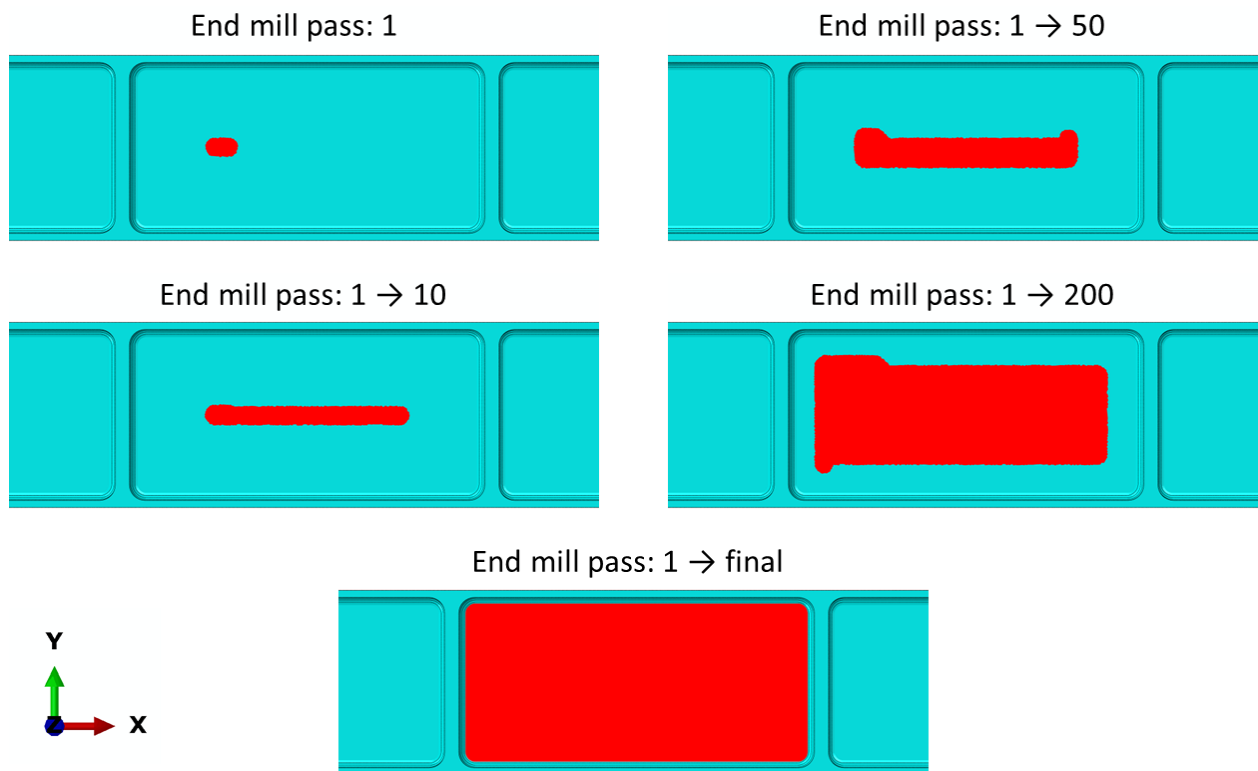


Figure 7-27: Nodal selection during stage 2 pocket one end milling simulation.

7.3.2 Fixture case

For the physical machining trials, the workpiece was fixtured during stage 1 and stage 2 with mechanical fixturing:

- Stage 1: Kopal side clamping to retain the part during face milling and drilling operations.
- Stage 2: M10 bolts to constrain the part in the break-off material regions by rigidly bolting the component via threaded holes in the machine bed during stage two face and end milling operations.

As discussed in section 4.3.4, variable boundary conditions have been used to simulate the fixture conditions utilised across stages in the demonstrator machining trails. In stage one modelling, displacement boundary conditions have been used to simulate the side clamps, as shown in Figure 7-28.

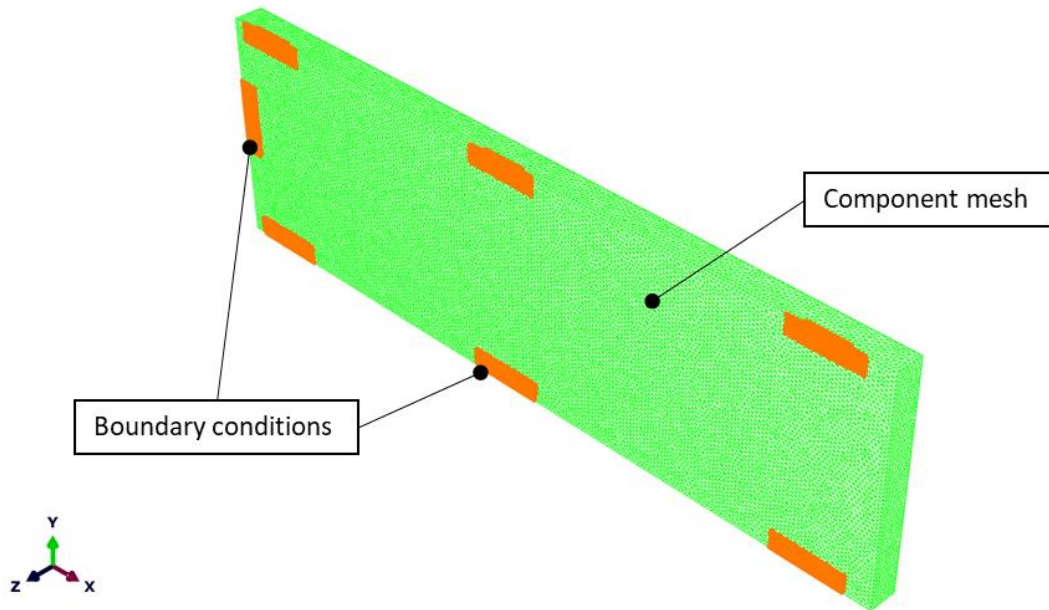


Figure 7-28: Stage 1 boundary conditions

The areas over which each clamping boundary condition acts are calculated based on the position of the clamps in the 3D coordinate system and the intersection of the clamp contact area with the surface nodes of the meshed component. The nodal degrees of freedom (DoF) is blocked across all clamping zones such that; $U_1 = U_2 = U_3 = 0$. It was deliberated that modelling the explicit clamping force or contact regime at these regions would have little impact on the resulting distortion during stage 1 modelling as the clamping regions are far from the machining surfaces, and therefore induced distortion is considered unimportant.

Therefore, modelling the forces through boundary conditions or clamps contacting rigid bodies only serves to increase the simulation complexity and computational expense.

In stage two, the boundary condition regime is more complex due to the evolving geometrical condition of the part, as the physical bodies involved are in contact and the progressive influence of the bulk and MIRS. To simulate the contact and transfer of forces between the machine bed and part and between the bolts and the part, the use of rigid bodies, general contact and continuum distributing coupling has been realised, as displayed in Figure 7-29.

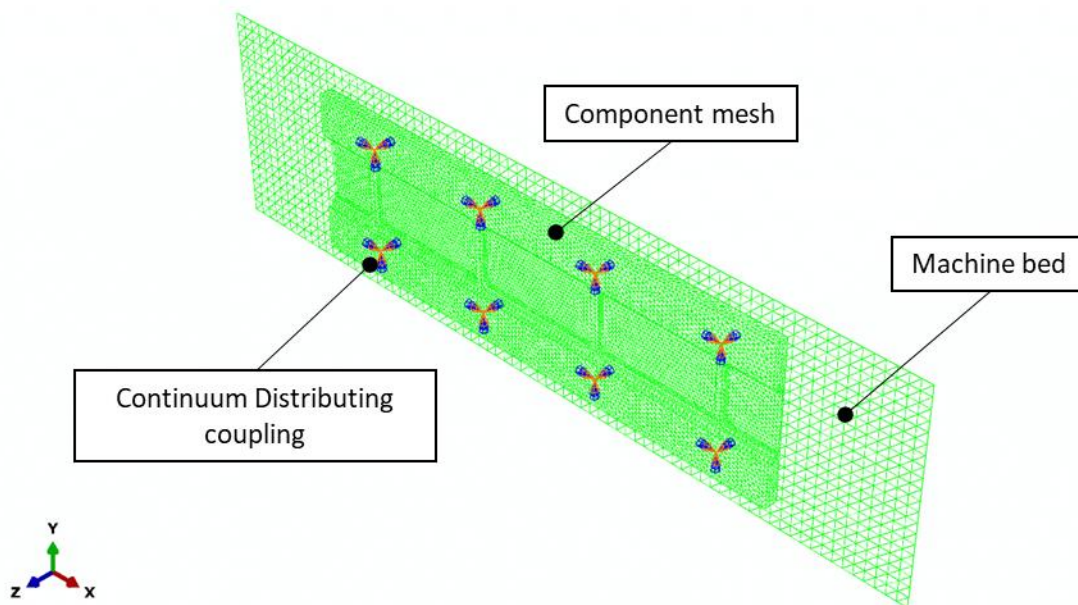


Figure 7-29: Stage 2 model boundary conditions

The interaction between the component and the machine bed is modelled by discretising the machine bed as a rigid body and employing the general contact algorithm in ABAQUS. The assumption to model the machine bed as a rigid body is valid as the machine bed is manufactured from hardened steel with a much higher rigidity than the aluminium billet. The ABAQUS general contact procedure with standard contact algorithms is used, as discussed in section 4.2.5. Contact properties defined for the mating surfaces include 'hard contact' normal behaviour and 'frictionless' tangential behaviour.

The bolt/part contact is simulated similarly to stage one clamping. The contact area is calculated between the saddle for each bolt head and the top surface of the component. The Python machining script 'looks' for the nodes on the component's surface intersected by the bolt search areas. Reference points (RP) are generated at the coordinate spacing of the bolt pattern. The node sets generated for each search area

(corresponding to the bolt spacing) are tied to the corresponding RP point using continuum-distributing coupling. The nodes of each set are tied to the RP point such that the RP points' displacement can control the nodes' displacement.

Additionally, a force can be applied at the RP point and distributed across the node set, simulating the bolt load. An additional simulation step is required between the machining stages to model the clamping of the distorted stage one intermediate stock condition to the machine bed. The previous method described generates the bolt load node sets and RP points to which forces representing the bolt loads are applied (-40.8 kN). For all subsequent machining models, bolt RP point displacement is fixed.

To simulate distortion of the component post-machining, the release of the bolts is simulated by removing the boundary conditions imposed by the RP points and applying the 3-2-1 method. The 3-2-1 boundary condition blocks the rigid body motion of the model without overconstraining the component such that it is free to deform. At the end of stage one and stage two, machining displacement boundary conditions are applied as depicted in Figure 7-30, where U1, U2 and U3 are displacements fixed in the X, Y and Z cartesian vector directions, respectively.

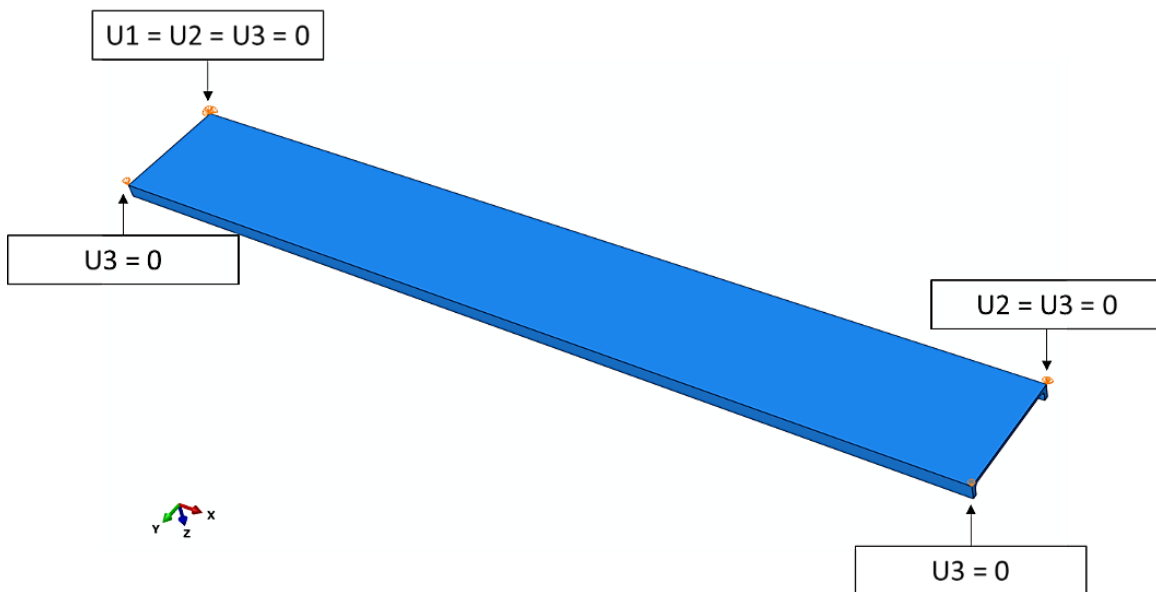


Figure 7-30: 3-2-1 boundary conditions applied to the distortion demonstrator component.

7.3.3 Distortion assessment and results

To compare numerical nodal displacements to the demonstrator distortion measurements, nodal sets are created across the meshed component replicating the measurement lines identified in sections 5.5.4. Through knowledge of the CMM process, it was possible to construct a reference point such that the measurement profiles could be aligned and compared. Figure 7-31 shows the nodal displacement sets for stage 1 machining and Figure 7-32 for stage 2.

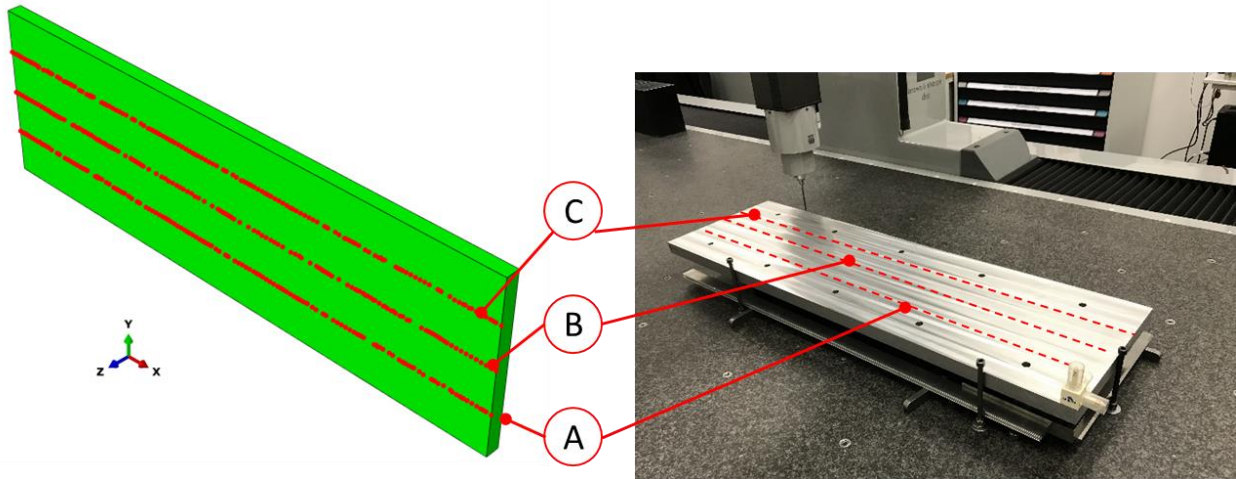


Figure 7-31: Stage 1 nodal displacement lines with reference to the measured profiles

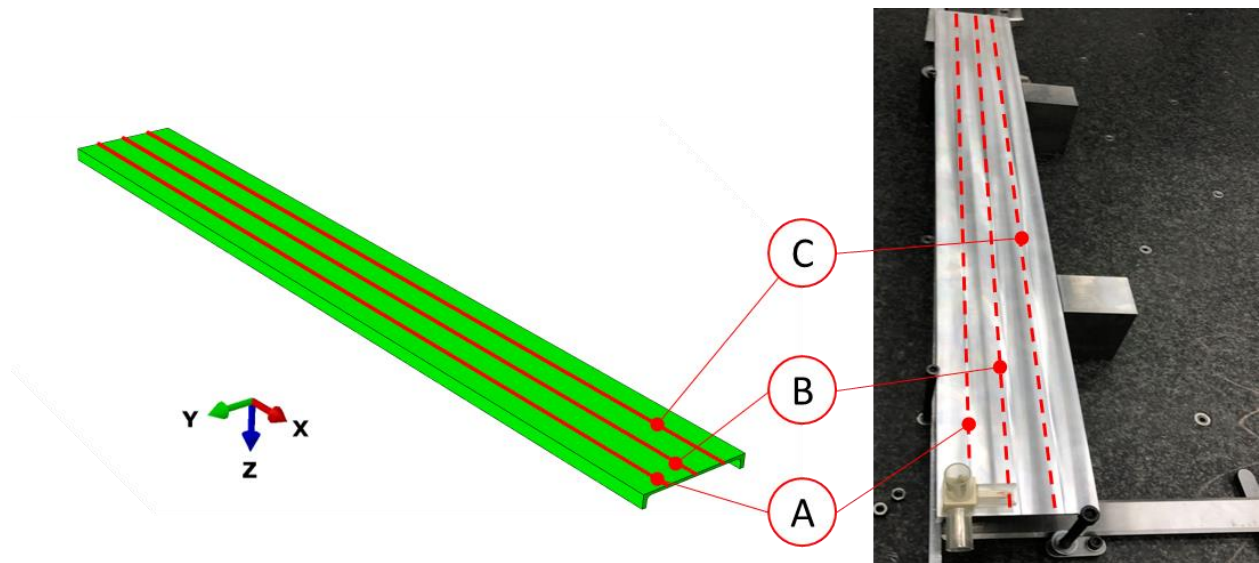


Figure 7-32: Stage 2 nodal displacement lines with reference to the measured profiles

Figure 7-33 displays stage 1 CMM measurement results vs the FEM nodal displacements after simulated clamp release. It can be seen that the FEM results match the measured profiles in terms of the bending mode and position of peak distortion at the mid-span of the component length. However, the peak distortion is underpredicted, where the difference between the CMM and the FEM average peak distortion is 0.080 mm. Nevertheless, the simulated curve falls within the standard deviation of the mean displacement measurements for each inspection line.

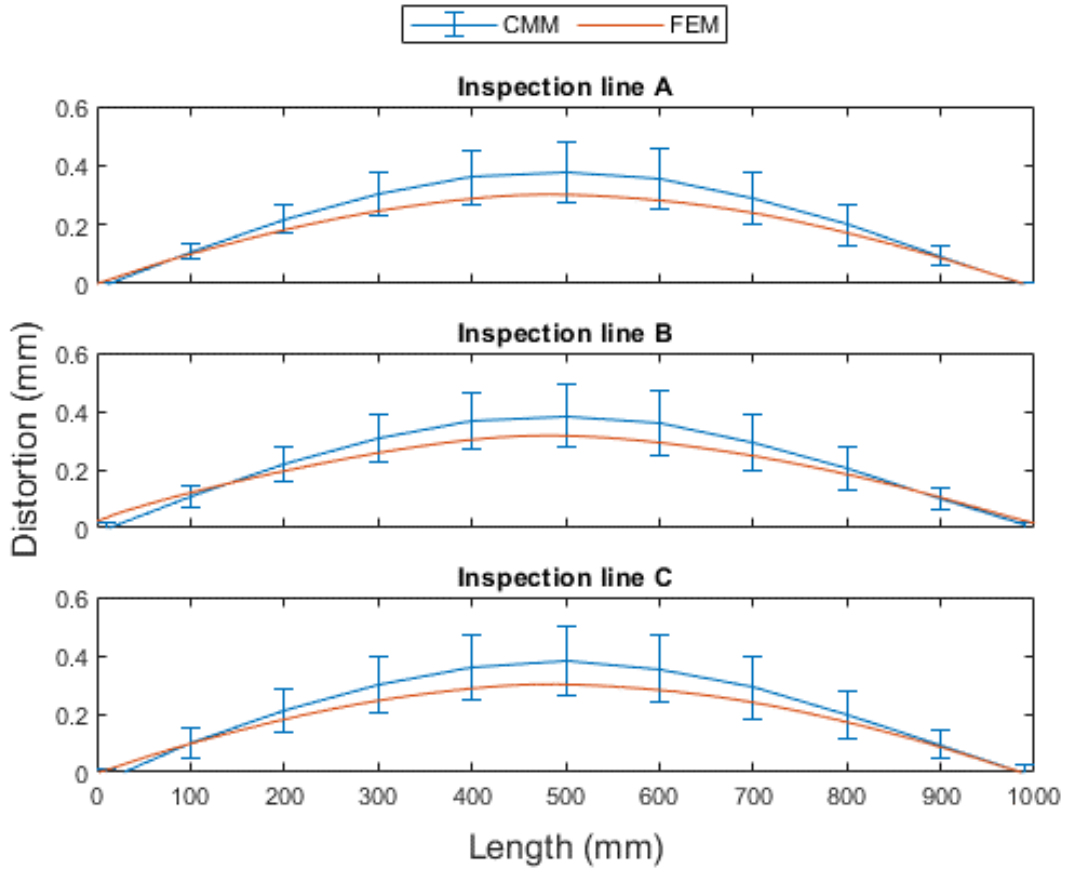


Figure 7-33: Stage 1 CMM vs FEM distortion

Figure 7-34 shows stage 2 CMM measurement results vs the FEM nodal displacements after the simulated removal of the break-off sections. Quantitatively, the CMM measurements and FEM nodal displacements are very similar. The measured max deflection of the component was 1.165 mm compared to the simulated max distortion of 1.212 mm. An average difference of 3.87% between the measured vs simulated peak distortion is calculated. In general, the simulation predicts well the distortion of the machined demonstrator component.

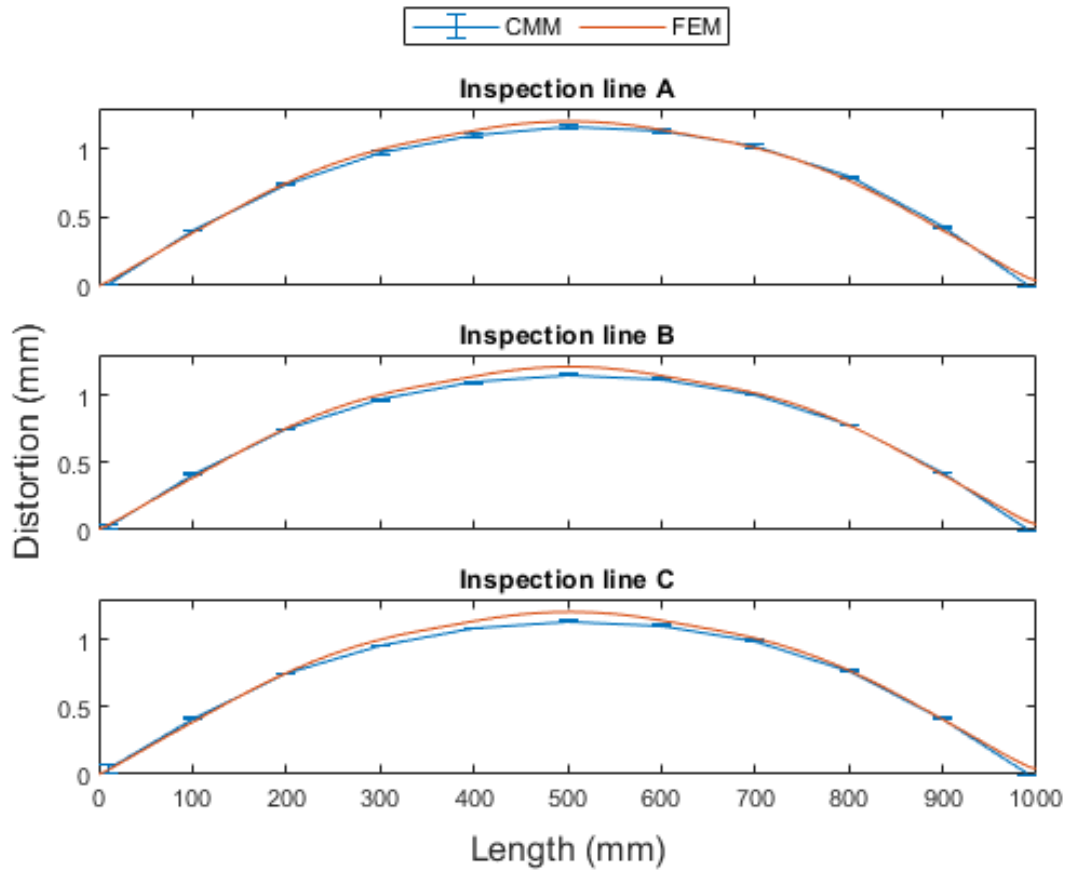


Figure 7-34: Stage 2 CMM vs FEM distortion

7.3.4 Discussion on Component Distortion Results

The simulation results matched the machined component distortion's final bending mode and magnitude to a reasonable level of accuracy compared with previous work reviewed (see section 2.6.4). However, stage one post-machining distortion underpredicted the peak deflection. One possible explanation is that the model suffers from an inaccuracy in the representation of the bulk residual stress induced deformation due mesh refinement. Figure 7-22 indicates that the stage one distortion model's peak deformation increased with increased mesh refinement. If that trend continued before convergence, the difference between the modelled peak distortion and measured values would have reduced. However, a decision was made not to refine the mesh further to keep the numerical cost, and therefore simulation solve time to a reasonable level. The reason this error was not reproduced in stage two is that both stages have a dominant source of residual stress contributing more to the distortion in the component. In stage 1, it is assumed that because the component is still relatively thick, most of the distortion is attributed to the bulk residual stress redistribution. After stage 2, the component comprises thin-walled features for

which MIRS have increased influence over the resulting distortion. The stage model is comprised of highly refined surface layer mesh to accurately map the MIRS. This also serves to create a relatively more refined through component element density compared with the stage one mesh, contributing to the accurate representation of the residual stress driven distortion.

Furthermore, the standard deviation of the stage one CMM results were large such that the predicted deformation was within this bad. Therefore, another potential reason for the discrepancy between model and measure distortion is that the measurement procedure has a source of systematic error. It is possible that the source of the error was due to the ground riser columns used to support the stage one component during CMM contact the unmachined as-rolled plate surface, as supplied by the mill. The flatness tolerance for the rolled surface according to the British standard for aluminium and aluminium alloys sheet, strip and plate (BS EN 485-3) [178]; The tolerance controlling the deviation from flatness resulting from arching, buckling or edge waves for a plate of 50 mm thick is 0.2% over its length and width. Based on the BS standard the plate used in these trials would have a max flatness deviation tolerance of ± 2 mm across the length and ± 0.6 mm across the width. When measuring distortions in the magnitude 0.3 mm post-stage one, it can be seen how the variable flatness may impact final measurement results. Because the ground riser columns contact the machined surface produced in stage one during stage two CMM measurements, the flatness error is removed. Further work is required to determine the source of the difference between the physical and simulated distortion.

7.4 Comparing modelling methodologies

The developed methodology has been shown to predict well the final distortion of the demonstrator component. The method described has been created by building upon modelling concepts considered from previous distortion modelling work. It will be attempted here to evaluate the established modelling concept against the methods considered in its conception (see section 3.1) through simulation of the distortion demonstrator component by closely replicating the modelling methods deliberated. These methods are (1) Dreier's single-step and tool path-dependent MIRS application model [150]; and (2) Cerruti's Boolean model [157]. Direct comparison of the methods is impossible due to not having access to the resource, software or time to regenerate these methods. Instead, it has been attempted to reproduce these concepts in ABAQUS/CAE software. The material properties and residual stress profiles are consistent across all models and are detailed in section 7.3.

7.4.1 Recreating Dreier's modelling method

To recreate Dreier's [150] distortion modelling method, the demonstrator component's final geometry (Figure 7-35 (a)) is meshed (Figure 7-35 (b)) and the bulk residual stress applied through the thickness of the component according to the part offset in the stock material. The MIRS is applied using the developed UMAT method as it has already been shown to be comparable to a simple beam distortion case (see section 7.1). C3D10 elements have been used in the bulk of the component, and C3D15 elements in the boundary layer. A global mesh seeding size of 4 mm was utilised, and the boundary layer reproduced as described in section 7.3. The Bulk Stress and MIRS are applied in one linear, static step. The release 3-2-1 boundary conditions presented in Figure 7-30 were applied to simulate the component's free deformation as shown in Figure 7-35 (c).

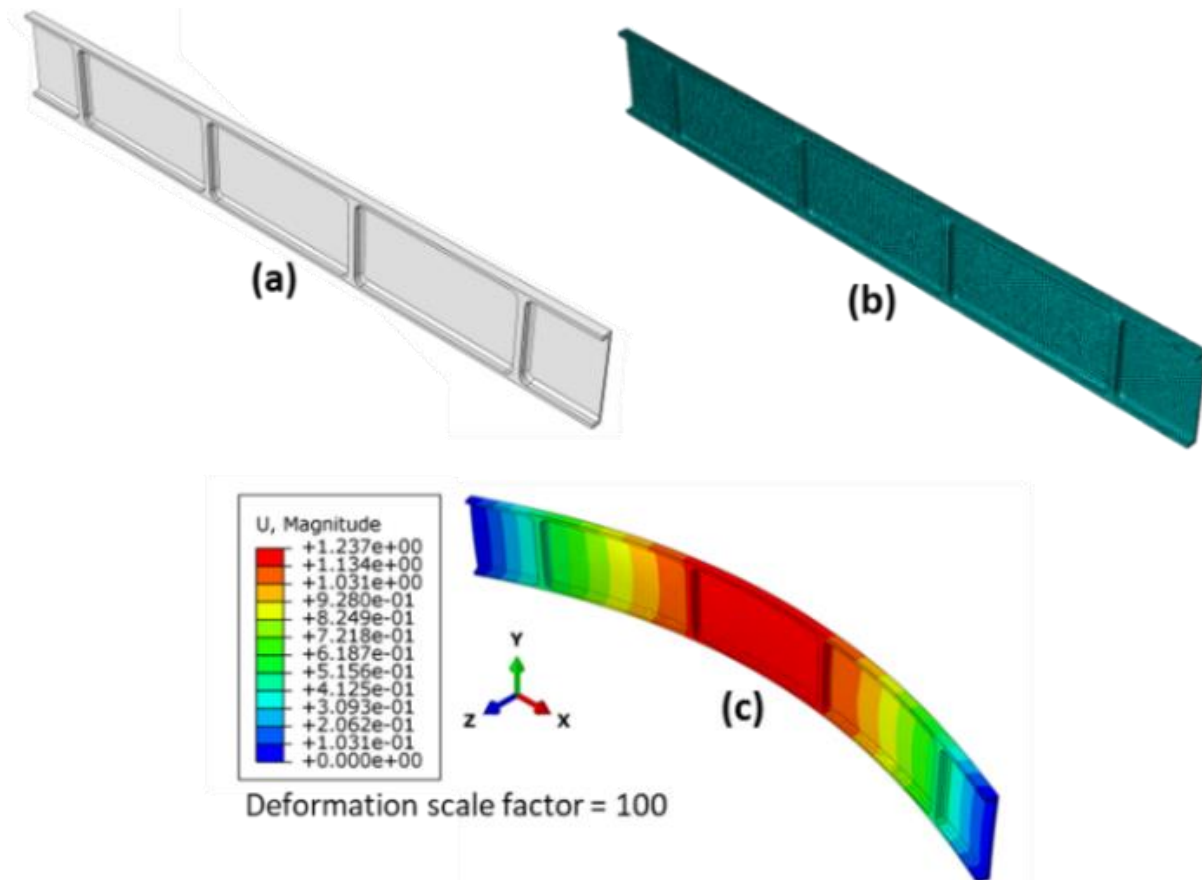


Figure 7-35: Recreating Dreier's modelling method where: (a) is the part geometry; (b) the mesh; and (c) the distorted model

7.4.2 Recreating Cerruti's modelling method

The top-level modelling methodology can be described as a Boolean material removal procedure, where the machining process is simulated through the subtraction of geometric volumes representing the removed material in the physical space. Cerruti's [157] modelling methodology only considered the bulk residual stresses in the deformation of machined aluminium components. Cerruti's work also detailed various 'levels' of distortion modelling attributed to the discretisation of the process. Based on these definitions, the modelling concept developed and presented earlier in this chapter (see section 7.3) can be described as a modified level 4 model. As per Cerruti's level 4 description, the developed distortion simulation process incorporates initial bulk residual stress mapping, the subtraction of material from the model as a function of predefined machining features (i.e., pockets, wall sections, floors sections etc.) and the inclusion of clamping/unclamping in the modelling regime including the use of contact in representing the fixture constraints. The modification in the method concerns using boundary conditions to simulate the fixtures and mapping MIRS to account for its influence over part distortion.

The boundary condition modification concerns the use of displacement conditions by way of blocking the degrees of freedom at clamping locations. This type of boundary condition was chosen to reduce the numerical cost of the models (the use of displacement boundary conditions is considered a level 3 modelling approach according to Cerruti's demarcation of the modelling methods). Cerruti also dismissed the inclusion of MIRS as a source of machining-related distortion as the components studied in his work were of a certain thickness, he considered not to be affected by MIRS.

Therefore, by not including the MIRS mapping process for the developed modelling protocol then, Cerruti's level 4 modelling procedure is realised. C3D10 elements are used throughout the mesh with a global element seed size of 5 mm. The general modelling procedure covered in section 7.3 is replicated without including the MIRS mapping process.

7.4.3 Comparing the modelling methods against the demonstrator distortion

Figure 7-36, Figure 7-37 and Figure 7-38 display the results of the individual stage 2 nodal displacements generated by various modelling methods against the average CMM measurements along distortion inspection profiles 'A', 'B' and 'C', respectively. The graph legend determines 'FEM' profiles for the model results generated in the thesis work, 'FEM Cerruti' & 'FEM Dreier', signifying the results obtained from the replicate models. Although the replicate Cerruti model captures the correct distortion mode, the peak distortion is well underpredicted. The significant error in the 'Cerruti' method can be attributed to the

omission of the MIRS, which is significant in the distortion of machined aluminium components with thin wall/floor sections.

The replicated 'Dreier' single-step method for all measurement profiles agrees with the average CMM and the UMAT modelling method results. However, it can be seen slight variation between the distortion profiles is exhibited. This variation along the distortion measurement profiles is attributed to the sequential Boolean material removal method developed in this work. The developed modelling method makes it possible to realise the over/undercuts due to inter-process part deformations due to evolving residual stress fields throughout the machining sequence. In contrast, the method developed by Dreier assumes that the part's geometrical characteristics are perfectly machined. To highlight the ability of the developed modelling method to determine the influence of the inter-process distortion on machining part quality, virtual thickness measurements have been made along three profiles, as identified in Figure 7-39. These thickness inspection profiles relate to the walls and floors of the distortion demonstrator component, as depicted in Figure 7-40, where points on the extremity of the part are compared with points internal to the pocket floors and walls. The distances between points were exported, and the thickness variation was calculated and plotted in Microsoft Excel.

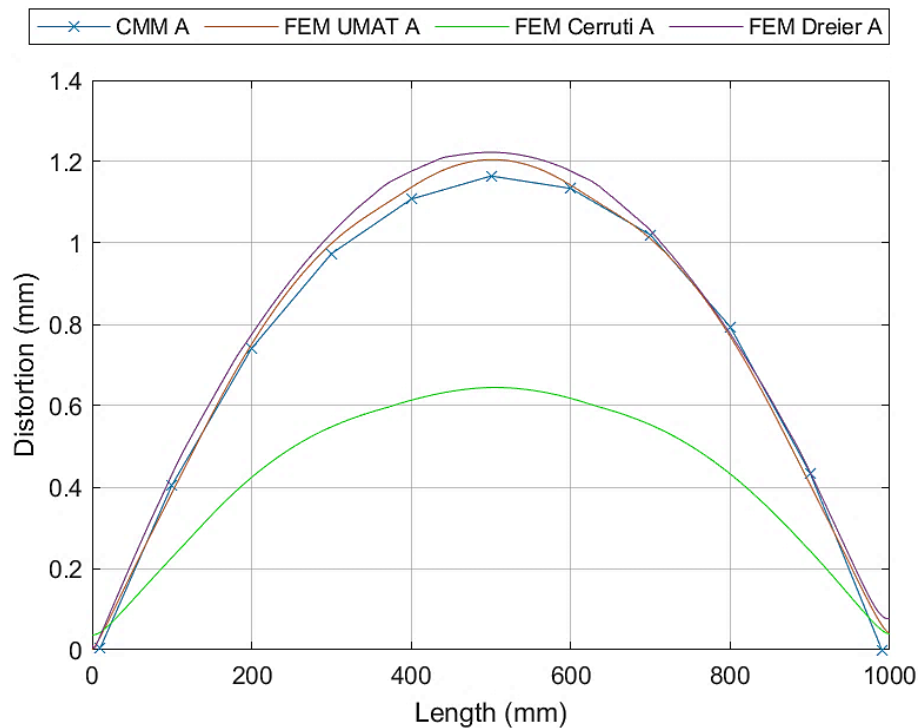


Figure 7-36: Comparison of stage 2 simulation results against CMM measurement profile line 'A'

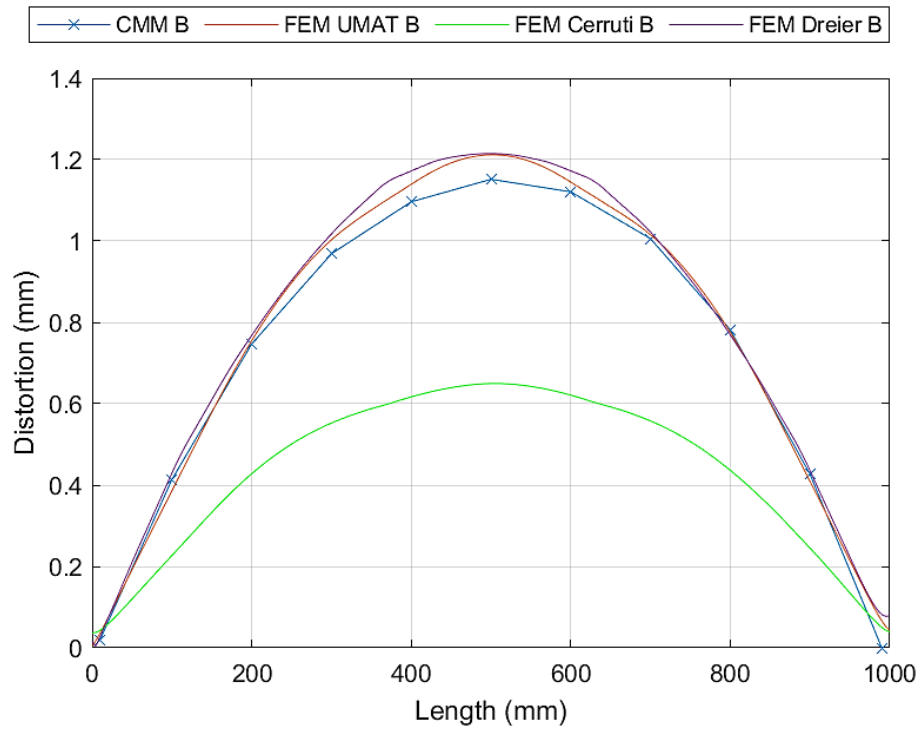


Figure 7-37: Comparison of stage 2 simulation results against CMM measurement profile line 'B'

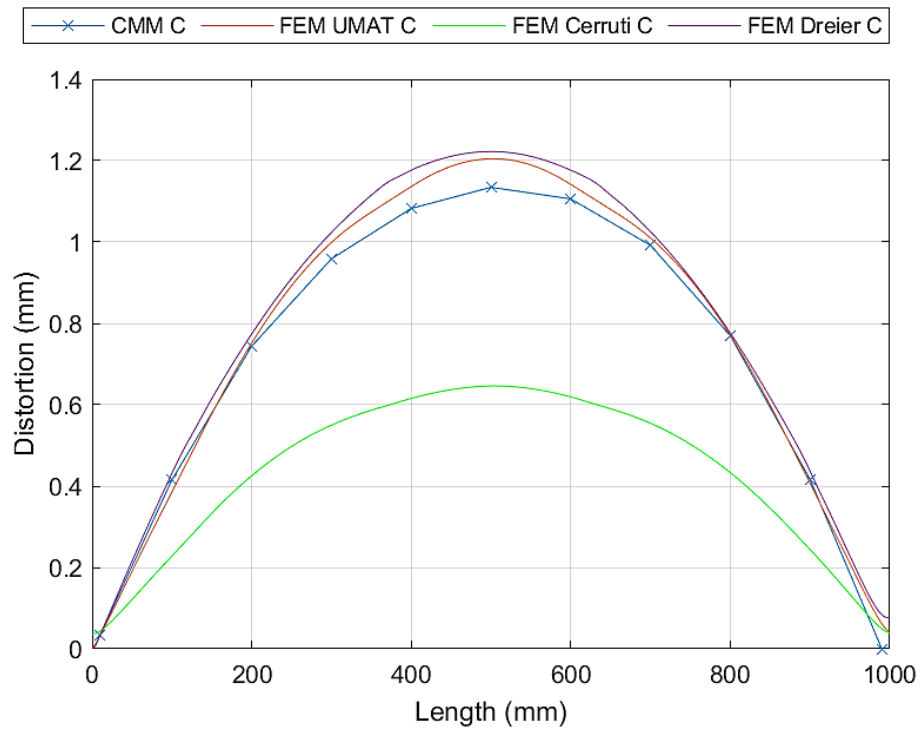


Figure 7-38: Comparison of stage 2 simulation results against CMM measurement profile line 'C'

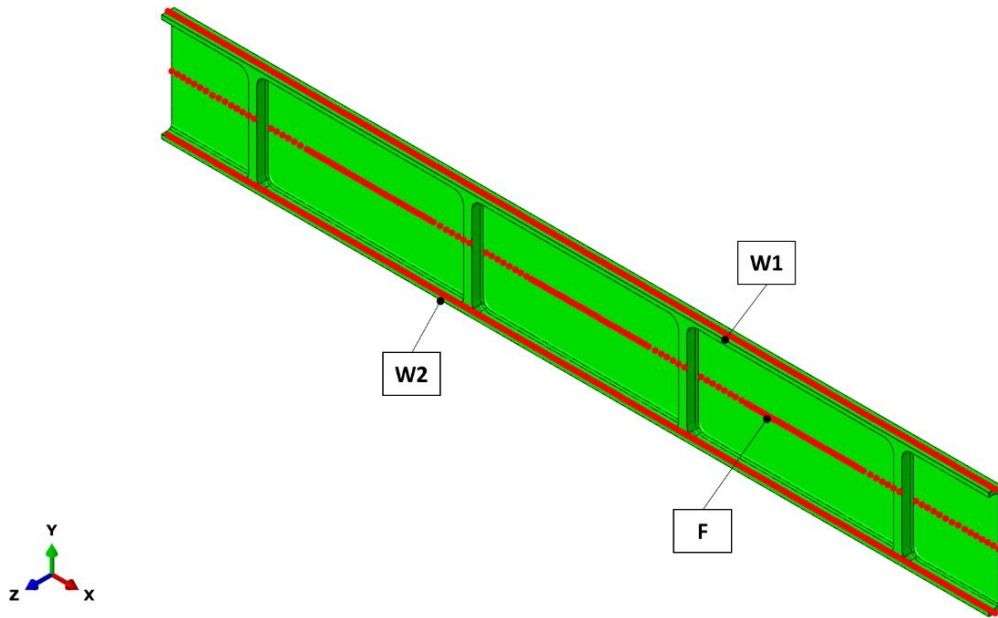


Figure 7-39: Thickness inspection lines: wall 1 (W1); Wall 2 (W2); and Floor (F)

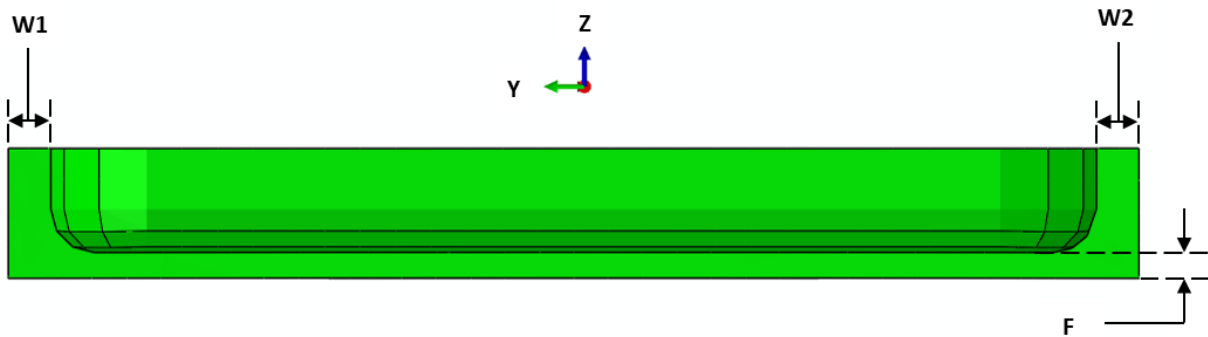


Figure 7-40: Identification of wall and floor thicknesses

Figure 7-41 and Figure 7-42 show the wall thickness variation compared with the nominal (4.9 mm). An arbitrary tolerance band of ± 0.100 mm has also been defined and plotted to provide context on how such inspection data could be presented and compared with metrology data (such as CMM thickness measurements currently employed today on aerospace wing structural components). Both wall thickness

comparisons indicate that the model features are undersized in localised regions. The position of max deviation corresponds to the mid-span of the external pocket walls, where the stiffness provided by the vertical stiffeners is at its minimum.

Considering the simulation process, removing the break-off waste material is modelled in one step. The previous two machining steps remove volumes of material associated with generating the break-off tabs. The reduction in the wall thicknesses highlights that after machining operations 7 and 8, the walls are distorting such that they are ‘leaning’ into the volume removal simulated in operation 9. This wall movement can be seen in the simulation results when viewing the inter-process distortion results after steps 7 & 8. Figure 7-43 and Figure 7-44 display the deformation of the component due to residual stress redistribution after machining steps 7 and 8, respectively, where the magnitude of the wall displacement reference to the y-coordinate direction is displayed. For both machining steps, the magnitude of the wall deflections corresponds to the reduction in wall thickness (0.018 mm for wall 1 and 0.016mm for wall 2). In reality, the wall thickness deviation due to residual stress-related deformation could also occur as sequential machining passes machine the break-offs.

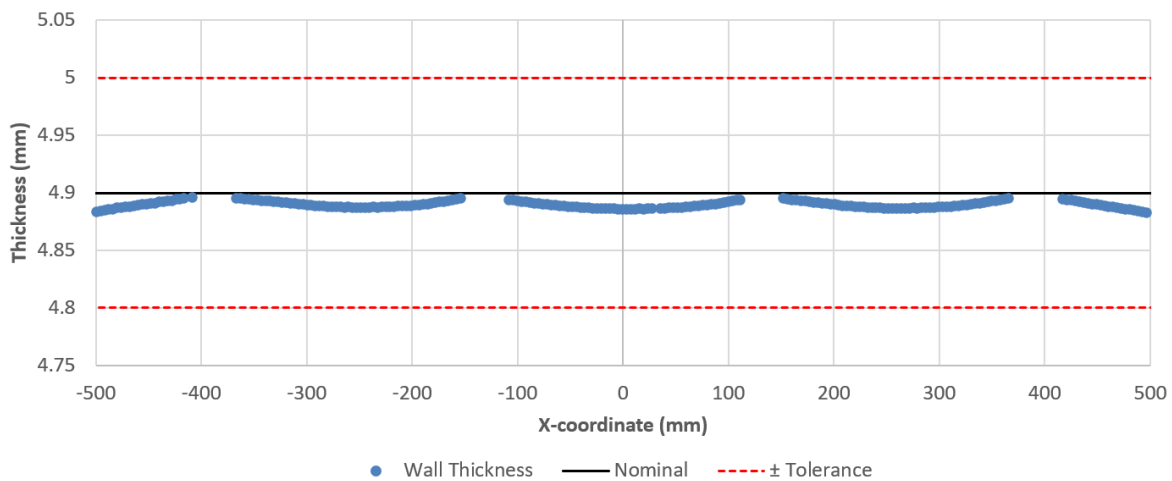


Figure 7-41: W1 - wall thicknesses

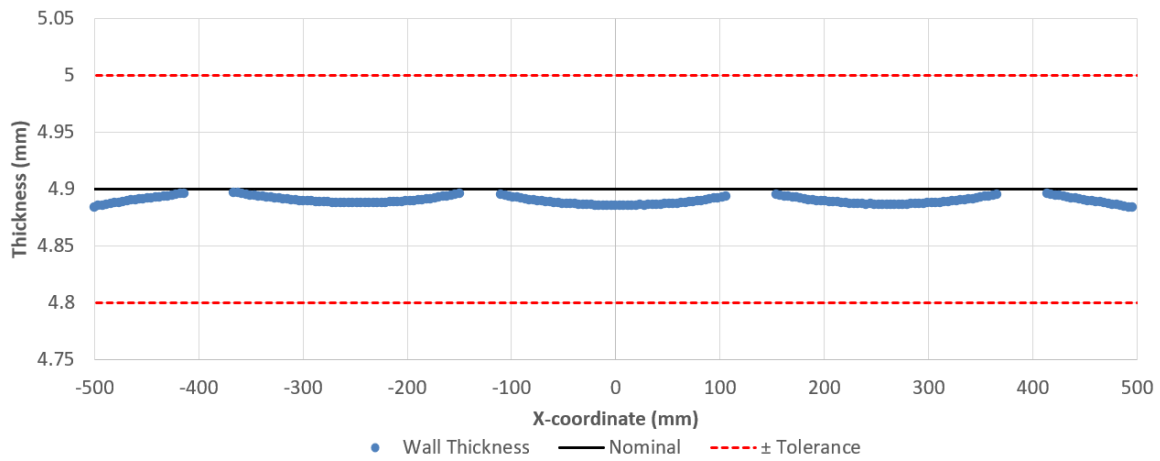


Figure 7-42: W2 - wall thicknesses

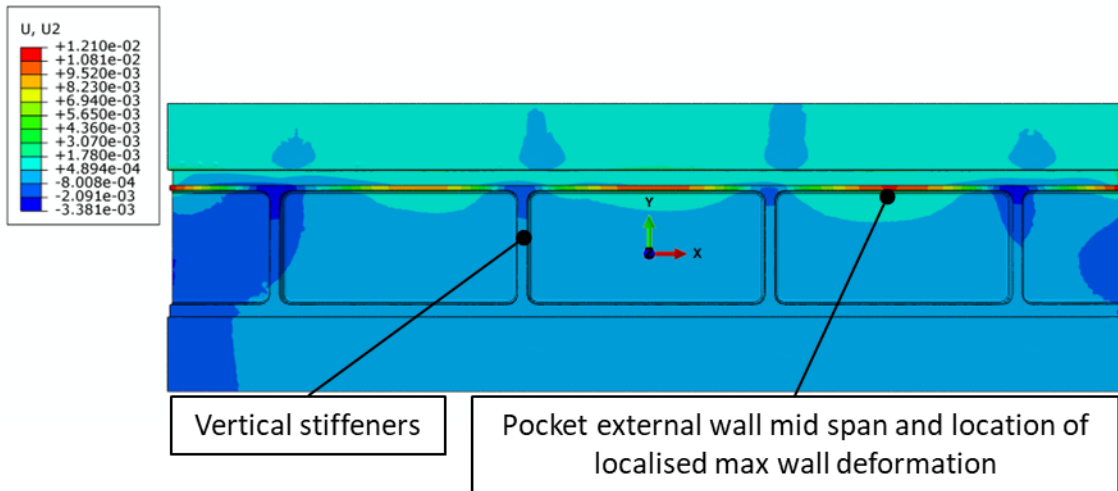


Figure 7-43: Distortion in U2 (Y coordinate) after machining simulation step 7

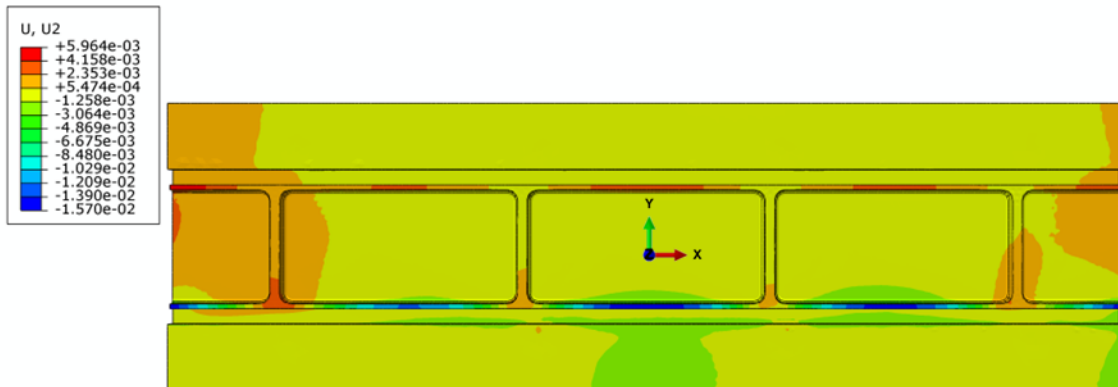


Figure 7-44: Distortion in U2 (Y coordinate) after machining simulation step 8

Figure 7-45 shows the variation of the pocket floor thickness along the midspan of the model. In general, the pocket floors' thicknesses are close to the nominal value of 3 mm across the span of the component, apart from a significant 0.42 mm thickness reduction observed at one end of the plate. This overcutting is due to the contact constraints modelled in stage 1 (see Figure 7-28) eliciting an inter-stage distortion response of the semi-machined component inconsistent across the x-coordinate direction. Therefore, the starting geometrical condition of the component induces a variable contact condition at stage 2 fixture modelling.

This can be seen in Figure 7-46 where COPEN indicates the contact condition between the bottom of the machined component and the machine bed (where positive COPEN indicates an opening between the contact pair and negative values indicate overclosure) projected onto the bottom of the machined component. A more considerable positive COPEN value indicates the part is further away from the machined bed and closer to the cutting volume, such that an overcutting condition is caused. Again, this is also possible in the physical machining condition as inter-stage component management is not a typical industrial practice. The designed fixturing solution is expected to compensate for the inter-process distortion. However, where a suitable fixture condition is not achievable or poorly designed, the modelling solution can highlight areas where potential over/under cutting conditions may occur.

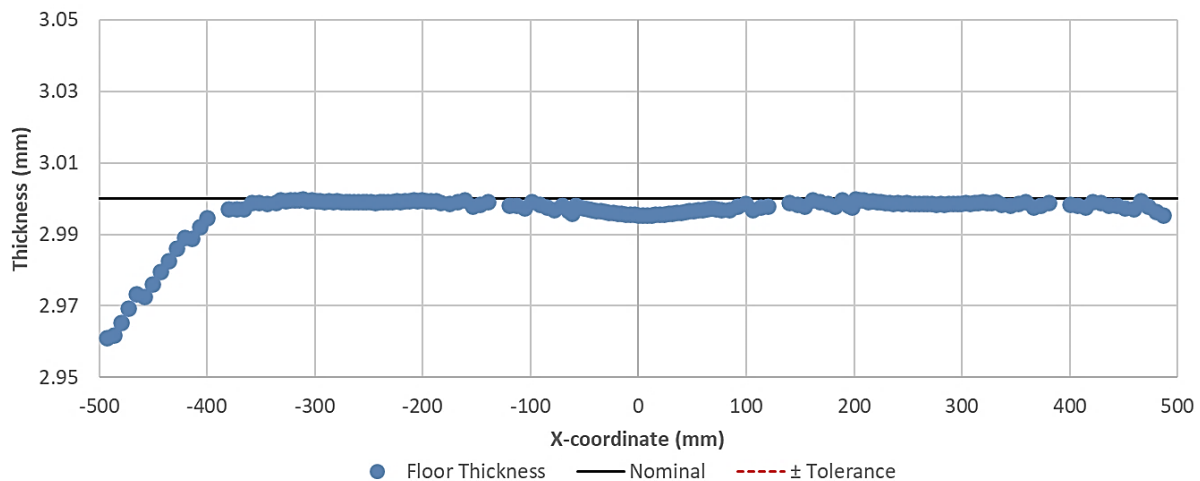


Figure 7-45: F – Floor Thickness

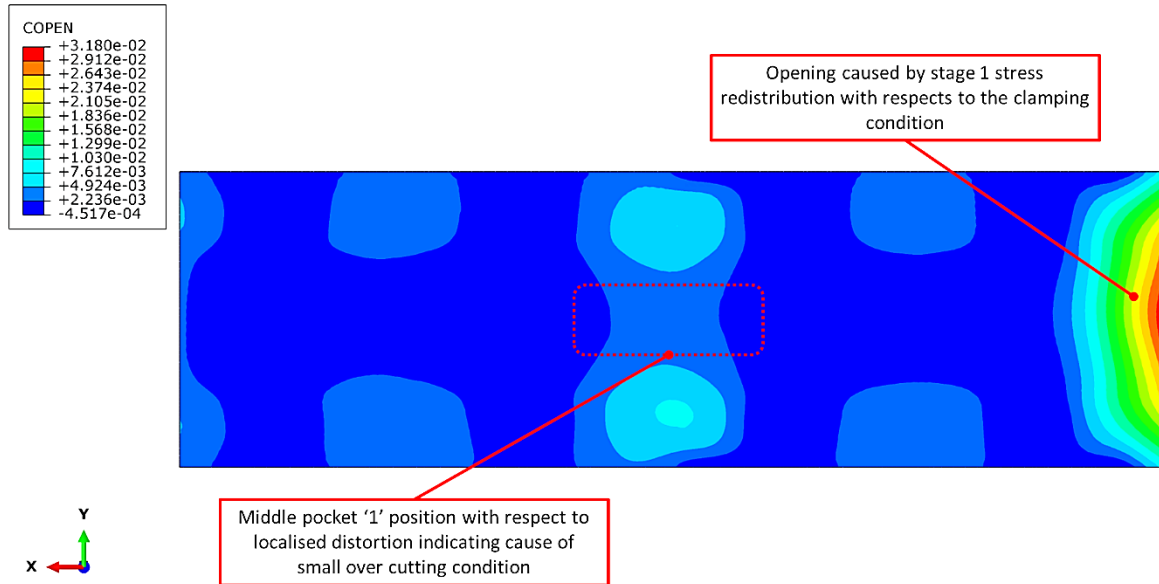


Figure 7-46: COPEN identifying gaps between the bottom of the machined component and machined bed

7.5 Concluding statements

Chapter 7 covered the application of the modelling methodology, implemented in ABAQUS finite element software and semi-automated with Python scripting. The simulation process was validated against another modelling methodology in the reviewed literature and experimental machining trials, where the distortion demonstrator component was produced and metrology data generated for comparison (see Chapter 6).

The material removal in the physical machining process is modelled by subtracting volumes representing key machined features from the initial model in several predefined steps. This process is also known as the mass removal material approach. The sequential removal of machining features is conducted from an initial stock material model to the finished product. The initial mesh representing the stock material condition is fitted with initial 'bulk' residual stress by ABAQUS user-defined subroutine. The bulk stresses are defined in the longitudinal and long-transverse mesh directions using a polynomial fit and applied as a function of the through-thickness integration point coordinate values. The redistribution of bulk stresses is calculated between material removal stages by mapping the stress fields from the previous mesh to the current mesh representing the newly generated geometry after cutting. The mapped stresses are unbalanced due to the removal of material and therefore redistribute to gain equilibrium over the numerical analysis step whilst interacting with the defined boundary conditions representing the machining fixtures in reality.

The machining-induced residual stresses are introduced into selectively defined boundary layers depending upon the process conditions of the current machining step. The boundary layer elements used are of a higher order than that of the bulk mesh and formulated such that they are suited to transmit loads even for thin element layers. The boundary layer is discretised by an optimal number of boundary layer elements defined by a simple plate bending analysis (results of which can be found in Chapter 7). The machining-induced residual stresses were applied across the boundary mesh according to the local tool path feed vector obtained using the CNC program data with Python programming. The elements are assigned a field variable value to indicate the direction in which the feed and normal bi-directional MIRS values will be orientated. These stress tensor values are defined at the integration points of the boundary layer elements as a function of depth from the machined surface. The sinusoidal decay function characterised the machining-induced stresses for face and end milling. The MIRS and bulk stresses are superimposed based on the superposition principle. The release of clamps and deflection of the part in the free state is simulated using 3-2-1 type boundary conditions. The modelling process is controlled by Python programming for a semi-automated modelling process.

A comparison of the method to an analytical beam bending solution and comparison to other modelling methods showed that the technique was suitable for simulating distortion due to process-induced residual stress. The results of the model distortion comparison against the residual stress-induced machining deformation in the demonstrator component showed good agreement validating the modelling procedure. Furthermore, the identified modelling methodologies used to derive the model concept have been reproduced to realise the evaluation against the developed methodology. The massive removal method showed a poor correlation with the experimental results, indicating the importance of defining the influence of MIRS for the designed demonstrator. The single-step procedure with MIRS applied as a function of the tool path showed a good correlation with both experimental and developed modelling concepts. However, this model assumes the part is perfectly manufactured. The developed modelling approach in this work captures the distortion of machined components due to bulk and machining-induced residual stress and the over/under-cutting geometrical error due to the components evolving internal stress field and inter-process displacement with respect to the applied boundary conditions, as identified in Chapter 7. However, the thickness variations suggested to be due to the inter-process distortions have not been verified with experimental data, and therefore further work to develop a metrology process for comparison to the model results is needed. However, comparing the developed modelling concept with other approaches, it can be concluded that the method is as accurate in modelling distortion but can also capture inter-process distortion-related quality issues.

8 Conclusion & Outlook

Residual stress-related part distortion causes non-conformance in machined aluminium thin-walled monolithic aero-structural components. Components with high length-to-width ratios and asymmetric designs are especially susceptible to residual stress-related distortion. Distorted components require corrective processes such as shot peening to bring the machined product back in line with design tolerances. Current industrial practice to address part distortion is to conduct costly and time-consuming iterative trials to reduce deformation in machined components based on empirically derived data by altering the machining process. This chapter provides an overall conclusion of the work and an outlook of further development potential. First, the conclusion will be provided concerning the research aim and objectives set out at the start of the thesis. Then the outlook will be given, focusing on the potential future development of the research concerning the experimental and modelling work.

8.1 Conclusion

The work aimed to generate knowledge in residual stress-related machining part distortion through experiments and the generation of part distortion simulation methodology. The following will evaluate the conducted work against each research objective set to meet the research aim.

The first research objective concerned an extensive literature review on residual stress and machining-related distortion. The literature review provided in Chapter 2 highlights the sources of residual stress-related post-machining distortion. The review also emphasised machining parameters and strategies that significantly influence the prevailing distortion upon machine fixture release due to their influence on the bulk residual stress redistribution and the introduction of near-surface machining-induced residual stress. However, it was found that some ambiguity and contradiction exist over the importance of specific machining strategies on process-induced residual stress formation and influence on final distortion. The literature review also draws attention to the efforts by researchers to develop modelling methodologies to predict the deformation of machined components due to residual stresses. A gap in the modelling methodologies was detailed where current methods do not account for the tool path machining-induced stress effects and the inter-process distortions of thin-walled components in the same simulation scheme.

The second research objective was created to address the knowledge gap on the influence of sequential machining operations and inter-tool path variation of process conditions on induced residual stress formation. Experimental trials were developed to address both areas using industrial machining tooling, processes and conditions such that relevant data for manufacturers could be generated. The sequential

machining trials used face-milling to study the MIRS in coupons machined with variable depths of cut sequencing. The MIRS measurements indicated that the variable sequencing trialled bared no influence on the final MIRS state. Therefore, the assumption that stresses imparted by the last machining pass must only be measured for use in finite element models simulating the effect of MIRS on part distortion is valid. The inter-tool path machining trial used the end-milling of pocket geometry to study the influence of variations of local cutting conditions on the induced residual stress at the component surface and sub-surface. The results showed that the choice of tool path strategy could significantly impact the magnitude of the peak compressive stresses in the machined component. Furthermore, it was shown that MIRS varies along the tool path at regions of variable cutting contact conditions (between straight line and corner cutting for a conventional spiral-out tool path). However, the change in MIRS was found to be localised. The results highlight the potential for altering the choice of tool path to produce a more favourable MIRS condition at the machined surface.

The third research objective developed to understand how altering sequential material removal operations might impact inter-process and post-process machining distortion in a 'distortion' demonstrator component. Aluminium plates were machined with variable machining DoC sequences. The test results here indicate that no observable influence was noted in the measured distortion of the component across the two stages of manufacture. Therefore, it can be proposed that further research be conducted to study the industrial practice of reducing the depth of cut when machining datum faces of aerospace components further, as for the test conducted in this work showed this practice only increased the machining cycle time and did not limit part distortion.

The final research objective was to develop a numerical simulation procedure to address the gap in other mythologies by including the influence of bulk residual stresses and machining-induced residual stresses on final part distortion with material removal sequenced based on the tool path progression so that inter-process and post-process distortion can be modelled. The numerical approach has been formed based on state-of-the-art distortion modelling methods. A multi-step material removal procedure with tool path dependant machining-induced residual stress mapping has been developed and implemented in ABAQUS finite element software and semi-automated with Python scripting. The simulation process was validated against another modelling methodology in the reviewed literature and experimental machining trials, where the distortion demonstrator component was produced, and metrology data generated for comparison (see Chapter 6).

8.2 Outlook

As detailed in section 8.1, experimental and numerical modelling has been undertaken to investigate residual stress formation and simulate related machining distortion. The following sections provide perspective on proposed future development for knowledge creation in residual stress and machining distortion and distortion modelling practises.

8.2.1 Empirical challenge of residual stress and machining distortion determination

Currently, MIRS is determined through expensive measurement techniques and empirical modelling (as carried out in this work). The lack of data limits the scenario-based optimisation that could be employed with the developed modelling method to determine more favourable distortion outcomes. Additionally, researchers have found that controlling key machining strategies and parameters is vital in managing part distortion due to residual stress definition in the final component [96]. Therefore, in the context of this work, other areas of further development are proposed:

- Determining a hybrid method of MIRS data generation where a suitable experimental testing scheme and supporting modelling regime are developed to extend the possible MIRS data used in distortion modelling. An extensive and reliable MIRS database can be generated and called upon so that changing process conditions can be reflected by alternating MIRS conditions in the modelled boundary layer. For example, artificial intelligence could define MIRS profiles between tested parameter ranges where empirical models fall short in describing the complex stress variation. This database of MIRS profiles would allow the modeller to trial variable process conditions and alternative machining strategies to find improved distortion cases.
- The work presented in the thesis showed that localised MIRS variation occurs across the machining tool path, such as corner transitioning for the helical spiral-type tool path. However, this change in MIRS was deemed very localised to the corner in the example tool path. A more intensive measurement scheme could be developed to understand further the phenomena discovered. Then the application of variable tool path strategies for intended process condition changes could be explored such that the imposed MIRS can be controlled to generate a more favourable distortion response.

- It was found that variable tool path strategies resulted in different near-surface residual stress values after finishing machining with consistent process conditions. However, the variable roughing strategies were not tested in the machining of the demonstrator component, and therefore, the impact on post-machining distortion was not studied. Hence, the influence of selected tool-path strategies on final distortion should be investigated.
- The numerical modelling procedure identified that the influence of boundary conditions on resulting deformation is a key consideration. This corresponds to findings in the literature [157]. Therefore further work testing the impact of variable and adaptive work-holding methods on post-machining distortion through experimental trials and the developed numerical tool should be explored [48].

8.2.2 Development and extension of the numerical model for distortion modelling

The numerical procedure presented in this work has been developed and validated for machining distortion caused by residual stresses. However, the numerical tool could be developed further as follows:

- The model can describe MIRS introduction as a function of complex tool paths. Currently, the method can describe stresses generated by conventional tool paths such as spiral-out and zig-zag milling. Updating the element detection procedure should be considered such that it can account for dynamic radial arching tool paths in applying process-induced residual stresses.
- Currently, the modelling process utilises Pythonic programming to control key modelling processes requiring minimal interaction to set up and run machining simulations. It also takes standard data format output from the current manufacturing process planning software (i.e., CAD models and CNC tool path files) as input to the model. It should be considered that the modelling method be fully automated and controlled through a guided user interface such that engineers with limited or no finite element modelling experience can set up and run distortion simulations for components of interest. This would allow for engineers within GKN aerospace to utilise the tool to assess distortion mitigation practices before physically manufacturing the components, allowing for productivity improvement investigations of legacy programs and potentially lowering the cost developing program for new product introduction through strategy study. Follow on projects are proposed by the sponsor to develop the model such that it is more autonomous and deployable within the process planning chain.

- It is possible to model the introduction of surface stresses caused by other manufacturing processes, such as shot peening or grinding, where the generated surface integrity is of primary concern. For example, shot peening introduces compressive stresses to improve the fatigue life of components. It is also utilised in the post-machining correction of distorted components. However, the corrective peening process is conducted based on the qualitative response of the product. Therefore, applying the numerical model could improve the surface treatment procedure's outcome through distortion prediction.
- The model can be extended to simulating distortion in other machined materials, such as Titanium components, where distortion is also a source of quality errors. By replicating the process outlined in this work, a suitable modelling methodology should be developed and adapted to simulate distortion in titanium components.

References

- [1] Boeing Commercial Aviation, "Commercial Market Outlook 2020-2039," 2020.
- [2] Airbus, "Airbus Global Market Forecast 2021 - 2040," p. 23, 2021.
- [3] ICAO, "Effects of Novel Coronavirus (COVID-19) on Civil Aviation: Economic Impact Analysis," *Int. Civ. Aviat. Organ. (ICAO), Montréal, Canada*, no. May, p. 125, 2021.
- [4] Precedence Research, "Aerospace Materials Market," 2022. [Online]. Available: <https://www.precedenceresearch.com/aerospace-materials-market>. [Accessed: 12-Jan-2023].
- [5] GKN Aerospace, "About GKN Aerospace." [Online]. Available: <https://www.gknaerospace.com/en/about-gkn-aerospace/>. [Accessed: 21-Dec-2022].
- [6] W. Sim, "Residual Stress Engineering in Manufacture of Aerospace Structural Parts," *Int. Conf. distorsions Eng.*, no. i, pp. 187–194, 2011.
- [7] W. M. Sim, "Challenges of residual stress and part distortion in the civil airframe industry," *Int. J. Microstruct. Mater. Prop.*, vol. 5, no. 4/5, p. 446, 2010.
- [8] A. Tiwari, K. Vergidis, R. Lloyd, and J. Cushen, "Automated inspection using database technology within the aerospace industry," *Proc. Inst. Mech. Eng. Part B J. Eng. Manuf.*, vol. 222, no. 2, pp. 175–183, 2008.
- [9] UNISIGN Machine Tools, "UNIAXLE: CNC machine for machining rear axles." 2021.
- [10] E. Brinksmeier, J. T. Cammett, W. König, P. Leskovic, J. Peters, and H. K. Tonshoff, "Residual stresses—measurement and causes in machining processes," *CIRP Ann. Technol.*, vol. 31, no. 2, pp. 491–510, 1982.
- [11] R. Bilkhu, S. Ayvar-Soberanis, C. Pinna, and T. McLeay, "Machining distortion in asymmetrical residual stress profiles," *Procedia CIRP*, vol. 82, pp. 395–399, 2019.
- [12] J. Guang Li and S. Qi Wang, "Distortion caused by residual stresses in machining aeronautical aluminum alloy parts: recent advances," *Int. J. Adv. Manuf. Technol.*, vol. 89, no. 1–4, pp. 997–1012, 2017.
- [13] W. Grzesik, *Advanced Machining Processes of Metallic Materials*. 2008.
- [14] H. K. Tonshoff and B. Denkena, "Basics of Cutting and Abrasive Processes," pp. 21–37, 2013.
- [15] A. P. Markopoulos, *Finite Element Method in Machining Processes*. 2013.
- [16] P. de Vos, *Applied metal cutting physics: best practices*. Fagersta: Seco Tools AB, 2016.
- [17] SECO, "High Performance Machining Solid Carbide End Mills | Secotools.com." [Online]. Available: https://www.secotools.com/#article/m_7468. [Accessed: 21-May-2018].
- [18] Modern Machine Shop, "Cylindrical Grinding Machine Grinds Non-Round Contours : Modern Machine Shop," 2013. [Online]. Available: <https://www.mmsonline.com/products/cylindrical-grinding-machine-grinds-non-round-contours>. [Accessed: 21-May-2018].

- [19] J. P. Davim, *Machining: Fundamentals and recent advances*. Springer Verlag, 2008.
- [20] P. J. Arrazola, T. Özel, D. Umbrello, M. Davies, and I. S. Jawahir, "Recent advances in modelling of metal machining processes," *CIRP Ann. - Manuf. Technol.*, vol. 62, no. 2, pp. 695–718, 2013.
- [21] H. K. Tönshoff and B. Denkena, *Basics of cutting and abrasive processes [electronic resource]*. Berlin Heidelberg: Springer Verlag, 2013.
- [22] M. E. Merchant, "Mechanics of the Metal Cutting Process. I. Orthogonal Cutting and a Type 2 Chip .Contributed 'Original Research Mechanics of the Metal Cutting Process. I. Orthogonal Cutting and a Type 2 Chip," *J. Appl. Phys.*, vol. 16, no. 16, 1945.
- [23] A. P. Markopoulos, *Finite Element Method in Machining Processes*. 2013.
- [24] J. Burek, M. Plodzien, L. Zylka, and P. Sulkowicz, "High-performance end milling of aluminum alloy: Influence of different serrated cutting edge tool shapes on the cutting force," *Adv. Prod. Eng. Manag.*, vol. 14, no. 4, pp. 494–506, 2019.
- [25] Kistler, "Measuring cutting forces in milling operations." [Online]. Available: <https://www.kistler.com/GB/en/measuring-cutting-forces-in-milling-operations/C00000127>. [Accessed: 12-Sep-2023].
- [26] B. L. D. L. Denkena, "Machining Induced Residual Stress in Wrought Aluminium Parts," *8th Int. Conf. Adv. Manuf. Syst. Technol.*, 2008.
- [27] I. Perez *et al.*, "Effect of cutting speed on the surface integrity of face milled 7050-T7451 aluminium workpieces," *Procedia CIRP*, vol. 71, pp. 460–465, 2018.
- [28] "Monolithic Machined Wing Rib – Kenco Aerospace LLC." .
- [29] "Zimmermann Inc." .
- [30] "Aerospace Aluminum Plate - Industrial Aluminum Plates Supplier | TW Metals." .
- [31] M. Jackson, "Aluminium Alloys Pt1." 2012.
- [32] M. Jackson, "Aluminium Alloys Pt2," vol. 222, no. 662. pp. 821–826, 1996.
- [33] MatWeb, "Aluminum 7050-T7451 (7050-T73651)." [Online]. Available: <http://www.matweb.com/search/DataSheet.aspx?MatGUID=142262cf7fbc4c83917ca5c3d17df1ed>. [Accessed: 17-Apr-2018].
- [34] MatWeb, "7010 Aluminum Composition Spec." [Online]. Available: <http://www.matweb.com/search/datasheet.aspx?matguid=bed879fd995c4c8e98f8d24d644b5db4&ckck=1>. [Accessed: 17-Apr-2018].
- [35] M. B. Prime and M. R. Hill, "Residual stress, stress relief and inhomogeneity in Al plate," *Scr. Mater.*, vol. 46, pp. 77–82, 2002.
- [36] C. Tom, "Achieving Stress Free Parts High Strength Aluminum Alloys ©," no. March, pp. 1–22, 2011.
- [37] M. S. Younger and K. H. Eckelmeyer, "Overcoming Residual Stresses and Machining Distortion in

- the Production of Aluminum Alloy Satellite Boxes,” no. November, 2007.
- [38] J. R. Davis, “Aluminum and Aluminum Alloys,” *Light Met. Alloy.*, p. 66, 2001.
- [39] M. H. Jacobs, “Introduction to Aluminium as an Engineering Material,” *Train. Alum. Appl. Technol.*, vol. Lecture 12, pp. 1–22, 1999.
- [40] J. Beddoes and M. J. Bibby, “Principles of Metal Manufacturing Processes,” *Princ. Met. Manuf. Process.*, pp. 232–269, 1999.
- [41] W. Sim, “A COncurrent approach to Manufacturing induced Part distortion in Aerospace ComponenTs,” 2009.
- [42] R. C. Hibbeler, *Mechanics of Materials*, 10th ed. Pearson Education, 2017.
- [43] G. Liu and S. Quek, *The Finite Element Method: A Practical Course*. Elsevier Science & Technology, 2013.
- [44] G. Totten, *Handbook of Residual Stress and Deformation of Steel*. Materials Park, UNITED STATES: A S M International, 2002.
- [45] P. J. Withers and H. K. D. H. Bhadeshia, “Residual stress. Part 2 – Nature and origins,” *Mater. Sci. Technol.*, vol. 17, no. 4, pp. 366–375, 2001.
- [46] P. J. Withers and H. K. D. H. Bhadeshia, “Residual stress. Part 1 – Measurement techniques,” *Mater. Sci. Technol.*, vol. 17, no. 4, pp. 355–365, 2001.
- [47] W. F. Hosford, “Mechanical Behavior of Materials,” *Zhurnal Eksp. i Teor. Fiz.*, p. 437, 2009.
- [48] X. Cerutti, K. Mocellin, S. Hassini, B. Blaysat, and E. Duc, “Methodology for aluminium part machining quality improvement considering mechanical properties and process conditions,” *CIRP J. Manuf. Sci. Technol.*, vol. 18, pp. 18–38, 2017.
- [49] J. CHATELAIN, J. LALONDE, and A. TAHAN, “A Comparison of the Distortion of Machined Parts Resulting From Residual Stresses Within Workpieces,” *Wseas.Us*, no. 1, pp. 2–7, 2010.
- [50] L. Zhang, H. Wang, S. Li, and Z. Lin, “Variation propagation modeling and pattern mapping method for aircraft assembly structure considering residual stress from manufacturing process,” *Proc. Inst. Mech. Eng. Part B J. Eng. Manuf.*, vol. 231, no. 3, pp. 437–453, 2017.
- [51] I. S. Jawahir *et al.*, “Surface integrity in material removal processes: Recent advances,” *CIRP Ann. - Manuf. Technol.*, vol. 60, no. 2, pp. 603–626, 2011.
- [52] VEQTER©, “Residual Stress Measurement Overview.” [Online]. Available: <http://www.veqter.co.uk/residual-stress-measurement/overview>. [Accessed: 21-May-2018].
- [53] G. S. Schajer, “Relaxation Methods for Measuring Residual Stresses: Techniques and Opportunities,” *Exp. Mech.*, vol. 50, no. 8, pp. 1117–1127, 2010.
- [54] P. J. Withers, M. Turski, L. Edwards, P. J. Bouchard, and D. J. Buttle, “Recent advances in residual stress measurement,” *Int. J. Press. Vessel. Pip.*, vol. 85, no. 3, pp. 118–127, 2008.

- [55] D. Walker, "Residual Stress Measurement Techniques," *Adv. Mater. Process.*, vol. 159, no. 8, pp. 30–33, 2001.
- [56] G. S. Schajer and M. B. Prime, "Use of Inverse Solutions for Residual Stress Measurements," *J. Eng. Mater. Technol.*, vol. 128, no. 3, p. 375, 2006.
- [57] S. Dreier and B. Denkena, "Determination of residual stresses in plate material by layer removal with machine-integrated measurement," 2014.
- [58] D. M. Goudar, C. E. Truman, and D. J. Smith, "Evaluating Uncertainty in Residual Stress Measured Using the Deep-Hole Drilling Technique," *Strain*, vol. 47, no. 1, pp. 62–74, Feb. 2011.
- [59] T. Lorentzen, "Nondestructive evaluation of residual stresses by neutron diffraction," *NDT Int.*, vol. 21, no. 6, pp. 385–388, 1988.
- [60] S. E. Pritchard, "The use of ultrasonics for residual stress analysis," *NDT Int.*, vol. 20, no. 1, pp. 57–60, 1987.
- [61] F. A. Kandil, J. D. Lord, A. T. Fry, and P. V Grant, "Review of Residual Stress Measurement Methods -A Guide to Technique Selection," 2001.
- [62] S. Masoudi, G. Amirian, E. Saeedi, and M. Ahmadi, "The Effect of Quench-Induced Residual Stresses on the Distortion of Machined Thin-Walled Parts," *J. Mater. Eng. Perform.*, vol. 24, no. 10, pp. 3933–3941, 2015.
- [63] X. Cerutti and K. Mocellin, "Influence of the machining sequence on the residual stress redistribution and machining quality: Analysis and improvement using numerical simulations," *Int. J. Adv. Manuf. Technol.*, vol. 83, no. 1–4, pp. 489–503, 2016.
- [64] I. Llanos, J. L. Lanzagorta, and A. Beristain, "Part Distortion Modeling on Aluminum Slender Structural Components for Aeronautical Industry," *Procedia CIRP*, vol. 58, pp. 158–162, 2017.
- [65] L. D'Alvise *et al.*, "Modelling of part distortion due to residual stresses relaxation: An aeronautical case study," *Procedia CIRP*, vol. 31, pp. 447–452, 2015.
- [66] D. Chantzis, S. Van-Der-Veen, J. Zettler, and W. M. Sim, "An industrial workflow to minimise part distortion for machining of large monolithic components in aerospace industry," *Procedia CIRP*, vol. 8, pp. 281–286, 2013.
- [67] Z. Zhang, L. Li, Y. Yang, N. He, and W. Zhao, "Machining distortion minimization for the manufacturing of aeronautical structure," *Int. J. Adv. Manuf. Technol.*, vol. 73, no. 9–12, pp. 1765–1773, 2014.
- [68] M. Araghchi, H. Mansouri, R. Vafaei, and Y. Guo, "A novel cryogenic treatment for reduction of residual stresses in 2024 aluminum alloy," *Mater. Sci. Eng. A*, vol. 689, no. January, pp. 48–52, 2017.
- [69] X. Huang, J. Sun, and J. Li, "Effect of initial residual stress and machining-induced residual stress on the deformation of aluminium alloy plate," *Stroj. Vestnik/Journal Mech. Eng.*, vol. 61, no. 2, pp. 131–137, 2015.
- [70] B. Denkena, L. De León-Garcia, and J. Kohler, "Influence of High Performance Cutting Operations

- on the Residual Stresses of aluminium structural workpieces,” *Proceeding 25TH Int. Congr. Aeronaut. Sci.*, pp. 1–7, 2006.
- [71] D. R. Garcia, M. R. Hill, J. C. Aurich, and B. S. Linke, “Characterization of Machining Distortion due to Residual Stresses in Quenched Aluminum,” no. 50725, p. V001T02A031, 2017.
- [72] S. Masoudi, S. Amini, E. Saeidi, and H. Eslami-Chalander, “Effect of machining-induced residual stress on the distortion of thin-walled parts,” *Int. J. Adv. Manuf. Technol.*, vol. 76, no. 1–4, pp. 597–608, 2014.
- [73] W. Zhang, K. Fang, Y. Hu, S. Wang, and X. Wang, “Effect of machining-induced surface residual stress on initiation of stress corrosion cracking in 316 austenitic stainless steel,” *Corros. Sci.*, vol. 108, pp. 173–184, 2016.
- [74] T. Segawa, H. Sasahara, and M. Tsutsumi, “Development of a new tool to generate compressive residual stress within a machined surface,” *Int. J. Mach. Tools Manuf.*, vol. 44, no. 11, pp. 1215–1221, 2004.
- [75] K. Jacobus, R. E. DeVor, and S. G. Kapoor, “Machining-Induced Residual Stress: Experimentation and Modeling,” *J. Manuf. Sci. Eng.*, vol. 122, no. 1, p. 20, 2000.
- [76] M. H. Miguélez, R. Zaera, A. Molinari, R. Cheriguene, and A. Rusinek, “Residual stresses in orthogonal cutting of metals: The effect of thermomechanical coupling parameters and of friction,” *J. Therm. Stress.*, vol. 32, no. 3, pp. 269–289, 2009.
- [77] J. Denkena, B. de Leon Garcia, L. and Kohler, “FEM-Simulation of High-Performance-Milling,” *10th CIRP Int. Work. Model. Mach. Oper.*, pp. 149–156, 2007.
- [78] B. Denkena and L. De Leon, “Milling induced residual stresses in structural parts out of forged aluminium alloys,” *Int. J. Mach. Mach. Mater.*, vol. 4, no. 4, p. 335, 2008.
- [79] X. Jiang, B. Li, J. Yang, X. Zuo, and K. Li, “An approach for analyzing and controlling residual stress generation during high-speed circular milling,” *Int. J. Adv. Manuf. Technol.*, vol. 66, no. 9–12, pp. 1439–1448, 2013.
- [80] L. Nowag, J. Sölter, A. Walter, and E. Brinksmeier, “Effect of machining parameters and clamping technique on residual stresses and distortion of bearing rings,” *Materwiss. Werksttech.*, vol. 37, no. 1, pp. 45–51, 2006.
- [81] J. D. Thiele, S. N. Melkote, R. A. Peascoe, and T. R. Watkins, “Effect of Cutting-Edge Geometry and Workpiece Hardness on Surface Residual Stresses in Finish Hard Turning of AISI 52100,” *J. Manuf. Sci. Eng.*, vol. 122, no. November, pp. 642–649, 2000.
- [82] J. Hua *et al.*, “Effect of feed rate, workpiece hardness and cutting edge on subsurface residual stress in the hard turning of bearing steel using chamfer + hone cutting edge geometry,” *Mater. Sci. Eng. A*, vol. 394, no. 1–2, pp. 238–248, 2005.
- [83] C. E. Ventura, B. Breidenstein, and B. Denkena, “Influence of customized cutting edge geometries on the workpiece residual stress in hard turning,” *Proc. Inst. Mech. Eng. Part B J. Eng. Manuf.*, p. 095440541668538, 2017.

- [84] D. Nespor, B. Denkena, T. Grove, and V. Böß, "Differences and similarities between the induced residual stresses after ball end milling and orthogonal cutting of Ti-6Al-4V," *J. Mater. Process. Technol.*, vol. 226, pp. 15–24, 2015.
- [85] K. Surya Sundara Rao and K. Viswanath Allamraju, "Effect on Micro-Hardness and Residual Stress in CNC Turning of Aluminium 7075 Alloy," *Mater. Today Proc.*, vol. 4, no. 2, pp. 975–981, 2017.
- [86] B. Li, X. Jiang, J. Yang, and S. Y. Liang, "Effects of depth of cut on the redistribution of residual stress and distortion during the milling of thin-walled part," *J. Mater. Process. Technol.*, vol. 216, pp. 223–233, 2015.
- [87] X. Ji and S. Y. Liang, "Model-based sensitivity analysis of machining-induced residual stress under minimum quantity lubrication," *Proc. Inst. Mech. Eng. Part B J. Eng. Manuf.*, vol. 231, no. 9, pp. 1528–1541, 2017.
- [88] J. Kenda, F. Pusavec, and J. Kopac, "Analysis of Residual Stresses in Sustainable Cryogenic Machining of Nickel Based Alloy—Inconel 718," *J. Manuf. Sci. Eng.*, vol. 133, no. 4, p. 041009, 2011.
- [89] Z. T. Tang, Z. Q. Liu, Y. Z. Pan, Y. Wan, and X. Ai, "The influence of tool flank wear on residual stresses induced by milling aluminum alloy," *J. Mater. Process. Technol.*, vol. 209, no. 9, pp. 4502–4508, 2009.
- [90] L. Chen, T. I. El-Wardany, and W. C. Harris, "Modelling the effects of flank wear land and chip formation on residual stresses," *CIRP Ann. - Manuf. Technol.*, vol. 53, no. 1, pp. 95–98, 2004.
- [91] J. C. Outeiro, J. P. Costes, and J. R. Kornmeier, "Cyclic variation of residual stress induced by tool vibration in machining operations," *Procedia CIRP*, vol. 8, pp. 493–497, 2013.
- [92] M. C. Santos, A. R. Machado, W. F. Sales, M. A. S. Barrozo, and E. O. Ezugwu, "Machining of aluminum alloys: a review," *Int. J. Adv. Manuf. Technol.*, vol. 86, no. 9–12, pp. 3067–3080, 2016.
- [93] M. N. A. Nasr, E.-G. Ng, and M. A. Elbestawi, "Effects of Strain Hardening and Initial Yield Strength on Machining-Induced Residual Stresses," *J. Eng. Mater. Technol.*, vol. 129, no. 4, p. 567, 2007.
- [94] Y. Ma, P. Feng, J. Zhang, Z. Wu, and D. Yu, "Prediction of surface residual stress after end milling based on cutting force and temperature," *J. Mater. Process. Technol.*, vol. 235, pp. 41–48, 2016.
- [95] E. Abboud, H. Attia, B. Shi, A. Damir, V. Thomson, and Y. Mebrahtu, "Residual Stresses and Surface Integrity of Ti-alloys during Finish Turning - Guidelines for Compressive Residual Stresses," *Procedia CIRP*, vol. 45, pp. 55–58, 2016.
- [96] S. Dreier, J. Brüning, and B. Denkena, "Simulation based reduction of residual stress related part distortion," *Materwiss. Werksttech.*, vol. 47, no. 8, pp. 710–717, 2016.
- [97] L. D'Alvise, D. Chantzis, B. Schoinochoritis, and K. Salonitis, "Modelling of part distortion due to residual stresses relaxation: An aeronautical case study," *Procedia CIRP*, vol. 31, pp. 447–452, 2015.
- [98] S. Jayanti *et al.*, "Predictive modeling for tool deflection and part distortion of large machined components," *Procedia CIRP*, vol. 12, pp. 37–42, 2013.
- [99] A. Madariaga, P. J. Arrazola, I. Perez, R. Sanchez, J. J. Ruiz, and F. J. Rubio, "Reduction of Distortion of Large Aluminium Parts By Controlling Machining-Induced Residual Stresses," pp. 1–15, 2017.

- [100] K. Ma, R. Goetz, and S. Srivatsa, "MODELING OF RESIDUAL STRESS AND MACHINING DISTORTION IN AEROSPACE COMPONENTS," 2010.
- [101] Y. Ma, J. Zhang, D. Yu, P. Feng, and C. Xu, "Modeling of machining distortion for thin-walled components based on the internal stress field evolution," *Int. J. Adv. Manuf. Technol.*, pp. 3597–3612, 2019.
- [102] Y. Ma, J. Zhang, P. Feng, D. Yu, and C. Xu, "Study on the evolution of residual stress in successive machining process," pp. 1025–1034, 2018.
- [103] O. Fergani, X. Jiang, and T. Welo, "Analysis of residual stress-induced distortions of thin sheet structures in multi- step milling Analysis of Residual Stress-Induced Distortions of Thin Sheet Structures in Multi-Step Milling," vol. 080014, no. October 2016, 2017.
- [104] C. R. Liu and Y. B. Guo, "Finite element analysis of the effect of sequential cuts and tool-chip friction on residual stresses in a machined layer," *Int. J. Mech. Sci.*, vol. 42, no. 6, pp. 1069–1086, 2000.
- [105] W. Callister and D. Rethwisch, *Materials science and engineering: an introduction*, vol. 94. 2007.
- [106] Curtiss-Wright, "controlled shot peening diagram | CURTISS-WRIGHT SURFACE TECHNOLOGIES." [Online]. Available: <https://www.cwst.co.uk/services/controlled-shot-peening/controlled-shot-peening-diagram/>. [Accessed: 11-Apr-2018].
- [107] M. Munthe, "The Method Of Corrective Shot Peening : How To Correct The Distortion On The Machined Parts."
- [108] H. C. Möhring and P. Wiederkehr, "Intelligent Fixtures for High Performance Machining," *Procedia CIRP*, vol. 46, pp. 383–390, 2016.
- [109] S. L. Jeng, L. G. Chen, and W. H. Chieng, "Analysis of minimum clamping force," *Int. J. Mach. Tools Manuf.*, vol. 35, no. 9, pp. 1213–1224, 1995.
- [110] A. Gameros, S. Lowth, D. Axinte, A. Nagy-Sochacki, O. Craig, and H. R. Siller, "State-of-the-art in fixture systems for the manufacture and assembly of rigid components: A review," *Int. J. Mach. Tools Manuf.*, vol. 123, no. April, pp. 1–21, 2017.
- [111] Y. Li, C. Liu, X. Hao, J. X. Gao, and P. G. Maropoulos, "Responsive fixture design using dynamic product inspection and monitoring technologies for the precision machining of large-scale aerospace parts," *CIRP Ann. - Manuf. Technol.*, vol. 64, no. 1, pp. 173–176, 2015.
- [112] O. Gonzalo *et al.*, "A method to minimize the workpiece deformation using a concept of intelligent fixture," *Robot. Comput. Integr. Manuf.*, vol. 48, no. March, pp. 209–218, 2017.
- [113] Y. Yang, M. Li, and K. R. Li, "Comparison and analysis of main effect elements of machining distortion for aluminum alloy and titanium alloy aircraft monolithic component," *Int. J. Adv. Manuf. Technol.*, vol. 70, no. 9–12, pp. 1803–1811, 2014.
- [114] X. Huang, J. Sun, and J. Li, "Finite element simulation and experimental investigation on the residual stress-related monolithic component deformation," *Int. J. Adv. Manuf. Technol.*, vol. 77, no. 5–8, pp. 1035–1041, 2015.
- [115] A. P. Markopoulos, *Finite Element Method in Machining Processes*. 2013.

- [116] D. a. Tanner and J. S. Robinson, "Residual stress prediction and determination in 7010 aluminum alloy forgings," *Exp. Mech.*, vol. 40, no. 1, pp. 75–82, 2000.
- [117] D. A. Tanner and J. S. Robinson, "Modelling stress reduction techniques of cold compression and stretching in wrought aluminium alloy products," *Finite Elem. Anal. Des.*, vol. 39, no. 5–6, pp. 369–386, 2003.
- [118] J. Robert, "PREDICTION OF RESIDUAL STRESS AND DISTORTION FROM RESIDUAL STRESS IN HEAT TREATED AND MACHINED ALUMINUM PARTS A Thesis Presented to The Faculty of the Department of Mechanical Engineering San José State University In Partial Fulfillment of the Requirement," no. May, 2014.
- [119] D. Hornbach and P. Prevéy, "Development of Machining Procedures to Minimize Distortion During Manufacture," *ASM Proc. 17th Heat Treat. Soc. Conf. Expo. Heat Treat.*, pp. 13–18, 1998.
- [120] N. Chobaut, D. Carron, S. Arsène, P. Schloth, and J. M. Drezet, "Quench induced residual stress prediction in heat treatable 7xxx aluminium alloy thick plates using Gleeble interrupted quench tests," *J. Mater. Process. Technol.*, vol. 222, pp. 373–380, 2015.
- [121] S. W. Dean, A. K. Nallathambi, Y. Kaymak, E. Specht, and A. Bertram, "Optimum Strategies to Reduce Residual Stresses and Distortion during the Metal Quenching Process," *J. ASTM Int.*, vol. 6, no. 4, p. 101806, 2009.
- [122] M. Wan, X. Y. Ye, D. Y. Wen, and W. H. Zhang, "Modeling of machining-induced residual stresses," *Journal of Materials Science*, vol. 54, no. 1. Springer US, pp. 1–35, 2019.
- [123] M. H. El-Axir, "A method of modeling residual stress distribution in turning for different materials," *Int. J. Mach. Tools Manuf.*, vol. 42, no. 9, pp. 1055–1063, 2002.
- [124] D. Ulutan, Y. M. Arisoy, T. Özel, and L. Mears, "Empirical modeling of residual stress profile in machining nickelbased superalloys using the sinusoidal decay function," *Procedia CIRP*, vol. 13, pp. 365–370, 2014.
- [125] T. J. Barrett, D. J. Savage, M. Ardeljan, and M. Knezevic, "An automated procedure for geometry creation and finite element mesh generation: Application to explicit grain structure models and machining distortion," *Comput. Mater. Sci.*, vol. 141, pp. 269–281, 2018.
- [126] S. M. Ratchev, S. M. Afazov, A. A. Becker, and S. Liu, "Mathematical modelling and integration of micro-scale residual stresses into axisymmetric FE models of Ti6Al4V alloy in turning," *CIRP J. Manuf. Sci. Technol.*, vol. 4, no. 1, pp. 80–89, 2011.
- [127] J. Wang, D. Zhang, B. Wu, and M. Luo, "Prediction of distortion induced by machining residual stresses in thin-walled components," *International Journal of Advanced Manufacturing Technology*, The International Journal of Advanced Manufacturing Technology, pp. 1–10, 2018.
- [128] C. S. Prasad, "Finite element modeling to verify residual stress in orthogonal machining," *MS Thesis, Dep. Mech. Eng. Blekinge Inst. Technol. Karlskrona, Sweden*, 2009.
- [129] J. Proudian, "SIMULATING RESIDUAL STRESS IN MACHINING ; FROM POST PROCESS MEASUREMENT TO PRE-PROCESS PREDICTIONS A Thesis Submitted to In Production Engineering and Management By," no. August, 2012.

- [130] Y.B. Guo, "Finite Element Modeling of Residual Stress Profile Patterns in Hard Turning," *Int. Cent. Diff. Data*, vol. 278–281, no. 1, pp. 151–157, 1998.
- [131] X. Yang and C. R. Liu, "A new stress-based model of friction behavior in machining and its significant impact on residual stresses computed by finite element method," *Int. J. Mech. Sci.*, vol. 44, no. 4, pp. 703–723, 2002.
- [132] Y. Ma, S. Liu, P. F. Feng, and D. W. Yu, "Finite element analysis of residual stresses and thin plate distortion after face milling," *Int. Bhurban Conf. Appl. Sci. Technol.*, pp. 67–71, 2015.
- [133] A. Attanasio, E. Ceretti, and C. Giardini, "3D FE modelling of superficial residual stresses in turning operations," *Mach. Sci. Technol.*, vol. 13, no. 3, pp. 317–337, 2009.
- [134] P. J. Arrazola *et al.*, "On the machining induced residual stresses in IN718 nickel-based alloy: Experiments and predictions with finite element simulation," *Simul. Model. Pract. Theory*, vol. 41, pp. 87–103, 2014.
- [135] M. Wan, X. Y. Ye, Y. Yang, and W. H. Zhang, "Theoretical prediction of machining-induced residual stresses in three-dimensional oblique milling processes," *Int. J. Mech. Sci.*, vol. 133, no. August, pp. 426–437, 2017.
- [136] J. C. Outeiro, D. Umbrello, R. M'Saoubi, and I. Jawahir, "Evaluation of present numerical models for predicting metal cutting performance and residual stresses," *Mach. Sci. Technol.*, vol. 19, no. 2, pp. 183–216, 2015.
- [137] Y. Ma, D. Yu, P. Feng, Z. Wu, and J. Zhang, "Finite element method study on the influence of initial stress on machining process," *Adv. Mech. Eng.*, vol. 7, no. 3, pp. 1–10, 2015.
- [138] G. Casalino, F. Facchini, M. Mortello, and G. Mummolo, "ANN modelling to optimize manufacturing processes: the case of laser welding," *IFAC-PapersOnLine*, vol. 49, no. 12, pp. 378–383, 2016.
- [139] D. Umbrello, G. Ambrogio, L. Filice, and R. Shivpuri, "A hybrid finite element method-artificial neural network approach for predicting residual stresses and the optimal cutting conditions during hard turning of AISI 52100 bearing steel," *Mater. Des.*, vol. 29, no. 4, pp. 873–883, 2008.
- [140] Q. Zhang *et al.*, *Prediction of Machining Induced Residual Stresses in Aluminium Alloys Using a Hierarchical Data-Driven Fuzzy Modelling Approach*, vol. 42, no. 23. IFAC, 2009.
- [141] Q. Zhang *et al.*, "Model fusion via a master fuzzy system with special application to engineering materials," *IFAC Proc. Vol.*, vol. 18, no. PART 1, pp. 11732–11737, 2011.
- [142] Q. Zhang, M. Mahfouf, J. R. Yates, C. Pinna, and G. Panoutsos, "Modeling and Optimal Design of Machining-Induced Residual Stresses in Aluminium Alloys Using a Fast Hierarchical Multiobjective Optimization Algorithm," pp. 508–520, 2011.
- [143] A. Reimer and X. Luo, "Prediction of residual stress in precision milling of AISI H13 steel," *Procedia CIRP*, vol. 71, pp. 329–334, 2018.
- [144] K. Ma, R. Goetz, and S. K. Svrivatsa, "Modeling of Residual Stress and Machining Distortion in Aerospace Components," *Am. Soc. Met. Handb.*, vol. 88ABW-2010, pp. 1–41, 2010.
- [145] I. Llanos, J. L. Lanzagorta, and A. Beristain, "Part Distortion Modeling on Aluminum Slender

- Structural Components for Aeronautical Industry,” *Procedia CIRP*, vol. 58, pp. 158–162, 2017.
- [146] O. Fergani, I. Lazoglu, A. Mkaddem, M. El Mansori, and S. Y. Liang, “Analytical modeling of residual stress and the induced deflection of a milled thin plate,” *Int. J. Adv. Manuf. Technol.*, vol. 75, no. 1–4, pp. 455–463, 2014.
- [147] J. C. R. Albino, L. A. Gonçalves Junior, and V. E. Beal, “On the convergence of solid meshes for the prediction of part distortions due to residual stresses,” *Proc. Inst. Mech. Eng. Part C J. Mech. Eng. Sci.*, vol. 233, no. 17, pp. 6209–6217, 2019.
- [148] X. Cerutti and K. Mocellin, “Parallel finite element tool to predict distortion induced by initial residual stresses during machining of aeronautical parts,” *Int. J. Mater. Form.*, vol. 8, no. 2, pp. 255–268, 2015.
- [149] B. Denkena and S. Dreier, “Simulation of Residual Stress Related Part Distortion,” pp. 105–113, 2014.
- [150] S. Dreier, “Simulation des eigenspannungsbedingten Bauteilverzugs,” Gottfried Wilhelm Leibniz Universität Hannover, 2018.
- [151] D. Weber *et al.*, “Simulation based compensation techniques to minimize distortion of thin-walled monolithic aluminum parts due to residual stresses,” *CIRP J. Manuf. Sci. Technol.*, vol. 38, pp. 427–441, 2022.
- [152] D. Weber *et al.*, “Analysis of machining-induced residual stresses of milled aluminum workpieces, their repeatability, and their resulting distortion,” *Int. J. Adv. Manuf. Technol.*, vol. 115, no. 4, pp. 1089–1110, 2021.
- [153] J. K. Rai and P. Xirouchakis, “Finite element method based machining simulation environment for analyzing part errors induced during milling of thin-walled components,” *Int. J. Mach. Tools Manuf.*, vol. 48, no. 6, pp. 629–643, 2008.
- [154] Z. T. Tang, T. Yu, L. Q. Xu, and Z. Q. Liu, “Machining deformation prediction for frame components considering multifactor coupling effects,” *Int. J. Adv. Manuf. Technol.*, vol. 68, no. 1–4, pp. 187–196, 2013.
- [155] X. Jiang, Y. Wang, Z. Ding, and H. Li, “An approach to predict the distortion of thin-walled parts affected by residual stress during the milling process,” *Int. J. Adv. Manuf. Technol.*, vol. 93, no. 9–12, pp. 4203–4216, 2017.
- [156] Q. Zhang *et al.*, “Prediction of Machining Induced Residual Stresses in Aluminium Alloys Using a Hierarchical Data-Driven Fuzzy Modelling Approach,” *IFAC Proc. Vol.*, vol. 42, no. 23, pp. 231–236, 2009.
- [157] X. CERUTTI, “Numerical modelling and mechanical analysis of the machining of large aeronautical parts: Machining quality improvement,” 2014.
- [158] O. Zienkiewicz, R. Taylor, and J. Z. Zhu, *The Finite Element Method: its Basis and Fundamentals: Seventh Edition*. 2013.
- [159] B. Szabó and I. Babuška, *Introduction to Finite Element Analysis: Formulation, Verification and*

Validation. 2011.

- [160] Dassault Systèmes Simuila Corp., “ABAQUS/CAE 2021.” 2021.
- [161] SIMULIA, “Abaqus - SIMULIA User Assistance 2021.” [Online]. Available: https://help.3ds.com/2021/English/DSSIMULIA_Established/SIMULIA_Established_FrontmatterMap/sim-r-DSDocAbaqus.htm?contextscope=all&id=b15ba98a76ce4305b417ecdd54e5394d. [Accessed: 13-Feb-2023].
- [162] K. Venkataraman and K. Venkataraman, *Design of Jigs, Fixtures and Press Tools*. New York, UNITED KINGDOM: John Wiley & Sons, Incorporated, 2015.
- [163] The MathWorks Inc., “MATLAB Version: 9.13.0.2193358 (R2022b) Update 5.” 2022.
- [164] O. Fergani, X. Jiang, Y. Shao, T. Welo, J. Yang, and S. Liang, “Prediction of residual stress regeneration in multi-pass milling,” *Int. J. Adv. Manuf. Technol.*, vol. 83, no. 5–8, pp. 1153–1160, 2016.
- [165] G. Liu, C. Huang, B. Zhao, W. Wang, and S. Sun, “Effect of Machined Surface Integrity on Fatigue Performance of Metal Workpiece: A Review,” *Chinese J. Mech. Eng. (English Ed.)*, vol. 34, no. 1, 2021.
- [166] P. Grant, J. Lord, P. Whitehead, and A. T. Fry, “The Application of Fine Increment Hole Drilling for Measuring Machining-Induced Residual Stresses,” *Appl. Mech. Mater.*, vol. 3–4, no. 2005, pp. 105–110, 2006.
- [167] Vishay Precision Group, “Measurement of Residual Stresses by the Hole-Drilling Strain Gage Method,” 2010.
- [168] E. G. Kirsch, “Die Theorie der Elastizität und die Bedürfnisse der Festigkeitslehre,” *J. Assoc. Ger. Eng.*, vol. 42, pp. 797–807, 1898.
- [169] G. S. Schajer, “Measurement of non-uniform residual stresses using the hole drilling method, a new integral formalism,” *Strain*, vol. 31, no. 2, pp. 63–68, 1995.
- [170] G. S. Schajer, “Application of finite element calculations to residual stress measurements,” *J. Eng. Mater. Technol. Trans. ASME*, vol. 103, no. 2, pp. 157–163, 1981.
- [171] P. Grant, J. Lord, P. Whitehead, and T. Fry, “The application of fine increment hole drilling for measuring machining-induced residual stresses,” *Appl. Mech. Mater.*, vol. 3–4, no. 2005, pp. 105–110, 2005.
- [172] J. Lu, *Handbook of Measurement of Residual Stresses*, Illustrate. Fairmont Press, 1996.
- [173] C. R. Chighizola *et al.*, “Intermethod Comparison and Evaluation of Measured Near Surface Residual Stress in Milled Aluminum,” *Exp. Mech.*, vol. 61, no. 8, pp. 1309–1322, 2021.
- [174] P. V Grant, J. D. Lord, and P. Whitehead, “The Measurement of Residual Stresses by the Incremental Hole Drilling Technique,” *Meas. Good Pract. Guid. No. 53 - Issue 2*, no. 2, p. 63, 2006.
- [175] VEQTER, “Centre-Hole Drilling Technique,” 2014. [Online]. Available: <https://www.veqter.co.uk/files/rsm-techniques/veqter-centre-hole-drilling-technique.pdf>.

- [176] S. Y. Lee, J. Ling, S. Wang, and J. Ramirez-Rico, "Precision and accuracy of stress measurement with a portable X-ray machine using an area detector," *J. Appl. Crystallogr.*, vol. 50, no. 1, pp. 131–144, 2017.
- [177] J. P. Davim, *Surface integrity in machining*. 2010.
- [178] BS EN 485-2, "Aluminium and aluminium alloys — Sheet , strip and plate Part 2: Mechanical properties," *Standards*, pp. 1–90, 2008.

Appendix A

Relaxed Strains depth (μm)	Calculated Stress depth (μm)
16	8
32	24
48	40
64	56
80	72
96	88
128	112
160	144
192	176
224	208
256	240
320	288
384	352
448	448
512	512
576	576
640	640
768	768
896	896
1024	1024
1152	-
1280	-
1408	-
